Hydraulic hazard exposure of humans swept away in a whitewater river

Michael A Strom[1]*, Gregory B Pasternack[1], Scott G Burman[1], Helen E Dahlke[1], Samuel Sandoval-Solis[1]

*Corresponding author

E-mail address: mastrom@ucdavis.edu

[1]Department of Land, Air and Water Resources, University of California, Davis, One Shields Avenue, Davis, CA, USA 95616

Cite as: Strom, M. A., Pasternack, G. B., Burman, S. G., Dahlke, H. E., Sandoval-Solis, S. 2017. Hydraulic hazard exposure of humans swept away in a whitewater river. Natural Hazards. doi:10.1007/s11069-017-2875-6

The final publication is available at Springer via http://dx.doi.org/10.1007/s11069-017-2875-6

Abstract

Despite many deaths annually worldwide due to floods, no strategy exists to mechanistically map hydraulic hazards people face when entrained in a river. Previous work determined water depth–velocity product thresholds for human instability from standing or walking positions. Because whitewater rivers attract diverse recreation that risks entraining people into hazardous flow, this study takes the next step by predicting the hazard pattern facing people swept away. The study site was the 12.2-km bedrock–alluvial upper South Yuba River in the Sierra Nevada Mountains. A novel algorithm was developed and applied to two-dimensional hydrodynamic model outputs to delineate three hydraulic hazard categories associated with conditions for which people may be unable to save themselves: emergent unsavable and steep emergent surfaces, submerged unsavable surfaces, and hydraulic jumps. Model results were used to quantify exposure of both an upright and supine entrained person to collision and body entrapment hazards. Hazard exposure was expressed with two metrics: passage proximity (how closely a body approached a hazard) and reaction time (time available to respond to and avoid a hazard). Hazard exposure maps were produced for multiple discharges, and the areal distributions of exposure were synthesized for the river segment. Analyses revealed that the maximum hazard exposure occurred at an intermediate discharge. Additionally, longitudinal profiles of the results indicated both discharge-dependent and discharge-independent hazards. Relative to the upright body, the supine body was overall exposed to less dangerous channel regions in passage down the river, but experienced more abrupt encounters with the danger that did occur.

Keywords: Hydraulic hazards; River rapids; Floods; Hydraulic jumps; Whitewater

1. Introduction

Worldwide, more than 175,000 people were killed by freshwater floods from 1975 to 2001 (Jonkman 2005), and a review of river flood events found that the majority of fatalities stemmed from drowning or physical trauma (Jonkman and Kelman 2005). Current strategies for flow-related, or hydraulic, hazard assessments involve identifying depth–velocity product thresholds above which humans lose stability from either a standing or walking position. Theoretical studies have characterized friction (sliding) and moment (toppling) instability mechanisms (Keller and Mitsch 1993; Lind et al. 2004; Jonkman and Penning-Rowsell 2008; Xia et al. 2014), and experimental studies have been used to evaluate the predicted thresholds for the occurrence of these mechanisms (Foster and Cox 1973; Abt et al. 1989; Takahashi et al. 1992; Karvonen et al. 2000; Jonkman and Penning-Rowsell 2008; Cox et al. 2010; Russo et al. 2013; Xia et al. 2014). Factors influencing the onset of human instability in a flow include body weight, height, clothing, ground surface composition, slope, entrained debris, flow turbulence, fluid density, psychology, experience, and other variables (Karvonen et al. 2000; Chanson et al. 2014; Milanesi et al. 2015).

Relative to investigating the conditions for instability, simulating the fate of people following the loss of stability has received little attention. McCarroll et al. (2015) modeled the transport of bathers in a rip current as a series of particles in a flow field and simulated multiple escape strategies to evaluate their success. The present study also sought to predict the fate of people carried away in a flow, but in a whitewater river that hosts multiple forms of recreation. The hydraulic hazard exposure of people swept down a river was described, defined herein as the potential for entrained bodies to encounter hazards and incur harm in the form of drowning or physical trauma. To be conservative, it was assumed that any hazard exposure could produce harm and therefore needed to be documented.

1.1. Whitewater river hydraulic hazards

Whitewater rivers contain a variety of elements that create channel complexity and rapids that can be hazardous to people. Boulders transported into a channel by tributaries and landsliding from cliff faces have been found to produce rapids (Dolan et al. 1978; Graf 1979; Webb et al. 1988). Debris flow fan deposits at the mouths of tributaries can be reworked by main channel flows to create downstream rock gardens and additional rapids (Kieffer 1985; Webb et al. 1989). These rock features impose lateral and vertical flow constrictions that generate several wave types, including abrupt transitions from supercritical to subcritical flow in the form of hydraulic jumps (Leopold 1969; Kieffer 1985). The diverse morphologies and arrangements of rock elements and their control on flow served as the basis for the classification of different channel units in bedrock rivers (Grant et al. 1990). The flow features associated with whitewater rivers also spurred the development of the International Scale of River Difficulty in the 1950s by the association American Whitewater in an effort to classify and convey the challenges of traversing rapids. The rating system was revised in 1998 to focus less on describing individual hazards and more on expressing the intangible measure of overall rapid difficulty (Belknap 1998). Consequently, by its design, the system offers no more than qualitative characterizations of each of the six difficulty ratings at the scale of individual rapids.

As an example of a hazardous whitewater river setting, the Mather Gorge and its Great Falls on the Potomac River upstream of Washington, D.C. are notorious for deaths due to deceptive waters and close proximity to a large urban center from which people with varying hazard awareness travel for recreation. The Washington Post published a visually interactive overview of hydraulic hazards present in this canyon where 27 people died 2001–2013 (The perils at Great Falls, The Washington Post, 2013) and 51% of river accidents here are fatal, with 72% of these incidents originating from shoreline-based activities that are not related to boating (Potomac River Gorge Safety Press Conference, National Park Service, 2013). After getting swept from shore or falling out of a craft, collisions and/or entrapment with emergent or submerged rocks can cause physical trauma and/or drowning, and entrapment inside hydraulic jumps exhibiting strong multiphase flow recirculation can hold a body underwater until death.

Although this study focuses on whitewater rivers, similar hydraulic hazards occur during urban flooding, including during storm surges and tsunamis. Instead of hazardous interactions with boulders and bedrock, collisions with and entrapment by features of the urban landscape can cause physical trauma and drowning (Jonkman 2005). Both whitewater rivers and urban floods can also contain floating debris that present an additional hazard, and Penning-Rowsell et al. (2005) introduced a flood hazard equation that uses a debris factor to account for this. Thus, the new methods presented in this study have broader significance to understanding natural flood hazards.

1.2. Meter-scale river maps and models

Characterizing the exposure of humans to hydraulic hazards required a digital terrain model of the topo-bathymetric surface and a hydrodynamic model with a resolution commensurate with the human scale. To determine the local occurrence of hydraulic hazards and then aggregate the results to coarser scales, data collection and mechanistic modeling methods that resolve meter-scale variations were required. Meter-scale data are increasingly available for free (e.g., http://www.opentopography.org) or can be collected at a rapidly decreasing cost with increasing detail. Key technologies include airborne LiDAR mapping of the terrestrial river corridor (Lane and Chandler 2003; Hilldale and Raff 2008), airborne bathymetric LiDAR mapping of shallow, clear water (McKean et al. 2008), and boat-based echosounding of the subaqueous riverbed (Vilming 1998; Muste et al. 2012). To characterize spatially distributed, meter-scale river hydraulics over tens of kilometers at many discharges, two-dimensional (2D) depth-averaged hydrodynamic modeling was used.

1.3. Study objectives

For a segment of the upper South Yuba River (SYR) in Northern California, the objectives of this study were to (1) conceptualize different hydraulic hazards and delineate their locations for multiple discharges, (2) design hydraulics-based metrics to quantify and map the exposure of an entrained human body in the upright and supine positions to these hazards, and (3) determine trends in the hazards as a function of discharge and longitudinal position in the river. This study introduces a systematic, objective, and detailed approach to quantifying and mapping hydraulic hazard exposure within the process-based research paradigm.

2. Study area

The 12.2-km SYR study segment was located on the west side of the Sierra Nevada Mountains beginning at the coordinates {39°20′48.34″N, 120°41′ 37.55″W} and terminating at the town of Washington, California, at the coordinates {39°21′28.55″N, 120°48′11.54″W} (Fig. 1). A thorough description of the study segment is available in Pasternack and Senter (2011), so only the essential details are provided here for brevity. This region is characterized by a Mediterranean climate with an average annual precipitation of 173.9 cm (Western Regional Climate Center) for 1914–2003 at Lake Spaulding, 8 km upstream of the upper extent of the study segment. The drainage area above Washington, CA, is 512.8 km^2 with 310.8 km^2 captured by Spaulding Dam. Regulated releases and unregulated spills occur at the dam. The average daily flow for 1965–2014 measured just downstream at Langs Crossing (USGS gage 11414250) was 3.03 m /s, while the average daily flow at Washington (USGS gage 11417000) for 1942–1972 was 8.44 m^3/s. Inadequate historical flow records prior to flow regulation, periodic, complex changes to flow regulation, interdecadal trends in the hydrologic regime due to forest cover changes, and cumulative, unabated geomorphic impacts from multiple, severe anthropogenic activities, such as hydraulic mining of hillsides, preclude reasonable determination of bankfull discharge. Four tributaries drain into the study segment and two more do so above the study segment but below the dam. The maximum elevation in the watershed is 2552 m above mean sea level, and the channel bed elevation within the study segment ranges from ~780 to 1015 m. Bed material

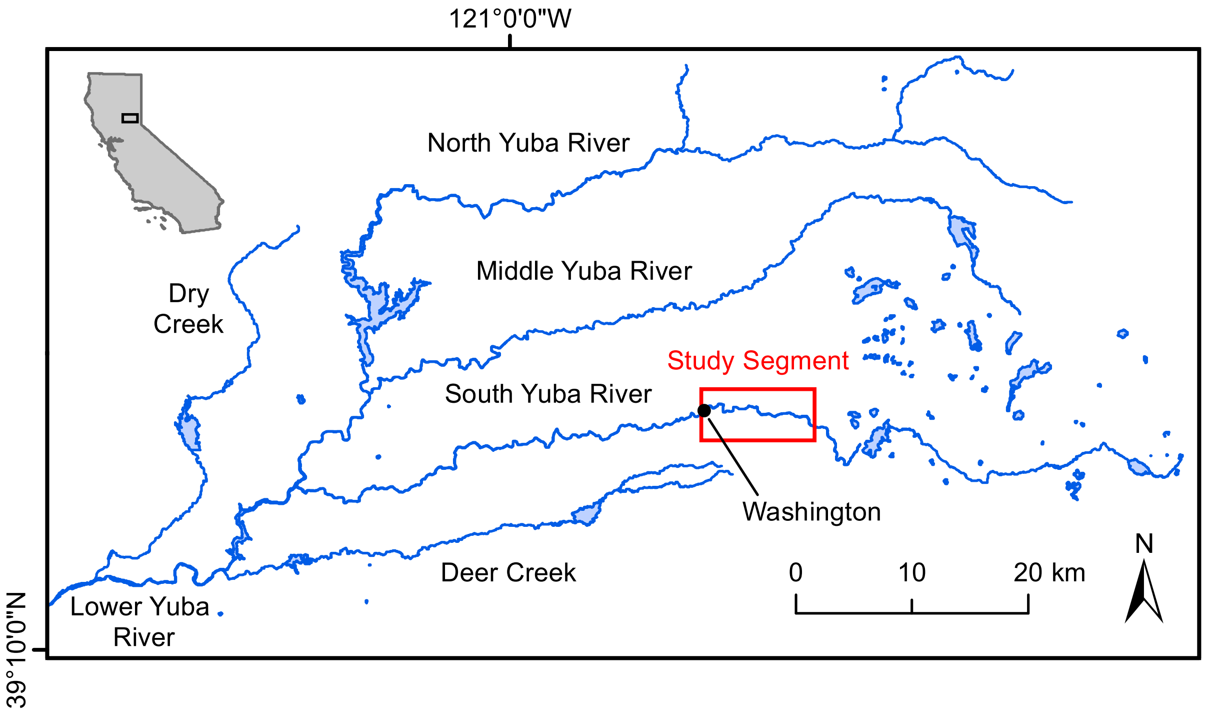
121°0'0"W
North Yuba River
Middle Yuba River
Dry
Creek
Study Segment
South Yuba River
Washington
Deer Creek
0
10
20 km
N
Lower Yuba
River
39°10'0"N

spans sand to large boulders, and extensive bedrock outcrops are associated with canyons and pools. Hydraulic mining was performed at multiple sites within the study segment and has contributed sediment to the channel (Pasternack and Senter 2011).

3. Methods

This article presents an approach to evaluate hydraulic hazards (Sects. 3.2 – 3.4) and then applies it to a case study to find new insights about whitewater rivers. A high-resolution DEM and 2D hydrodynamic model were used in this study, but those elements and data underpinning them are not the focus herein. Increasingly, the frontiers of river science are being built upon such models (e.g., Hauer et al. 2009; Wyrick and Pasternack 2014; Gonzalez and Pasternack 2015; Strom et al. 2016), with the aim of journal articles to present the novel developments. The underpinnings and validation of the data and model are important background and thus explained in Online Resource 1 to keep the article's focus on new science.

3.1. Meter-scale data and hydrodynamic model

Field data were used to characterize geomorphic, hydrologic, and hydraulic attributes of the remote and hazardous SYR at ~1-5 m resolution, including 2D hydrodynamic modeling. An airborne LiDAR survey mapped 34,113 large, emergent boulders within the wetted area at the heavily regulated low base flow−an important and unique aspect of this study in order to address hydraulic hazards (Pasternack and Senter 2011).

A previously peer-reviewed, meter-scale 2D hydrodynamic model of the SYR was used in this study. Three-dimensional (3D) hydrodynamic models are available, but have high computational demands for the >10 km range and 1-m resolution needed. The new science and methods in this study do not depend on whether the model is 2D or 3D, just that the outputs are meter-scale to resolve hydraulic hazards. Scientific exploration with 3D models is ongoing and can be expected to eventually surpass the current use of 2D models. The use of a morphodynamic model was also not considered, because this study only investigated a range of flows for which large boulders would not be in transport (Pasternack and Senter 2011). This decision was made because most recreational risk and mortality occur at flows when coarse sediment is not in motion. Non-recreational mortality often does occur during extreme floods that are channel-changing events, and this study does not address such geomorphic dynamism. The Sedimentation and River Hydraulics Two-dimensional Model (Lai 2008) solved the depth-averaged St. Venant equations using the finite-volume method to simulate both subcritical and supercritical flows, which was key to predicting the occurrence of hydraulic jump hazards. Model validation is detailed in Online Resource 1. Validation results were within accepted standards (e.g., Gard 2003; Pasternack et al. 2006b; Reinfelds et al. 2010).

The assumption of 2D flow is strictly violated through waterfalls and inside hydraulic jumps, but these are a small fraction of the model domain. Additionally, our field experience with evaluating model performance for point velocity in waterfalls of the SYR revealed that the problem primarily affects the positioning of the peak velocity in a vertical drop and not the presence and position of the hydraulic jump, which were more critical for this study. Support for this viewpoint and application exists in the literature where 2D models have been used to investigate settings with complex 3D flows, such as dam-break-induced floods (Peng 2012), spillway flow (Ying and Wang 2012), and other boulder-bed streams (Harrison and Keller 2007). Therefore, 2D modeling was appropriate to use for this purpose of mapping hydraulic jumps.

Model results used in this study were for snowmelt-driven flows of 15, 31, 85, and 196 m^3/s, which correspond to the 70^{th}, 82^{nd}, 89^{th}, and 92^{nd} percentile values, respectively, for the daily mean discharge series at the Langs Crossing gage. These discharges are also higher than the daily mean flow reported for the Washington gage at the downstream end of the segment, and they span the approximate discharge range across which kayakers and rafters have been reported to run the river (Jolly Boys and Golden Quartz runs of the South Yuba River, A Wet State, http://www.awetstate.com/1Alph.html#CA).

3.2. Human body abstraction

A human body can assume multiple positions in a flow, which changes the exposure to surrounding hazards. Floating with feet pointed downstream in the supine position is a commonly reported strategy for safe passage known as defensive swimming (Whitewater skill: How to swim, Rapid Media, https://www.rapidmedia.com/rapid/categories/skills/1288-whitewater-skill-how-to-swim.html), while floating with legs extended downward into the water column may be used by someone who does not have this training or is otherwise unable to maintain the supine position. While there are positions that are intermediate between these two, the supine and upright positions correspond to the end members of exposure to hazards beneath the water surface assuming that the head remains unsubmerged. The supine position maximizes the distance between the body and a submerged hazard while the upright position minimizes this distance. To represent both positions, two safety zones were defined as the cylinders formed when a 1.8 m tall body was rotated about its centroid in the upright (Fig. 2a) and supine (Fig. 2b) positions, giving cylinder radii of 0.9 m (Table 1). A cylinder height of 1.5 m was used for the upright body safety zone as it was assumed that a person moving with legs fully extended downward was able to maintain their head above the water. A height of 0.75 m was used for the supine body safety zone. By tracking the location of the safety zone perimeter in relation to hazards, a variety of different upright and supine body positions were accounted for.

3.3. Delineation of hydraulic hazards

To identify hydraulic hazards, hazard types were first defined and then algorithms were developed to map their locations for each of the four discharges investigated. A 2D modeling approach was determined to be suitable for addressing two risks associated with people in a river. First, people can collide with emergent and submerged rocks that cause physical trauma. Second, people can get trapped below the water surface by submerged rocks or hydraulic jumps, leading to drowning. There was value in distinguishing between emergent and submerged rocks, because this attribute affects one's ability to see the hazard and avoid it. Also, each one poses a different kind of hazard. Emergent rocks primarily cause blunt force trauma and also pose a risk of partial pinning or wrapping. Submerged rocks may also cause those, but they are especially dangerous due to their potential to cause drowning due to foot entrapment and pinning beneath the water surface by the flow. In conceptualizing the hazards associated with rock elements, there existed significant uncertainty concerning what sizes and spatial arrangements of rocks were most prone to causing physical

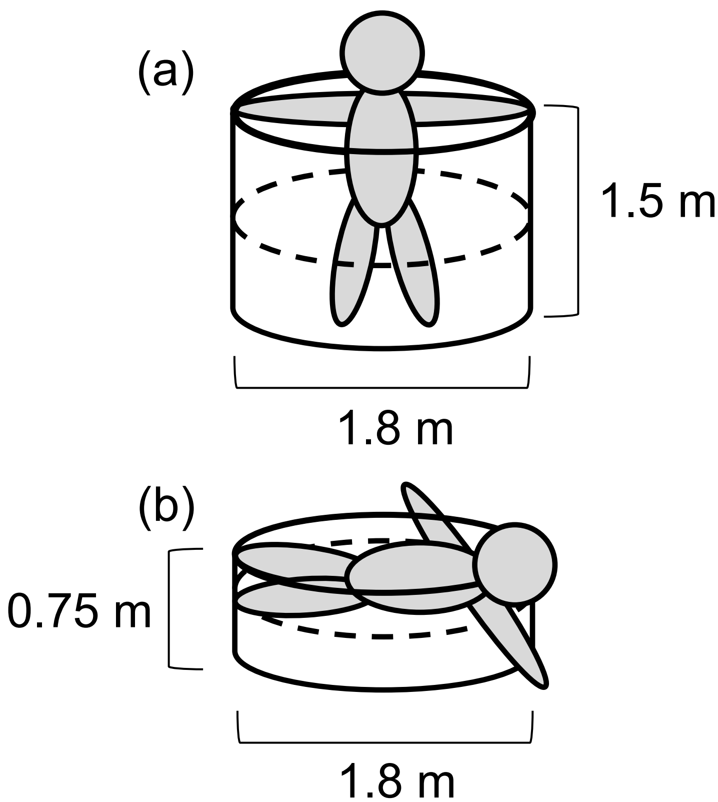

(a)
1.5 m
1.8 m
(b)
0.75 m
1.8 m

Table 1 Model parameters with values used for this study

Parameter	Value used	
Threshold orientation angle for node in jump (°)	150	
Intermediate passage proximity (m)	0.9	
Max passage proximity (m)	1.8	
Intermediate reaction time (s)	5	
Max reaction time (s)	10	
	Body position	
	Upright	Supine
Safety zone radius (m)	0.9	0.9
Safety zone height (m)	1.5	0.75
Freely floating savability threshold (m^2/s)	0.3	0.3
Foot-entrapped savability threshold (m^2/s)	0.3	0.3
Distance required for a freely floating person to save themselves (m)	0	0
Max depth to assess freely floating savability (m)	1.5	0.75
Max depth to assess foot-entrapped savability (m)	1.5	0.75
Min depth to assess freely floating savability (m)	0	0
Min depth to assess foot-entrapped savability (m)	0	0

trauma or body entrapment. Assuming that substrate of any size and configuration had the potential to cause harm under certain flow conditions, the literature on human stability in a flow provided some basis for determining the flow conditions that would make the substrate hazardous. A conservative assumption was also made to treat all hydraulic jumps as hazardous since quantifying jump severity required complex analyses beyond the scope herein. The below section introduces a concept used to discriminate between safe and hazardous flow conditions for an entrained body followed by sections that explain how each of the hydraulic hazard categories were defined and delineated.

3.3.1. Savability

In keeping with past research concerned with human stability in a flow, this study used a depth-velocity product for delineating the surface hazard types. Reported depth-velocity product thresholds above which adult humans lose stability from an already standing or walking position range from about 0.6-2 m^2/s (Abt et al. 1989; Karvonen et al. 2000), though the topic at hand for this study was not a statics problem involving the loss of stability, but a dynamics problem involving the potential to regain stability beginning from an entrained position. For a freely floating body, savability was defined as the ability for the person to overcome further transport by regaining footing in a stable, standing position with head above the water surface. For an entrained body that suddenly experienced foot entrapment, savability referred to the capacity to avoid getting swept over and held underwater, and instead maintain a controlled upright position. A rock surface could therefore be described as savable if the ambient flow conditions allowed a freely floating or foot-entrapped person to save themselves by achieving a stable standing position. Halting one's forward progression while moving freely with the flow or righting oneself following foot entrapment were not assumed to be equivalent to maintaining upright stability from an already standing or walking position, and it was reasoned that the threshold depth-velocity product below which saving was possible must be lower than that for upright stability due to an entrained body's momentum. A value of 0.3 m^2/s was chosen for this study to be the threshold depth-velocity product for savability (Table 1) with lower values corresponding to the absence of hydraulic hazards given a person's ability to save themselves and avoid harm. A similar approach was taken by McCarroll et al. (2015) to determine whether a simulated bather had escaped a rip current and reached a safe area by evaluating both the depth and a hazard rating that uses a depth-velocity product. Co-author Pasternack has extensive personal experience with savability in whitewater rivers and training beginners with river safety. From his experience, the threshold value is reasonable for normal recreational boaters and swimmers. It will be significantly lower for inebriated inadvertent swimmers (a common presence on whitewater rivers) and higher for whitewater experts.

It is important to note that this threshold value is only a rough estimate as this study did not aim to experimentally determine this value, but instead to introduce the concept of savability for which future investigation is needed. For comparison, 0.3 m^2/s falls within the low hazard category proposed by Cox et al. (2010) for children and adults that permits stable standing and wading. These authors also suggested 0.8 m^2/s as the working limit for trained safety personnel. While no depth and velocity data were collected to identify the threshold for regaining stability, Cox et al. (2004) posited that once footing is lost, less hazardous flow conditions are required for footing to be regained due to greater bodily surface area presented to the flow. It is also more challenging to perform an athletic dynamic maneuver to regain footing than it is to make small weight shifts to sustain existing footing, especially as one becomes more tired through the exertions of avoiding hydraulic hazards.

3.3.2. Emergent unsavable surface hazards

Since no strong basis existed for discriminating among different substrate sizes and arrangements in terms of the associated hazard, the full topographic surface was considered in the hydraulic hazard delineation. The perimeters of emergent surfaces where depth = 0 m were first identified. Next, the perimeters were delineated as emergent unsavable surface hazards for a freely floating or foot-entrapped body in the upright position if the adjacent water had a depth <1.5 m and a depth-velocity product >0.3 m^2/s (Fig. 3; Table 1). This meant that upon encountering an emergent surface under these flow conditions, a person could not save themselves to regain a stable standing position and was instead at risk of experiencing involuntary physical contact and associated harm.

In areas where emergent surfaces abutted water deeper than 1.5 m, the depth was considered too great to permit a 1.8 m tall person to save themselves into a standing position with head above the water surface. Therefore, the depth-velocity product threshold was not evaluated in these situations. It was reasoned that emergent surfaces next to deep, slow water were less likely to be hazardous than those next to deep, fast water. However, no threshold velocity could be discerned for what constituted hazardous due to the complexities of describing the interaction of a body with a near-

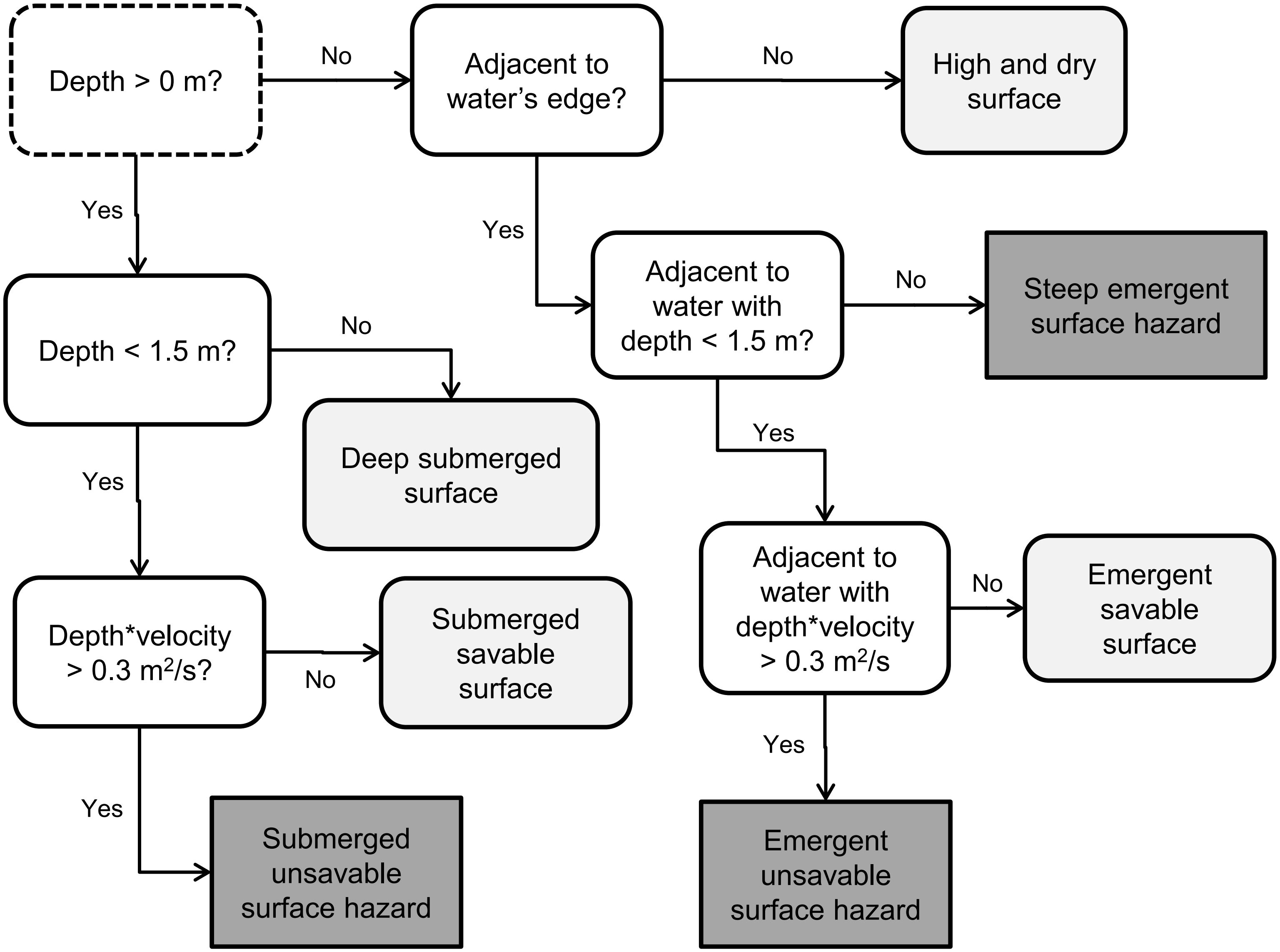
Depth > 0 m?
No
Adjacent to water's edge?
No
High and dry surface
Yes
Yes
Adjacent to water with depth < 1.5 m?
No
Steep emergent surface hazard
Depth < 1.5 m?
No
Deep submerged surface
Yes
Yes
Adjacent to water with depth*velocity > 0.3 m²/s
No
Emergent savable surface
Depth*velocity > 0.3 m²/s?
No
Submerged savable surface
Yes
Yes
Submerged unsavable surface hazard
Emergent unsavable surface hazard

vertical rock surface, so the entirety of these surfaces was designated as steep emergent surface hazards for the sake of caution. Very few of these hazards were present along the study site, so they were lumped with the emergent unsavable surface hazards.

3.3.3. Submerged unsavable surface hazards

Submerged surfaces were designated as unsavable and therefore hazards if flow conditions prevented someone from regaining a standing position in these locations such that a traumatic collision or underwater entrapment could result. Specifically, submerged surfaces with depth <1.5 m and a depth-velocity product >0.3 m^2/s were identified as submerged unsavable surface hazards for a freely floating or foot-entrapped body in the upright position (Fig. 3; Table 1). The savability threshold was only evaluated for surfaces shallower than 1.5 m as deeper surfaces were considered to be out of reach for a 1.8 m tall upright person to save themselves on. While there conceivably existed a minimum depth for which a body was not at risk of submergence and drowning regardless of velocity, regaining a controlled stance to avoid hazard contact and physical trauma could still be inhibited given high velocity. Therefore, 0 m was used as the lower depth limit for evaluating the savability threshold (Table 1). Additionally, savable surfaces were also delineated as these locations were relevant to later analyses.

Unsavable and savable surfaces exposed to a body in the supine position (Fig. 2b) were mapped using the same steps as those described above but with savability evaluated down to a depth of 0.75 m (Table 1). This was intended to represent the situation in which a freely floating or foot-entrapped person in the supine position attempted to save themselves into a standing position on surfaces less than 0.75 m in depth. While it was reasoned that the savability threshold for a supine body that's either freely floating or foot entrapped should still fall below the threshold for stability from an already standing position, there was no strong basis for altering the threshold relative to that used for the freely floating or foot-entrapped upright body. Therefore, the savability threshold was maintained at 0.3 m^2/s.

3.3.4. Hydraulic jump hazards

The final hazard described in this study was hydraulic jumps, which can occur due to submerged surfaces and therefore account for an additional hazard associated with these inundated features. The presence of aeration is a critical component of the jump hazard (Valle and Pasternack 2002, 2006), as the level of aeration can be large enough to prevent lifejacket buoyancy from supporting a person above the water surface while also small enough to make the multiphase zone unbreathable. This study only investigated the presence or absence of hydraulic jumps, as identified by the transition from supercritical to subcritical flow in the 2D model output. The scheme introduced in this study for locating hydraulic jumps is itself a novel tool that could be used in the study of spatially explicit mountain river hydraulics. The general steps involved identifying supercritical regions, isolating the perimeters of these regions, and then analyzing the flow vectors at the model mesh nodes adjacent to the perimeters to determine those downstream of and within a jump. The same hydraulic jumps hazards were used for the supine body scenario as for the upright body, as these features were assumed to be exposed to anything moving along at the water's surface.

For each modeled discharge, supercritical flow regions were identified, and the orientations of the flow vectors at computational mesh nodes were computed to isolate the nodes immediately downstream of the supercritical flow where jumps, by definition, occurred. Given the angle α of the flow vector at each mesh node (Fig. 4a) and the angle β associated with the line segment connecting that node to a point on the perimeter of a supercritical flow region, the orientation angle γ of the flow vector to the point was computed using the expressions below.

$$\beta > \alpha: \gamma = |\beta - 180 - \alpha| \quad (1)$$

$$\beta < \alpha: \gamma = |\beta + 180 - \alpha| \quad (2)$$

It was necessary to select a certain threshold orientation angle γ to isolate mesh nodes sufficiently downstream of the supercritical flow to represent the jump location. An angle of γ = 90° was tried initially, but this value erroneously included too many mesh nodes on the upstream side of the supercritical flow due to raster edge effects. A stricter threshold of γ = 150° was ultimately chosen such that the majority of the isolated mesh nodes occurred along the appropriate downstream boundary of the supercritical flow (Fig. 4b).

3.4. Characterizing hazard exposure

After delineating hazard locations, two criteria were introduced to describe the instantaneous hazard exposure at any point in the river where a body might be located during transit. These included passage proximity, i.e., how close a person would be swept toward a hazard if they were unable to save themselves along the way, and reaction time, i.e., how much time was available for the person to swim against the

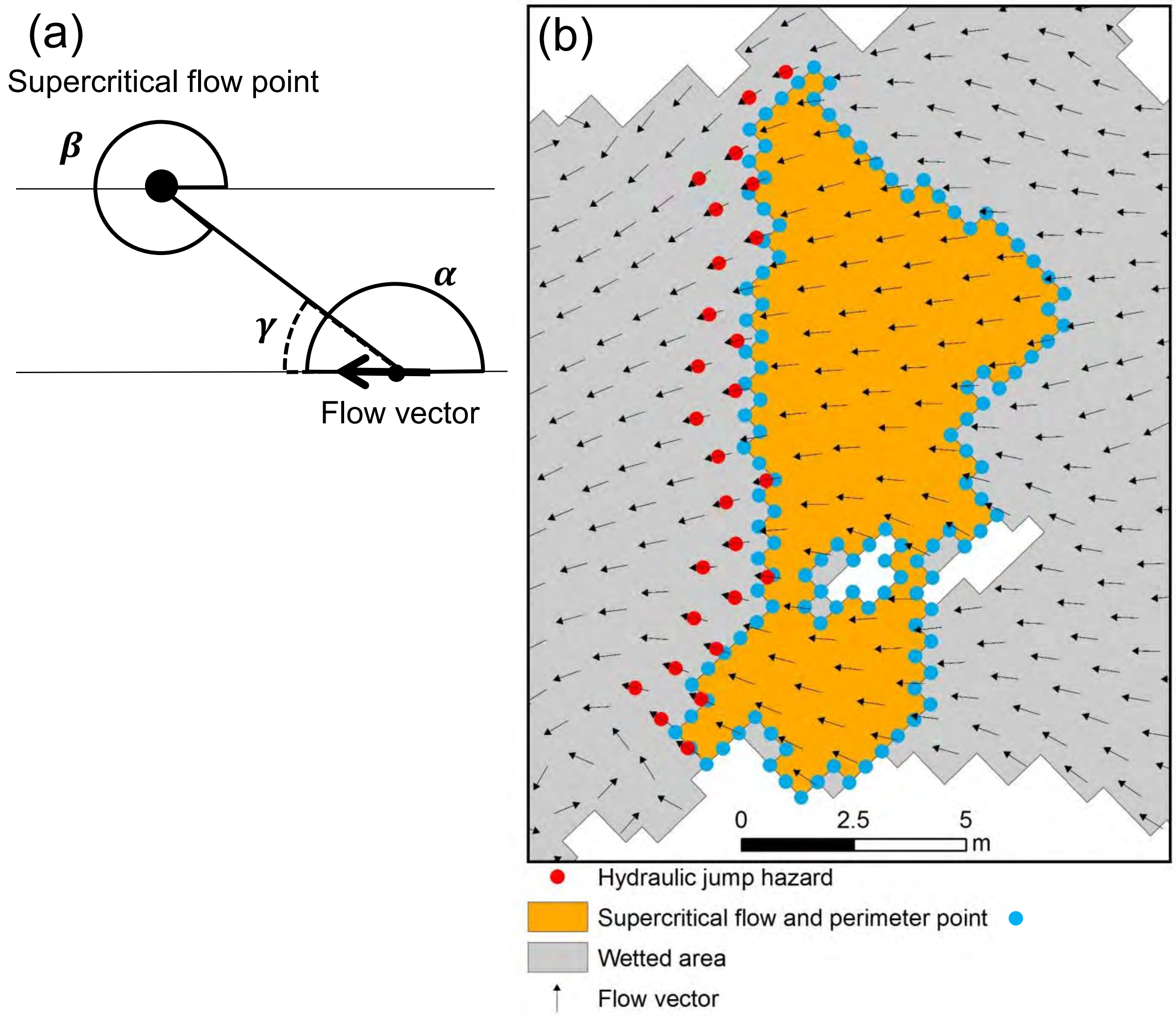

(a)
Supercritical flow point
β
α
γ
Flow vector
(b)
0
2.5
5
m
Hydraulic jump hazard
Supercritical flow and perimeter point
Wetted area
Flow vector

current to change their trajectory and avoid a close hazard encounter. A key factor in evaluating hazard exposure is human motility that complicates the prediction of where a body will move through a flow. Instead of trying to guess or simulate motile behavior and determine the effects on hazard exposure, this study used the instantaneous trajectory at all positions in the flow to map the hazard exposure and gage the need for motility to avoid hazards. While hazard exposure was described using the hazard locations, flow direction, and velocity magnitude, characterizing the vulnerability of people to harm upon encountering a hazard was beyond the scope of this study. The risk of physical trauma or drowning was represented by describing the hazard exposure with the passage proximity and reaction time metrics and assuming that harm would result if a hazard encounter were to occur.

An instantaneous trajectory of constant velocity and direction was projected from the flow vector at each 2D model node, and these trajectory attributes were used to quantify the two metrics as a means of characterizing the hazard exposure associated with each node in the flow. This approach of projecting constant direction and velocity can both over and underestimate the exposure to hazards, because at any given node in the flow, the direction and velocity can either be more or less conducive to hazard exposure than the conditions experienced by the body along the remainder of its actual path. For example, the trajectory at one location might have a high velocity and be directed at a hazard, while further down the path the velocity could decrease and the direction change to a safer area, or vice versa.

3.4.1. Passage proximity

For a body moving along a constant trajectory set by the flow vector at the mesh node to which the body's centroid was momentarily coincident, the passage proximity represented the closest distance reached between the centroid and a point along the perimeter of an unsavable surface, savable surface, or hydraulic jump. This occurred when the orientation angle γ as calculated with Equations (1) or (2) between the centroid and point equaled 90°, so this angle was used as the threshold for isolating mesh nodes upstream of the points. For each of the four discharges, orientation angles were calculated between each mesh node and each of the points. An upstream position with an orientation angle less than 90° meant that the coincident centroid had yet to reach its passage proximity p to the point (Fig. 5), while a downstream position meant that the centroid would only be carried further away from the point. For those pairs of nodes and points exhibiting an upstream node orientation, the orientation angle was used to calculate the passage proximity as given below, while it was not appropriate to compute the metric in the case of downstream node orientation.

$$\mathrm{p} = \sin(\gamma)\,\mathrm{x} \quad (3)$$

3.4.2. Reaction time

Reaction time was introduced as the second metric to characterize exposure, specifically to account for velocity and convey the imminence of a potential encounter. This metric refers to the time available to avoid a hazard given the flow velocity regardless of whether this time is sufficient for a person to actually avoid it, which depends on a person's swimming ability, consciousness, etc. For a body moving along

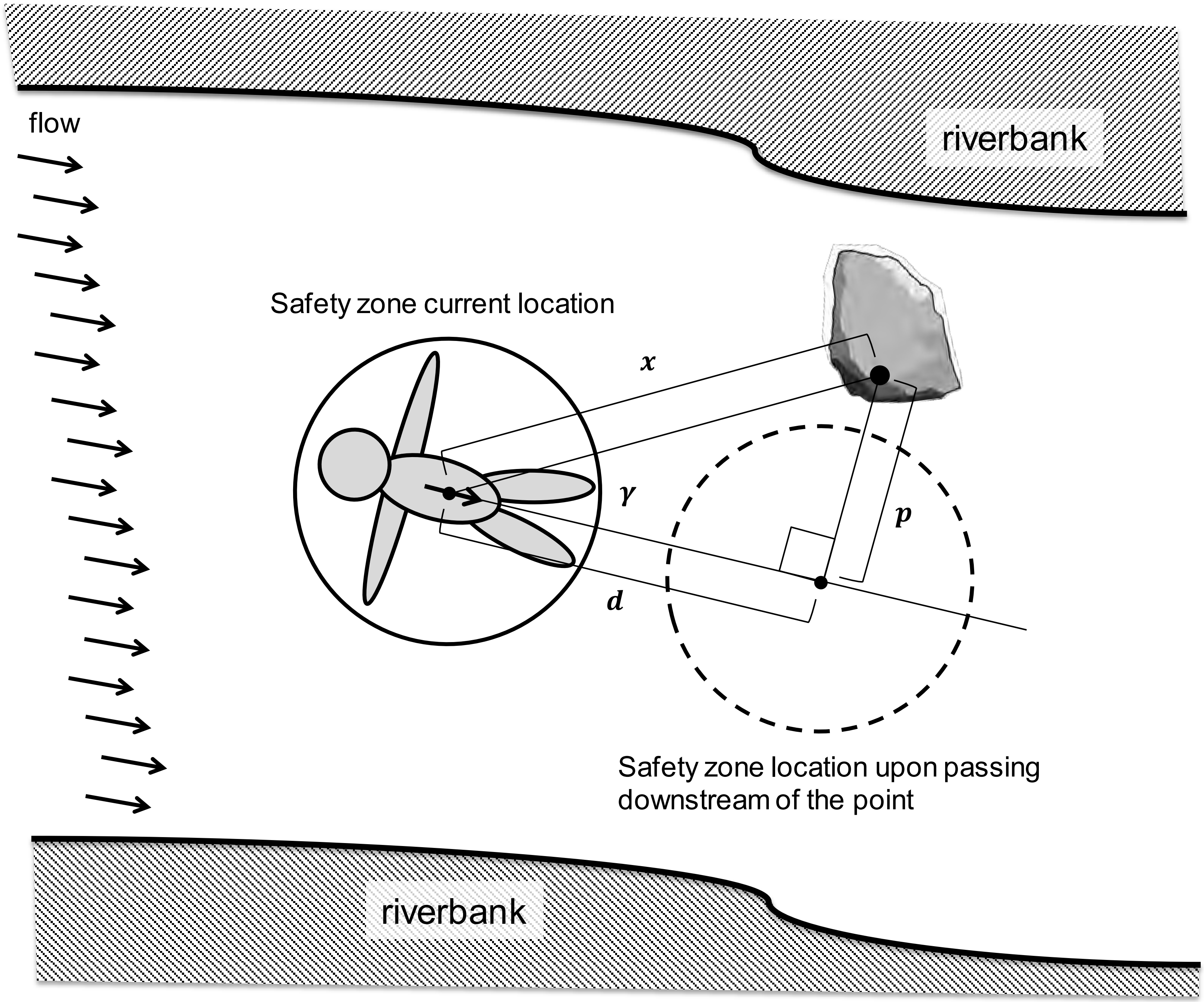

flow
riverbank
Safety zone current location
x
γ
p
d
Safety zone location upon passing downstream of the point
riverbank

a constant trajectory at a velocity v, the reaction time computation depended on whether the body's centroid would reach within 0.9 m of an unsavable surface, savable surface, or hydraulic jump point. If the centroid was not going to approach the point within this distance (p > 0.9 m) as depicted in Fig. 5, then the reaction time was calculated as follows with d equal to the distance traveled by the body before passing downstream of the point.

$$t = \frac{d}{v} = \frac{\cos(\gamma)x}{v} \quad (4)$$

Conversely, if the body's centroid was going to approach the point within this distance (p < 0.9 m), then the reaction time was computed using the below equations where lengths b, c, and r and angles e, f, and g are defined in Fig. 6.

$$b = \tan(\gamma)\, x \quad (5)$$

$$e = 90 - f - g = 90 - \cos^{-1}\left(\frac{p}{r}\right) - \cos^{-1}\left(\frac{p}{b}\right) \quad (6)$$

$$c = \sin(e)\, r \quad (7)$$

$$t = \frac{d}{v} = \frac{c}{\sin(\gamma)v} \quad (8)$$

3.4.3. Total hazard exposure

For each discharge, the computation of passage proximity and reaction time was first made separately for emergent unsavable surfaces, submerged unsavable surfaces, and hydraulic jumps to assess the exposure to each hazard category irrespective of the presence of the others. Savable surfaces were included in each computation to account for encounters with these safe areas that were assumed to permit saving. Only surfaces

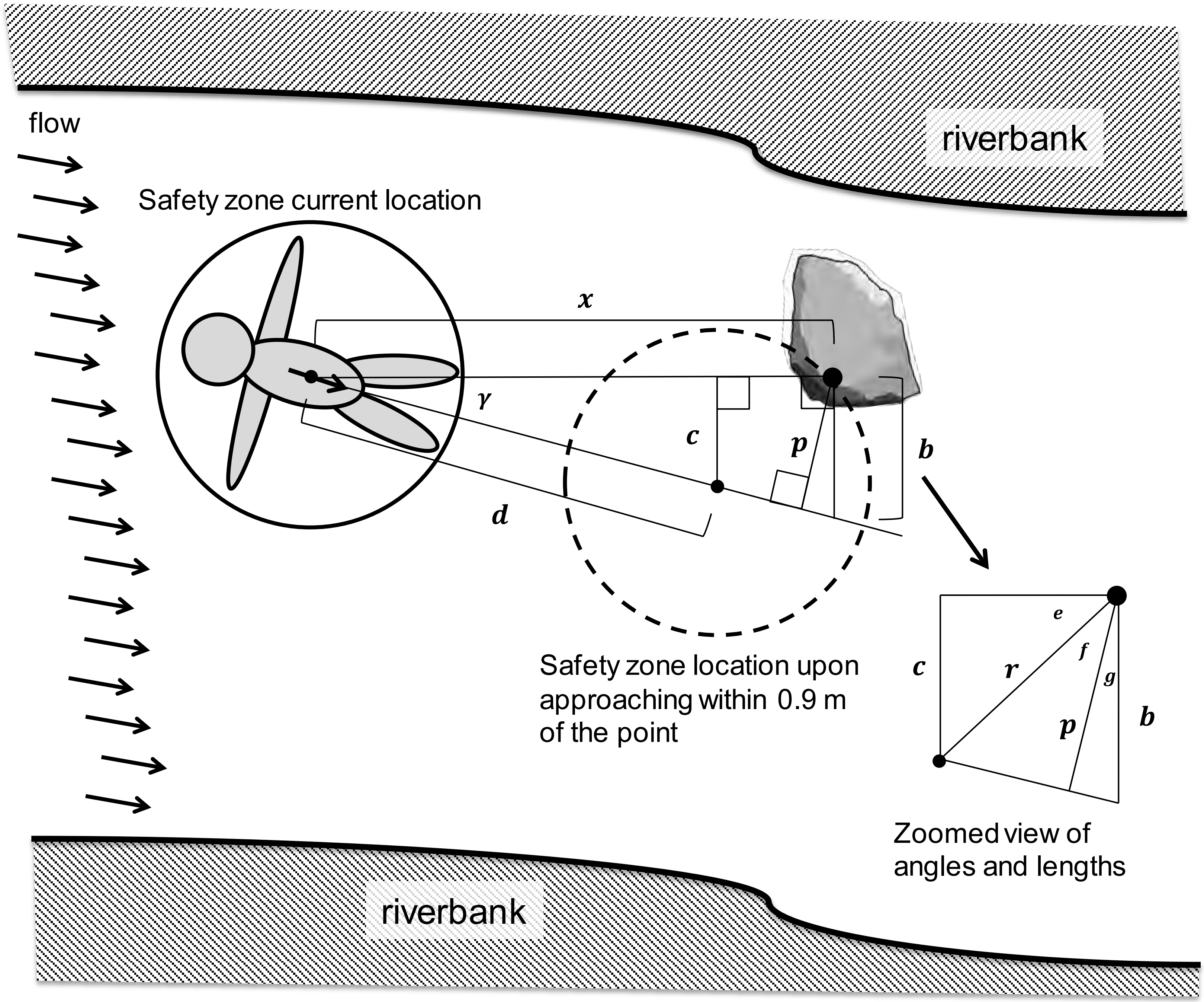

flow
riverbank
Safety zone current location
x
γ
c
p
b
d
Safety zone location upon approaching within 0.9 m of the point
e
f
g
c
r
p
b
Zoomed view of angles and lengths
riverbank

delineated with respect to the upright body's 1.5-m tall safety zone were used in these individual hazard category computations. Next, the points for all the hazard categories and savable surfaces were combined and the two metrics were again calculated to characterize the total hazard exposure for the upright body. Total hazard exposure was defined to be the exposure of a body to all of the three hazard types, and lastly it was also calculated with the hazards delineated for the supine body such that a comparison could be made with the total hazard exposure for the upright body.

3.4.4. Mapping hazard exposure

The next step was to bin the values of the two metrics for visual purposes as well as to quantify the resulting areal extent of each bin. For example, how much of the river segment at a given discharge exhibited the potential for encountering a hazard within 5 s? A baseline level of hazard exposure relevant for mapping was first established by constraining the range of values for the metrics. A hazard with a sufficiently large passage proximity, here defined as greater than twice the safety zone radius (1.8 m), was treated as posing no threat to a body regardless of how short the reaction time was (Table 1). Similarly, it was decided that hazards with reaction times larger than 10 s were not a threat no matter how close the passage proximity was. These values were somewhat arbitrarily chosen, but greater than 10 s was considered to be relatively safe with adequate time for a person to evaluate the situation and react accordingly to the flow, and over 1.8 m was judged to be plenty of distance between the hazard and body's centroid to avoid an encounter.

Two scenarios were considered for assigning a passage proximity and reaction time to each mesh node. Where encounters were predicted to occur between the safety zone and multiple hazard points based on the velocity and trajectory associated with a given node, the hazard point with the shortest reaction time for an encounter determined both the passage proximity and reaction time for the node (Fig. 7a). Values weren't assigned if the shortest reaction time was associated with a savable surface point because these encounters were assumed to permit a person's saving and avoidance of downstream hazards. If the safety zone was predicted to near miss hazard points with passage proximities between 0.9 and 1.8 m, then the point with the closest passage proximity was selected to set the values of the two metrics at the node (Fig. 7b).

After assigning metric values, rasters were created for passage proximity and reaction time. To classify the values of the passage proximity (PP) raster in the context of the human body safety zone dimensions, a rating of two (PP2) was assigned for passage proximities less than 0.9 m that corresponded to hazard encounters (Fig. 7a). This rating was also given to cells upstream and within 0.9 m of a hazard point, as bodies in this area were being actively pushed into the hazard. A rating of one (PP1) was given for passage proximities between 0.9 and 1.8 m, which represented the near-miss scenario (Fig. 7b). A rating of zero (PP0) was assigned for cells with no downstream hazards less than 10 s away or with passage proximities under 1.8 m. The reaction times (RT) were assigned a rating of zero (RT0) for greater than 10 s or for passage proximities over 1.8 m, one (RT1) for between 5 and 10 s, and two (RT2) for under 5 s or if a cell was already within 0.9 m of a hazard point. For mapping the exposure to submerged unsavable surface hazards, PP3 and RT3 were given to cells that exhibited unsavable conditions to represent the immediate exposure of the body's

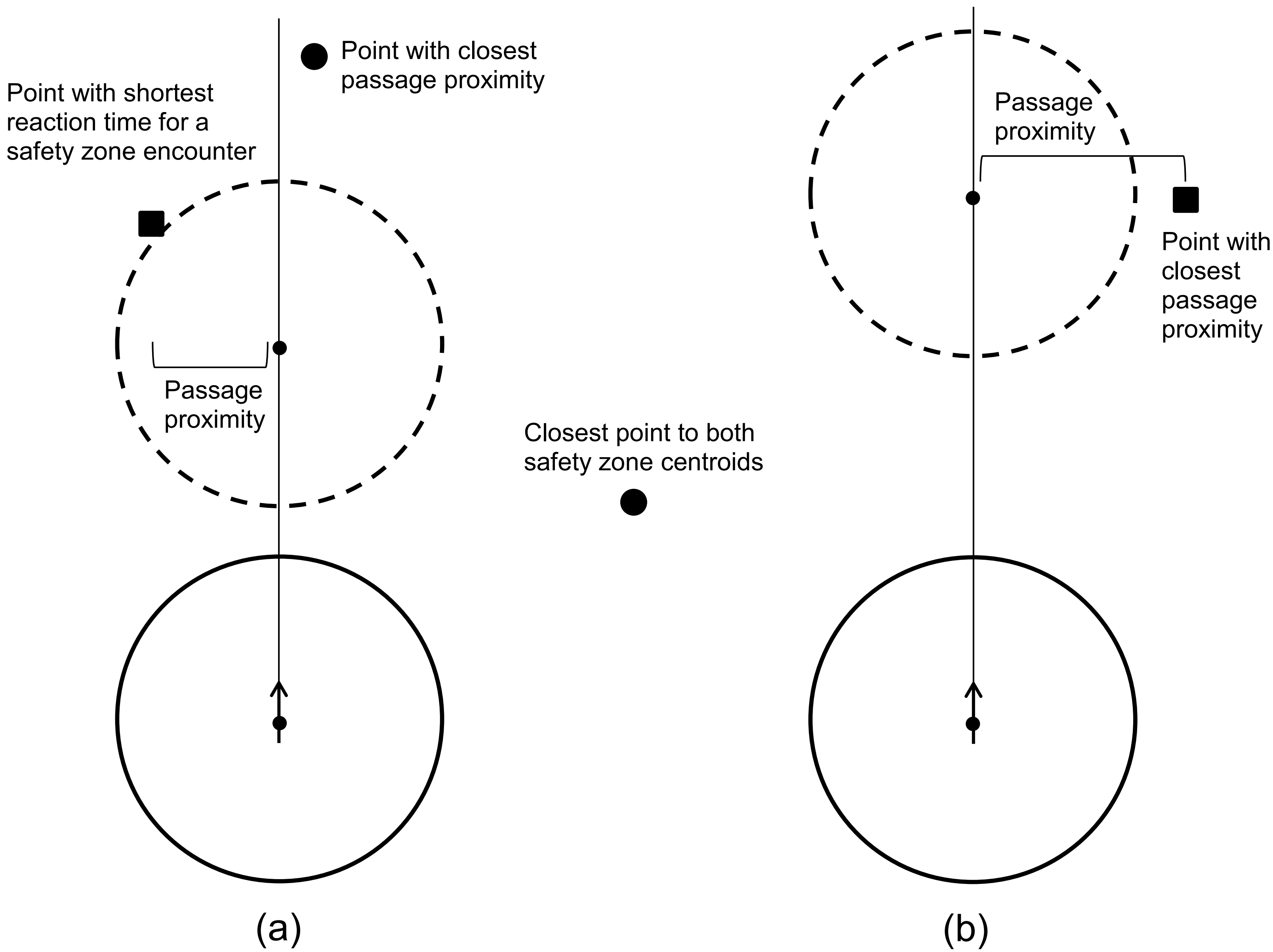
Point with closest
passage proximity
Point with shortest
reaction time for a
safety zone encounter
Passage
proximity
Closest point to both
safety zone centroids
Passage
proximity
Point with
closest
passage
proximity
(a)
(b)

centroid to the underlying hazard. Overlapping passage proximity and reaction time rating areas were then paired to express hazard exposure with six different ratings: no hazard (PP0/RT0), distant near miss (PP1/RT1), imminent near miss (PP1/RT2), distant collision (PP2/RT1), imminent collision (PP2/RT2), and immediate exposure (PP3/RT3). For example, Fig. 8 shows an emergent surface bound by a dashed line with hypothetical paired passage proximity and reaction time ratings on the upstream side of the surface. Lastly, the fraction of the wetted area occupied by each paired rating for a given discharge was computed.

3.4.5. Longitudinal profiles

To provide a basic landscape context for the hazard analysis, the average elevation at each longitudinal position through the river valley was computed for the study segment. Next, the longitudinal distribution of total hazard exposure for each discharge was determined by computing the fraction of the wetted area at each position along the river that exhibited some form of exposure, e.g., PP1/RT1 or PP1/RT2, from at least one of the hazards. These hazard exposure, or danger, fractions were plotted as a longitudinal series in the downstream direction to reveal the locations of more and less dangerous regions encountered in passage down the river. Additionally, the covariance between the danger fraction distribution at 15 m^3/s and that at each of the higher discharges was computed and plotted as longitudinal series to reveal how increasing discharge influenced the locations of dangerous regions. Lastly, the cumulative distribution of the longitudinal series of danger fractions was plotted for each discharge. The raw danger areas were not used to generate these cumulative distributions because the danger fractions more meaningfully represented the exposure

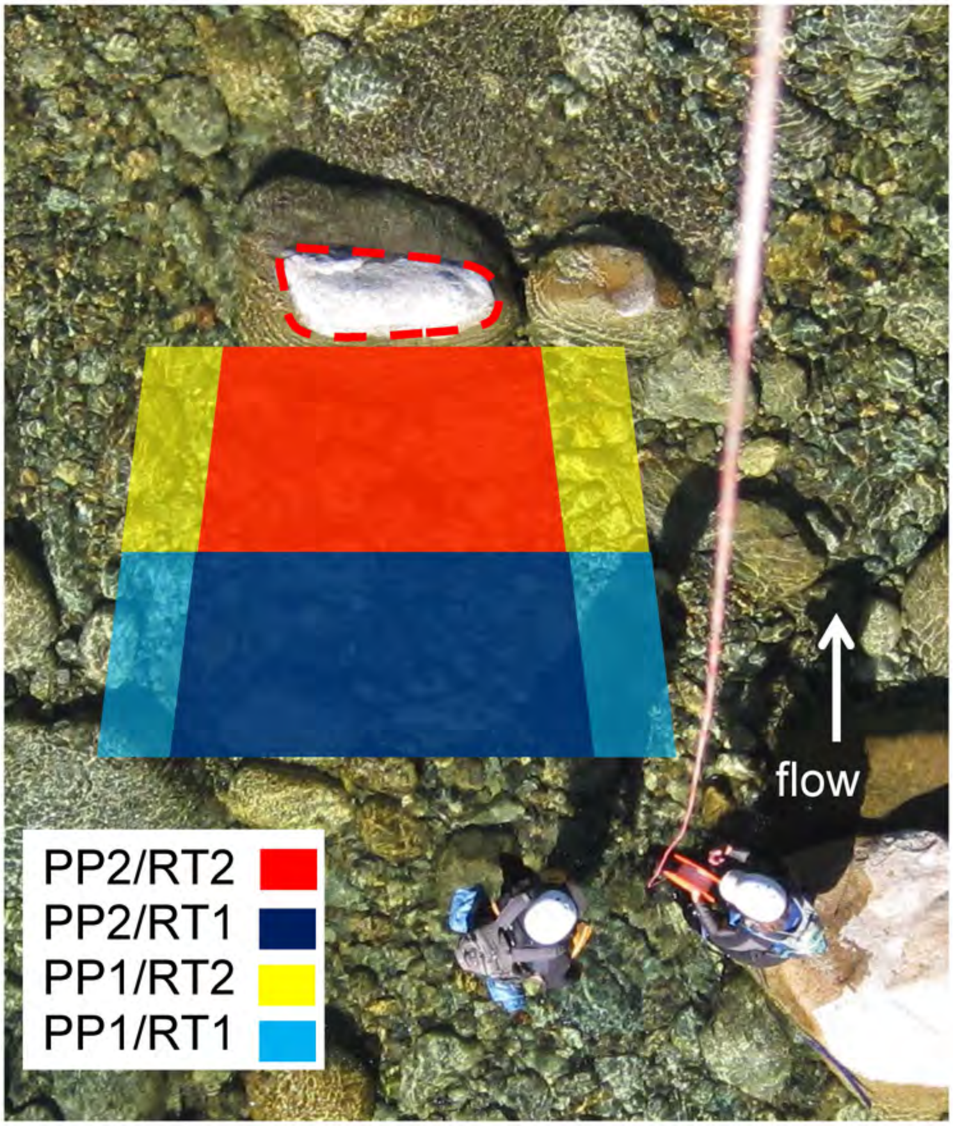
flow
PP2/RT2
PP2/RT1
PP1/RT2
PP1/RT1

of a body to danger while in transit downstream. For example, a person could enter a region of the river with a large total danger area, but the channel could be very wide here such that the danger fraction is low. In contrast, a region that has less danger area but is also very narrow would exhibit a high danger fraction, which accurately expresses a more unavoidable exposure to hazards.

3.4.6. Adjustable model parameters

At this time, the model relies on new parameters that are logical and meet whitewater expert judgment, but not well constrained with high scientific certainty. Most scientific theories and engineering applications are first published and used with less-constrained parameterizations as done here, and then future studies provide practical refinements. The iterative development of the Universal Soil Loss Equation (Wischmeier and Smith 1978; Renard et al. 1994) is a good example of that. Some highly popular scientific parameters, such as channel roughness, remain contentious and uncertain despite widespread study and application (Lane 2005; Ferguson 2010). In this case, the model involved a highly hazardous phenomenon with many dangers in attempting field-scale parameter calibration at the study site under the discharges of interest. In light of this uncertainty, the assumptions behind the current model parameter values are reported to convey the uncertainty of the results and highlight opportunities for refinement.

Experiments in controlled flume settings can inform adjustments to the model parameters listed in Table 1. The concept of savability was used to describe the capacity for a person to regain a controlled upright stance with head above the water surface starting from either a freely floating or foot-entrapped upright or supine position.

A single threshold was used to account for all four of these situations, but the ability to save oneself in each scenario may actually correspond to different thresholds. Additionally, a depth-velocity product might not be sufficient for capturing the savability in the two freely floating situations as saving could also hinge on the distance over which one is exposed to flow that does not exceed a certain threshold. Experimental analysis could determine, for example, that a distance of 3 m is required for an adult moving along with a current exhibiting a depth-velocity product of 0.2 m^2/s to save themselves. In this study, it was assumed that instantaneous saving was possible upon encountering water with a depth-velocity product below 0.3 m^2/s. The minimum and maximum depth for assessing savability could also be clarified as a function of subject height. Lastly, the threshold orientation angle used to isolate mesh nodes downstream of supercritical flow could be field validated by mapping the locations of hydraulic jumps and comparing these to the node locations.

In contrast, other parameter values may be adjusted a priori depending on the application. These include the safety zone dimensions, which are tied to the height of the human subjects of interest as well as the maximum passage proximity and reaction time used to map and analyze the hazard exposure.

3.4.7. Hazard model validation

At this time only limited validation of the hydraulic hazard model theorized and applied to the validated 2D model was performed, which involved a visual comparison of the predicted and observed hydraulic jump hazard locations. In addition, co-author Pasternack used his expert whitewater experience and training in whitewater safety to qualitatively evaluate whether the model results were reasonable at individual rapids in the SYR as he has kayaked and swam portions of the river at different discharges. Whole branches of science involve exploration of nature using back-of-the-envelope calculations and numerical models with no chance for validation presently, such as Earth's interior dynamism, landscape evolution modeling over thousands to millions of years, geomorphic modeling of other planets, and various solar and galactic dynamics. Natural hazards present a unique situation, because they involve the Earth's extreme dynamics, with infrequent periodicity, large size, flashiness, and deadly hazards. A good case in point of a model development arc is the SHALSTAB model for predicting maps of shallow landslide hazards, whose equations and results were published with no validation (Dietrich et al. 1992), leading to widespread usage in hazard management. The authors published a field study with some model validation nine years later (Dietrich et al. 2001). Even now, many flood hazard studies lack hydrodynamic validation data (e.g., Chen and Liu 2016). Nevertheless, planners must design evacuation schemes and management plans on the basis of whatever they can, so having the best analysis possible is warranted regardless of the ideal of model validation.

If a sponsor were to fund a model validation effort to test the results of this model in a future study, then the ideal approach would be to deploy human analogs into a flood and use large-scale particle image velocimetry to measure passage proximity and reaction time associated with each hydraulic hazard, and then compare those to model predictions. Whitewater rivers with roads that run along them, like the one used in this study or the North Fork of the Payette River in Idaho are excellent locations for testing. Human test dummies replicate the dimensions, weight proportions and articulation of the human body, while pig carcasses are widely regarded as the best organic analog of humans. These could be positioned upstream either manually or using the robotic river truss (Pasternack et al., 2006a). Pole-mounted cameras or tethered kite-blimps would be deployed to capture the velocity field of the ambient flow and track the motion of the test subject. These data would be used to measure passage proximities and compute reaction times, ideally for a wide range of flows. Although this is not difficult to envision, it would be costly and difficult to schedule in light of flood unpredictability. Since the underlying topographic and hydraulic data for this study was collected in 2009, California has experienced a historic drought and only a few days of flooding have occurred between then and when this hazard study was completed.

One aspect of the model that was more amenable to validation was the delineation of the hydraulic jump hazards since these could be safely photographed in the field and compared to the locations mapped using the approach developed in this study. For example, jump hazards were photographed during a flow of 4.4 m^3/s at the Langs Crossing gage and were visually compared to the locations of jumps delineated with 2D model results for this flow. Figure 9 shows the confluence of Canyon Creek with the South Yuba River where hydraulic jumps are associated with several steps. Features such as the steps in the photo were represented well in the DEM, and the corresponding flow acceleration was therefore reproduced closely by the 2D model. In contrast, other locations with smaller-scale causes of flow acceleration, such as individual boulders or shaped bedrock protrusions, were not as well captured in the DEM and 1-m resolution computational mesh, so the occurrence of supercritical flow was often underpredicted by the 2D model in these locations, leading to an underpredicted occurrence of jump hazards. The eddy viscosity coefficient also affected

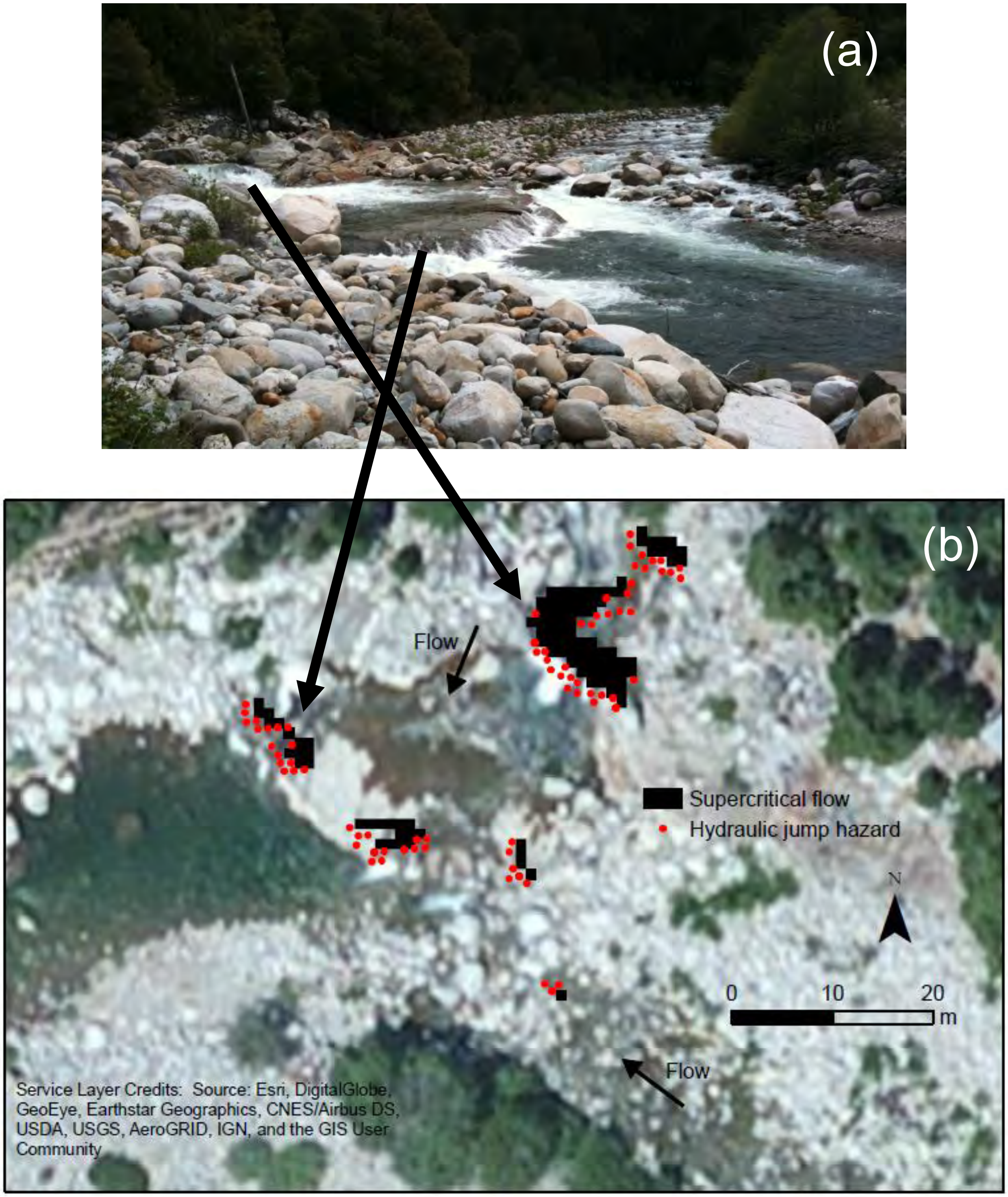
(a)
(b)
Flow
Supercritical flow
Hydraulic jump hazard
N
0
10
20
m
Flow
Service Layer Credits: Source: Esri, DigitalGlobe, GeoEye, Earthstar Geographics, CNES/Airbus DS, USDA, USGS, AeroGRID, IGN, and the GIS User Community

the extent of supercritical flow predicted by the 2D model as it determined the efficiency of momentum transfer.

4. Results

4.1. Hazard exposure maps

Mapping the hazard exposure permitted visual assessment of how the algorithms captured the interaction of the hazards with the hydraulics. Hazard exposure maps for the full study segment at 31 m^3/s for each hazard type as well as the total of all hazards are provided in Online Resources 2-5. Fig. 10 illustrates the results for four different scenarios for hazard encounters in the study segment, with the first two maps (Fig. 10a, b) involving emergent unsavable surfaces, hydraulic jumps for the third map, and submerged unsavable surfaces for the bottom map. While present in each of the maps, the submerged unsavable surfaces (PP3/RT3) were only displayed in Fig. 10d. Excluding the non-hazard area (PP0/RT0), the remaining PP/RT rating areas in each map composed the danger zones for the mapped hazards. The danger zones and component areas exhibited different shapes and sizes depending on the flow direction, velocity magnitude, depth, and hazard configuration. In Fig. 10a, the danger zone showed a flared upstream end due to convergent flow with more vectors oriented directly to the hazard to produce either a near miss or an encounter. The danger zone in Fig. 10b had a tapered tip because of flow that diverged from the hazard here and expanded out toward the right bank, but bank narrowing just downstream converged flow toward the hazard and enlarged the danger zone midsection.

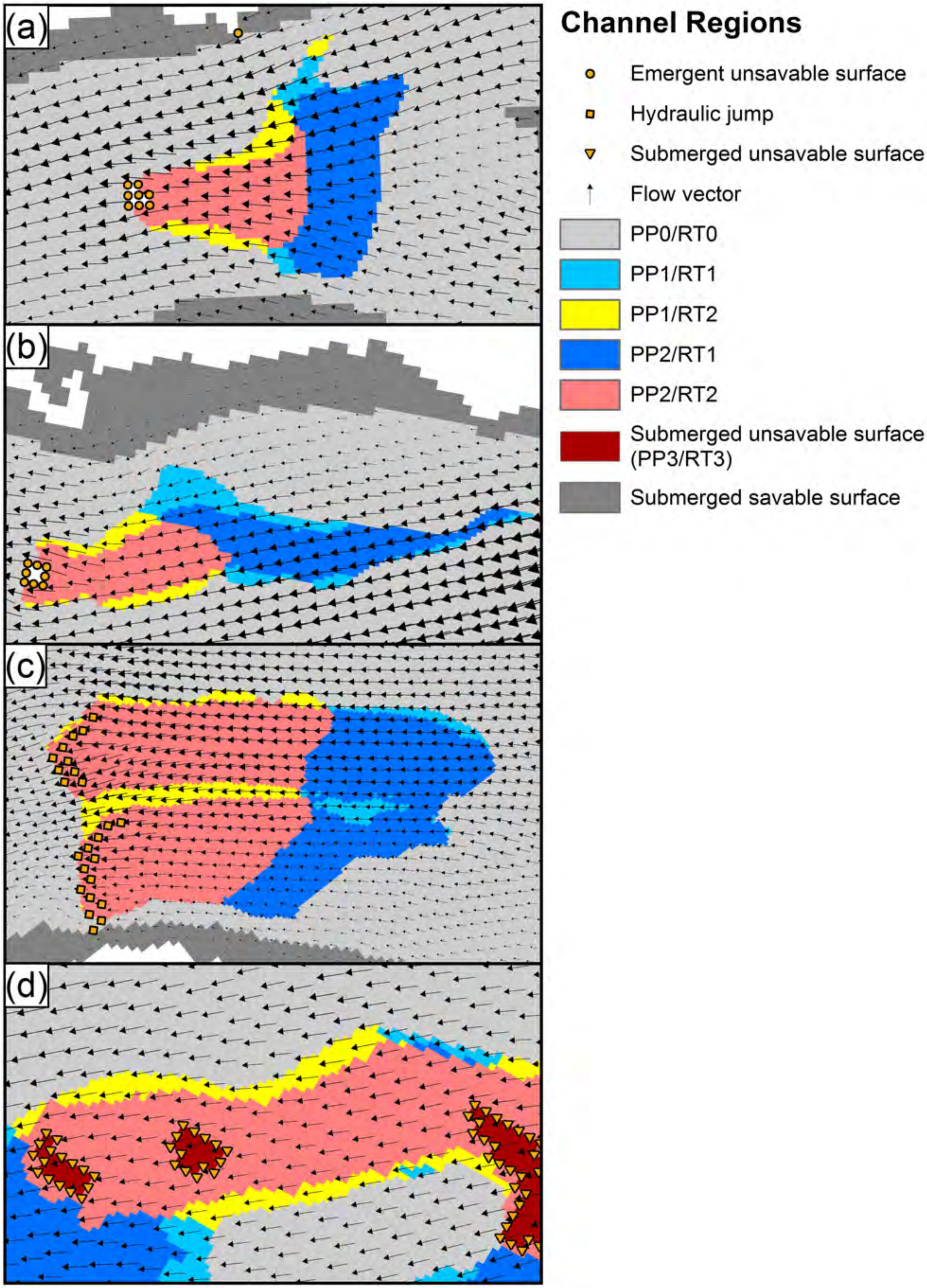
(a)
(b)
(c)
(d)
Channel Regions
Emergent unsavable surface
Hydraulic jump
Submerged unsavable surface
Flow vector
PP0/RT0
PP1/RT1
PP1/RT2
PP2/RT1
PP2/RT2
Submerged unsavable surface (PP3/RT3)
Submerged savable surface

In addition to flow direction, velocity magnitude and depth influenced the danger zones. The hazard points associated with two jumps are shown in Fig. 10c, with the lower jump exhibiting a danger zone with a tip skewed away from the left bank. The boundary between PP2/RT2 and PP2/RT1 also showed this skew which resulted from a gradient in velocity laterally across the danger zone with slower velocities closer to the left bank. The danger zone of the upper jump showed comparatively little skew due to more uniform velocities across the width of the zone. However, the longitudinal extents of the danger zone areas containing RT2 versus RT1 differed due to a velocity gradient along the length of the zone. Flow accelerated toward the jump such that more of the danger zone was within 5 s of a jump point, whereas the absence of a gradient would yield equal longitudinal extents of areas within 5 and 10 s of a hazard. Depth was relevant to the danger zones because the depth-velocity product determined the distribution of submerged savable surfaces that suppressed the extent of the danger zones. The left side of the lower danger zone in Fig. 10c lacked PP1/RT2 and PP1/RT1 area because the adjacent submerged savable surface was already within a body's safety zone here for which saving was assumed to be possible.

The hazard configuration specifically affected the danger zone component areas. The jumps present within the segment consisted of laterally distributed clusters of hazard points such as those displayed in Fig. 10c. As a result, the danger zone areas with PP2 were much more extensive than those with PP1 as hazard encounters rather than near misses were more likely. Longitudinally distributed clusters of hazard points like those shown in Fig. 10d favored areas with RT2 and not RT1, since flow was consistently within 5 s of an encounter or near miss with a hazard. The PP2/RT1 and

PP1/RT1 area in the lower left and right corners of Fig. 10d was associated with downstream submerged unsavable surface hazards not visible in the panel.

For a given site, increasing discharge had the potential to change flow direction, velocity magnitude, depth, and hazard configuration to elicit the aforementioned changes in danger zone shape and size. At 15 m^3/s for the site shown in Fig. 11, extensive submerged savable surface area limited the presence of emergent unsavable surface hazards. Savable surfaces shrank considerably at 31 m^3/s as depths and velocities increased such that multiple emergent surfaces became hazards and grew danger zones, including a particularly well-developed one just right of the map center. Increasing discharge further reduced the savable surface area but also submerged the emergent surfaces. This limited the longitudinal clustering of emergent unsavable surface hazards, so the component areas with RT1 were not suppressed in the mid-channel danger zones at 85 m^3/s. While only one small mid-channel emergent surface remained at the site in Fig. 11 at 196 m^3/s, there was a prominent emergent surface along the left bank that was not bordered by savable water and therefore showed a substantial danger zone here. Increasing velocity as discharge rose resulted in longer danger zones since more distant flow was within 10 s of a downstream hazard.

Lastly, Fig. 12 shows a site with two class IV+ rapids (“Fingers” and “Ledge” of the Jolly Boys run of the South Yuba River, http://www.awetstate.com/SYubaJB.html) and the interaction among all three hazards types that are individually displayed for the upright body scenario at 31 m^3/s. The upstream rapid was relatively shallow and strewn with boulders that created multiple emergent unsavable surface hazards at 31 m^3/s (Fig. 12b). Small patches of savable water were present around these emergent surfaces at

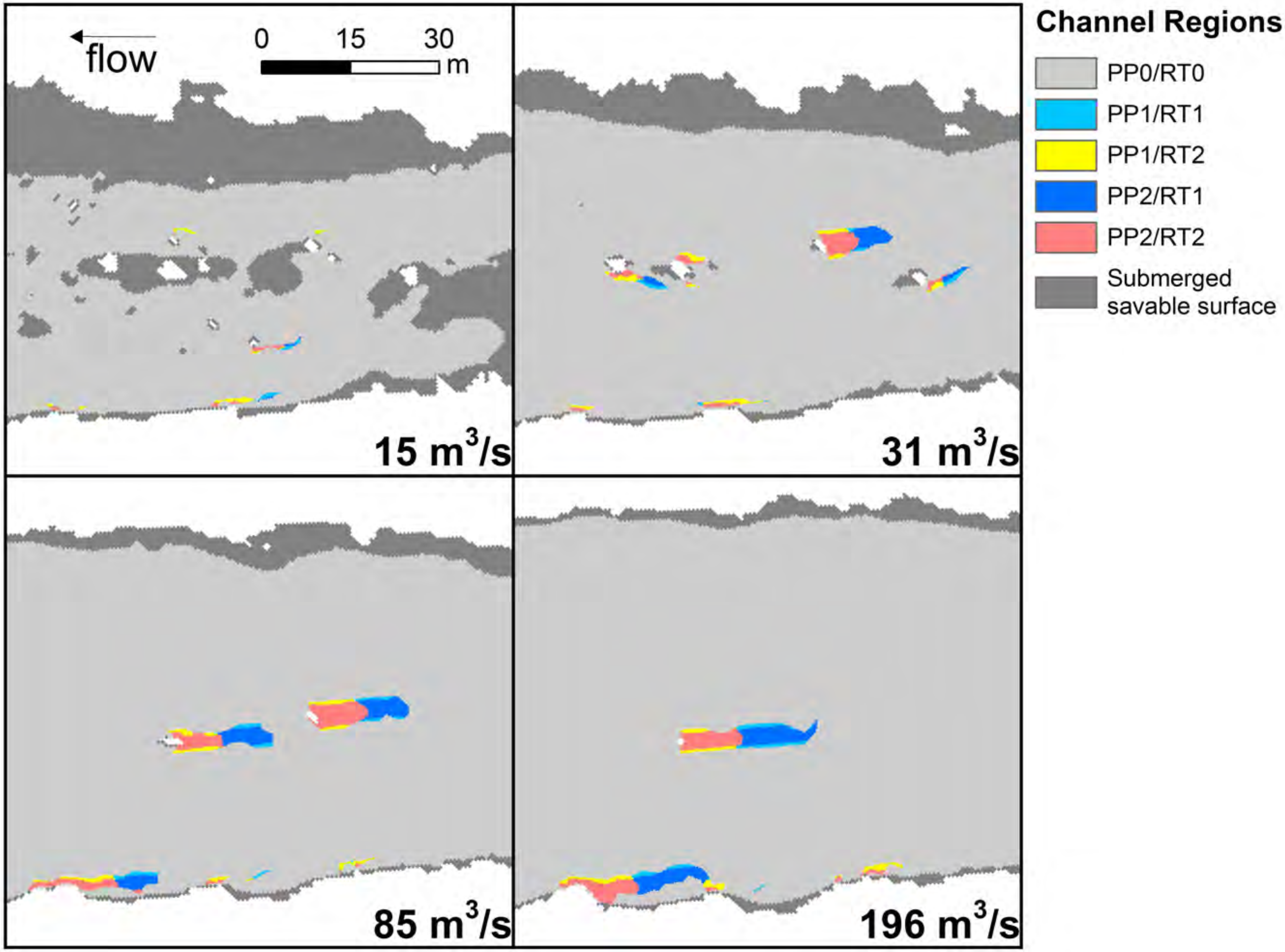
flow
0 15 30
m
15 m3/s
31 m3/s
85 m3/s
196 m3/s
Channel Regions
PP0/RT0
PP1/RT1
PP1/RT2
PP2/RT1
PP2/RT2
Submerged
savable surface

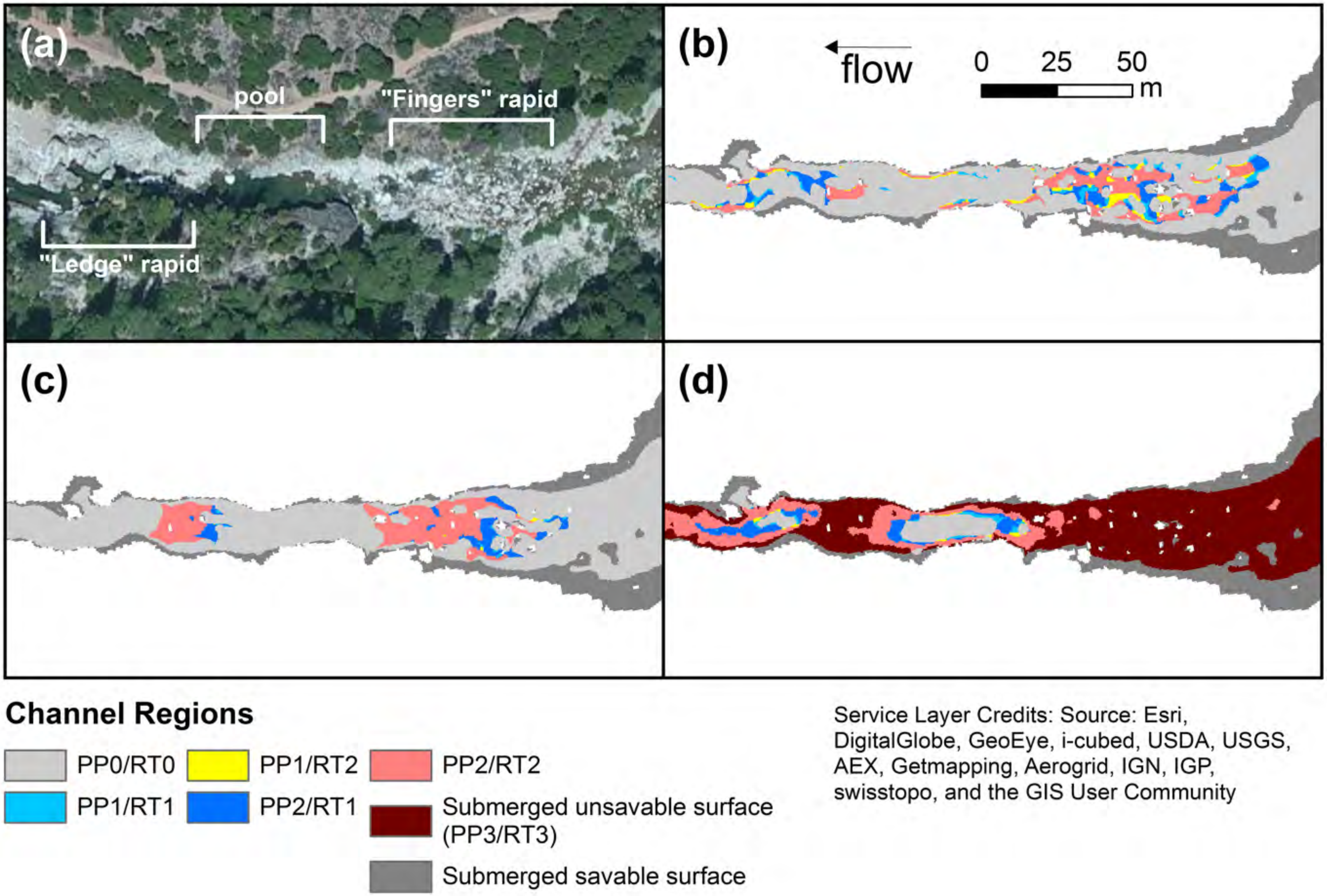
(a)
pool
"Fingers" rapid
"Ledge" rapid
(b)
flow
0 25 50
m
(c)
(d)
Channel Regions
PP0/RT0
PP1/RT2
PP2/RT2
PP1/RT1
PP2/RT1
Submerged unsavable surface (PP3/RT3)
Submerged savable surface
Service Layer Credits: Source: Esri, DigitalGlobe, GeoEye, i-cubed, USDA, USGS, AEX, Getmapping, Aerogrid, IGN, IGP, swisstopo, and the GIS User Community

this discharge that limited the extent of the danger zones in some places. These boulders also accelerated flow to form jump hazards here (Fig. 12c). Due to depths <1.5 m and high velocities, nearly all of the submerged surfaces here were unsavable (Fig. 12d). Just downstream was a pool adjacent to steep bedrock walls (Fig. 12a) where slow velocities and large depths produced few hazards at 31 m^3/s. The next rapid occurred immediately downstream where the higher bed elevation and the narrow bedrock walls converged flow to form a large jump hazard. Only a couple mid-channel surfaces were emergent here, and the surfaces that were <1.5 m deep were mostly unsavable.

4.2. Segment-scale areal fractions of hazard exposure

When the hazard exposure results were aggregated to the segment scale in the form of areal fractions, multiple discharge-dependent trends were evident (Fig. 13). For all discharges, the emergent unsavable surface (Fig. 13a) and jump hazards (Fig. 13b) showed limited danger zone areas that occupied <10% of the river segment. In contrast, over 45% of the segment contained the danger zones of submerged unsavable surface hazards across all discharges (Fig. 13c). Both the emergent and submerged unsavable surface hazards showed concave-down trends with peak danger zone areal fractions of 3.3% and 67%, respectively, at 31 m^3/s, while the jump hazards exhibited a monotonic increase in danger zone areal fraction as discharge rose, peaking at 6.0%. The danger zone areal fractions for the total hazards exposed to an upright body (Fig. 13d) were nearly identical to those for the submerged unsavable surfaces since these hazards greatly outnumbered the jump and emergent unsavable surface hazards for all

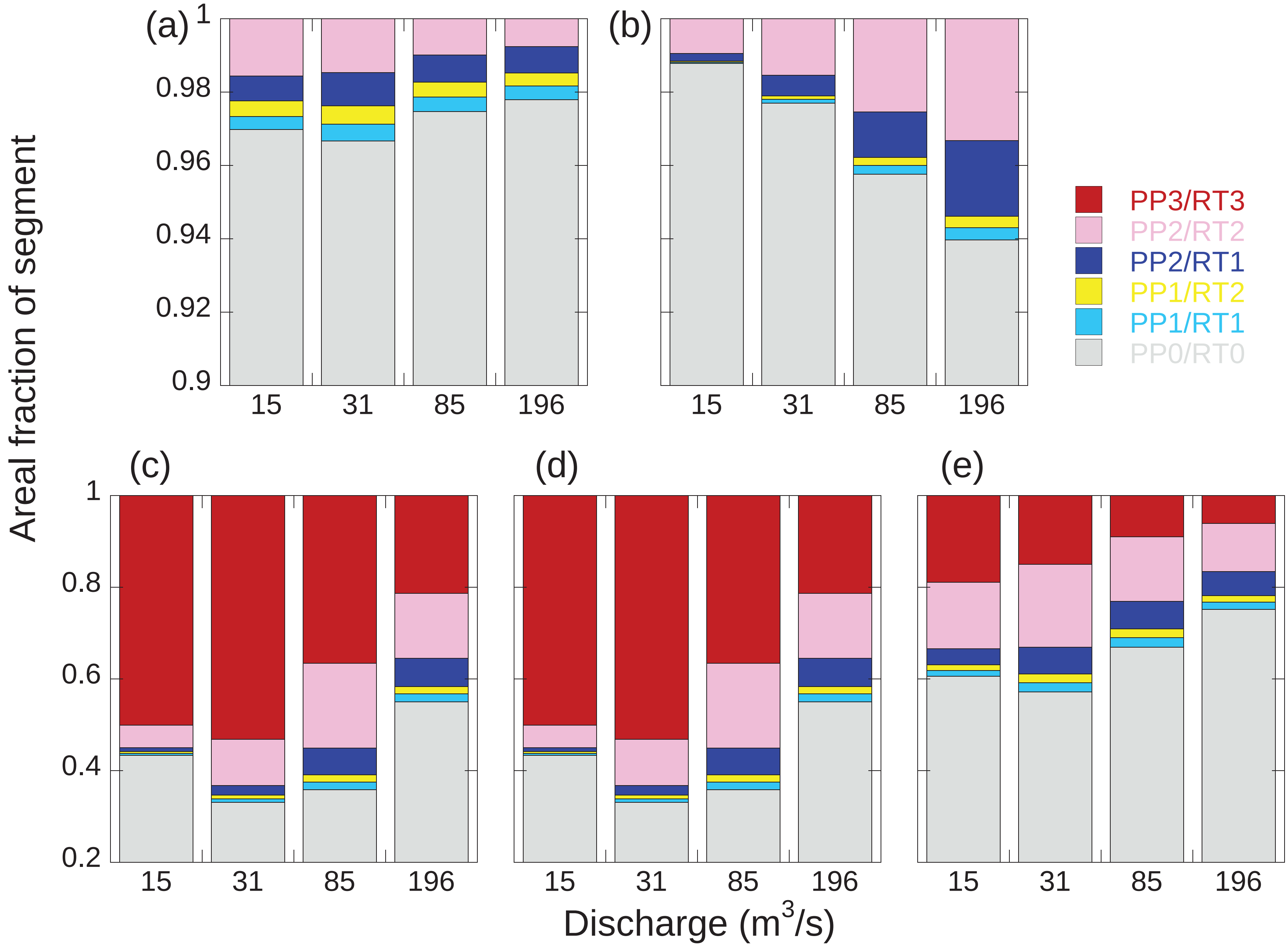

Areal fraction of segment
(a)
(b)
(c)
(d)
(e)
1
0.98
0.96
0.94
0.92
0.9
0.8
0.6
0.4
0.2
15
31
85
196
Discharge (m3/s)
PP3/RT3
PP2/RT2
PP2/RT1
PP1/RT2
PP1/RT1
PP0/RT0

discharges. The total hazard areal fractions for the supine body position (Fig. 13e) were substantially lower than these for the upright position.

The component fractions of the danger zones also changed across discharges, i.e., the fractions of the danger zone areas occupied by the paired passage proximity and reaction time ratings. For emergent unsavable surface and jump hazards, increasing discharge coincided with an overall increase in each component area except for clear declines in PP2/RT2 (Table 2). For submerged unsavable surface hazards and the total hazards for both body positions, the PP3/RT3 area declined significantly as discharge increased, while the remaining component areas showed overall increases. PP3/RT3 was particularly dominant within the danger zones at 15 and 31 m^3/s for submerged unsavable surface hazards and total hazards for the upright position.

4.3. Longitudinal profiles

The profile of elevation along the valley centerline indicated the presence of two dominant slopes across the study segment, with the steeper upstream region ending abruptly at a large waterfall around river kilometer two (Fig. 14). Due to the local variability in hazard occurrence and the associated danger zone extents, the longitudinal distributions of the polygon danger fractions exhibited considerable noise. The average danger fractions within 0.5-km windows along the study segment were instead plotted to help visualize the trends (Fig. 14a, b). For both the upright (Fig. 14a) and supine (Fig. 14b) body positions, high danger fractions for all discharges occurred just upstream of the waterfall at river kilometer two with sharp drops in the danger fractions immediately downstream. For the upright position, the danger fractions at 15,

Table 2 Danger zone component fractions for each hazard category

Hazard	Discharge (m^3/s)	Component fractions for PP/RT rating area				
		PP1/RT1	PP1/RT2	PP2/RT1	PP2/RT2	PP3/RT3
Emergent unsavable surface	15	0.119	0.140	0.225	0.516	-
	31	0.136	0.151	0.271	0.442	-
	85	0.156	0.163	0.292	0.388	-
	196	0.170	0.162	0.324	0.344	-
Submerged unsavable surface	15	0.007	0.008	0.015	0.087	0.883
	31	0.012	0.011	0.032	0.150	0.795
	85	0.026	0.025	0.090	0.289	0.570
	196	0.039	0.037	0.136	0.314	0.474
Jump	15	0.029	0.029	0.169	0.774	-
	31	0.044	0.043	0.244	0.669	-
	85	0.056	0.053	0.290	0.601	-
	196	0.054	0.051	0.343	0.552	-
Total hazards-upright body	15	0.007	0.008	0.015	0.087	0.883
	31	0.012	0.011	0.032	0.150	0.795
	85	0.025	0.025	0.090	0.290	0.570
	196	0.037	0.035	0.135	0.321	0.471
Total hazards-supine body	15	0.032	0.032	0.089	0.367	0.480
	31	0.047	0.045	0.135	0.423	0.350
	85	0.064	0.058	0.182	0.425	0.272
	196	0.065	0.057	0.211	0.422	0.246

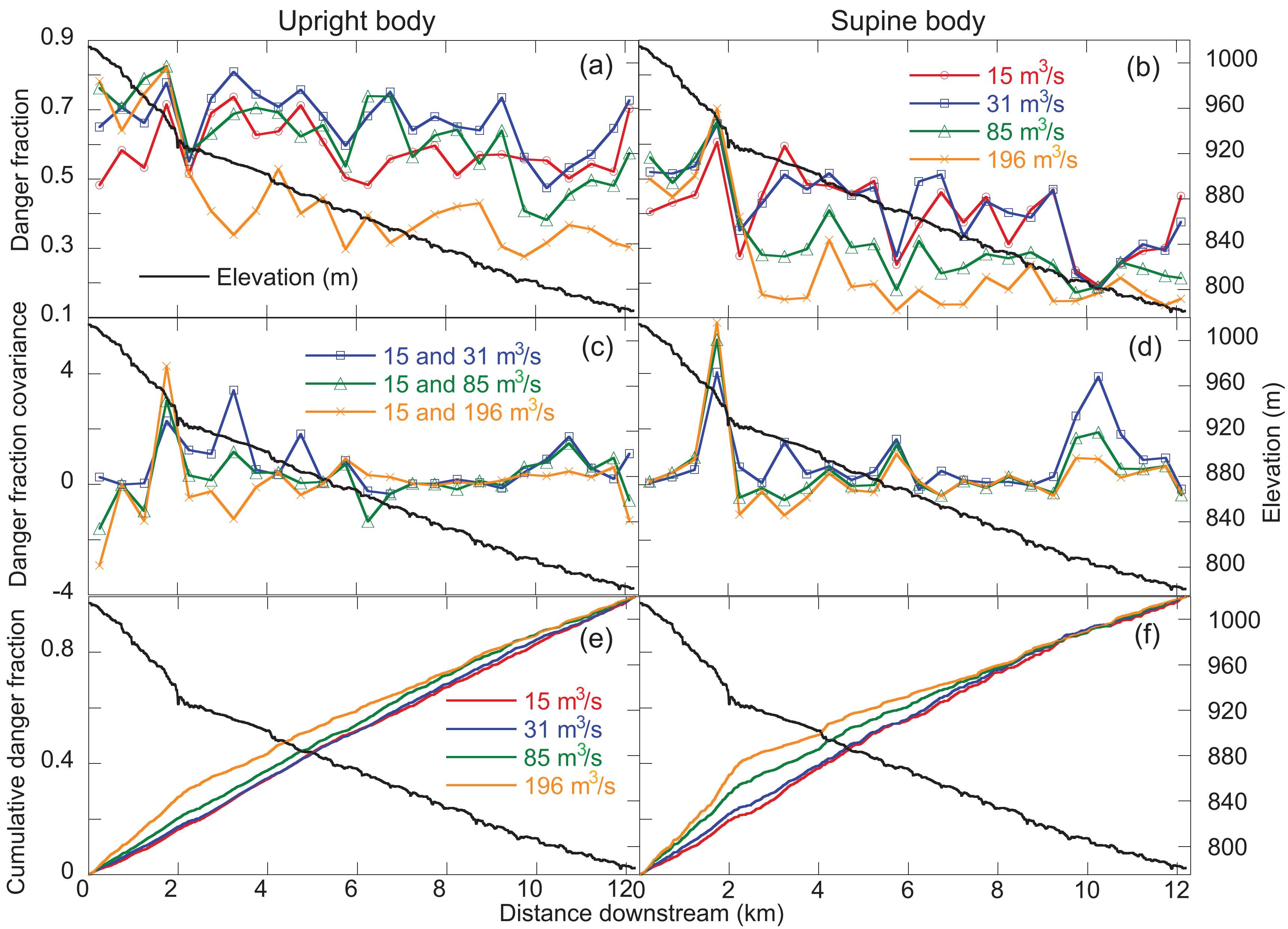
Upright body
Supine body
(a)
(b)
(c)
(d)
(e)
(f)
Danger fraction
Danger fraction covariance
Cumulative danger fraction
Elevation (m)
Distance downstream (km)
15 m3/s
31 m3/s
85 m3/s
196 m3/s
15 and 31 m3/s
15 and 85 m3/s
15 and 196 m3/s
0.9
0.7
0.5
0.3
0.1
4
0
-4
0.8
0.4
0
1000
960
920
880
840
800
0
2
4
6
8
10
12

31, and 85 m^3/s rose rapidly downstream of this point of low danger, while for the supine position, only the 15 and 31 m^3/s danger fractions showed a rapid increase here.

The covariance distributions revealed the presence of both discharge-dependent and discharge-independent danger (Fig. 14c, d). A positive value of covariance at any location in the profile meant that danger, or lack thereof, was discharge independent between the two flows (i.e., between 15 m^3/s and a higher flow), while negative values indicated that the danger changed between the flows. Danger fraction covariance showed more positive values for the supine (Fig. 14d) than the upright (Fig. 14c) position, and both positions showed peaks for each distribution just upstream of the waterfall. The cumulative distributions of danger fractions for all four discharges under the supine body scenario (Fig. 14f) deviated more from a uniform distribution of danger than those for the upright position (Fig. 14e), and the less smooth curves for the supine position indicated greater local accumulations of danger fractions. Within the first two river kilometers, the 196 m^3/s distribution for both body positions showed the most pronounced accumulation of danger fractions with progressively reduced accumulations in order of decreasing discharge.

5. Discussion

5.1. Understanding hazard exposure across the study segment

In aggregating the hazard exposure results to the segment scale, there existed a balance at 31 m^3/s between the extent of surfaces that were exposed to a body in either position and the extent of unsavable water that made these surfaces hazardous. The overall decline in the danger zone areal fractions for emergent unsavable surface hazards over the discharge series indicated that mid-channel emergent surfaces were overwhelmingly inundated at the highest discharge. While emergent surface hazards arose along the banks where unsavable water became more extensive with increasing discharge, the danger zone areal fractions declined in part because these bank locations constituted one-sided hazard exposure. Mid-channel hazards could be encountered by a body from either side of the hazards, and the associated danger zones were therefore larger than those for hazards along the banks. The decline was additionally attributed to the decreasing wetted-perimeter-to-wetted-area ratio with rising discharge as hazard recruitment along the banks did not counter the expansion in channel area. The submerged unsavable surface hazards also declined overall with discharge, as once the mid-channel surfaces were submerged too deeply, only narrow bands of these submerged hazards were present along the banks. The danger zone areal fractions for both surface hazards did increase from 15 to 31 m^3/s before declining, as the factors responsible for the occurrence of these hazards were optimized at this intermediate discharge. Velocities overall continued to increase beyond 31 m^3/s, and the extent of unsavable water expanded. However, the mid-channel surfaces were inundated too deeply at higher discharges to be hazards. In contrast, the inundation of surfaces created additional flow-accelerating features, e.g., boulders over which water spilled at high velocity, that expanded the extent of not only unsavable water but also supercritical flow and jump hazards. These conditions were prevalent enough to compensate for the drowning out of features that accelerated flow at lower discharges, such that the danger zone areal fractions for jump hazards monotonically rose with discharge.

Regarding the danger zone component fractions, relatively low velocities and hazard clustering favored immediate hazard exposure. At 15 m^3/s, the majority of the danger zone area for emergent unsavable surface and jump hazards consisted of immediate exposure in the form of PP2/RT2, as low velocities limited the extent of upstream waters within 10 s of the hazards. For submerged hazards, the unsavable surfaces themselves (PP3/RT3) dominated not only the danger zones but also much of the entire channel, such that the remaining component areas occupied limited space. Lateral and longitudinal clustering of the hazards interacted with relatively low velocities to restrict the expression of the other component areas. With increasing discharge, these other component fractions rose because increasing velocities enlarged the channel area not immediately exposed to but within 10 s of the hazards.

Relative to the upright body, the supine body was subjected to lower total hazard exposure while passing down the river, but this danger was less uniformly experienced with sudden transitions from safe pools to hazardous rapids. The differences in the results between the two positions were explained by the channel geometry in the lateral and longitudinal directions. The safety zone height was reduced by a factor of two from 1.5 to 0.75 m to account for the supine body position, and the extent of the submerged unsavable surfaces (PP3/RT3) for each discharge was reduced to less than half of that for the upright position. This indicated that the cross-sectional channel geometry overall produced a disproportionately greater decrease in hazardous surface area for every unit decrease in depth. The longitudinal profiles of danger fractions for both body positions showed a discharge-independent presence of hazard exposure just upstream of the waterfall near river kilometer two. Regardless of the discharge and body position, there were always features here that generated hazards and yielded a peak in the danger fraction profile. The discharge independence of the danger upstream of the waterfall was confirmed by the positive covariance values for each distribution at this location along the river. The 85 m^3/s profile for the upright position increased between river kilometers two and 3.75 but remained low for the supine position, as this region of the segment was plane bed with few features to create hazards under high discharges and a supine body position. Deep pools, such as the one present around river kilometer 5.75, had slow velocities and drowned-out surfaces that produced discharge-independent safety as supported by low danger fractions and positive covariance for each distribution here. The negative covariance between 15 and 196 m^3/s for the upright body revealed that channel locations switched from dangerous to safe (river kilometers 3.25 and 12.1) or vice versa (river kilometer 0.25) for this position between these two discharges. The region that became more dangerous was explained by a secondary channel thread that was relatively calm at 15 m^3/s but became much more hazardous at 196 m^3/s. For both body positions, increasing discharge corresponded to an upstream loading of the danger fraction cumulative distributions as hazards were largely drowned out beyond river kilometer two. Relative to the cumulative distributions for the upright body, the more abrupt increases in the distributions for the supine body indicated a greater sensitivity to the dichotomous step-pool channel geometry that was present along much of the segment.

5.2. Model implications

This study has broached the topic of how to mechanistically characterize the exposure of people to hazards upon entrainment in a whitewater river. Flood-related deaths are not linked exclusively to whether or not people have been swept away. A survey of people affected by the Bangladesh cyclone of 1991 found that 112 out of 285 people (39%) who were carried away by the storm surge died (Bern et al., 1993). The hazard delineation procedure used herein offers a foundation for identifying the locations of hazards for which refinements can be adopted depending on the setting. For example, the automated mapping of unsavable surfaces in an urban flood environment can be paired with the manual delineation of specific features that are of particular concern for causing physical trauma and body entrapment. However, the model developed in this study does not account for changes to the landscape as a result of flood flows that may alter the hydraulics and the distribution of hazards, such as the mobilization of debris in an urban setting (Chanson et al., 2014). The methods introduced in this study also do not address other urban flood hazards including drowning within a vehicle that’s driven into floodwaters.

Given the complexity of predicting where a volitional, inertial body would move within a flow field, multiple simplifications were made that permitted a substantive first step for this line of research. Instantaneous hazard exposure was quantified for any point in the flow where a body could be present, though Lagrangian particle tracking would be the next logical step to more rigorously assess the hazard exposure of a body moving along a path through the flow under a variety of different scenarios. This includes someone who has fallen out of their raft within a rapid or someone who has lost stability while evacuating a residence and swept down a flooded street. This could also help determine the connectivity of safe flow regions present along a river or flooded neighborhood through which people may be carried with relatively low exposure to hazards.

6. Conclusion

This study presented a new, analytical approach to characterizing the exposure of people to hazards within a flow. LiDAR and two-dimensional model results for a segment of the South Yuba River offered a unique opportunity to delineate hazards and mechanistically describe the exposure of an entrained body to these features for a whitewater river setting. Passage proximity and reaction time were introduced as metrics derived from the velocity magnitude and direction to express a body's hazard exposure. Increasing discharge produced concave-down trends in the body's exposure to emergent and submerged unsavable surface hazards, while a monotonic increase occurred for exposure to jump hazards. The total hazard exposure faced by a body moving down the river in the upright position was greater than that for a supine body, although the supine body experienced a less uniform exposure to hazards including abrupt encounters with dangerous channel regions. Further investigation is needed for the concept of savability given its importance to quantifying hazard exposure, such that the model may be applied to other dangerous flow settings like urban floods.

Acknowledgements

No external grant was provided directly for this work. Indirect support was received from the USDA National Institute of Food and Agriculture, Hatch project number #CA-D-LAW-7034-H. Precursor data were collected for different purposes with an award from the Instream Flow Assessment Program of the Public Interest Energy

Research Program of the California Energy Commission. The Instream Flow Assessment Program was administered by the Center of Aquatic Biology and Aquaculture of the University of California, Davis. This project involved a large collaborative effort that was only possible by gracious contributions of effort and resources by many people, including relicensing stakeholders, their consultants, our paid project staff, and UC Davis student volunteers. Helpful reviews and feedback of the final technical report with the 2D model and other precursor study components leading up the work herein were provided by Professor Allen James (University of South Carolina), Dudley Reiser (R2 Resource Consultants, Inc), Michael Barclay (HDR/DTA), Thomas Studley (PG&E), and Dr. Joshua Wyrick (Lafayette College). Lastly, Daniel Brasuell provided assistance in locating the rapids present along the study segment.

References

Abt SR, Wittler RJ, Taylor A, Love DJ (1989) Human stability in a high flood hazard. Water Resour Bull 25(4):881-890. doi: 10.1111/j.1752-1688.1989.tb05404.x

Belknap L (1998) Upgrading the American version of the International Scale of River Difficulty. American Whitewater. https://www.americanwhitewater.org/content/Wiki/safety:introratings?.

Bern C, Sniezek J, Mathbor GM, Siddiqi MS, Ronsmans C, Chowdhury AMR, Choudhury AE, Islam K, Bennish M, Noji E, Glass RI (1993) Risk Factors for Mortality in the Bangladesh Cyclone of 1991. Bulletin of the WHO 71:73-78.

Chanson H, Brown R, McIntosh D (2014) Human body stability in floodwaters: the 2011 flood in Brisbane CBD. 5th IAHR International Symposium on Hydraulic Structures 1-9, The University of Queensland

Chen WB, Liu WC (2016) Assessment of storm surge inundation and potential hazard maps for the southern coast of Taiwan. Nat Hazards 82(1): 591-616 doi: 10.1007/s11069-016-2199-y

Cox RJ, Yee M, Ball JE (2004) Safety of people in flooded streets and floodways, National Conference on Hydraulics in Water Engineering, Engineers Australia

Cox RJ, Shand TD, Blacka MJ (2010) Australian Rainfall and Runoff revision project 10: Appropriate safety criteria for People, Engineers Australia

Dietrich WE, Bellugi D, Real de Asua R (2001) Validation of the Shallow Landslide Model, SHALSTAB, for forest management. In: Wigmosta MS, Burges SJ (eds) Land Use and Watersheds: Human influence on hydrology and geomorphology in urban and forest areas, vol Water Science and Application 2. American Geophysical Union, pp 195-227

Dietrich WE, Wilson CJ, Montgomery DR, McKean J, Bauer R (1992) Erosion Thresholds and Land Surface-Morphology Geology 20:675-679Dolan R, Howard A, Trimble D (1978) Structural control of the rapids and pools of the Colorado River in the Grand Canyon. Science 202(4368): 629-631 doi: 10.1126/science.202.4368.629

Ferguson R (2010) Time to abandon the Manning equation? Earth Surf Proc Land 35:1873-1876 doi: 10.1002/esp.2091

Foster DN, Cox RJ (1973) Stability of children on roads used as floodways. University of New South Wales Water Research Laboratory Technical Report 73(13)

Gard M (2003) Flow-habitat relationships for spring-run Chinook salmon spawning in Butte Creek. Energy Planning and Instream Flow Branch Butte Creek 2D Modeling Final Report, U.S. Fish and Wildlife Service

Gonzalez RL, Pasternack GB (2015) Re-envisioning cross-sectional hydraulic geometry as spatially explicit hydraulic topography. Geomorphology 246:394–406 doi: 10.1016/j.geomorph.2015.06.024

Graf WL (1979) Rapids in canyon rivers. J Geol 533-551

Grant GE, Swanson FJ, Wolman MG (1990) Pattern and origin of stepped-bed morphology in high-gradient streams, Western Cascades, Oregon. Geol Soc Am Bull 102(3):340-352 doi: 10.1130/0016-7606(1990)102<0340:PAOOSB>2.3.CO;2

Harrison LR, Keller EA (2007) Modeling forced pool–riffle hydraulics in a boulder-bed stream, southern California. Geomorphology 83(3):232-248 doi: 10.1016/j.geomorph.2006.02.024

Hauer C, Mandlburger G, Habersack H (2009) Hydraulically related hydromorphological units: description based on a new conceptual mesohabitat evaluation model (MEM) using LiDAR data as geometric input. River Res Appl 25:29-47 doi:10.1002/rra.1083

Hilldale RC, Raff D (2008) Assessing the ability of airborne LiDAR to map river bathymetry. Earth Surf Proc Land 33(5):773-783 doi: 10.1002/esp.1575

Jonkman SN (2005) Global perspectives on loss of human life caused by floods. Nat Hazards 34(2):151-175 doi: 10.1007/s11069-004-8891-3

Jonkman SN, Kelman I (2005) An analysis of the causes and circumstances of flood disaster deaths. Disasters 29(1):75-97 doi: 10.1111/j.0361-3666.2005.00275.x

Jonkman SN, Penning-Rowsell E (2008) Human Instability in Flood Flows. J Am Water Resour As 44(5):1208-1218 doi: 10.1111/j.1752-1688.2008.00217.x

Karvonen RA, Hepojoki A, Huhta HK, Louhio A (2000) The use of physical models in dam-break analysis. RESCDAM Final Report, Helsinki University of Technology, Helsinki, Finland

Keller RJ, Mitsch B (1993) Safety aspects of the design of roadways as floodways. Urban Water Research Association of Australia

Kieffer SW (1985) The 1983 hydraulic jump in Crystal Rapid: Implications for river-running and geomorphic evolution in the Grand Canyon. J Geol 385-406

Lai YG (2008) SRH-2D version 2: Theory and User's Manual. U.S. Department of the Interior, Bureau of Reclamation

Lane SN (2005) Roughness – time for a re-evaluation? Earth Surf Proc Land 30:251-253 doi: 10.1002/esp.1208

Lane SN, Chandler JH (2003) Editorial: the generation of high quality topographic data for hydrology and geomorphology: new data sources, new applications and new problems. Earth Surf Proc Land 28(3):229-230 doi: 10.1002/esp.479

Leopold LB (1969) The rapids and the pools—Grand Canyon. U.S. Geological Survey Professional Paper 669:131-145

Lind N, Hartford D, Assaf H (2004) Hydrodynamic Models of Human Instability in a Flood. J Am Water Resour As 40(1):89-96 doi: 10.1111/j.1752-1688.2004.tb01012.x

McCarroll RJ, Castelle B, Brander RW, Scott T (2015) Modelling rip current flow and bather escape strategies across a transverse bar and rip channel morphology. Geomorphology 246:502-518 doi: 10.1016/j.geomorph.2015.06.041

McKean JA, Isaak DJ, Wright CW (2008) Geomorphic controls on salmon nesting patterns described by a new, narrow-beam terrestrial-aquatic lidar. Front Ecol Environ 6(3):125–130 doi: 10.1890/070109

Milanesi L, Pilotti M, Ranzi R (2015) A conceptual model of people's vulnerability to floods. Water Resour Res 51(1):182-197 doi: 10.1002/2014WR016172

Muste M, Kim D, Merwade V (2012) Modern Digital Instruments and Techniques for Hydrodynamic and Morphologic Characterization of River Channels. In: Church M et al. (ed) Gravel-Bed Rivers: Processes, Tools, Environments, John Wiley & Sons, Ltd., Chichester, UK pp 315-341

Pasternack GB, Valle BL, Paige D, Shaw M (2006a) Portable apparatus and method for measuring hydraulic features in rivers and streams. United States Patent Office, Patent #7062962

Pasternack GB, Ellis CR, Leier KA, Valle BL, Marr JD (2006b) Convergent hydraulics at horseshoe steps in bedrock rivers. Geomorphology 82(1):126-145

Pasternack GB, Senter AE (2011) 21st Century instream flow assessment framework for mountain streams. California Energy Commission, PIER, CEC-500-2013-059

Peng SH (2012) 1D and 2D Numerical Modeling for Solving Dam-Break Flow Problems Using Finite Volume Method. J Appl Math 2012 http://dx.doi.org/10.1155/2012/489269.

Penning-Rowsell EC, Floyd P, Ramsbottom D, Surendran S (2005) Estimating injury and loss of life in floods: A deterministic framework. Nat Hazards 36:43-64 doi: 10.1007/s11069-004-4538-7

Reinfelds I, Lincoln-Smith M, Haeusler T, Ryan D, Growns I (2010) Hydraulic assessment of environmental flow regimes to facilitate fish passage through natural riffles: Shoalhaven river below Tallowa Dam, New South Wales, Australia. River Res Appl 26(5):589–604 doi: 10.1002/rra.1262.

Renard KG, Foster GR, Yoder DC, McCool DK (1994) RUSLE Revisited - Status, Questions, Answers, and the Future J Soil Water Conserv 49:213-220

Russo B, Gómez M, Macchione F (2013) Pedestrian hazard criteria for flooded urban areas. Nat Hazards 69(1):251-265 doi: 10.1007/s11069-013-0702-2

Strom MA, Pasternack GB, Wyrick JR (2016) Reenvisioning velocity reversal as a diversity of hydraulic patch behaviours. Hydrol Process 30(13):2348-2365 doi: 10.1002/hyp.10797

Takahashi S, Endoh K, Muro ZI (1992) Experimental study on people's safety against overtopping waves on breakwaters. Report on the Port and Harbour Institute 34(4):4-31

Valle BL, Pasternack GB (2002) TDR Measurements of Hydraulic Jump Aeration in the South Fork of the American River, California. Geomorphology 42(1):153-165 doi:10.1016/S0169-555X(01)00083-6

Valle BL, Pasternack GB (2006) Air concentrations of submerged and unsubmerged hydraulic jumps in a bedrock step-pool channel. J Geophys Res 111(F3):1-12 doi: 10.1029/2004JF000140

Vilming S (1998) The development of the multibeam echosounder: An historical account. J Acoust Soc Am 103(2935) http://dx.doi.org/10.1121/1.422177

Webb RH, Pringle PT, Reneau SL, Rink GR (1988) Monument Creek debris flow, 1984: Implications for formation of rapids on the Colorado River in Grand Canyon National Park. Geology 16(1):50-54 doi: 10.1130/0091-7613(1988)016<0050:MCDFIF>2.3.CO;2

Webb RH, Pringle PT, Rink GR (1989) Debris flows from tributaries of the Colorado River, Grand Canyon National Park, Arizona. U.S. Geological Survey Professional Paper 87-118

Western U.S. Historical Summaries by State, Annual Precipitation Averages and Extremes. Western Regional Climate Center. http://www.wrcc.dri.edu/htmlfiles/ca/ca.ppt.ext.html. Accessed 23 October 2010

Wischmeier WH, Smith DD (1978) Predicting rainfall erosion losses: a guide to conservation planning. Agriculture Handbook 537, United States Department of Agriculture, Washington, DC

Wyrick JR, Pasternack GB (2014) Geospatial organization of fluvial landforms in a gravel-cobble river: beyond the riffle-pool couplet. Geomorphology 213:48-65 doi: 10.1016/j.geomorph.2013.12.040

Xia J, Falconer RA, Wang Y, Xiao X (2014) New criterion for the stability of a human body in floodwaters. J Hydraul Res 52(1):93-104 doi: 10.1080/00221686.2013.875073

Ying X, Wang SS (2010) Evaluation of 2D shallow-water model for spillway flow with a complex geometry. J Hydraul Res 48(2):265–268 doi: 10.1080/00221681003704178

Figure Captions

Fig. 1 Study segment location in California and within the Yuba River watershed

Fig. 2 Human body safety zones for the (a) upright and (b) supine positions

Fig. 3 Decision tree for the surface hazard delineation that begins with the dashed-line rounded box in the upper left and ends with hazardous surfaces in the dark-shaded squared boxes and safe surfaces in the light-shaded rounded boxes

Fig. 4 (a) Orientation γ of the flow vector to the supercritical flow point given the vector angle α and the angle β of the line connecting the vector to the point; (b) a site demonstrating the delineated jump hazard points

Fig. 5 Scenario in which the body's centroid does not approach within 0.9 m of a hazardous surface, savable surface, or hydraulic jump point

Fig. 6 Scenario in which the body's centroid does approach within 0.9 m of a hazardous surface, savable surface, or hydraulic jump point

Fig. 7 The appropriate hazard points, marked as squares, for setting the reaction time rating at a mesh node given (a) a PP2 rating and (b) a PP1 rating

Fig. 8 Kite-blimp imagery of the SYR with the dashed-line perimeter of an emergent surface plus the associated hypothetical paired rating areas

Fig. 9 (a) Photo looking upstream at hydraulic jumps at the confluence of Canyon Creek (left) and the South Yuba River (right); (b) predicted locations of supercritical flow and hydraulic jumps for the discharge in (a) (aerial imagery shows a lower baseflow)

Fig. 10 Four scenarios with different danger zone shapes and sizes and flow vectors scaled independently for each panel to the velocity magnitude

Fig. 11 A site at four different discharges with danger zones mapped for emergent unsavable surface hazards only

Fig. 12 (a) Aerial imagery of two rapids with (b) emergent unsavable surface hazards, (c) jump hazards, and (d) submerged unsavable surface hazards for an entrained upright body at 31 m^3/s

Fig. 13 Segment-scale areal fractions of exposure to (a) emergent unsavable surface hazards, (b) jump hazards, (c) submerged unsavable surface hazards, (d) total hazards for the upright body, and (e) total hazards for the supine body

Fig. 14 Longitudinal profiles of valley centerline elevation and danger fractions averaged within 0.5 km windows for (a) the upright and (b) supine bodies; longitudinal profiles of danger fraction covariance averaged within 0.5 km windows for (c) the upright and (d) supine bodies; longitudinal profiles of cumulative danger fractions for (e) the upright and (f) supine bodies

Supplemental materials

Topographic mapping data

For the SYR, the entire 12.2 km study segment was surveyed in the summer of 2009. Airborne LiDAR data of the terrestrial river corridor as well as bedrock outcrops and emergent boulders in the wetted base flow channel averaged 1 point per 0.74 m. Because the SYR had many large emergent boulders within the wetted area at base flow, the LiDAR survey was able to map many of them with multiple points; then a novel data-processing and object identification workflow was used to delineate each boulder as an object (Pasternack and Senter 2011). In this way, 34,113 individual boulders were explicitly resolved in the DEM–an important and unique aspect of this study in order to address hydraulic hazards. Ground-based wadeable channel surveys were done using a Leica TPS1200 robotic total station, a Topcon GTS-603 total station, and Trimble 5700 RTK GPS. Survey point density was ~1 point every 5 m on a rough grid and 1 point every 1 m along the thalweg. Bathymetric data was collected in pools using a pontoon-mounted Sonarmite echosounder coupled to a Trimble 5700 RTK GPS. This rig was floated laterally and longitudinally along pool cross-sections spaced ~5 m apart, and with data collected on a 5 s time interval. Combining these data collection methods, the segment-averaged topographic point density was 38-39 points per 100 m^2 both within and beyond the 0.283 m^3/s base flow domain.

Data collected using different observational methods were compared (i.e., every method against every other method) where they overlapped to assess uncertainty, with full details reported in Pasternack and Senter (2011). Each survey method involved internal performance tests, such as backsight checks, GPS root mean square values, and comparison of airborne LiDAR observations to ground-based observations on flat, smooth roads. Internal checks were within typical high-quality standards, which is within 0.5-10 cm for vertical accuracy in rough terrain and over long distances with a steep valley slope. Uncertainty assessment becomes more complicated when comparing methods, because (1) LiDAR and echosounders observe an area, while pole-mounted instruments observe mm-scale points and (2) grain-scale topographic relief in the SYR mountain channel easily ranges from 2 to 200 cm. Even with the rapid advancements in landform mapping detail and accuracy as used in this study and even if the technologies are performing equally in both settings, mountain channel comparisons will underperform lowland channel comparisons, because of the greater range of topographic variability in the mapped units, including sharp slope breaks. For instance, whereas 208 observed deviations between LiDAR and RTK GPS points on flat, smooth roads showed that 45% of deviations were within 2.5 cm of each other, 66% within 5 cm, and 96% within 10 cm, 247 observed deviations between LiDAR and ground-based instruments in the topographically complex river corridor showed that 18% were within 5 cm, 43% within 10 cm, 85% within 25 cm and 98% within 50 cm. Nevertheless, accuracy performance within the river corridor was well within the range of grain-scale relief, a key performance target.

Two-dimensional hydrodynamic modeling

Two-dimensional models of both segments were made using the Surface-water Modeling System v.10.0 (Aquaveo, LLC, Provo, UT) and run using Sedimentation and River Hydraulics (SRH-2D, v. 2.1) according to the procedures of Pasternack (2011). SRH-2D is a 2D finite-volume model that solves fluid mechanics equations to produce an estimate for depth and velocity at each computational node (Lai 2008). SRH-2D implements a hybrid structured-unstructured mesh that can use both quadrilateral and triangular elements of any size allowing for mesh detail comparable to any finite-element model.

Although this study focuses on four modeled flows associated with the spring snowmelt hydrological regime with respect to investigating hydraulic hazards, flows were actually modeled over three orders of magnitude for three hydrologic seasons (dry, wet, and snowmelt) for additional hydraulic, geomorphic, and ecological analyses (Pasternack and Senter 2011). Input discharge was obtained from USGS gaging stations on the South Yuba River at Lang's Crossing (#11414250) and on Canyon Creek below Bowman (#11416500). The South Yuba River has substantial ungaged accretionary flows, so a thorough hydrological analysis was completed (Pasternack and Senter, 2011) yielding regression relations to estimate accretionary flows from the major ungaged tributaries for three different hydrological seasons (wet, dry, and snowmelt). A stage-discharge relation was made between the total gaged inflows (SYR at Lang's Crossing plus Canyon Creek below Bowman) and observed water surface elevations at the exit of the study segment for total inflows ranging from 0.424 to 200.65 m^3/s. The time lag between inflow gage values and outflow WSE values was estimated for both gages and accounted for in the stage-discharge relation. For the remote outlet of the upstream computational mesh there was no appropriate location for a stage recorder. That model's downstream WSE was set to equal the simulated WSE at the entrance to the downstream computational mesh for that flow simulation.

To simulate hydrodynamics over the discharge range investigated with reasonable computational efficiency, it is beneficial to create different computational meshes that span key inundation extents and divide the length of a river segment into two or more linked sections. For the SYR, two inundation extents (< ~30 m^3/s and < ~200 m^3/s) and two longitudinal sections (study entrance to upstream of confluence with Canyon Creek, and upstream of Canyon Creek to study terminus) were used, all with 1-m internodal spacing. The downstream low and high flow meshes had 331,593 and 467,272 elements, respectively. The upstream low and high flow meshes had 284,461 and 396,615 elements, respectively. For each flow-regime simulation, the results from the two reaches were merged to create a single point file for evaluation in GIS using the output processing workflows explained in Pasternack (2011).

Roughness associated with resolved bedform topography (e.g., alluvial bars, partially to fully emergent boulders and boulder clusters, and bedrock outcrops) was explicitly represented in the detailed channel DEM and the 1 m resolution computational mesh. Given the heterogeneity of bed material, bedrock, and vegetation as well as the presence of all such features impacting hydraulic roughness across a wide range of flows, unresolved bed roughness was parameterized using a spatially and flow independent Manning's n value of 0.1. This value was confirmed through depth and velocity validation as well as sensitivity analysis.

Extensive model validation was performed for model simulations over two orders of magnitude of flow ranges (~0.62 to 26.5 m^3/s combined flow from the two inflow gages). Mass conservation between specified input flow and computed output flows for simulations of observed conditions was within 1%, except for the lowest flow simulation of the upstream mesh. That one run had a loss of 1.9%, which was considered reasonable given the extreme complexity of the channel topography and uncertainty in accretionary flows at the lowest discharge (which is well below the base flow discharge used for MU mapping in this study). WSE performance was tested by comparing 17,198 pairs of model predictions against LiDAR observations throughout the two meshes at base flow for a mean signed deviation of -2.8 cm. Performance was best where the water surface was flat and smooth and worst in steep sites with waves, but data from all areas were aggregated to obtain the unsigned statistical distribution of error. For unsigned deviations, 34% of test points were within 5 cm vertical, 51% within 10 cm, and 91% within 25 cm. Surface velocity magnitude was measured at 273 locations and compared to depth-averaged model predictions using the method of Barker (2011), yielding a good predicted versus observed r^2 of 0.61. Further analysis revealed that r^2 was 0.8 when velocities were limited to those in pools or transitional areas between pools and other morphological units. It was 0.5-0.64 on planar surfaces in the channel and in the floodway. The only unsatisfactory performance occurred in steep sites with waves where r^2 was 0.06. Median unsigned velocity magnitude error was 28% for all observations, but also varied depending on morphological unit type from 21-36%. Interestingly, steep sites with waves had a reasonable median unsigned error of 25%. Overall, the SYR 2D model met all common standards of 2D model performance in aggregate, but some care was needed in the use of values at the steepest sites where the horizontal flow assumption was violated. Even though SRH-2D is assumed to be stable for simulating extremely steep reaches, model performance in predicting precise velocities appears to suffer in such areas. Prediction accuracy only matters to the extent that velocity and depth values are above the thresholds to correctly classify locations as hydraulic jumps or proximal to emergent and submerged rocks and banks.

References

Barker JR (2011) Rapid, abundant velocity observation to validate million-element 2D hydrodynamic models. M.S. thesis, University of California Davis, Davis, California

Lai YG (2008) SRH-2D version 2: Theory and User's Manual. U.S. Department of the Interior, Bureau of Reclamation

Pasternack GB (2011) 2D Modeling and Ecohydraulic Analysis. Createspace, Seattle, WA

Pasternack GB, Senter AE (2011) 21st Century instream flow assessment framework for mountain streams. California Energy Commission, PIER, CEC-500-2013-059

SYR Emergent Unsavable Surface Hazards at 31 m^3/s, p. 1

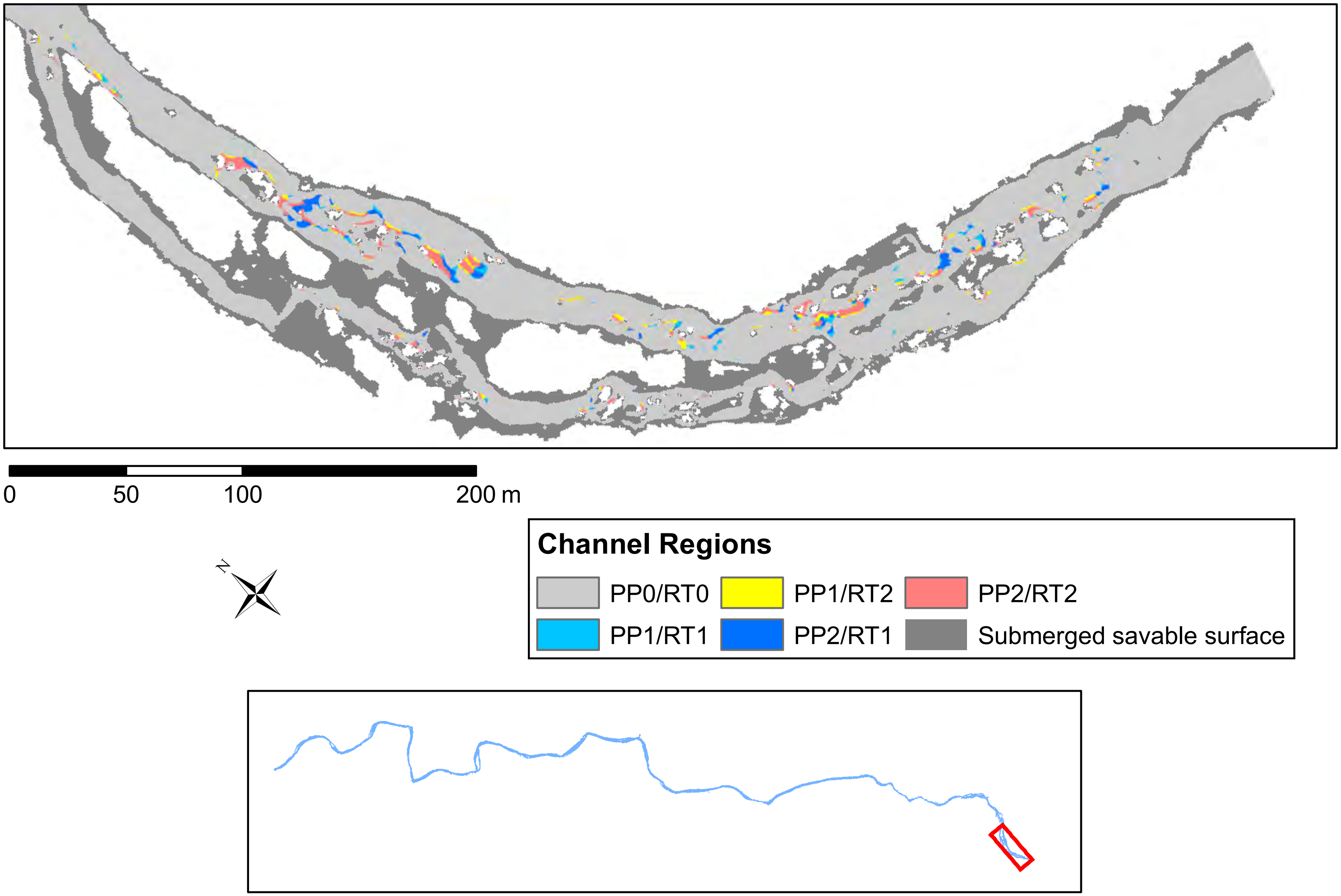

SYR Emergent Unsavable Surface Hazards at 31 m^3/s, p. 2

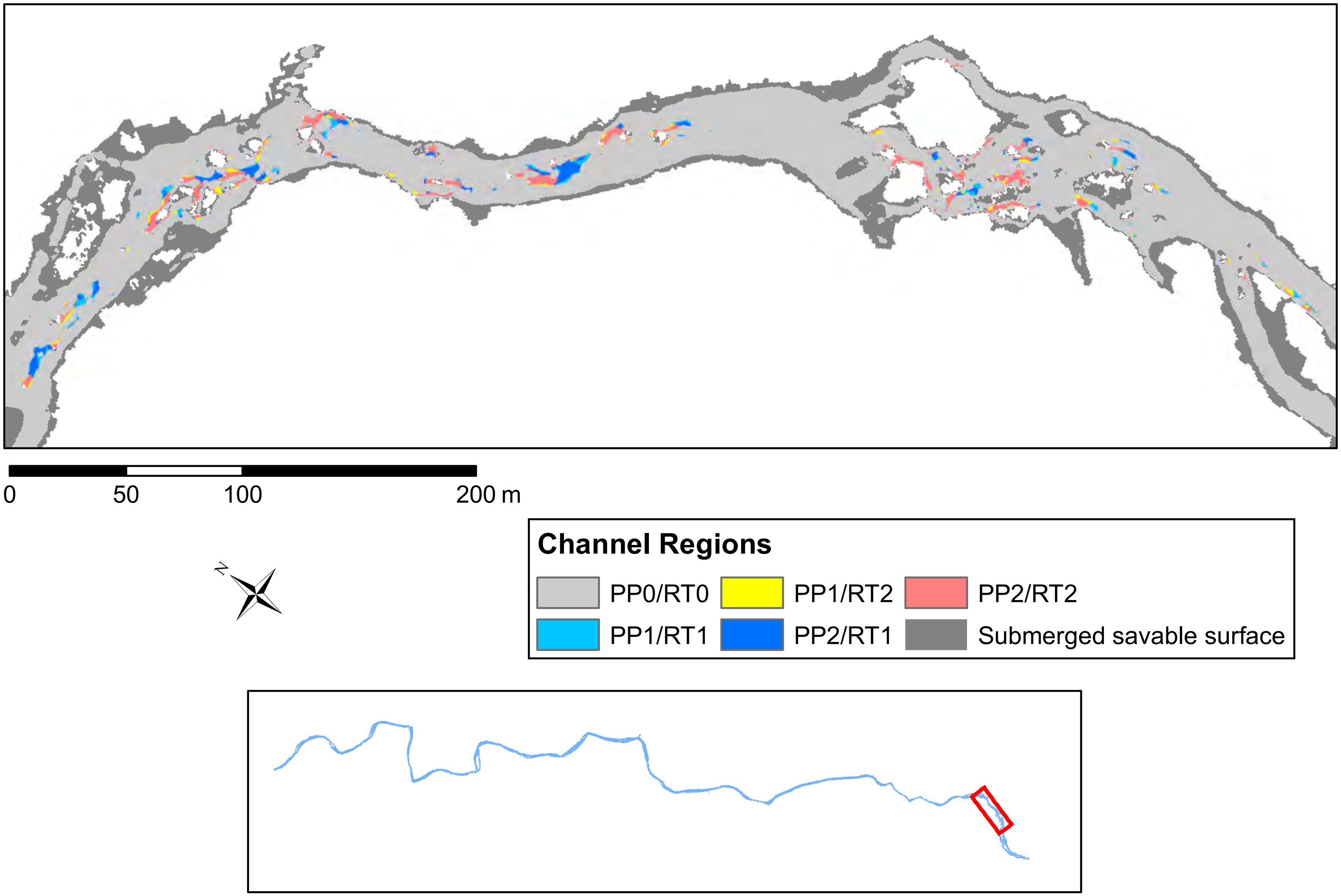

SYR Emergent Unsavable Surface Hazards at 31 m^3/s, p. 3

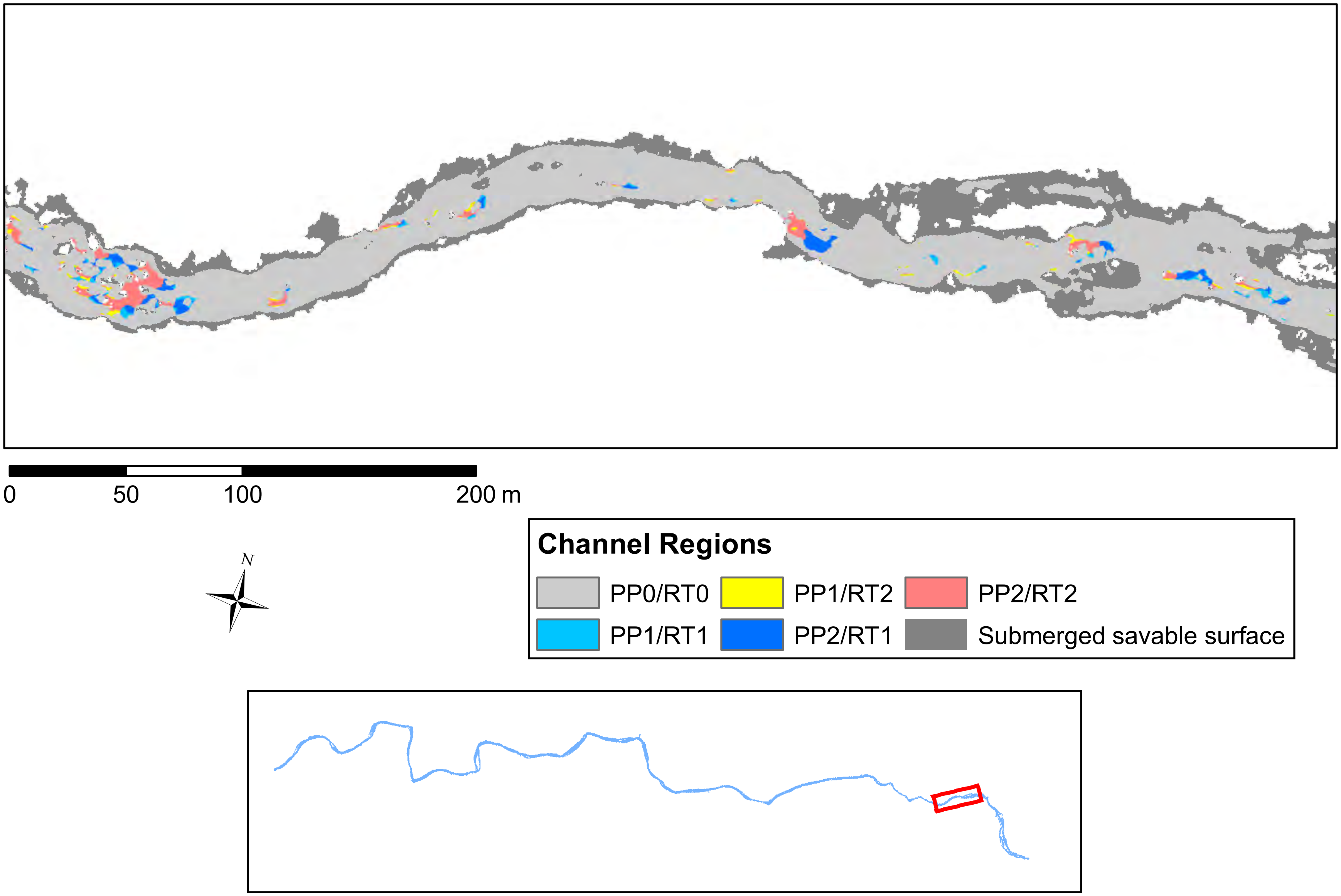

SYR Emergent Unsavable Surface Hazards at 31 m^3/s, p. 4

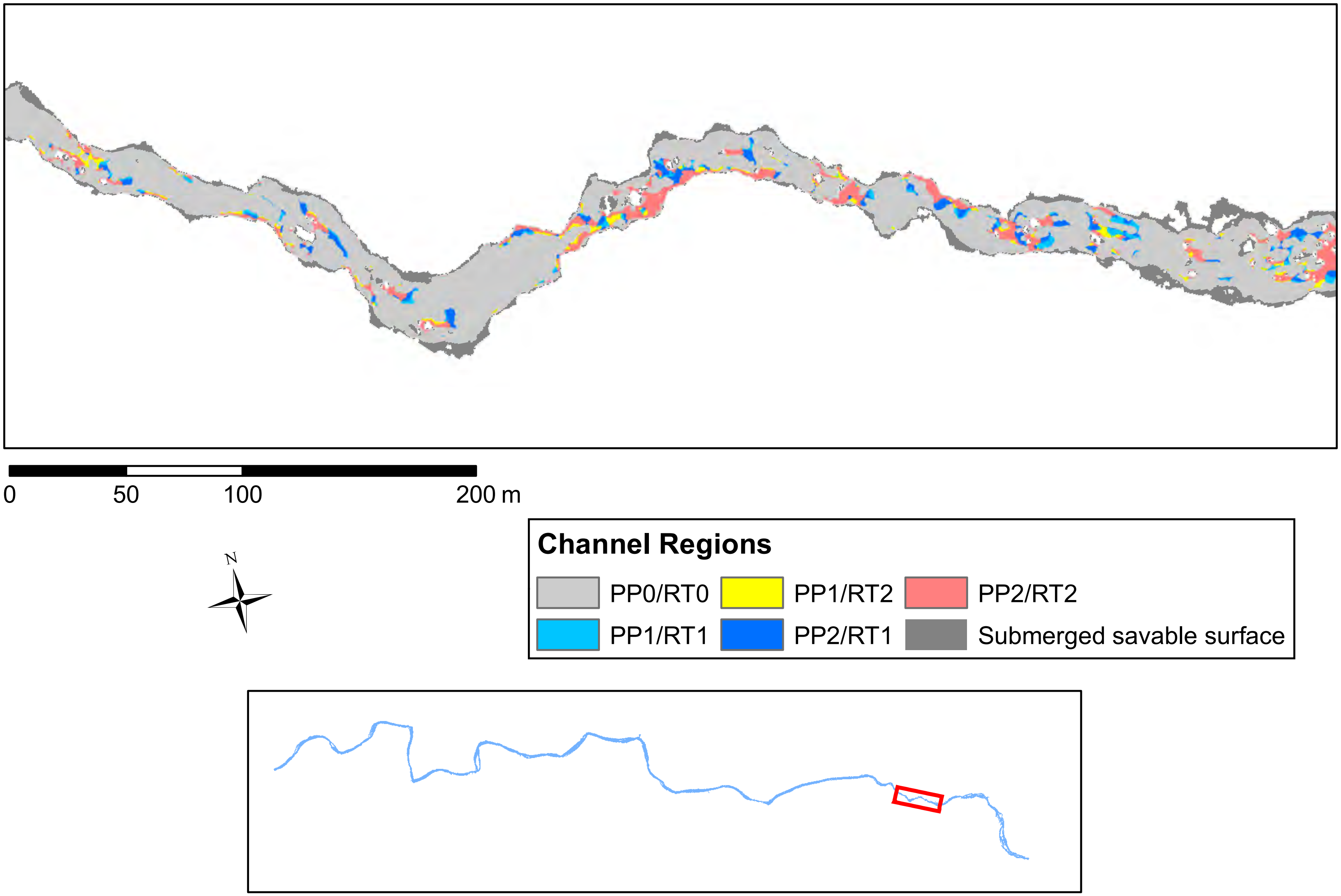

SYR Emergent Unsavable Surface Hazards at 31 m^3/s, p. 5

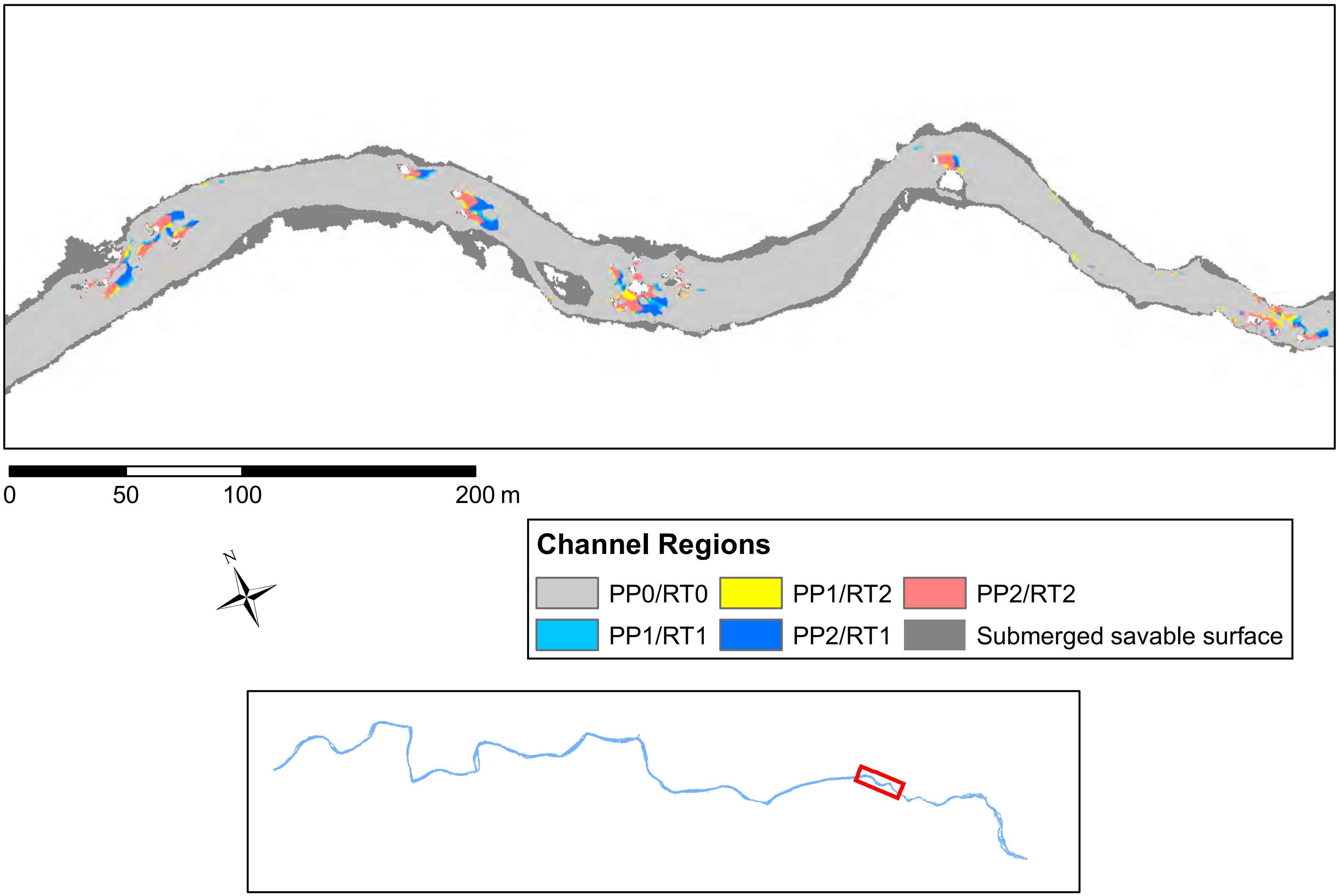

SYR Emergent Unsavable Surface Hazards at 31 m^3/s, p. 6

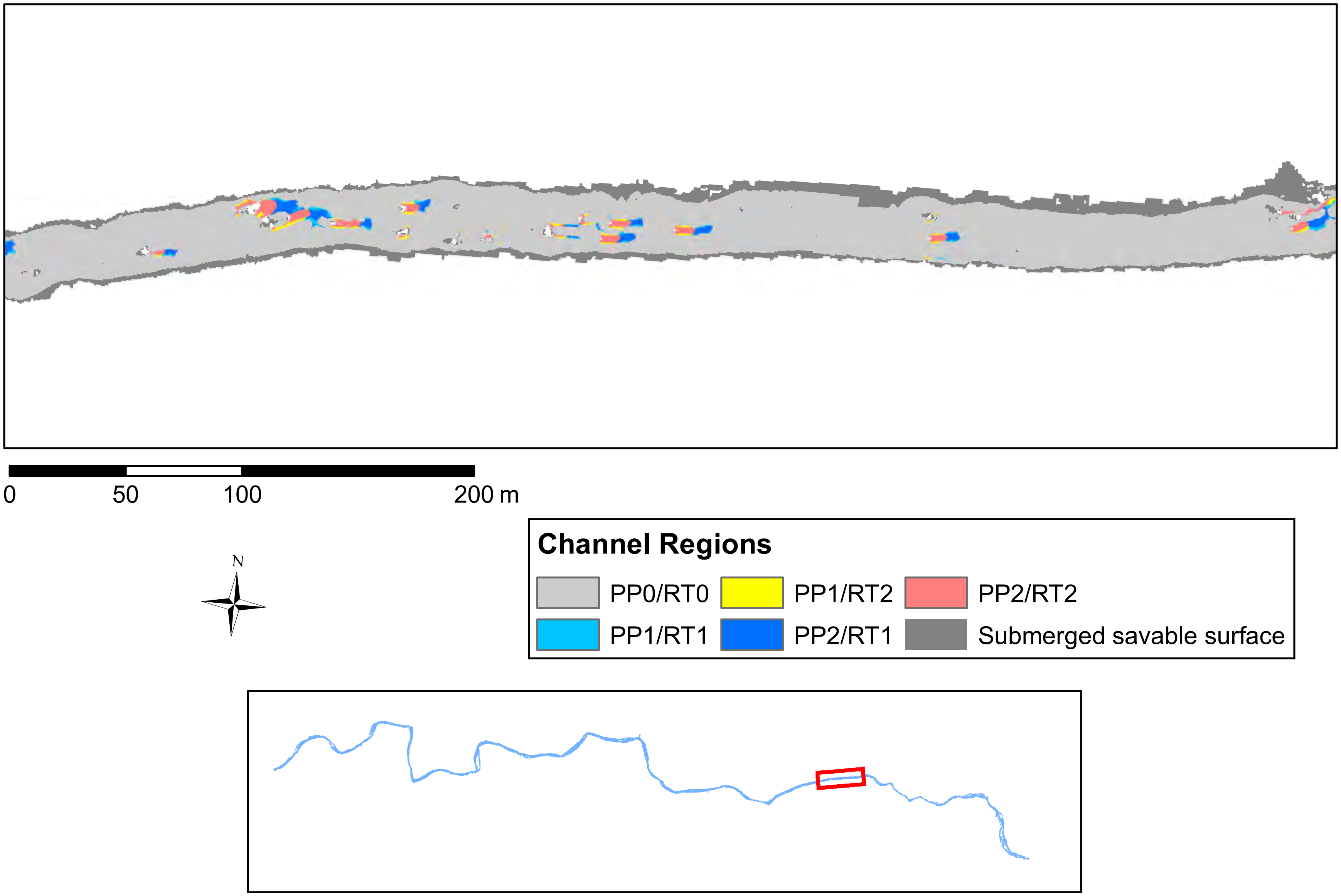

SYR Emergent Unsavable Surface Hazards at 31 m^3/s, p. 7

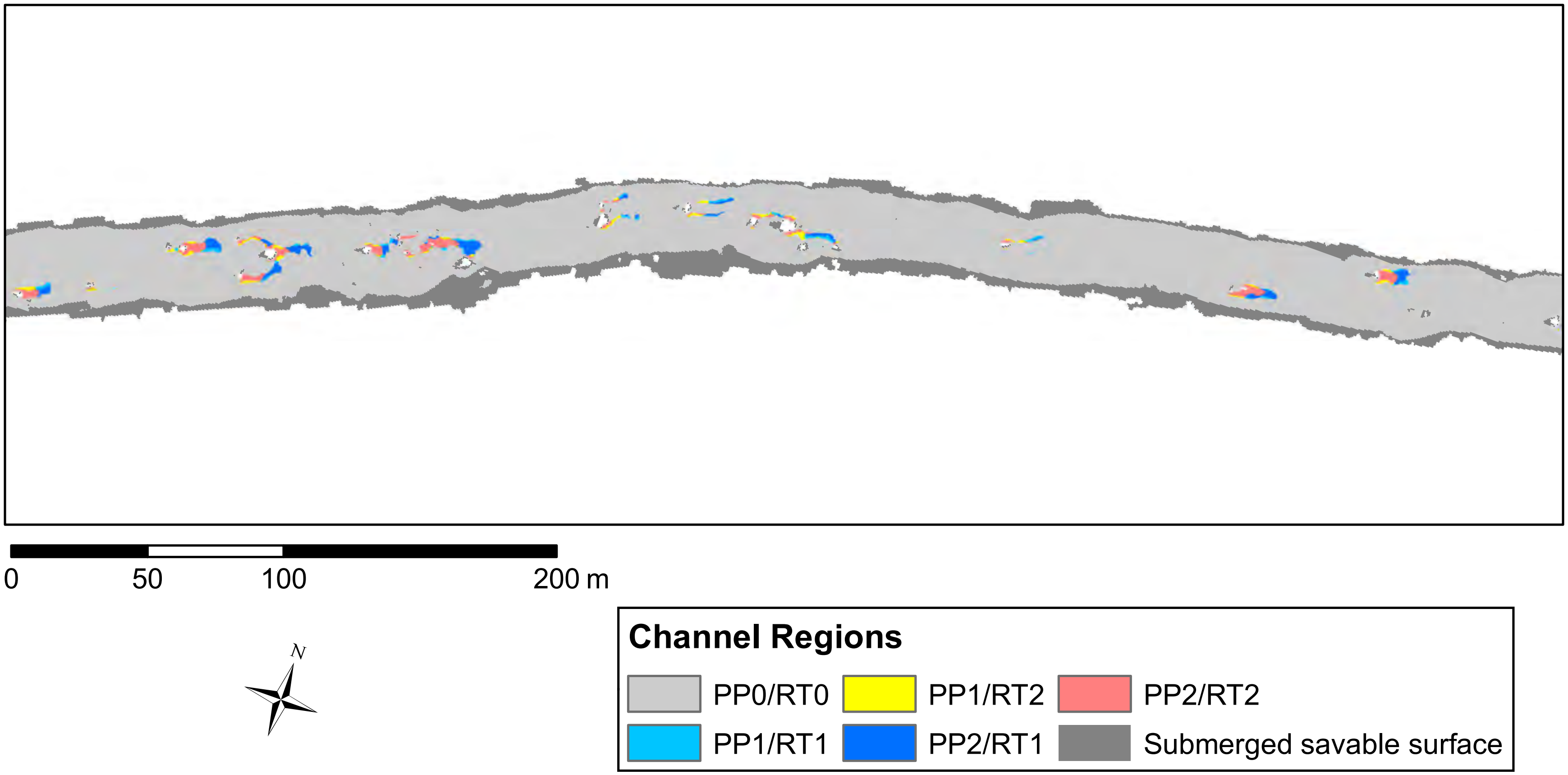

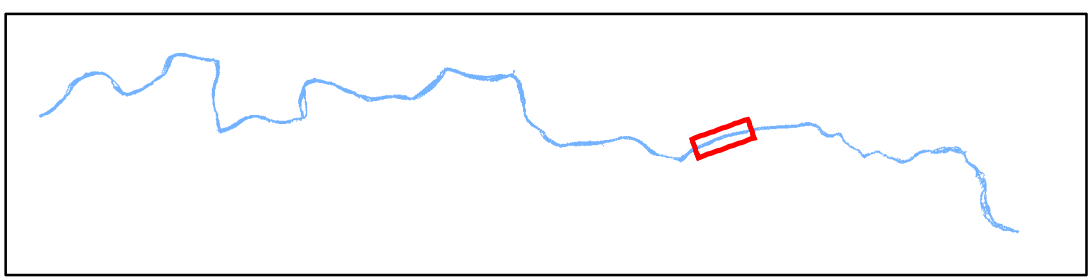

SYR Emergent Unsavable Surface Hazards at 31 m^3/s, p. 8

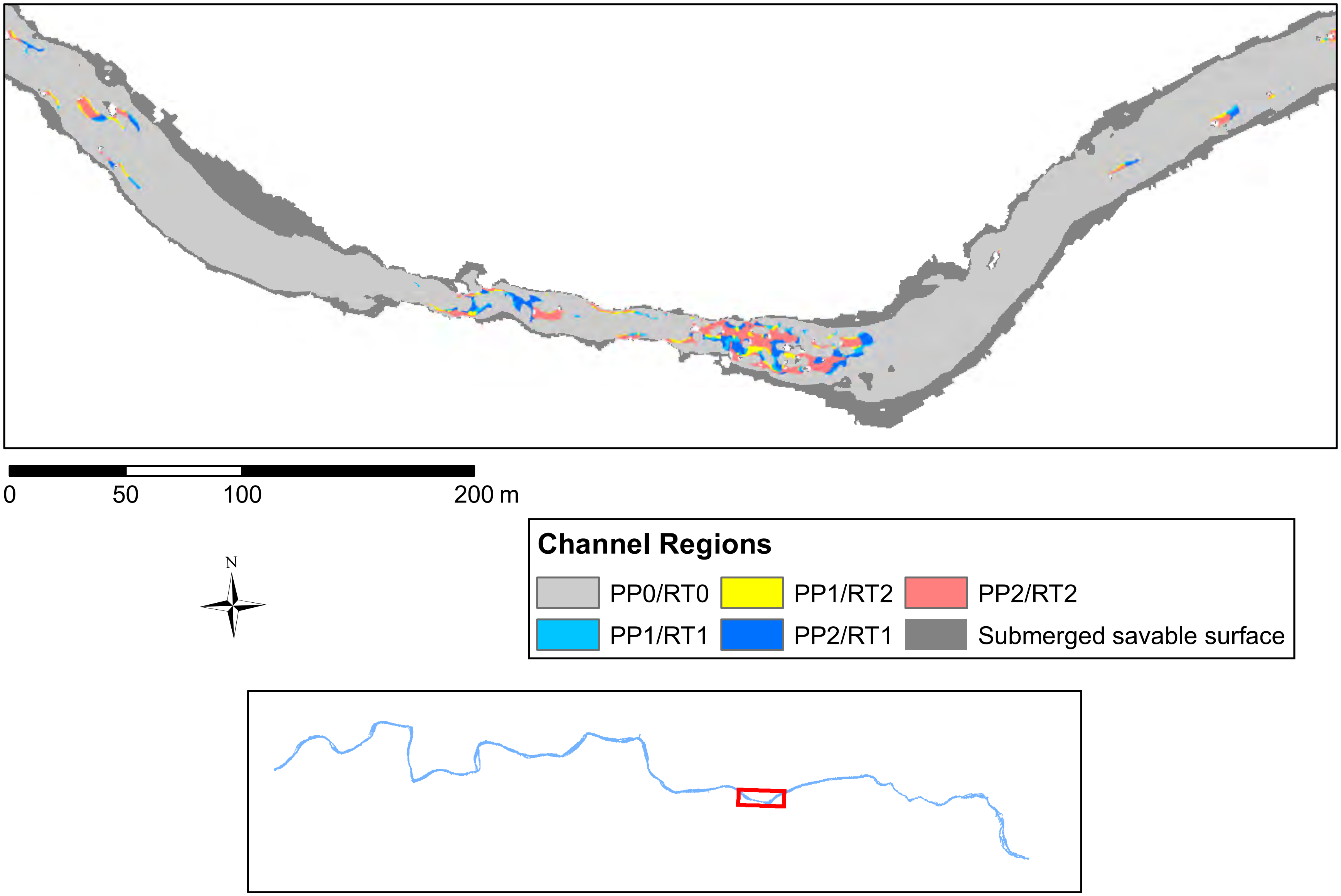

SYR Emergent Unsavable Surface Hazards at 31 m^3/s, p. 9

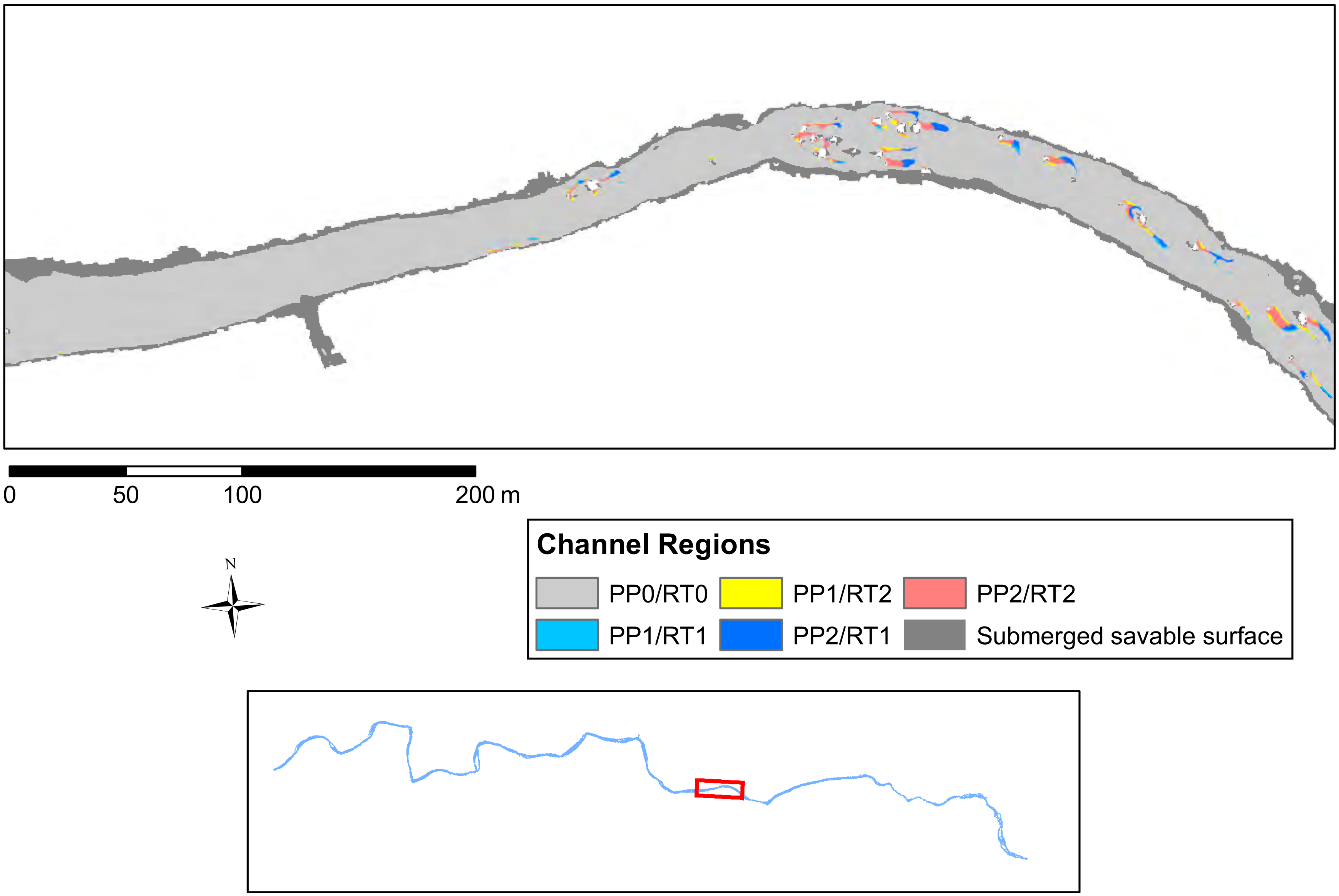

SYR Emergent Unsavable Surface Hazards at 31 m^3/s, p. 10

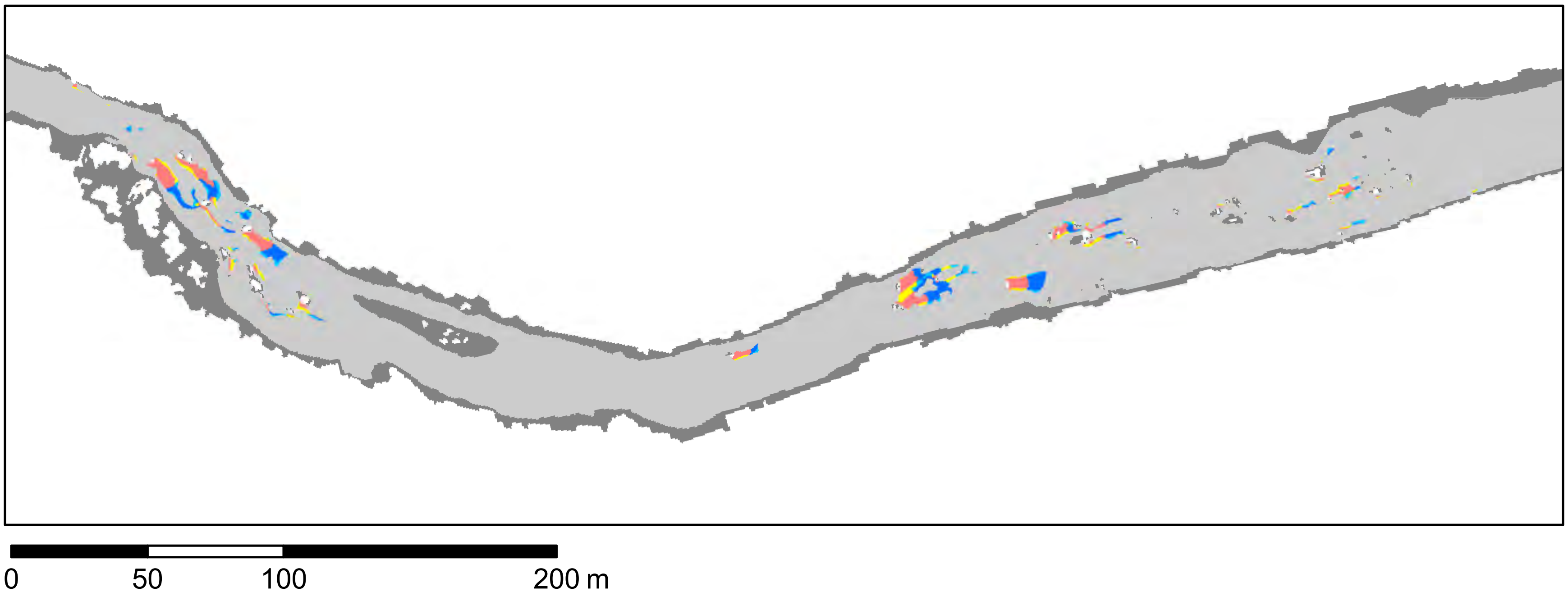

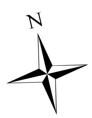

Channel Regions

PP0/RT0
PP1/RT2
PP2/RT2
PP1/RT1
PP2/RT1
Submerged savable surface

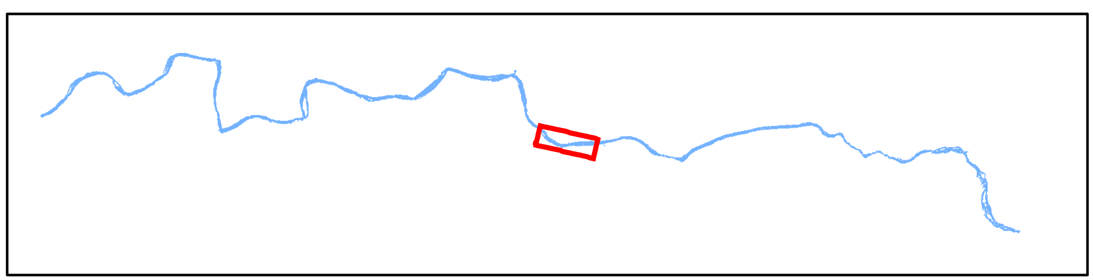

SYR Emergent Unsavable Surface Hazards at 31 m^3/s, p. 11

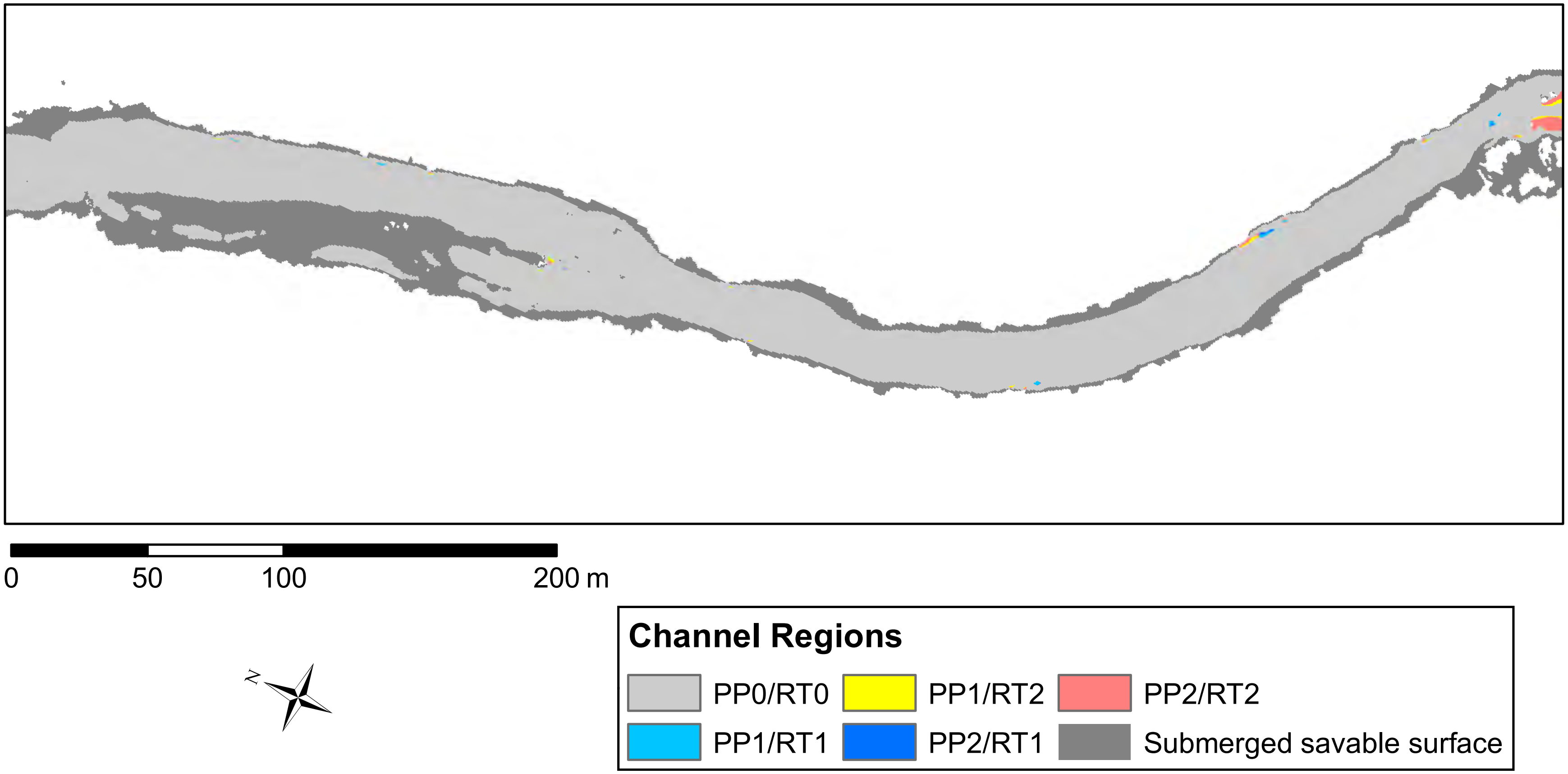

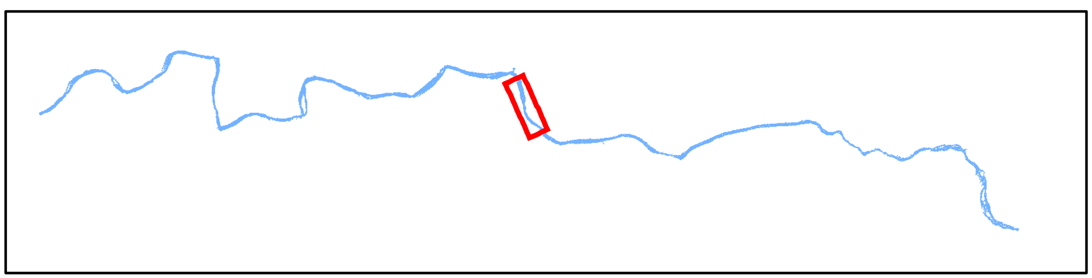

SYR Emergent Unsavable Surface Hazards at 31 m^3/s, p. 12

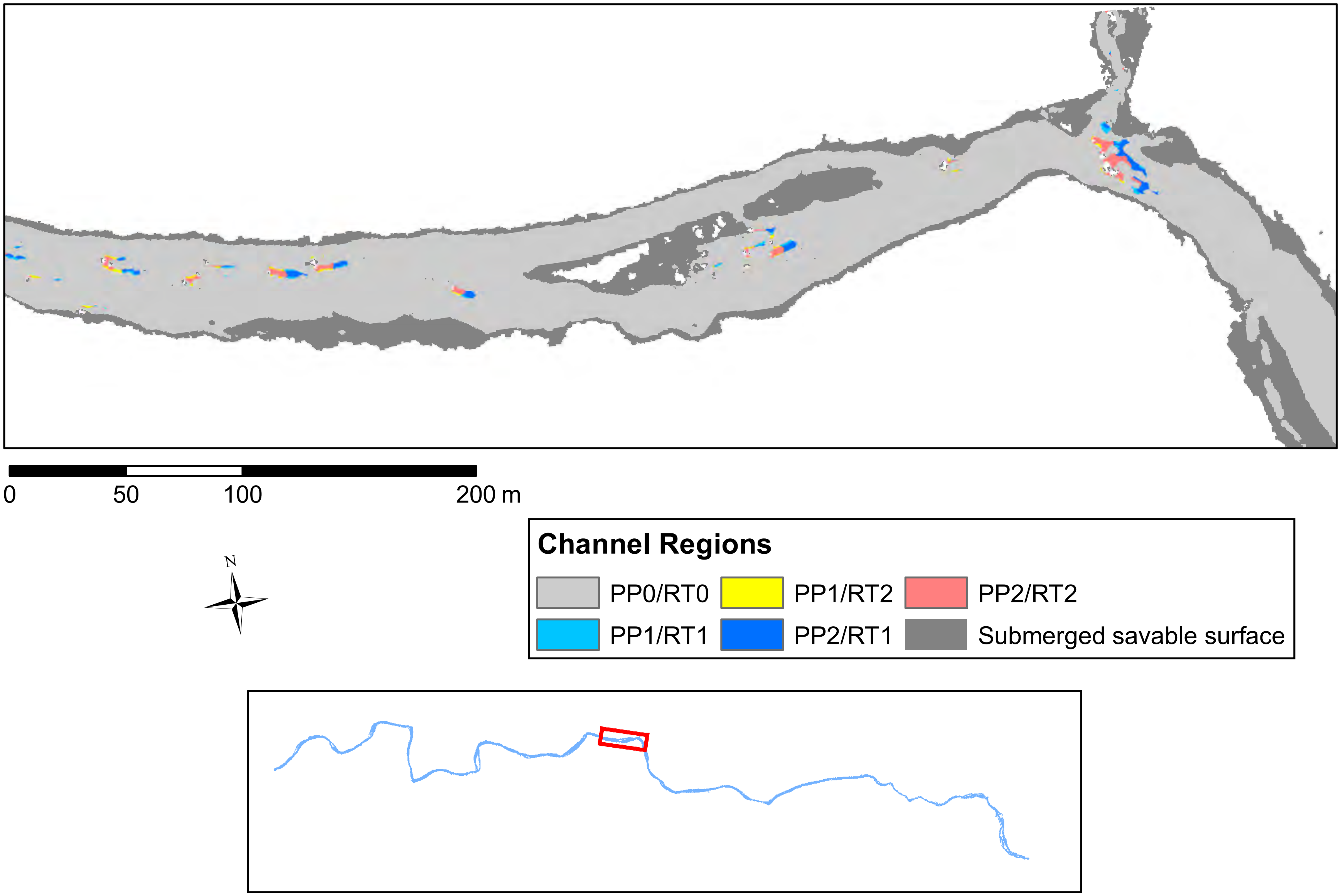

SYR Emergent Unsavable Surface Hazards at 31 m^3/s, p. 13

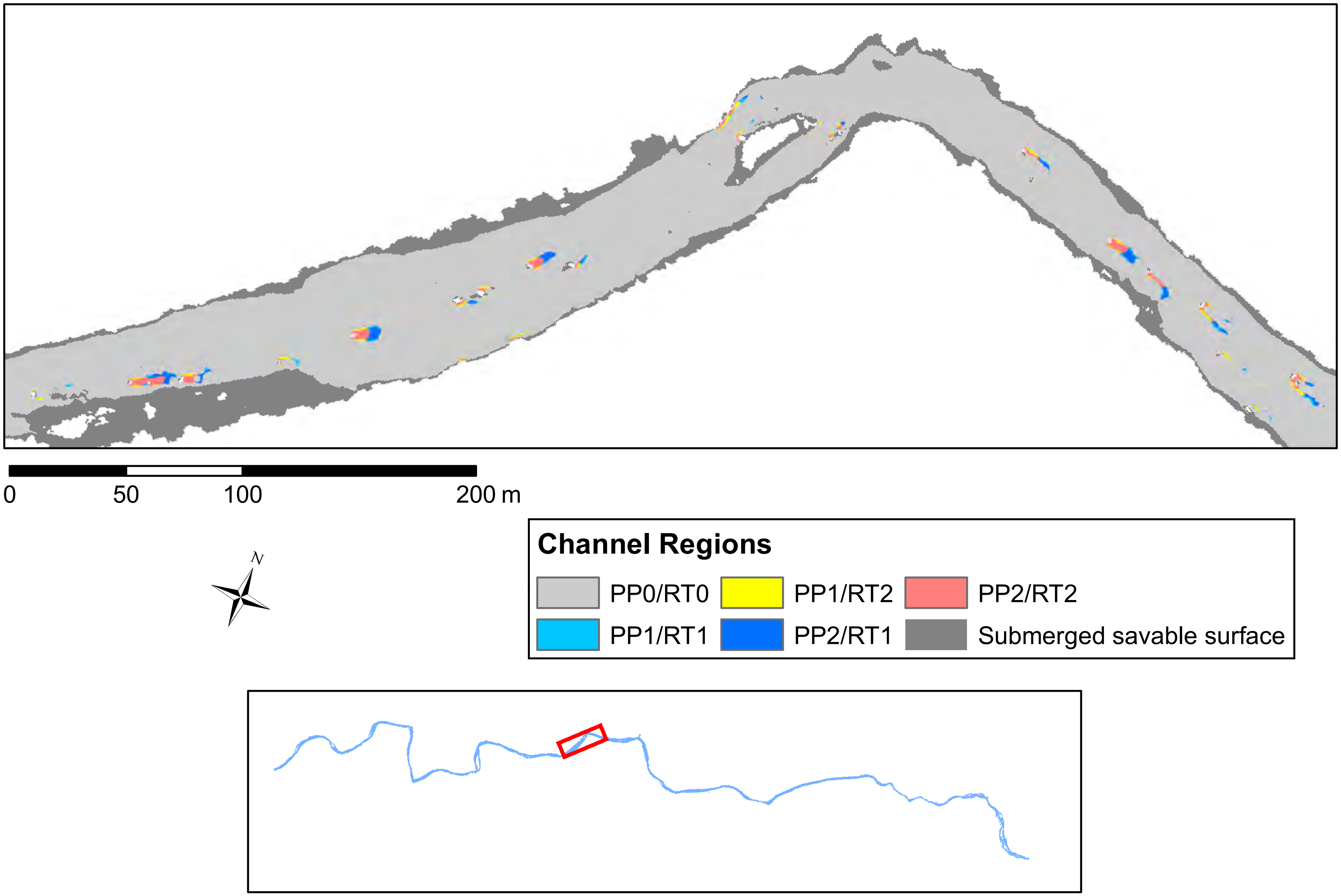

SYR Emergent Unsavable Surface Hazards at 31 m^3/s, p. 14

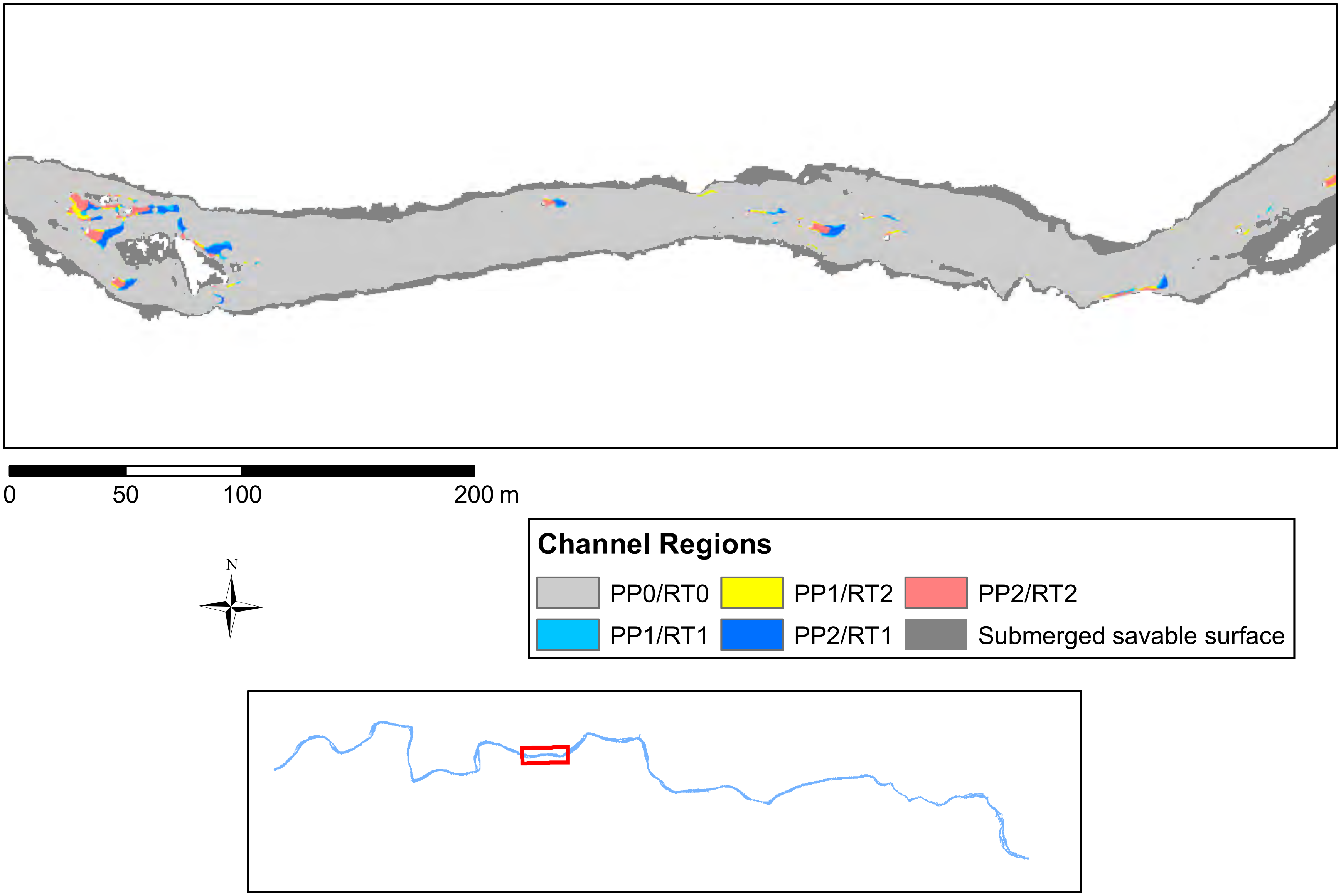

SYR Emergent Unsavable Surface Hazards at 31 m^3/s, p. 15

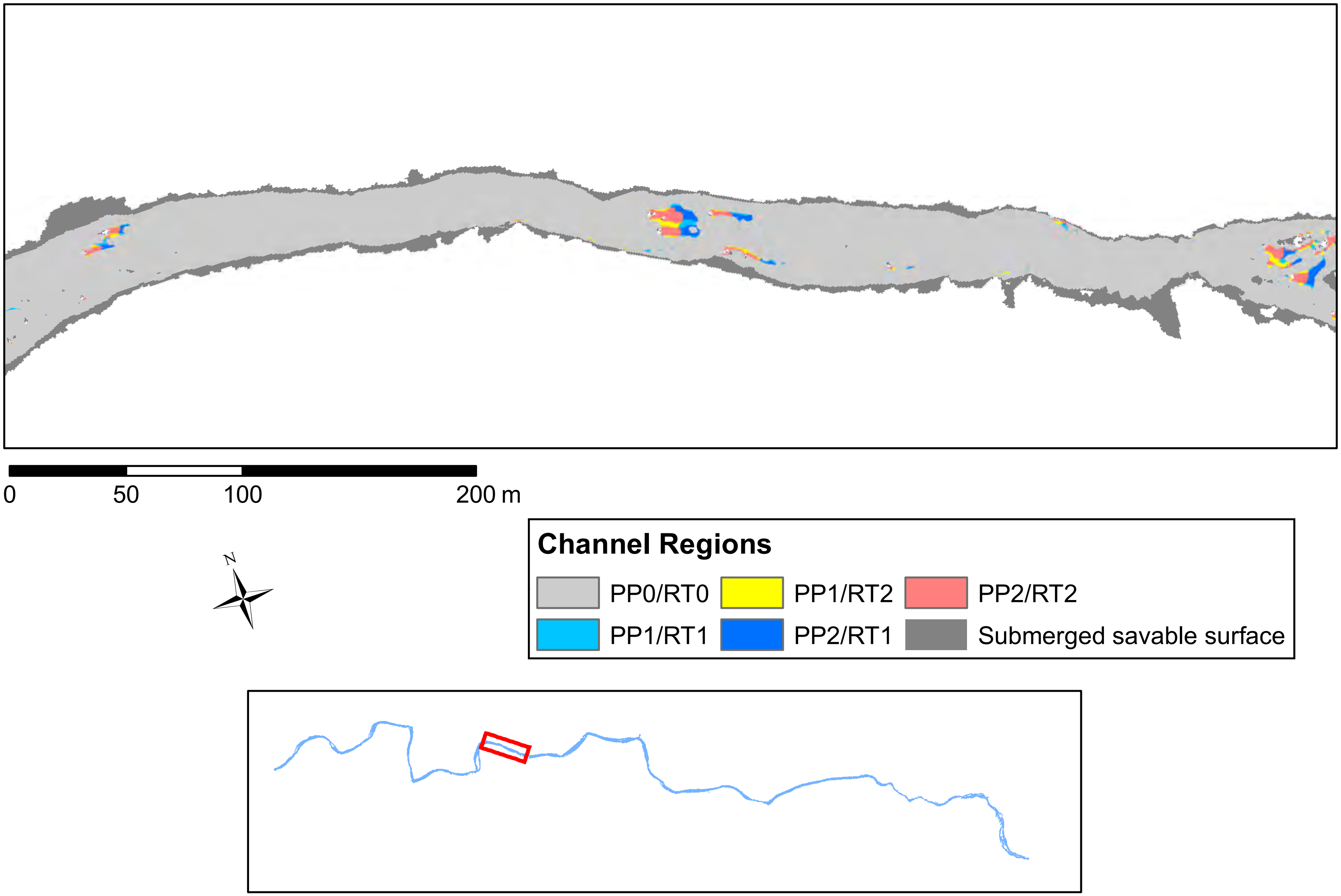

SYR Emergent Unsavable Surface Hazards at 31 m^3/s, p. 16

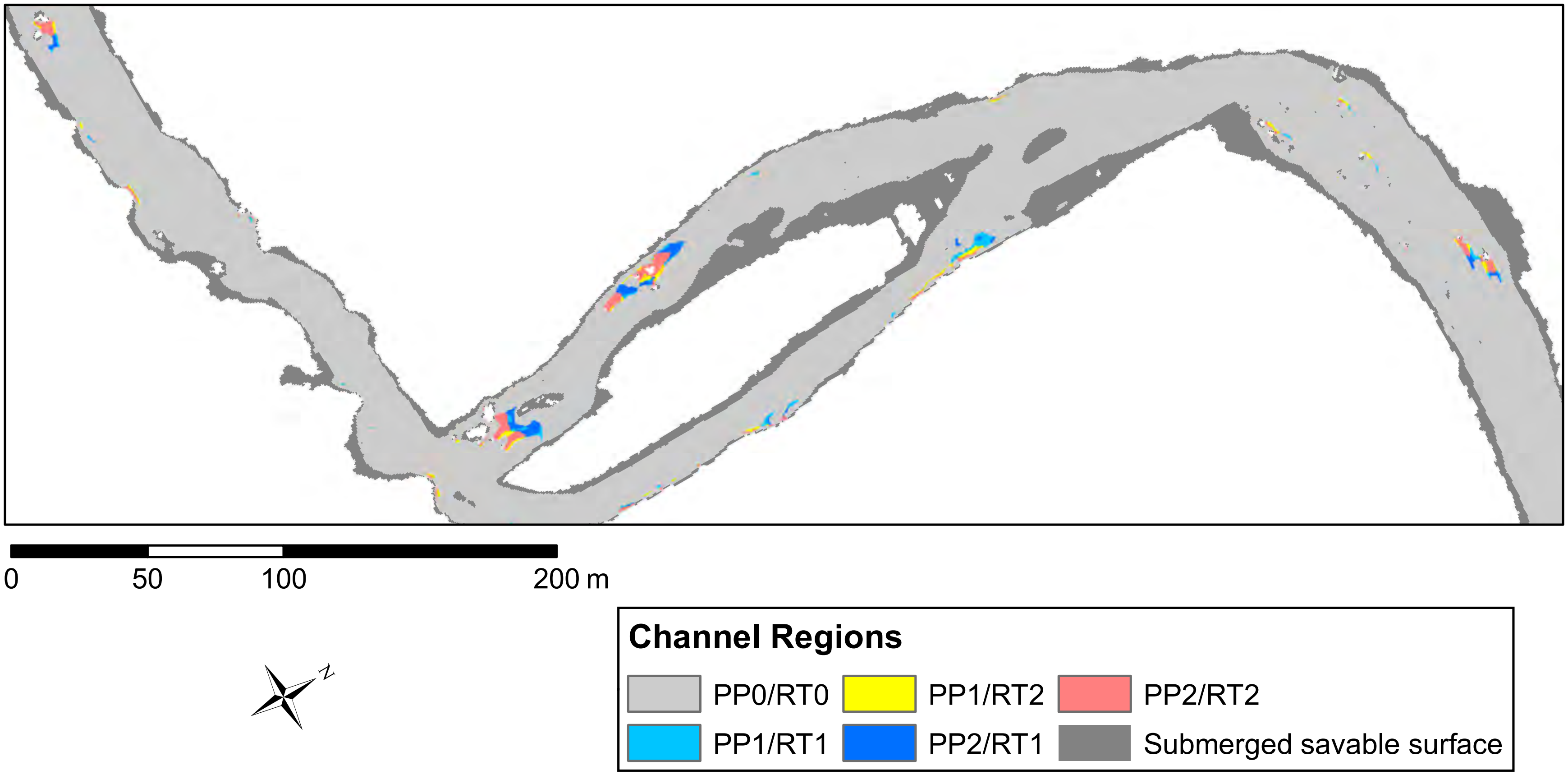

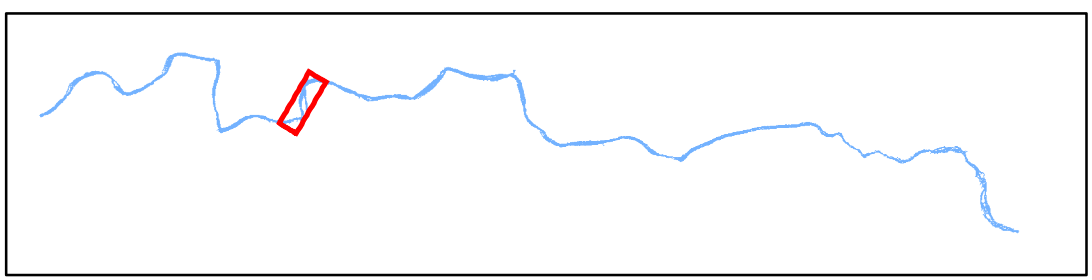

SYR Emergent Unsavable Surface Hazards at 31 m^3/s, p. 17

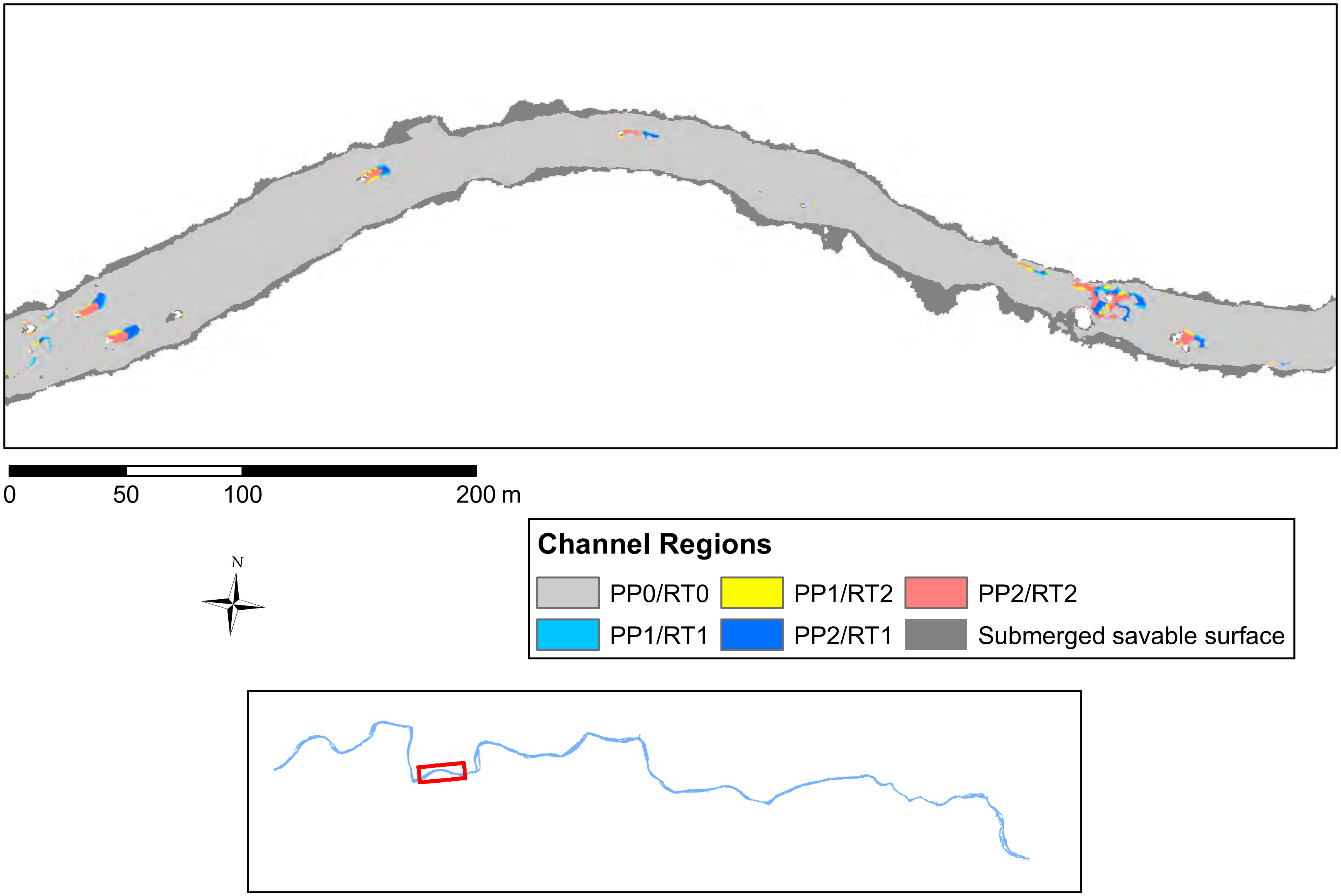

SYR Emergent Unsavable Surface Hazards at 31 m^3/s, p. 18

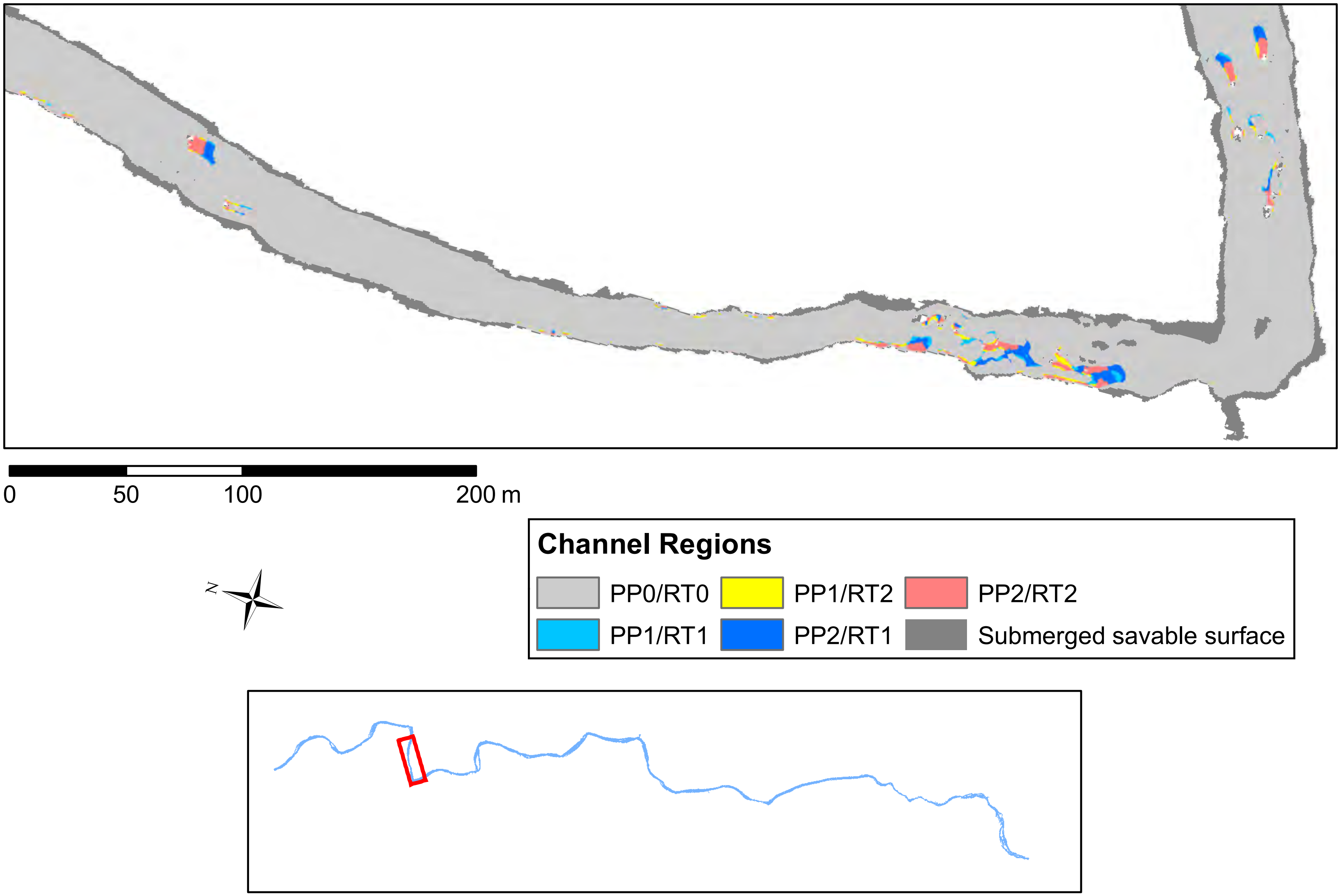

SYR Emergent Unsavable Surface Hazards at 31 m^3/s, p. 19

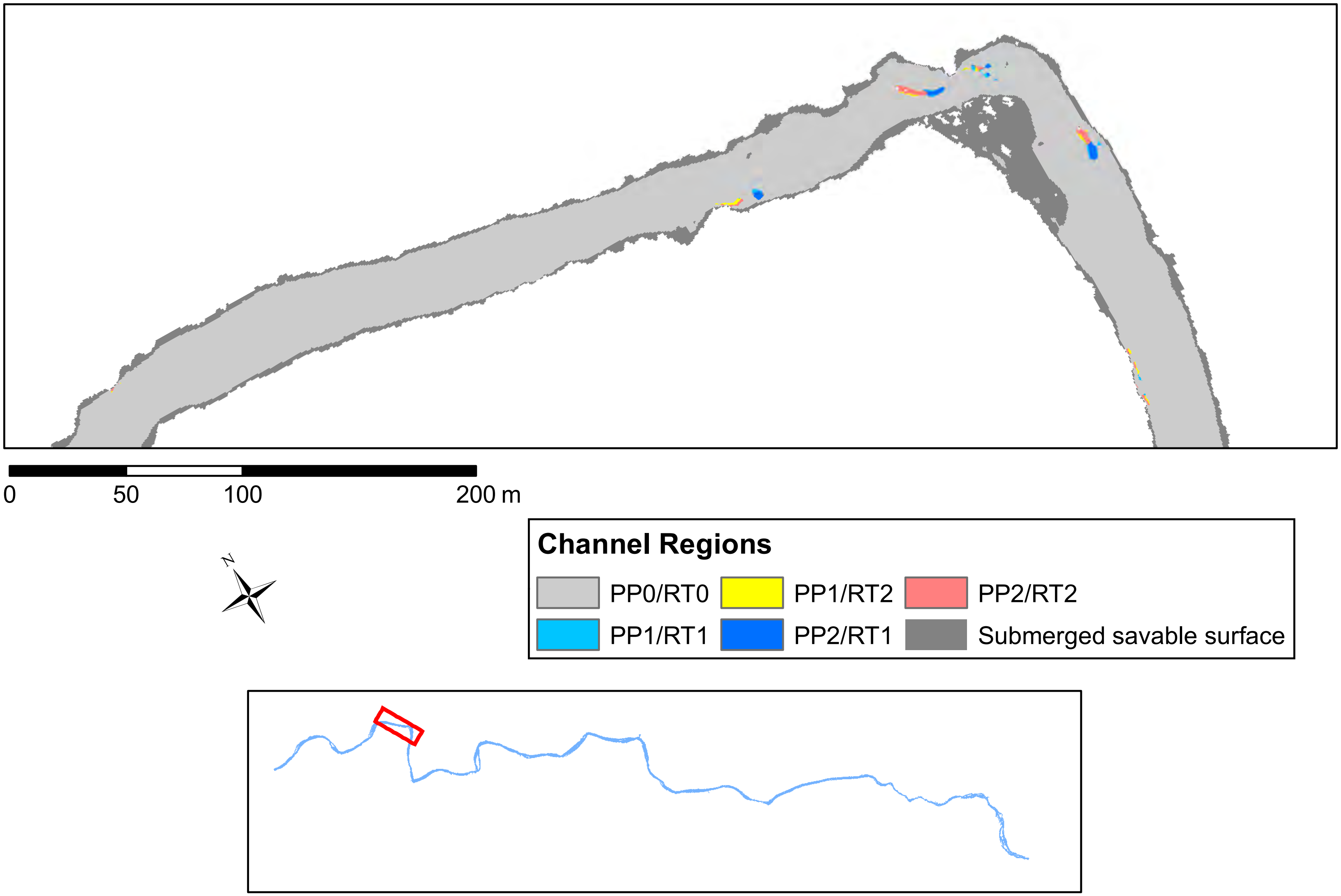

SYR Emergent Unsavable Surface Hazards at 31 m^3/s, p. 20

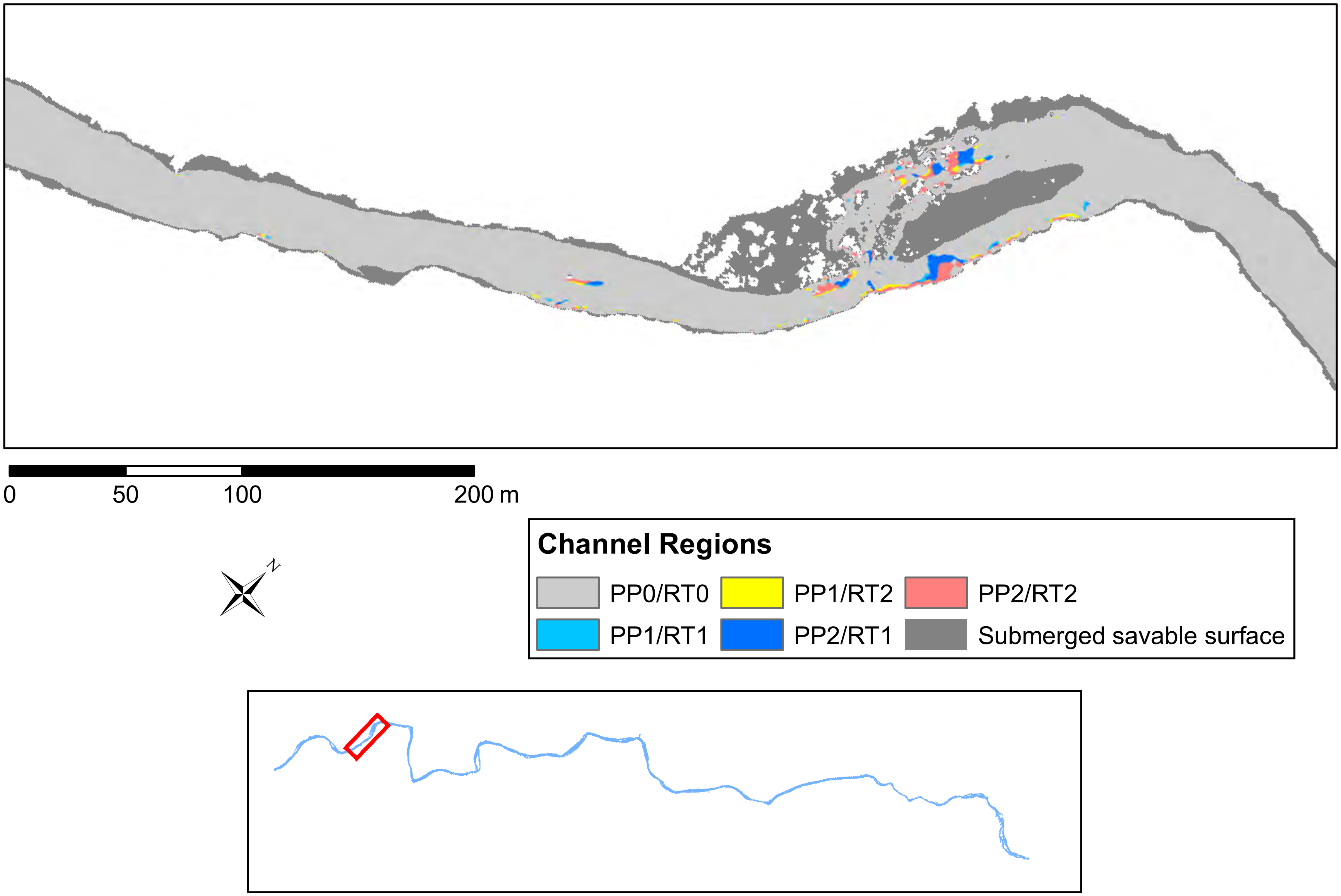

SYR Emergent Unsavable Surface Hazards at 31 m^3/s, p. 21

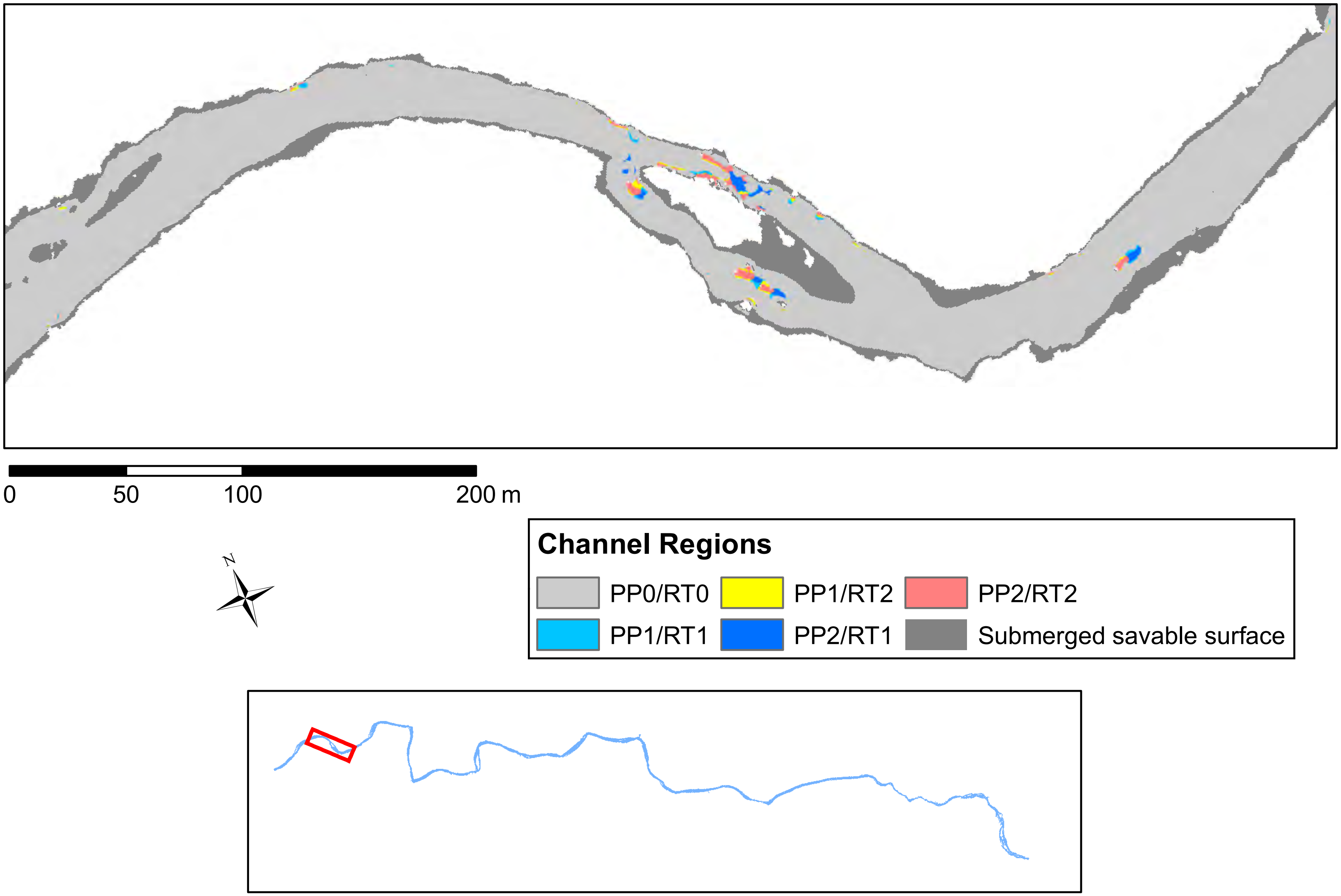

SYR Emergent Unsavable Surface Hazards at 31 m^3/s, p. 22

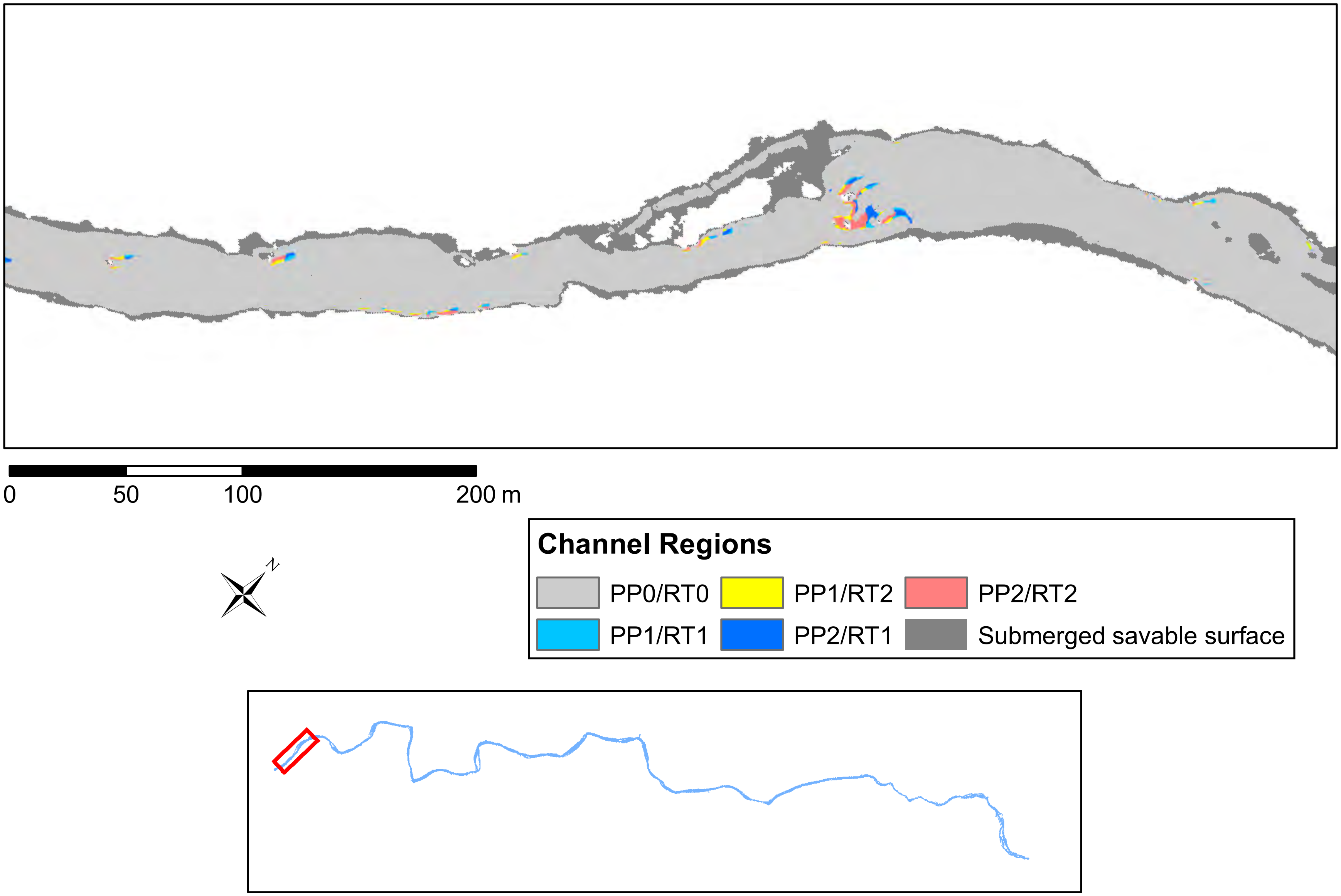

SYR Emergent Unsavable Surface Hazards at 31 m^3/s, p. 23

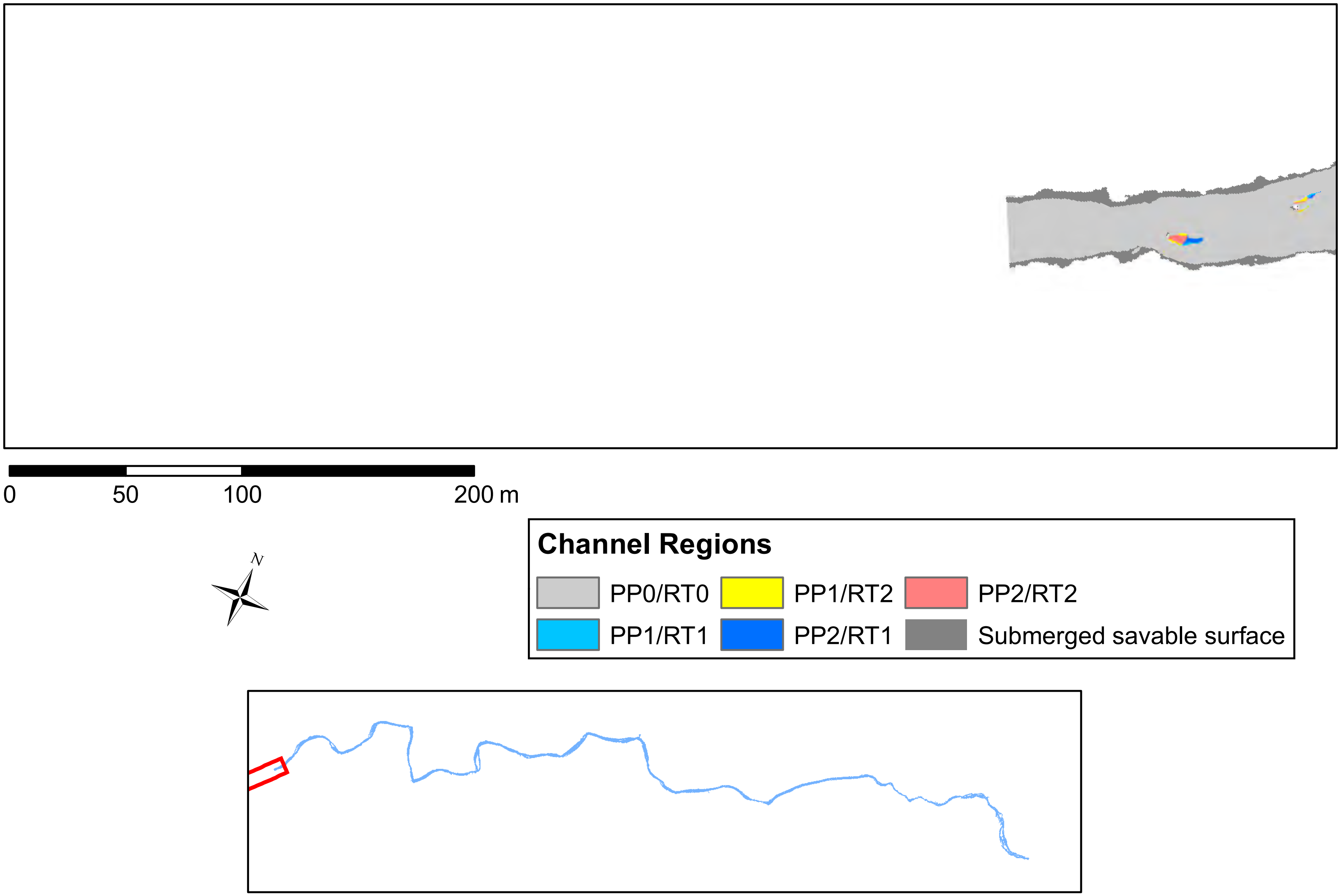

SYR Jump Hazards at 31 m^3/s, p. 1

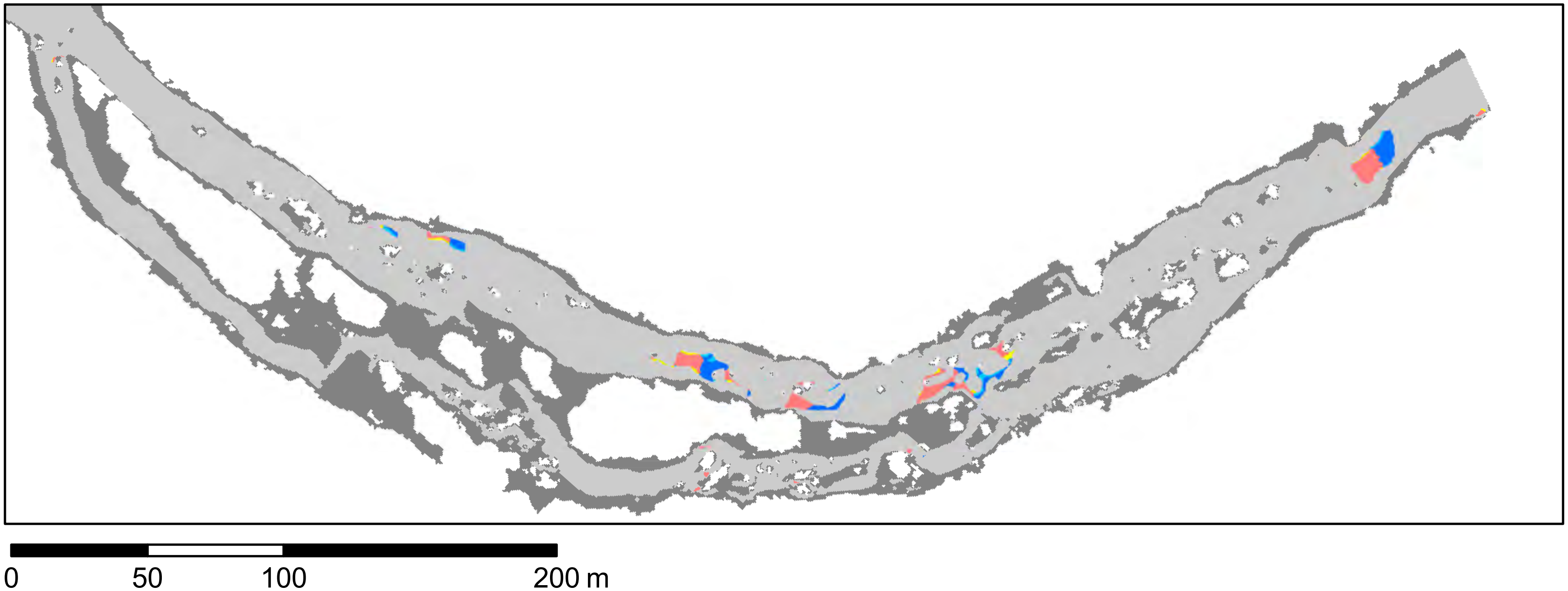

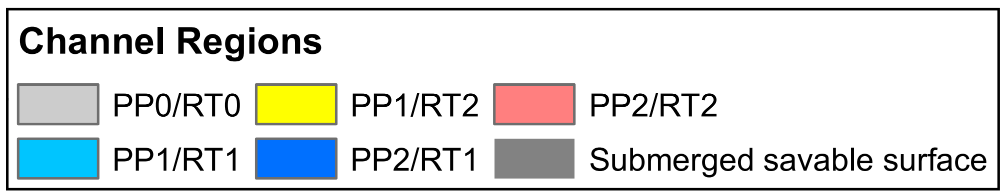

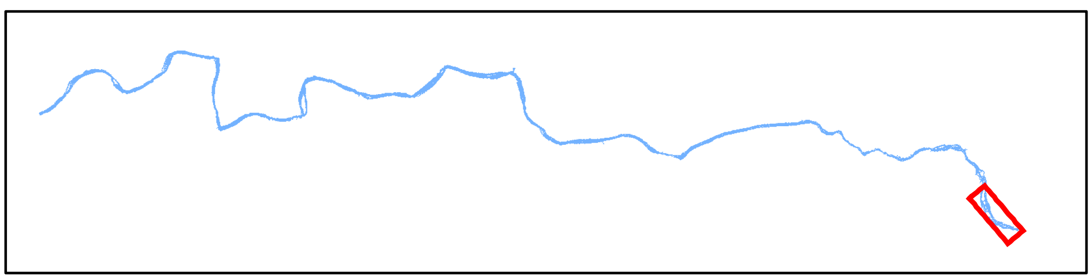

SYR Jump Hazards at 31 m^3/s, p. 2

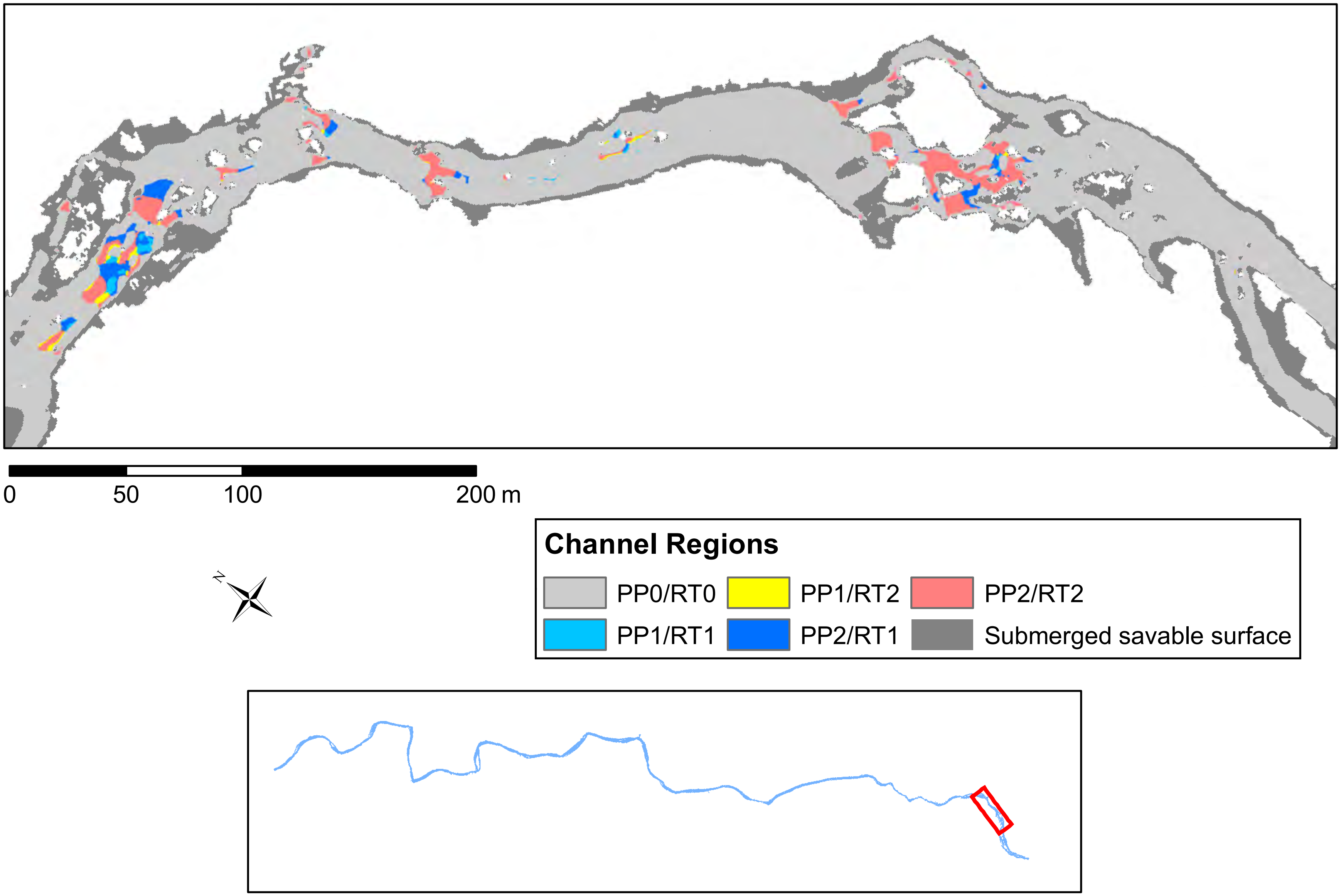

SYR Jump Hazards at 31 m^3/s, p. 3

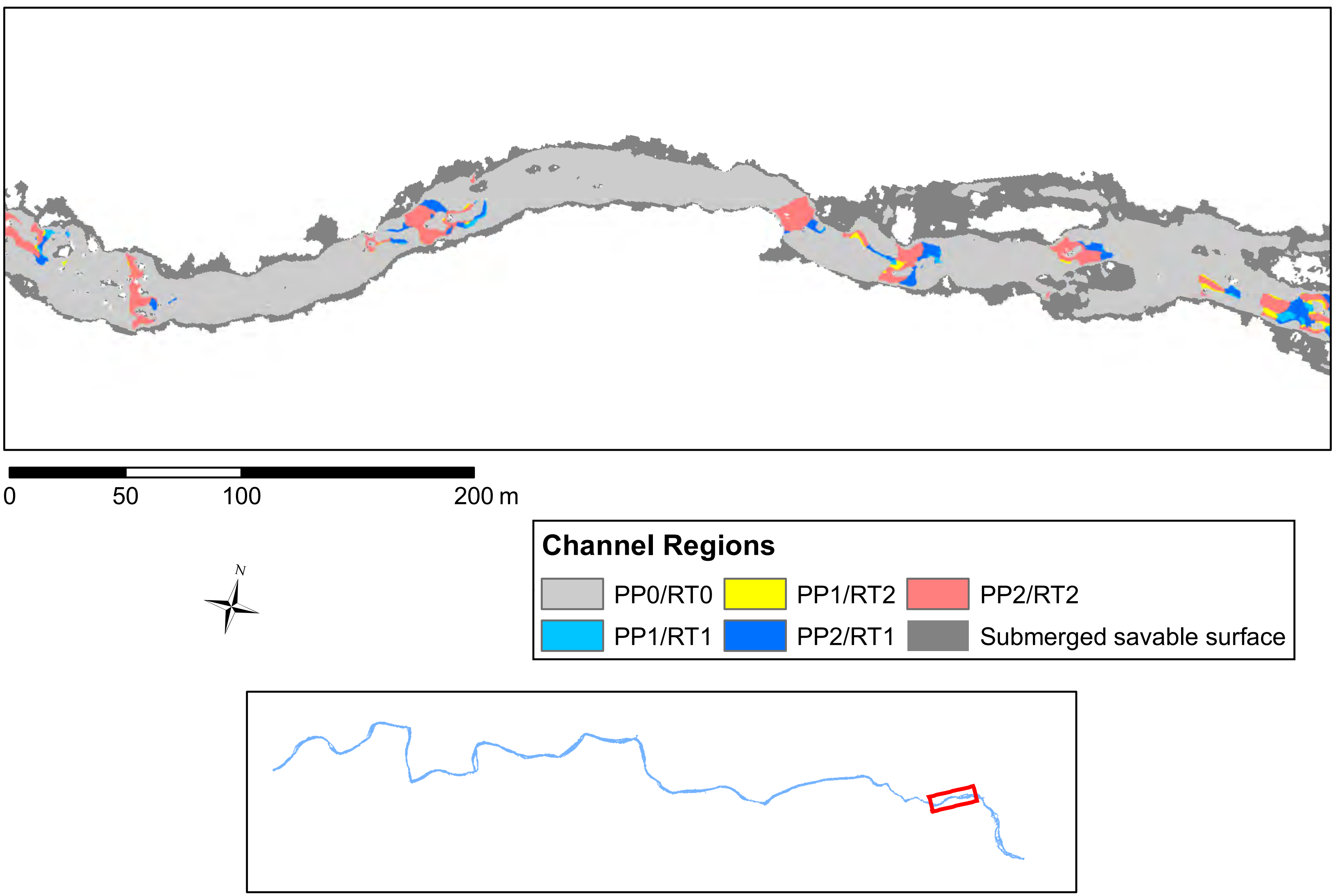

SYR Jump Hazards at 31 m^3/s, p. 4

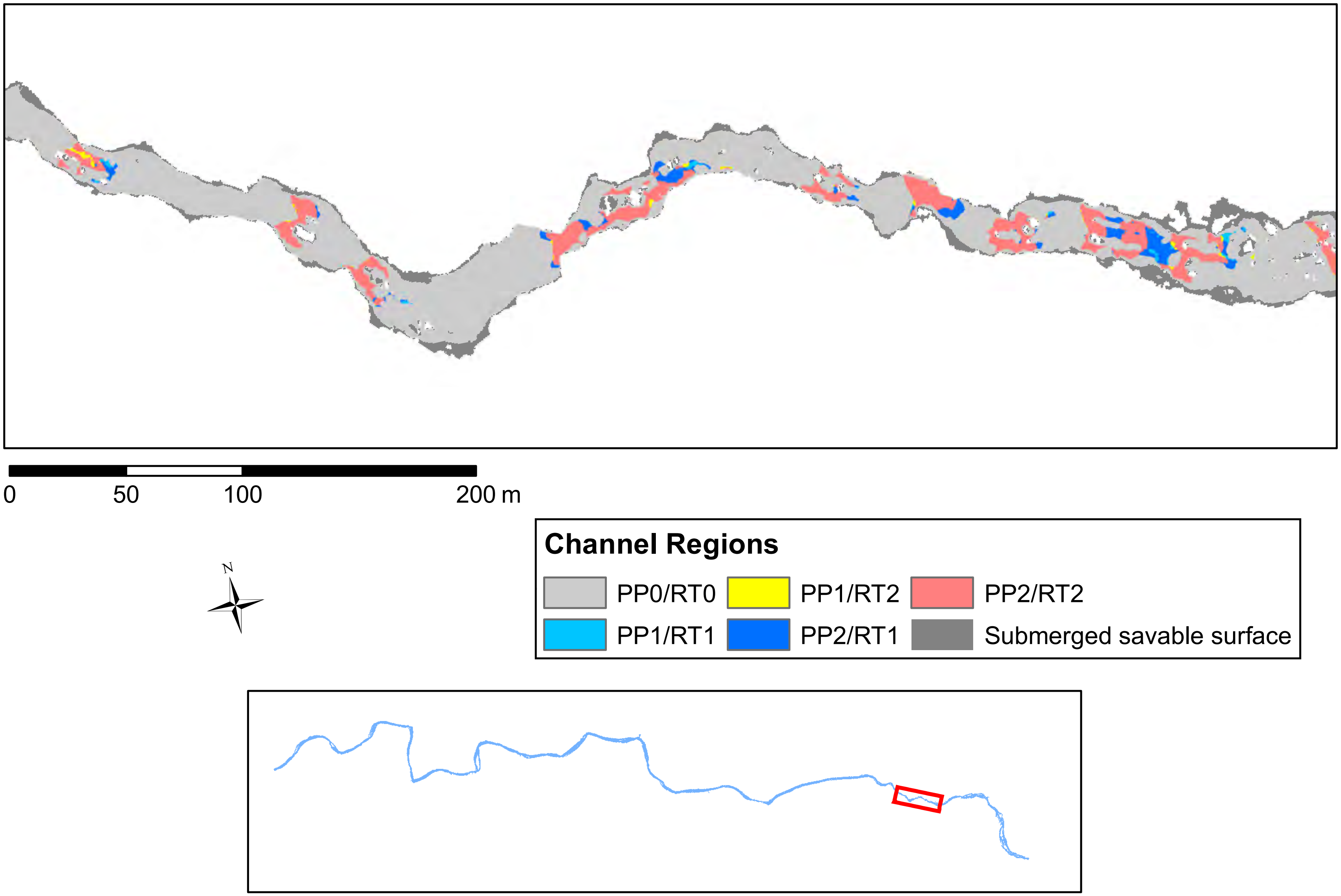

SYR Jump Hazards at 31 m^3/s, p. 5

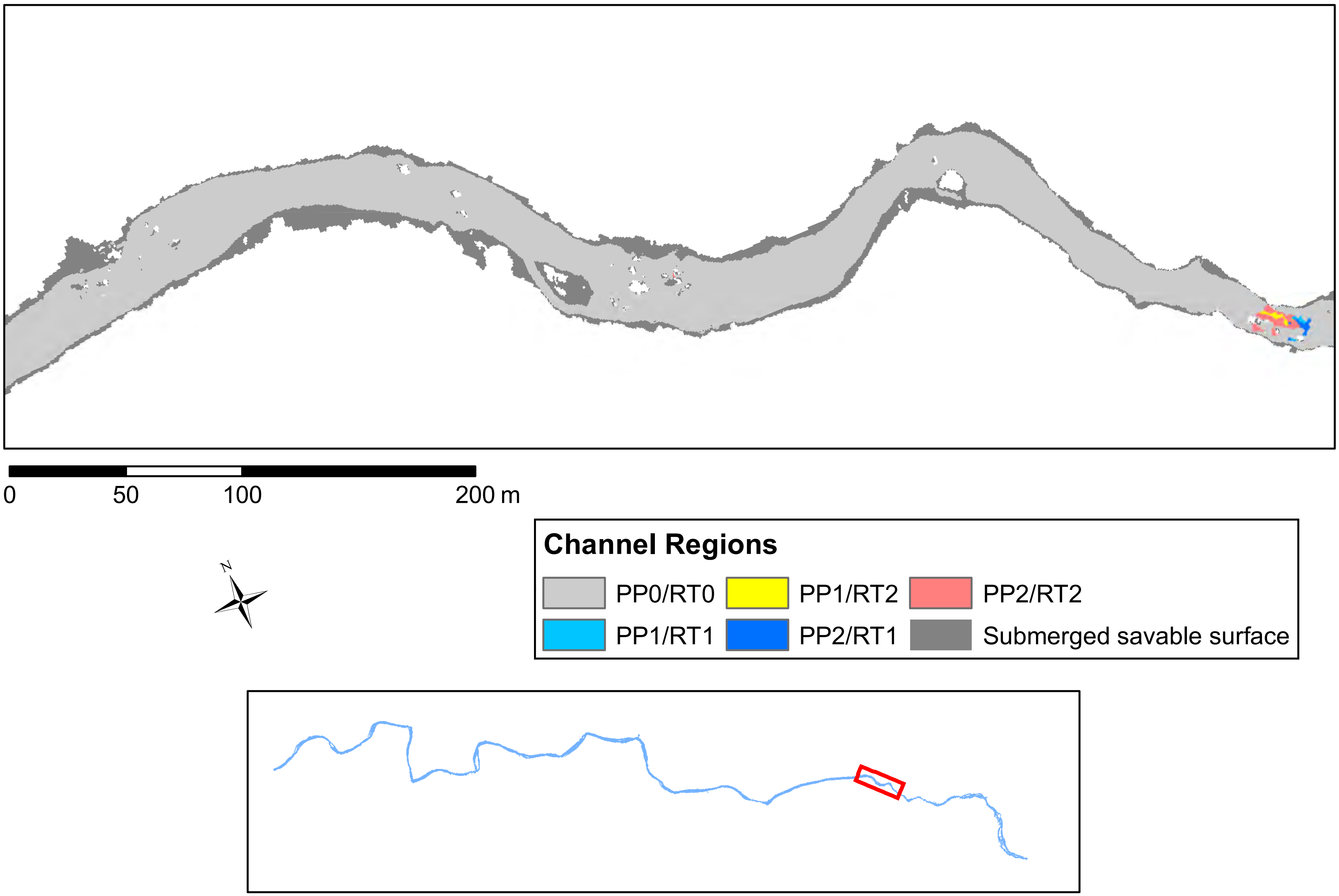

SYR Jump Hazards at 31 m^3/s, p. 6

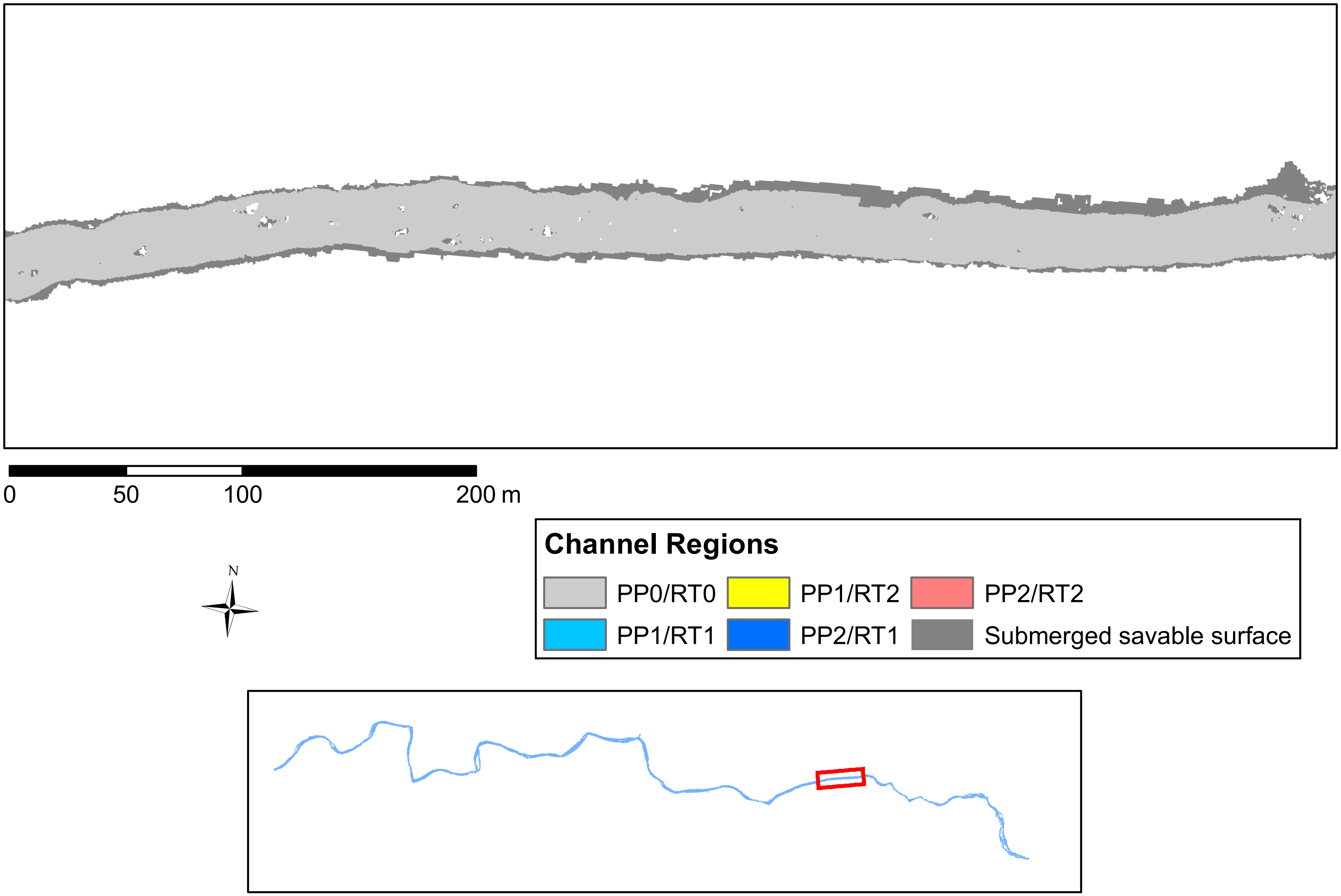

SYR Jump Hazards at 31 m^3/s, p. 7

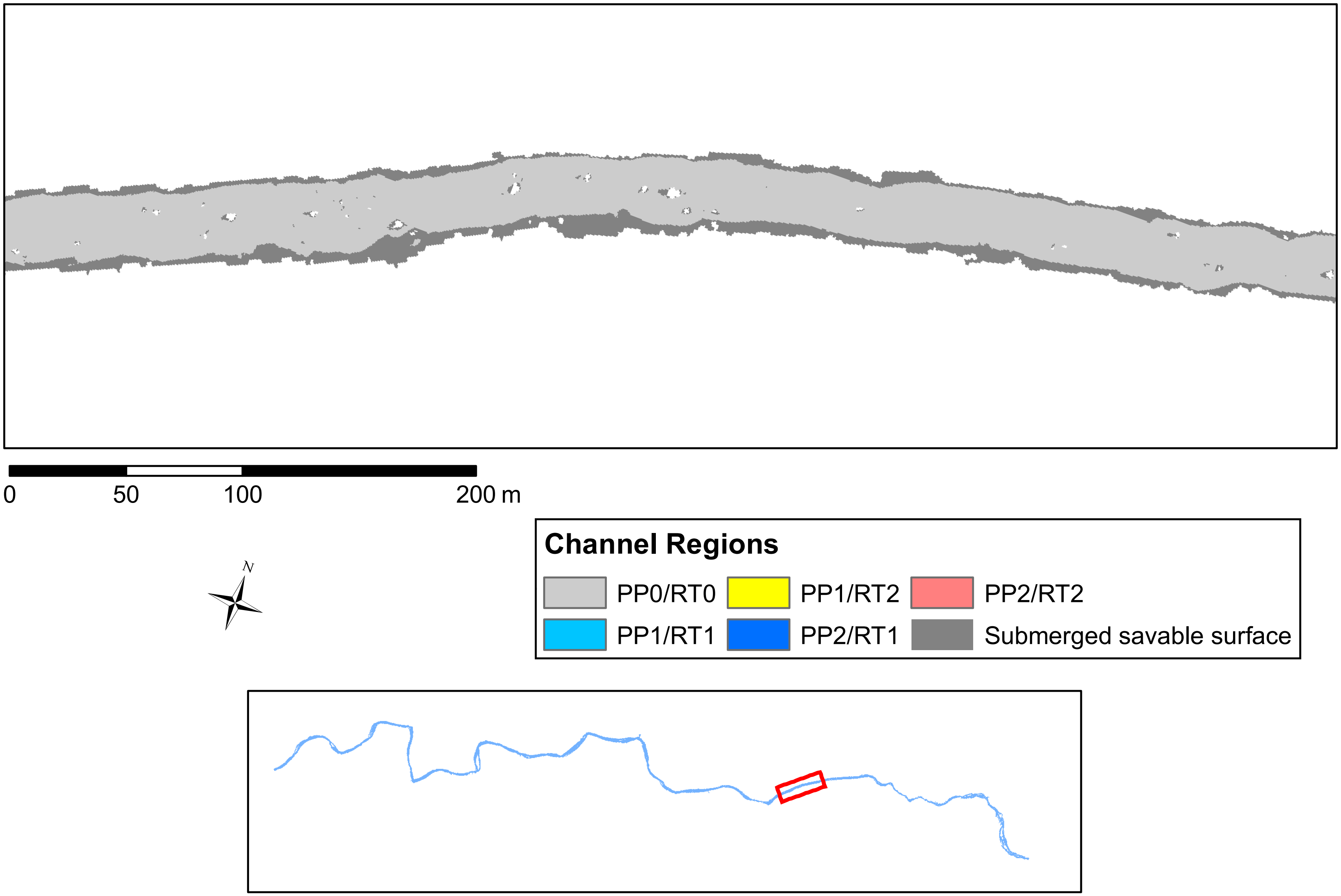

SYR Jump Hazards at 31 m^3/s, p. 8

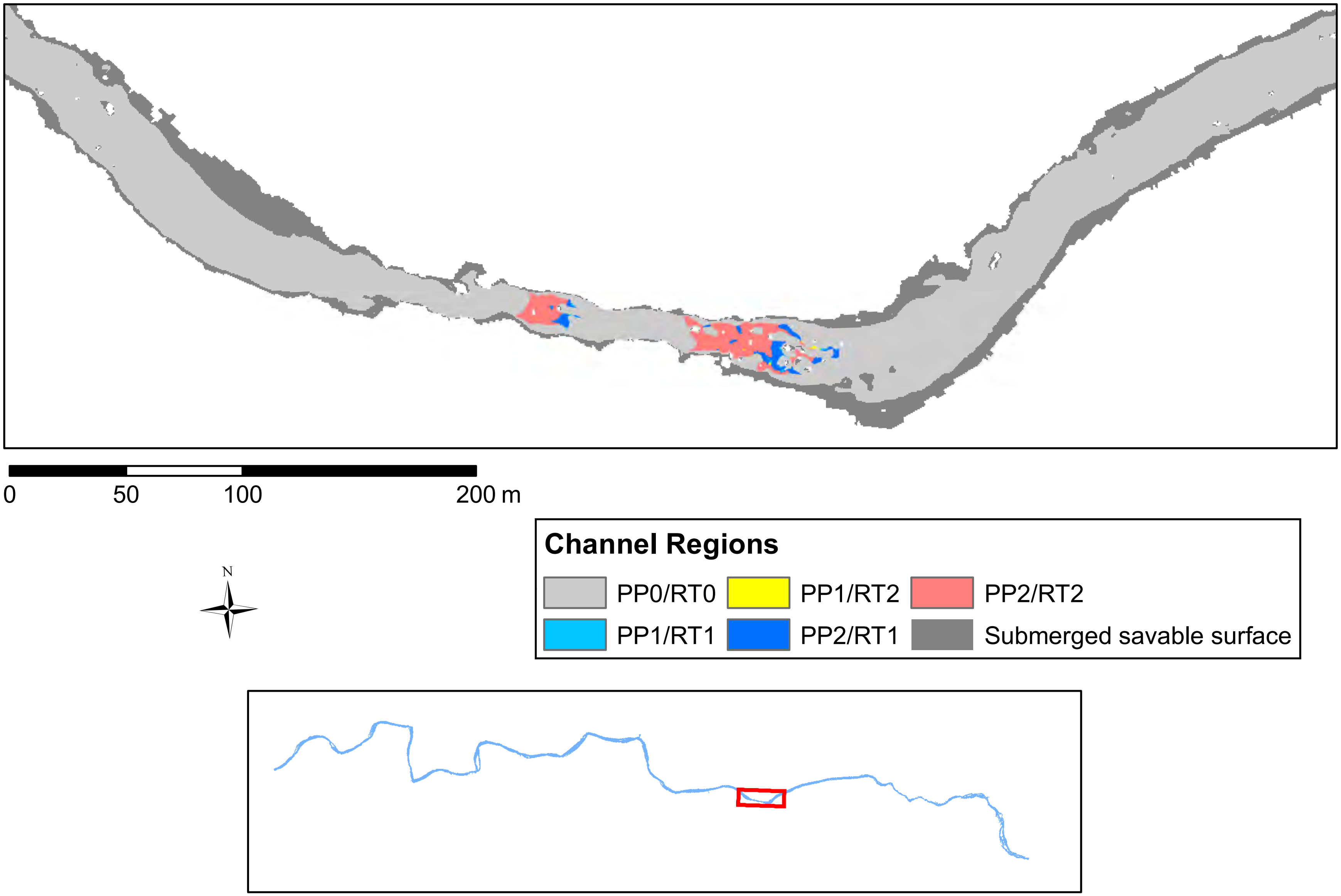

SYR Jump Hazards at 31 m^3/s, p. 9

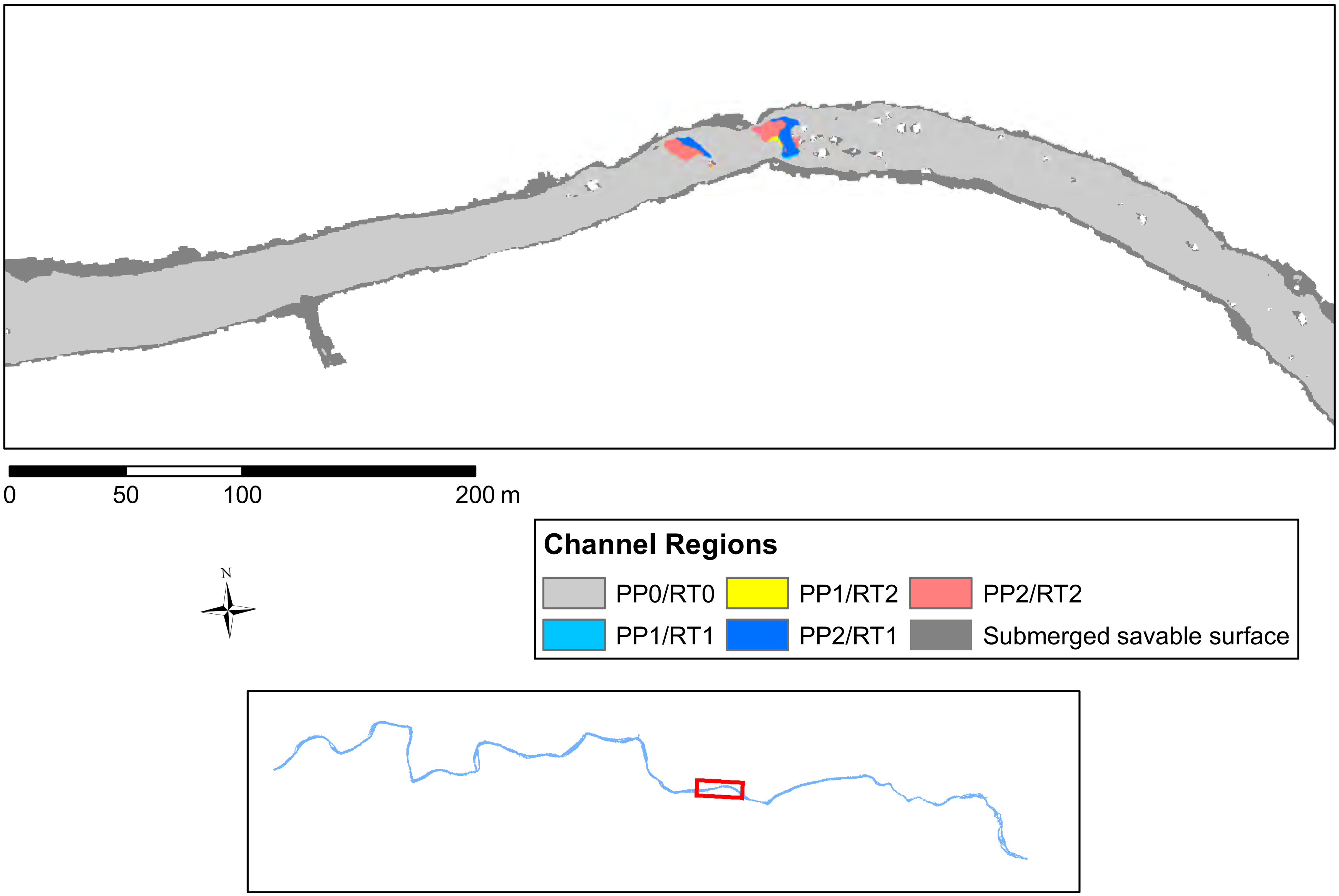

SYR Jump Hazards at 31 m^3/s, p. 10

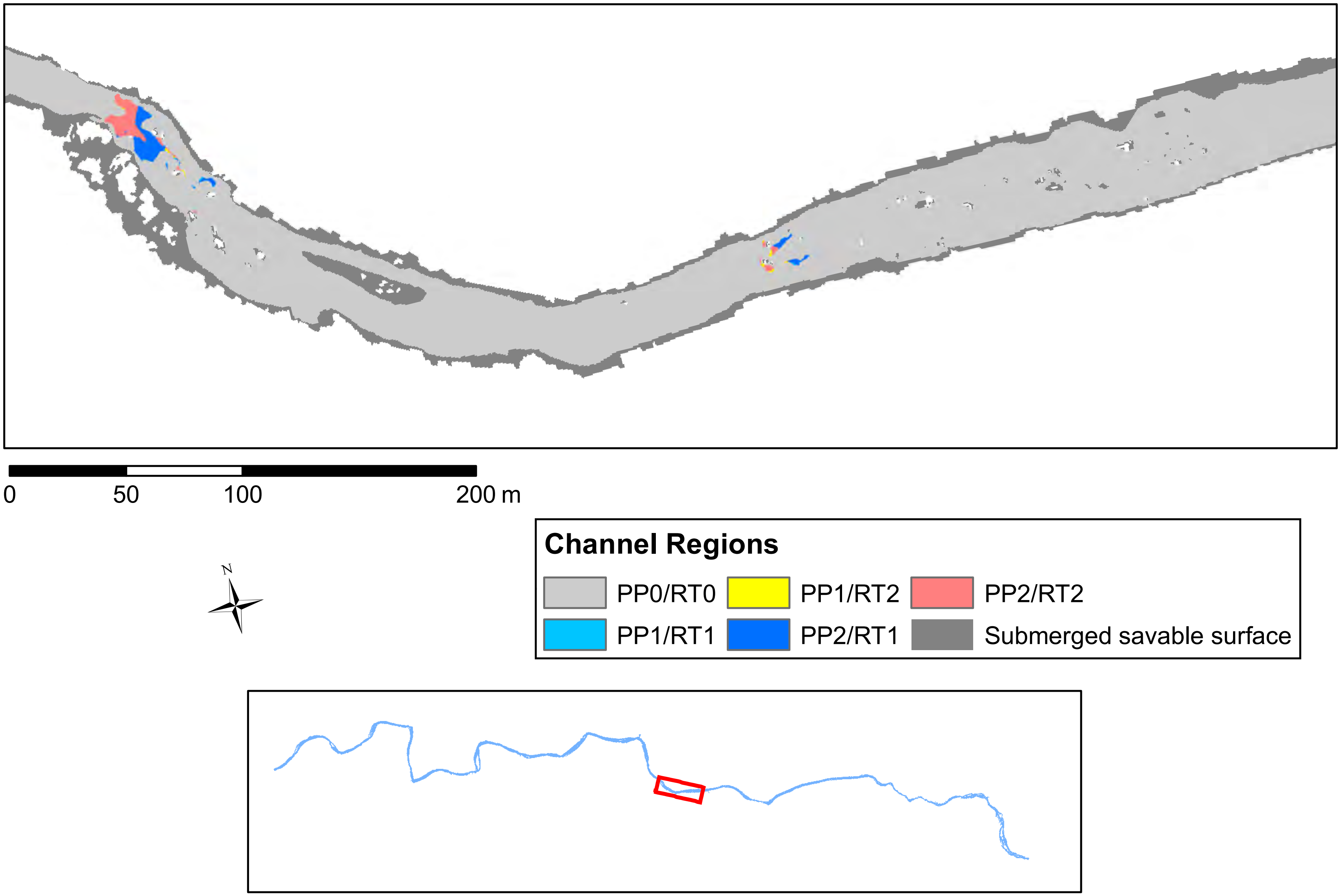

SYR Jump Hazards at 31 m^3/s, p. 11

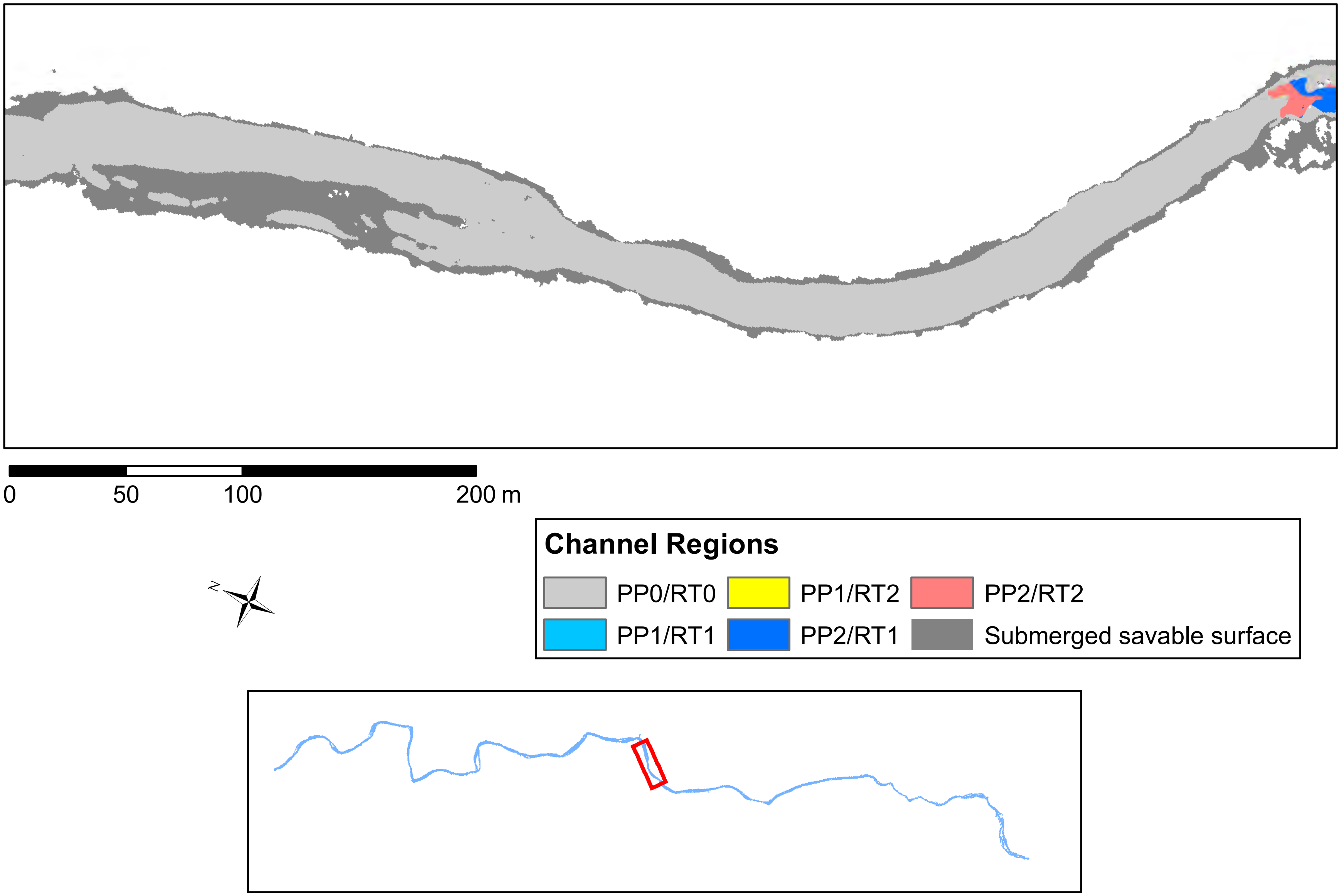

SYR Jump Hazards at 31 m^3/s, p. 12

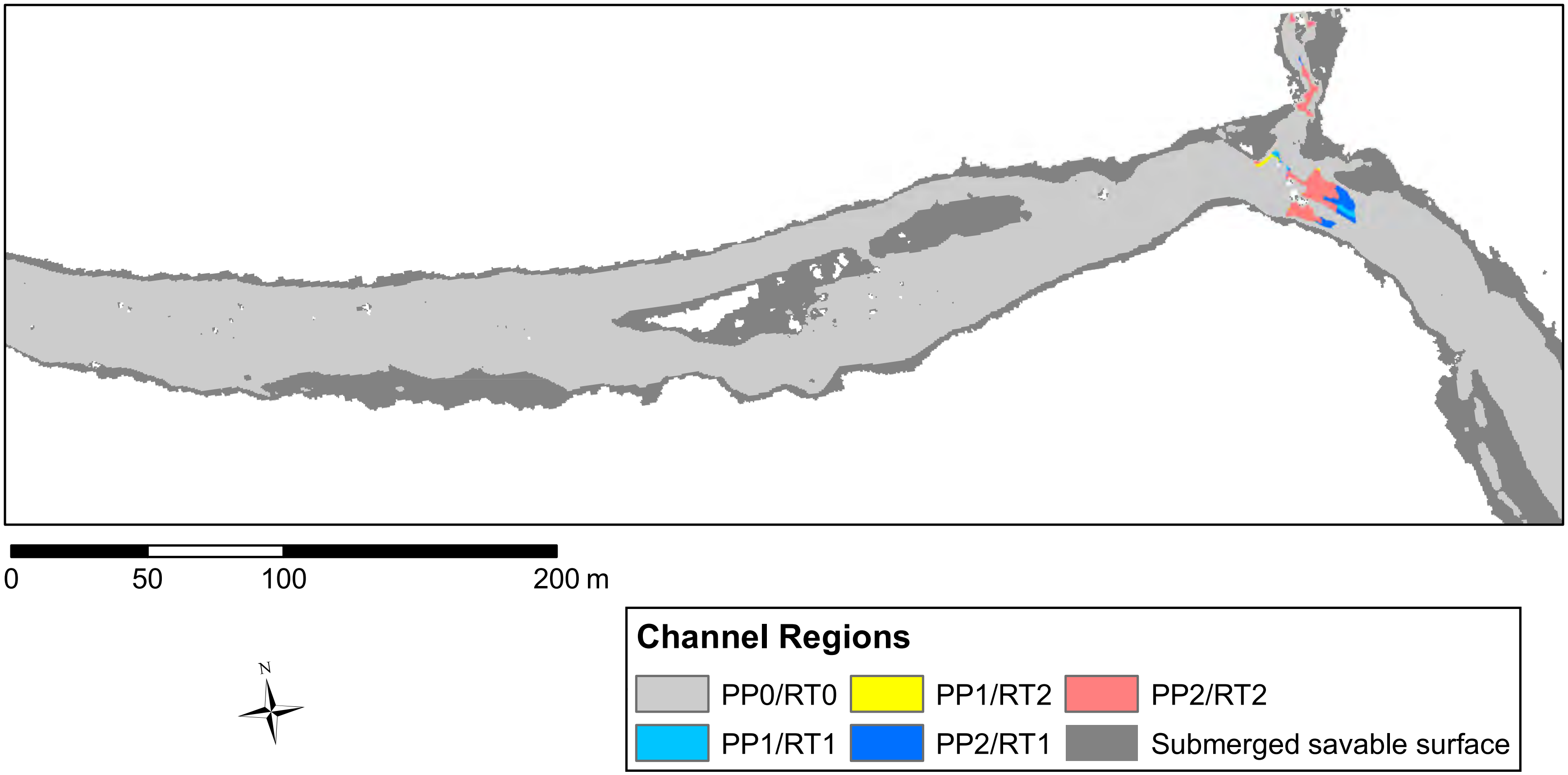

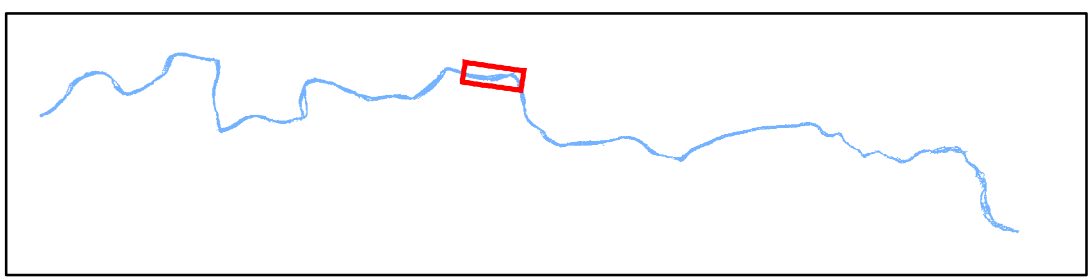

SYR Jump Hazards at 31 m^3/s, p. 13

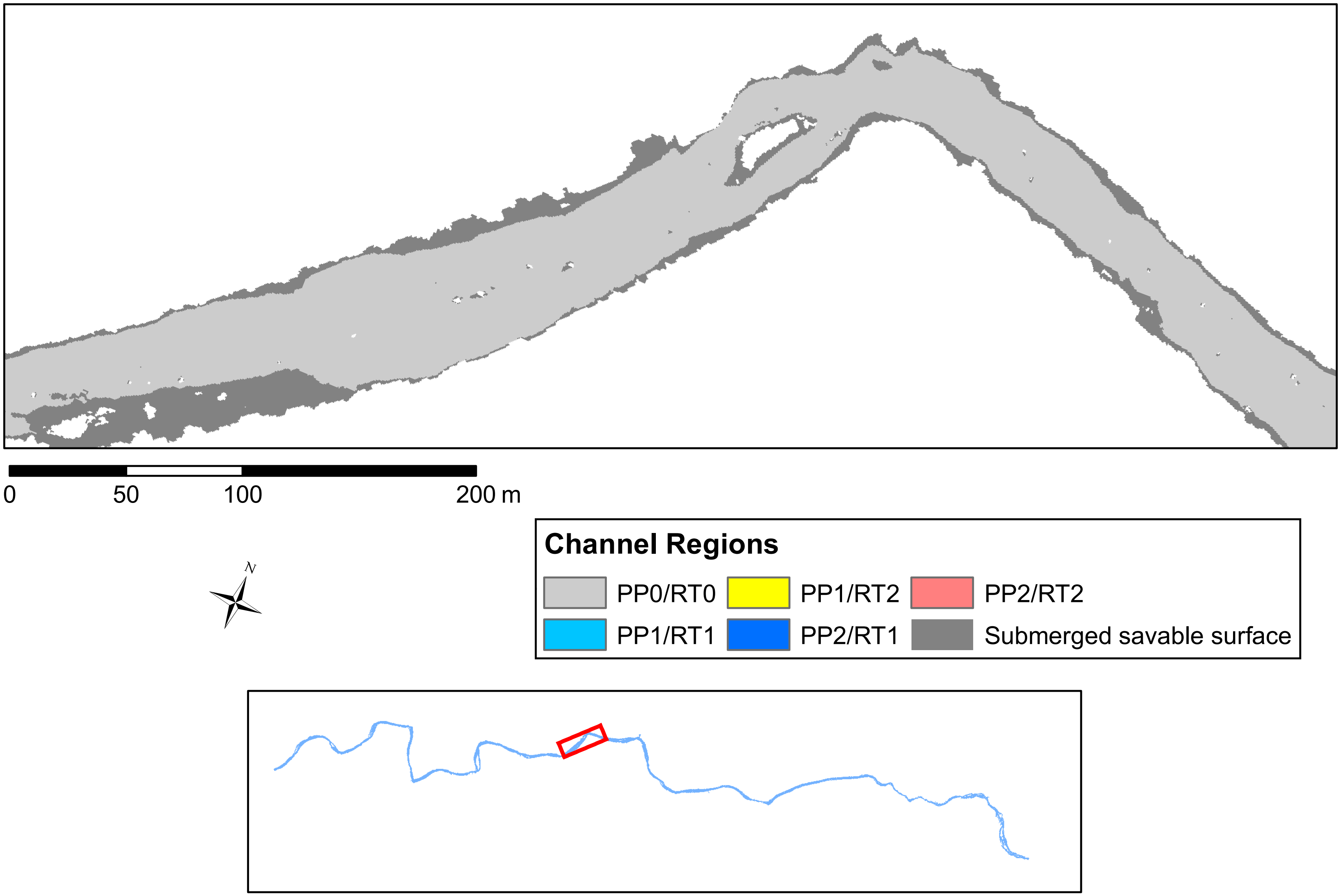

SYR Jump Hazards at 31 m^3/s, p. 14

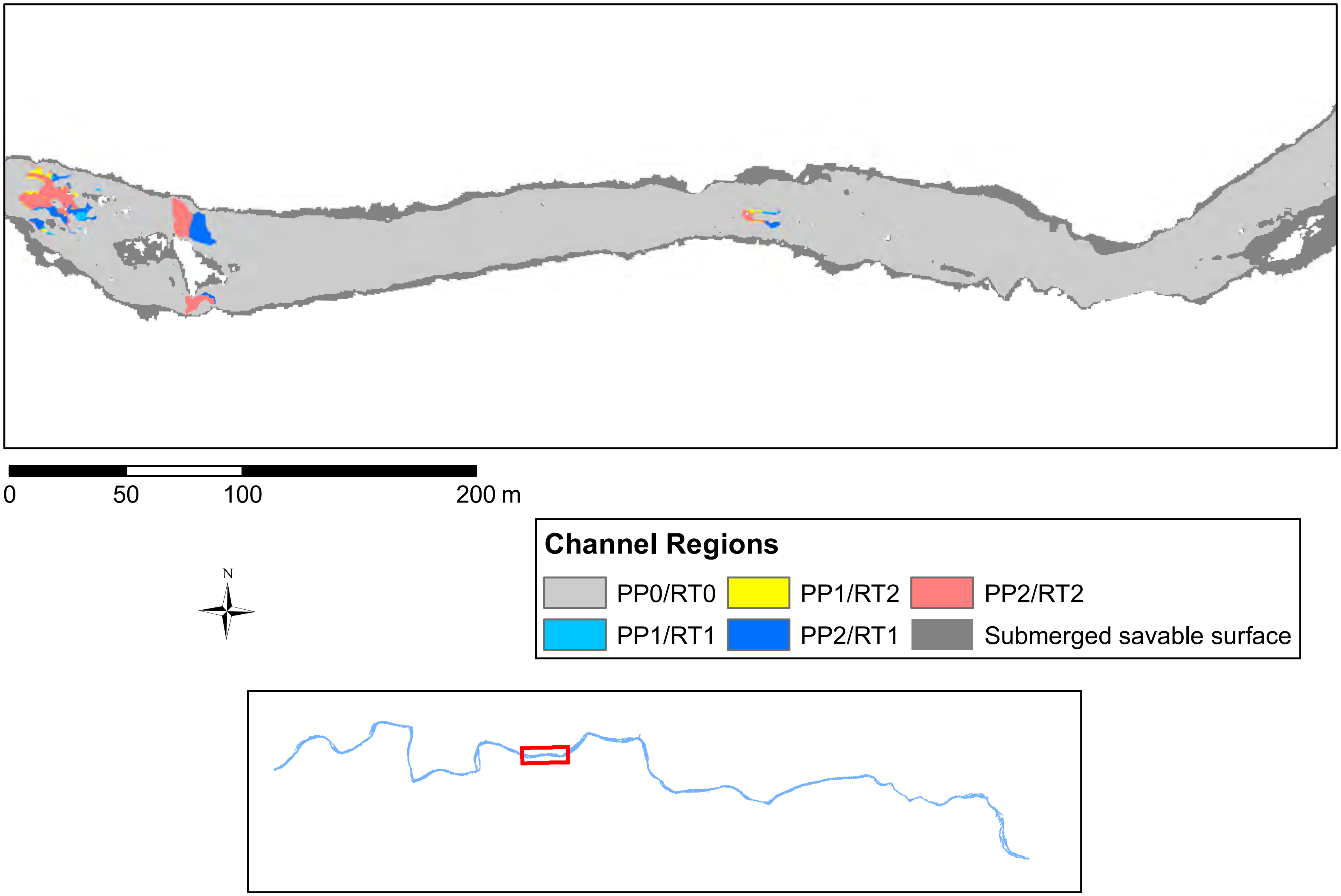

SYR Jump Hazards at 31 m^3/s, p. 15

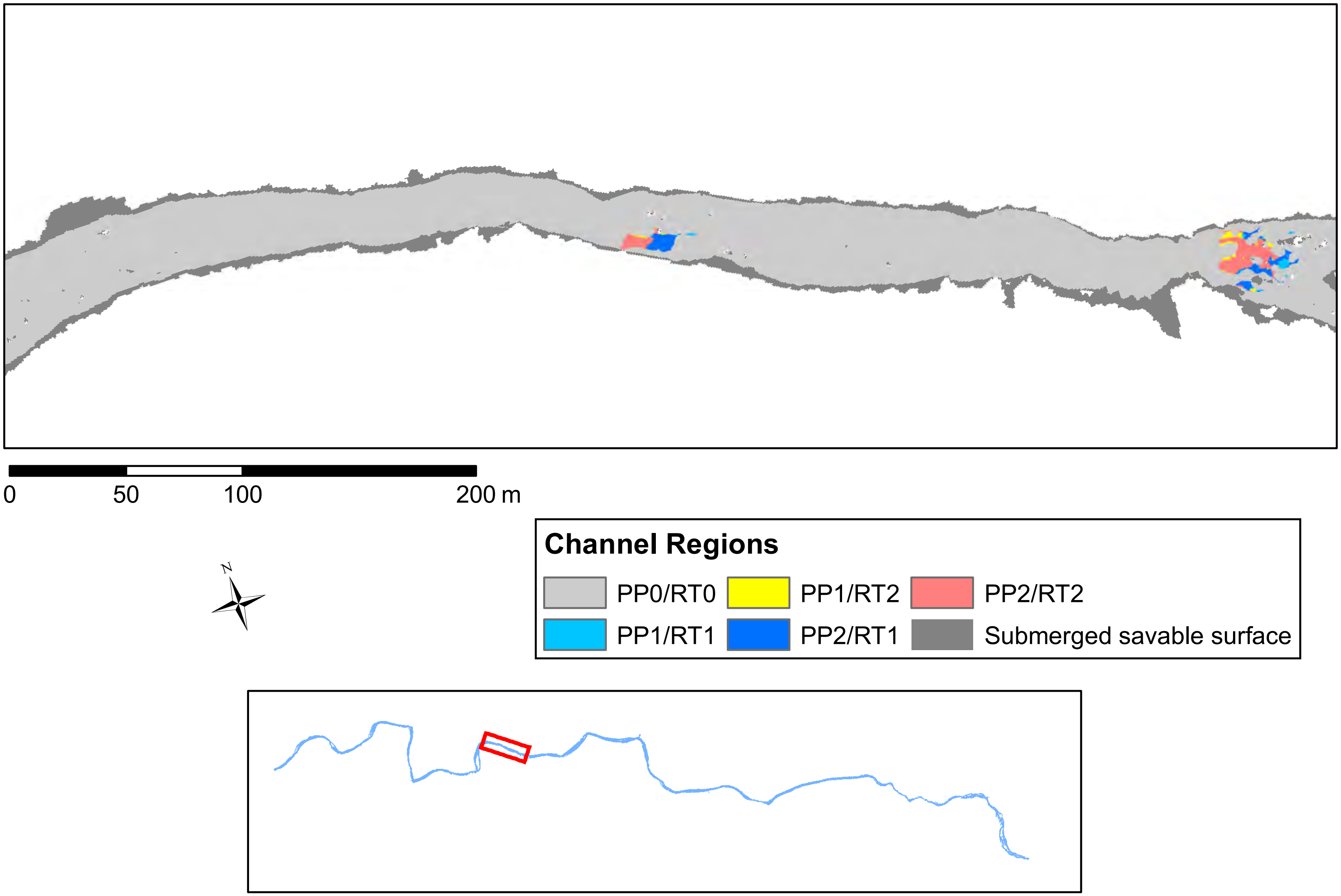

SYR Jump Hazards at 31 m^3/s, p. 16

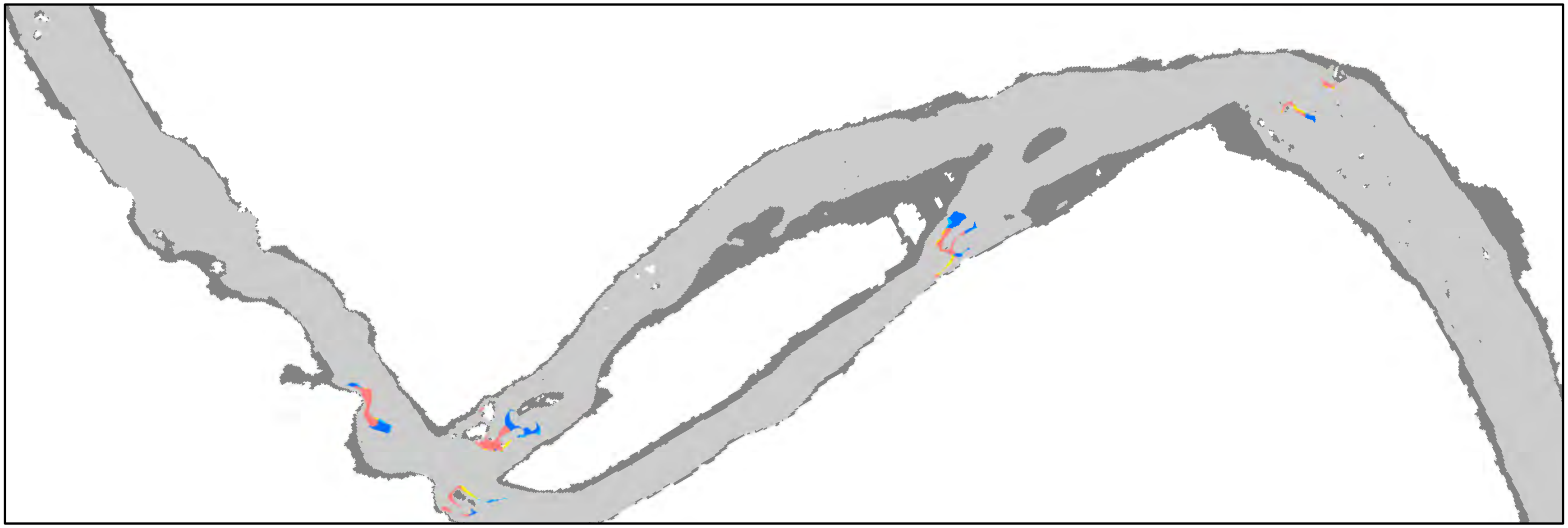

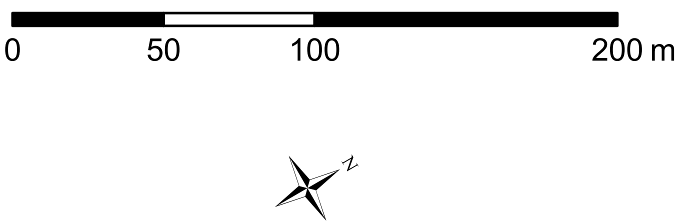

Channel Regions

PP0/RT0	PP1/RT2	PP2/RT2
PP1/RT1	PP2/RT1	Submerged savable surface

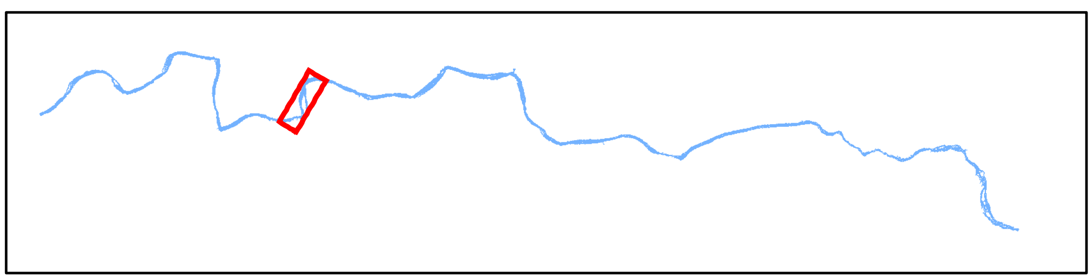

SYR Jump Hazards at 31 m^3/s, p. 17

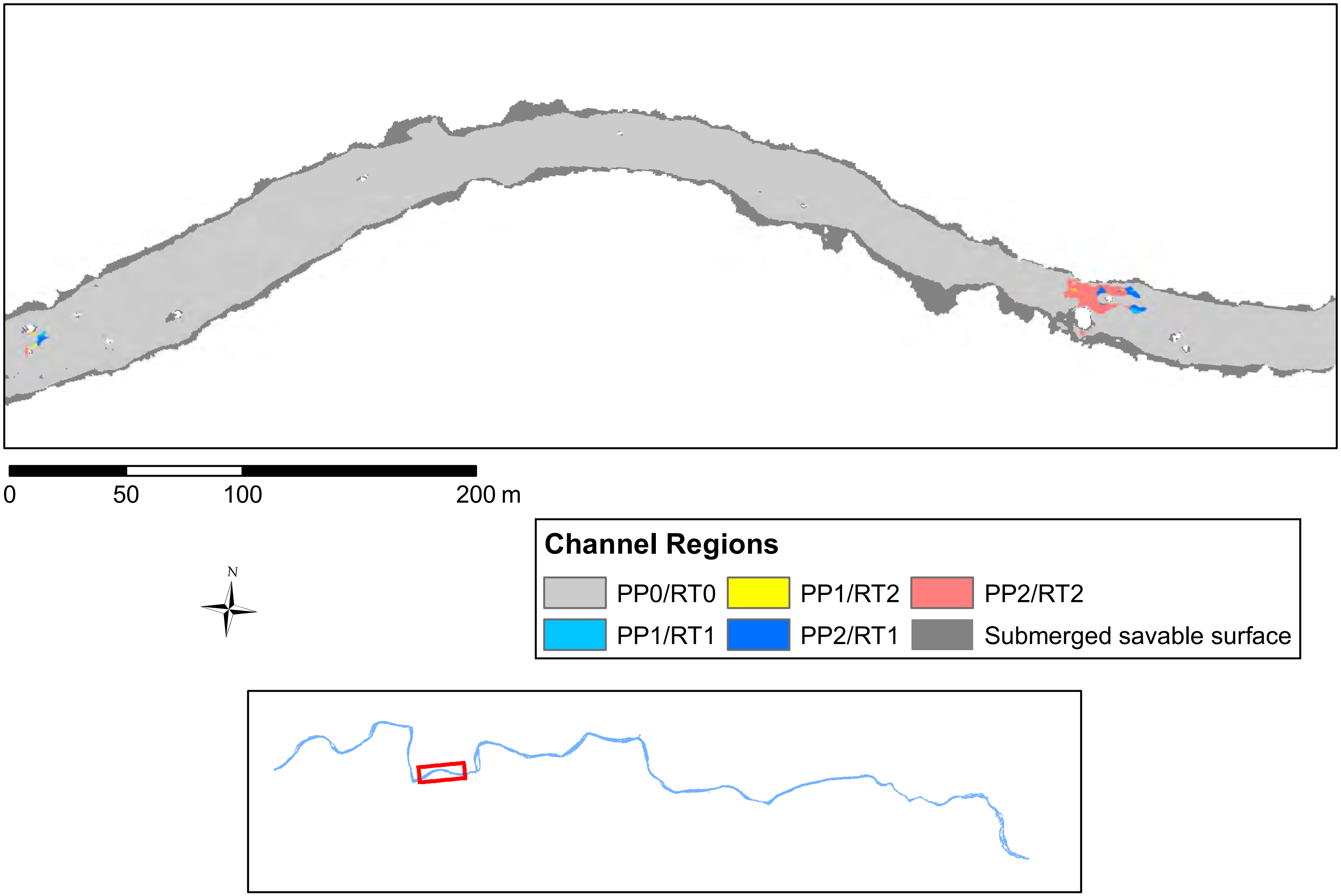

SYR Jump Hazards at 31 m^3/s, p. 18

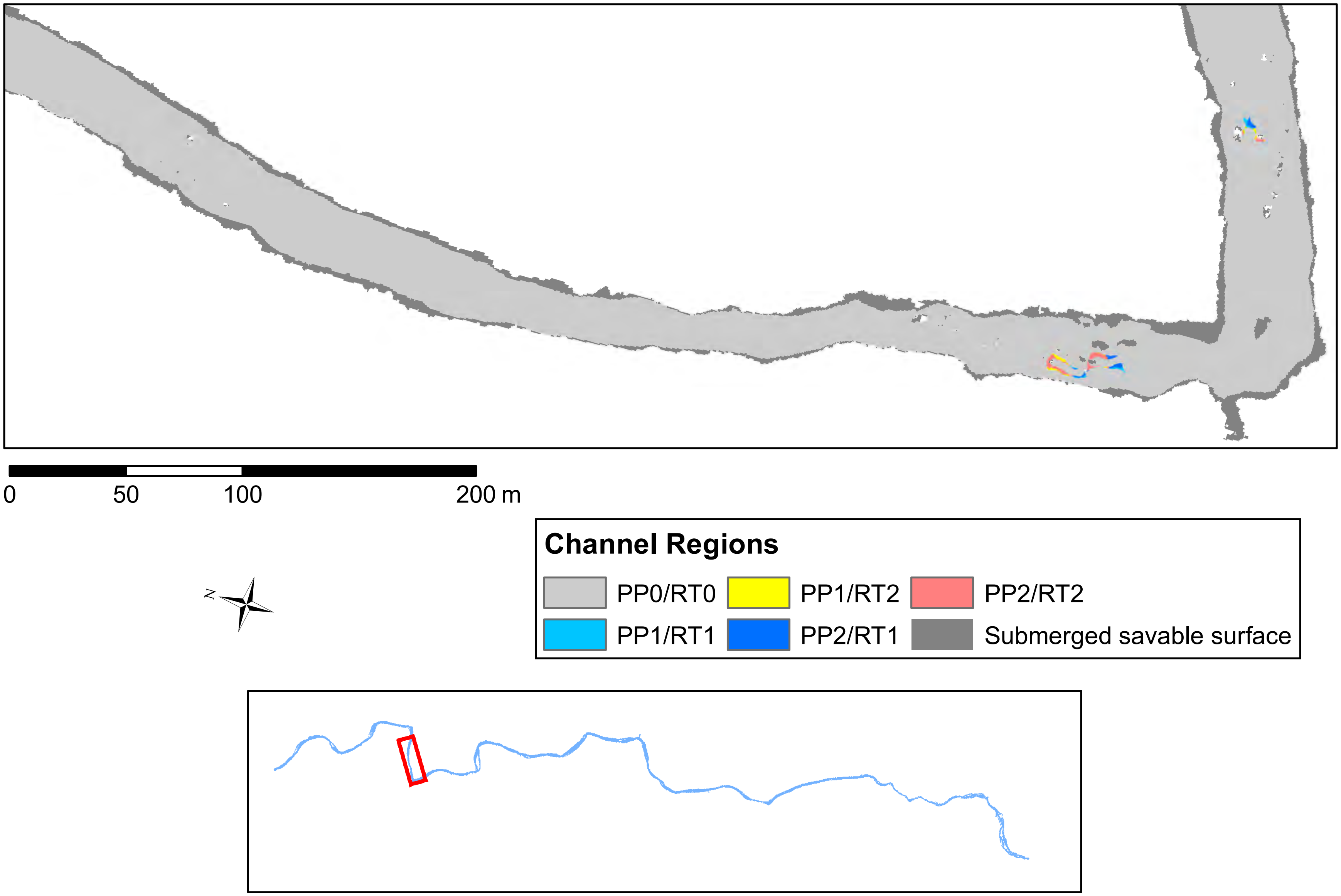

SYR Jump Hazards at 31 m^3/s, p. 19

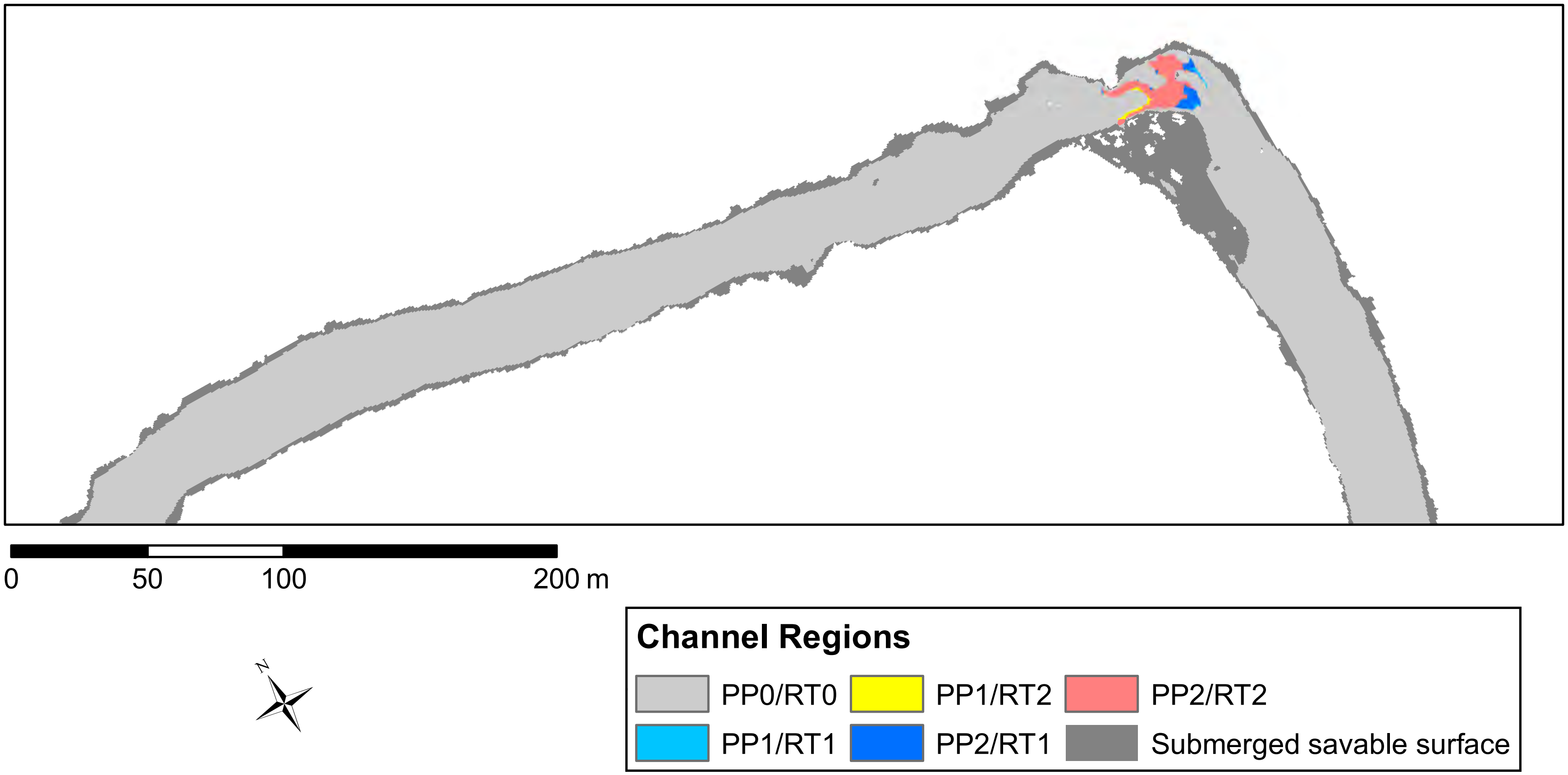

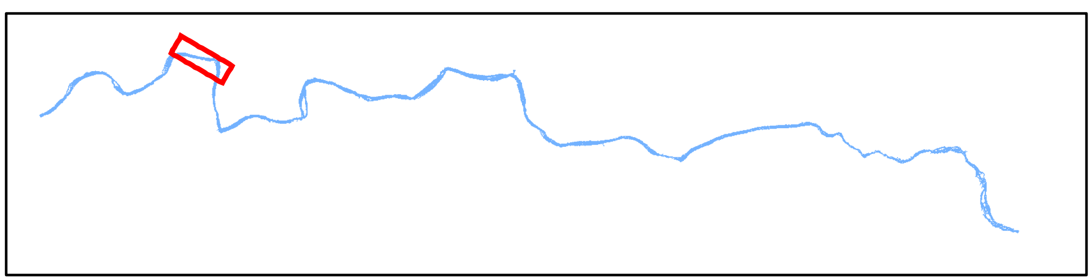

SYR Jump Hazards at 31 m^3/s, p. 20

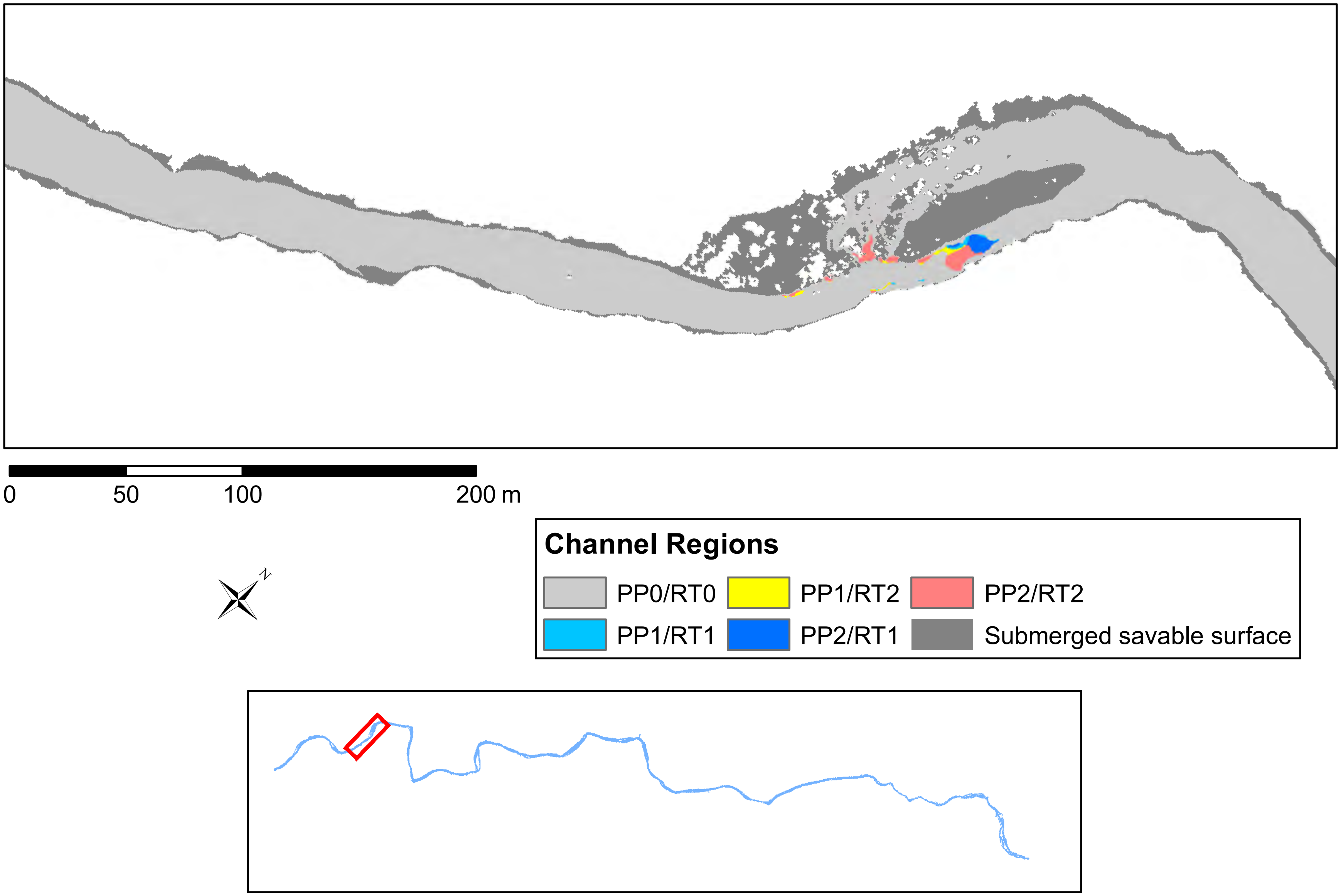

SYR Jump Hazards at 31 m^3/s, p. 21

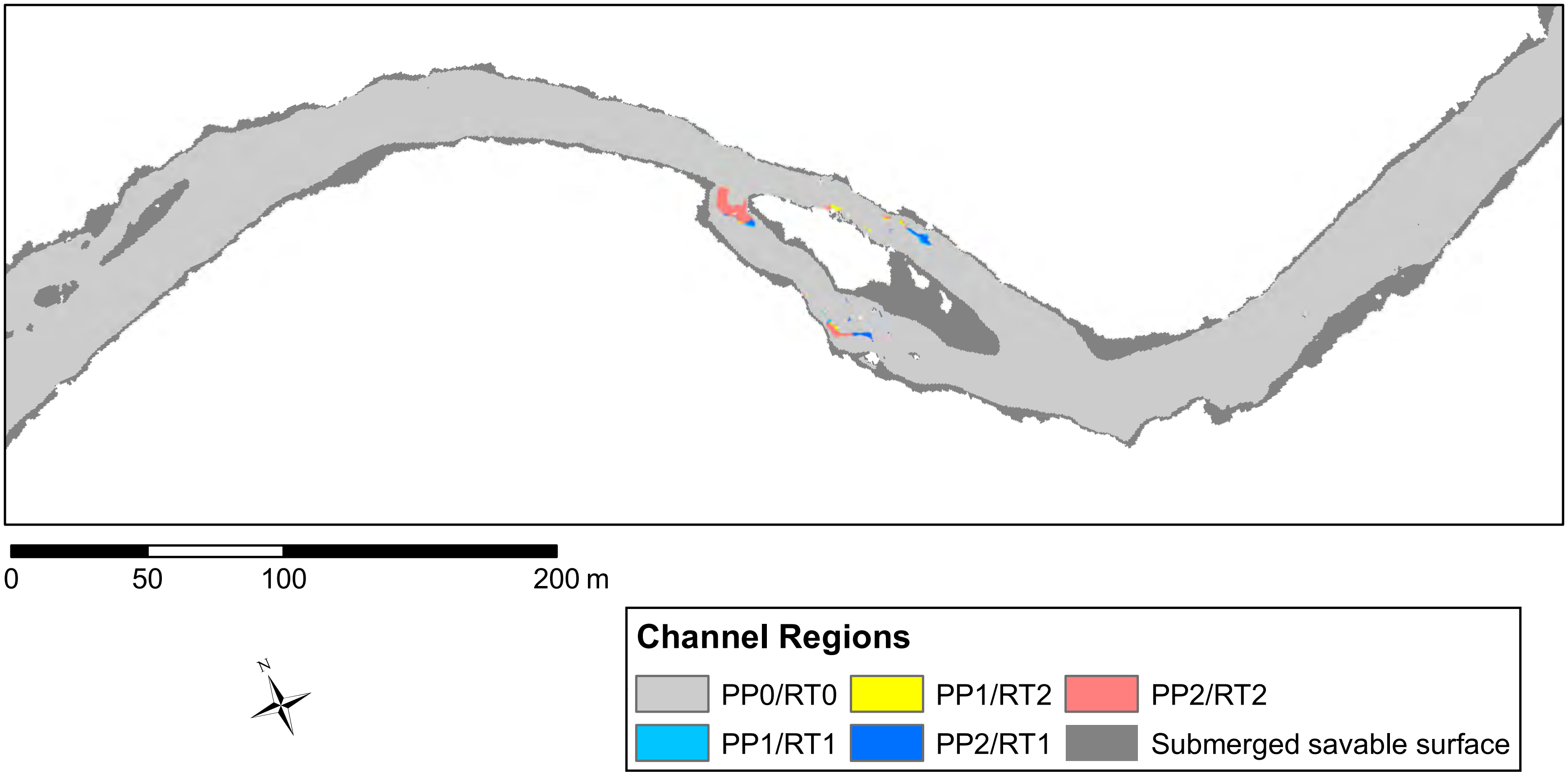

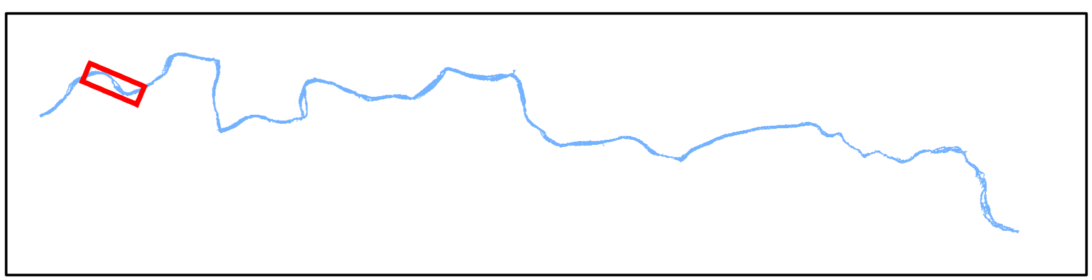

SYR Jump Hazards at 31 m^3/s, p. 22

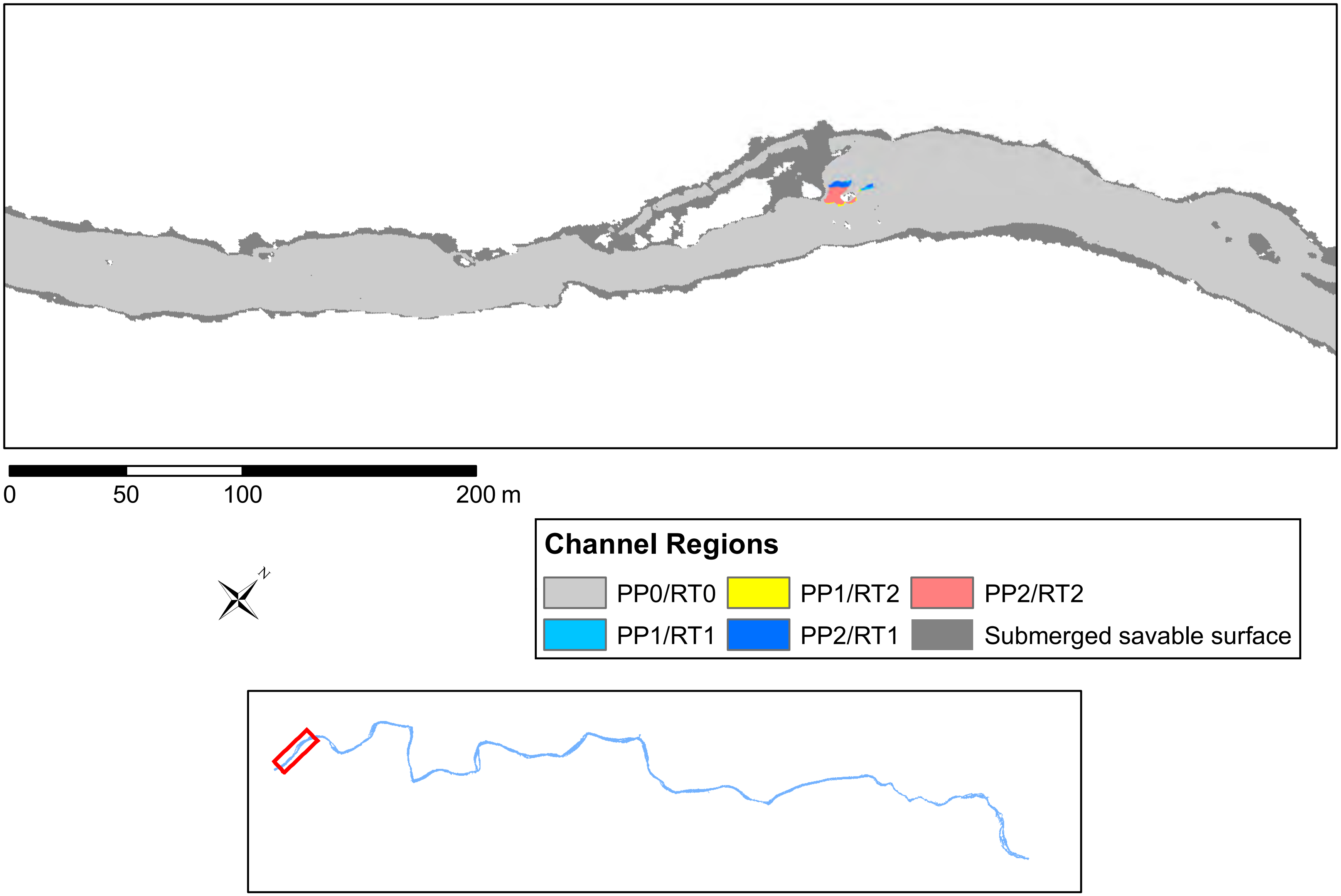

SYR Jump Hazards at 31 m^3/s, p. 23

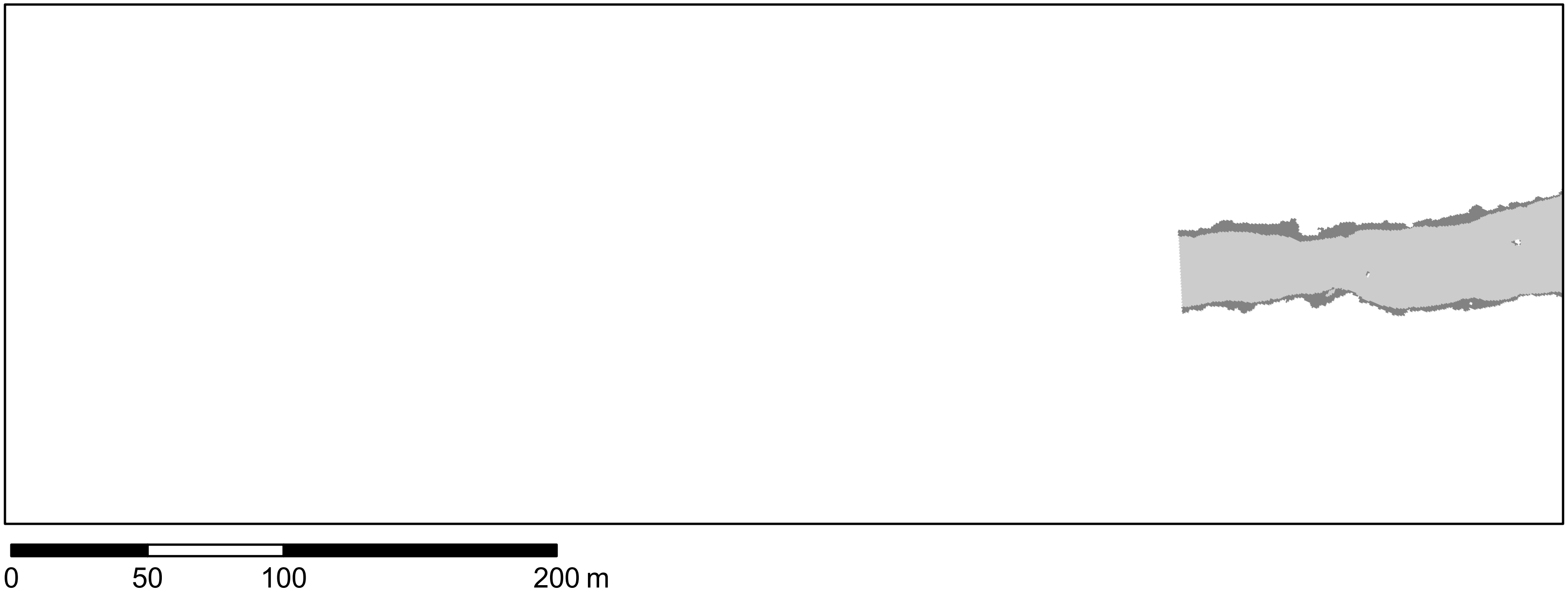

Channel Regions

- PP0/RT0
- PP1/RT2
- PP2/RT2
- PP1/RT1
- PP2/RT1
- Submerged savable surface

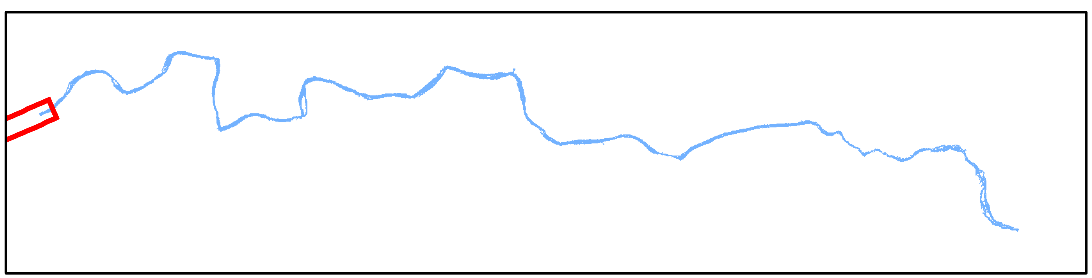

SYR Submerged Unsavable Surface Hazards for Upright Body at 31 m^3/s, p. 1

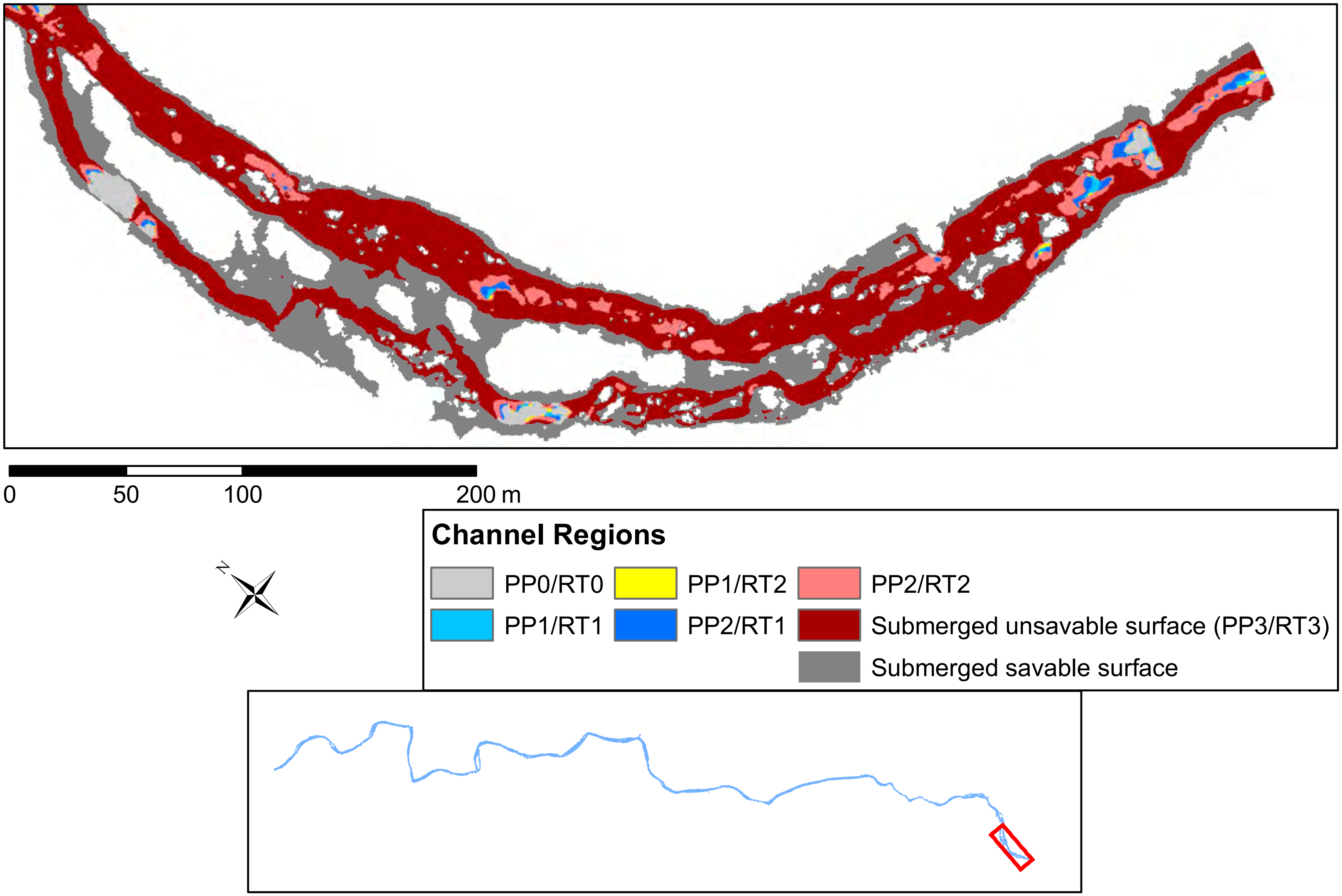

SYR Submerged Unsavable Surface Hazards for Upright Body at 31 m^3/s, p. 2

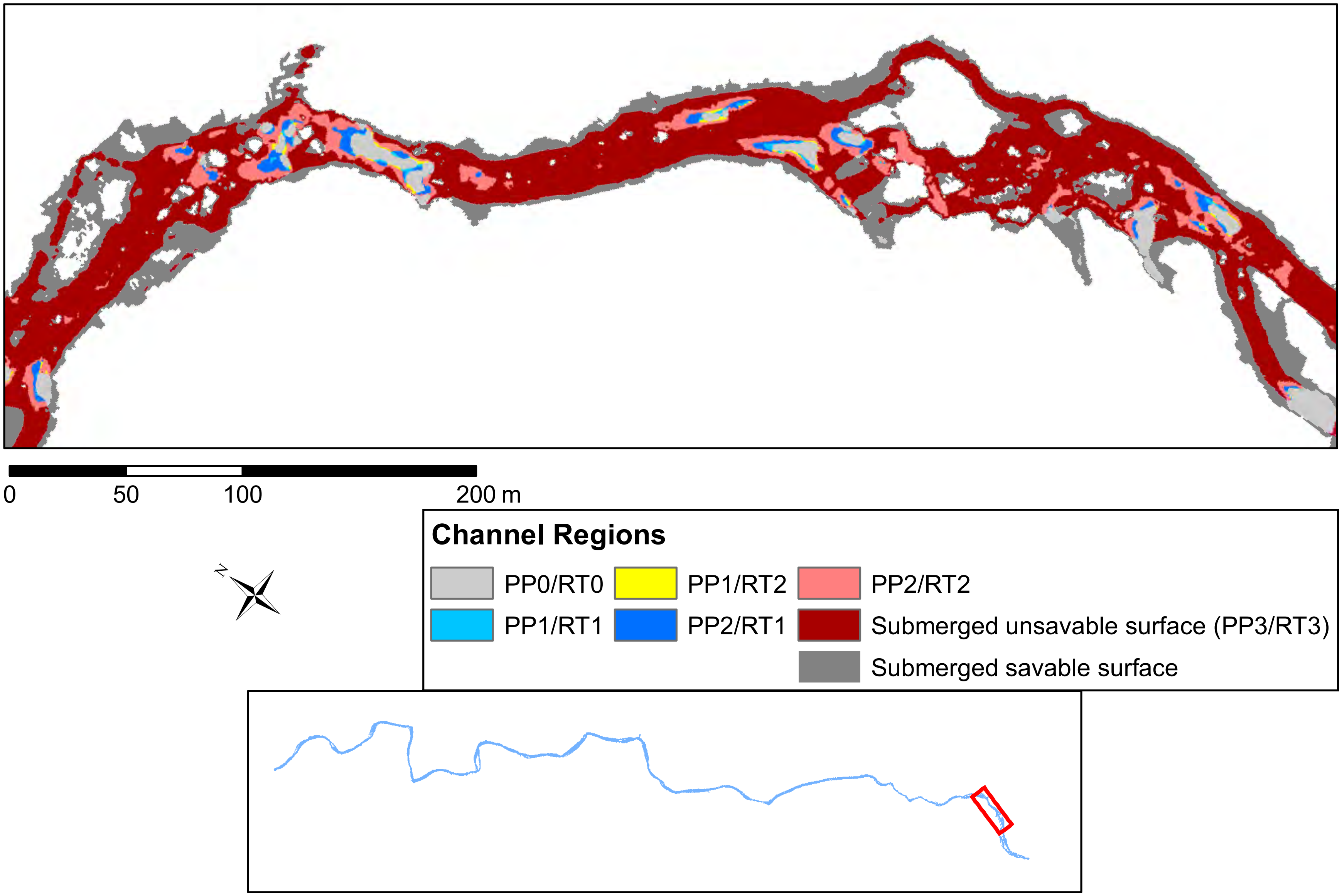

SYR Submerged Unsavable Surface Hazards for Upright Body at 31 m^3/s, p. 3

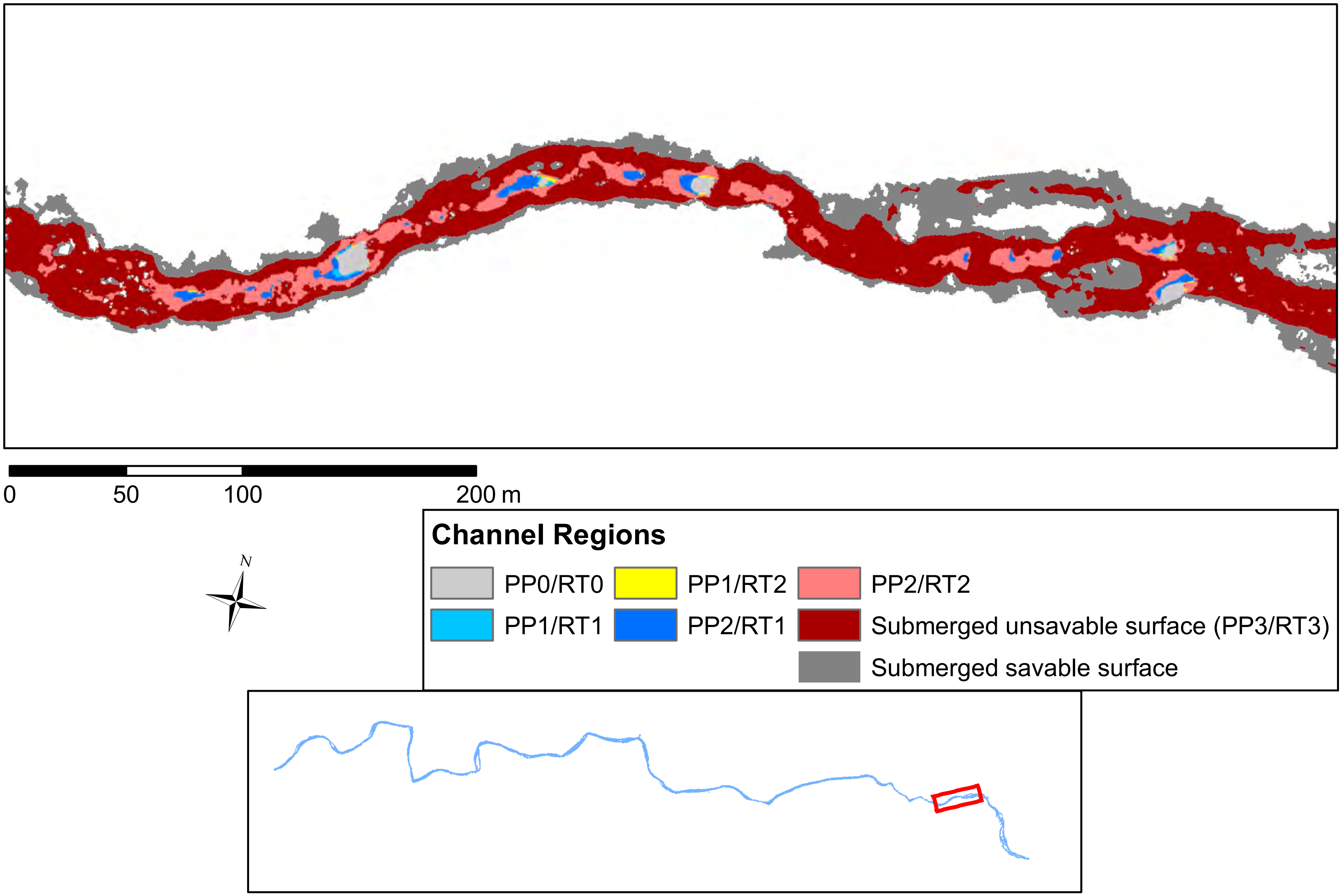

SYR Submerged Unsavable Surface Hazards for Upright Body at 31 m^3/s, p. 4

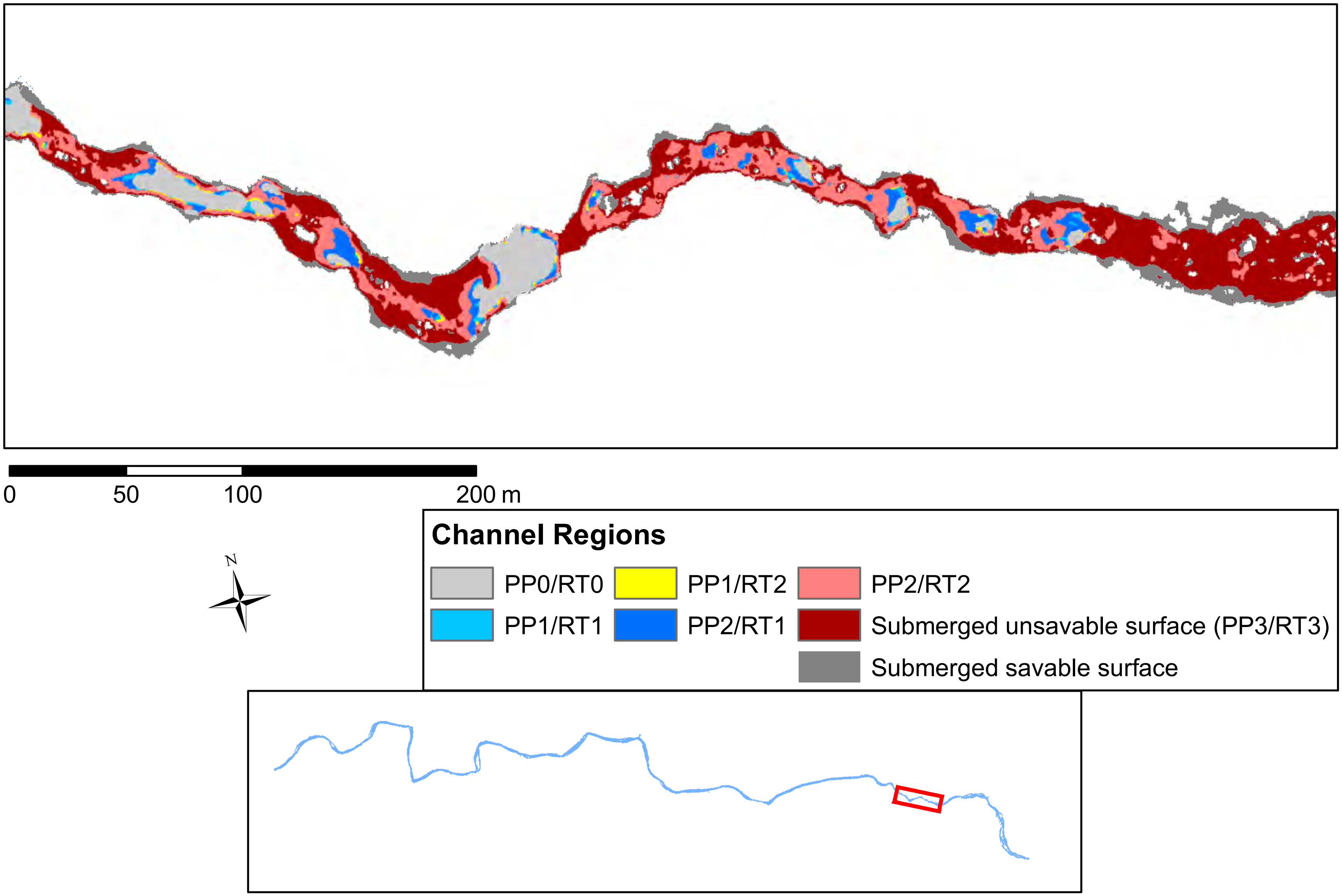

SYR Submerged Unsavable Surface Hazards for Upright Body at 31 m^3/s, p. 5

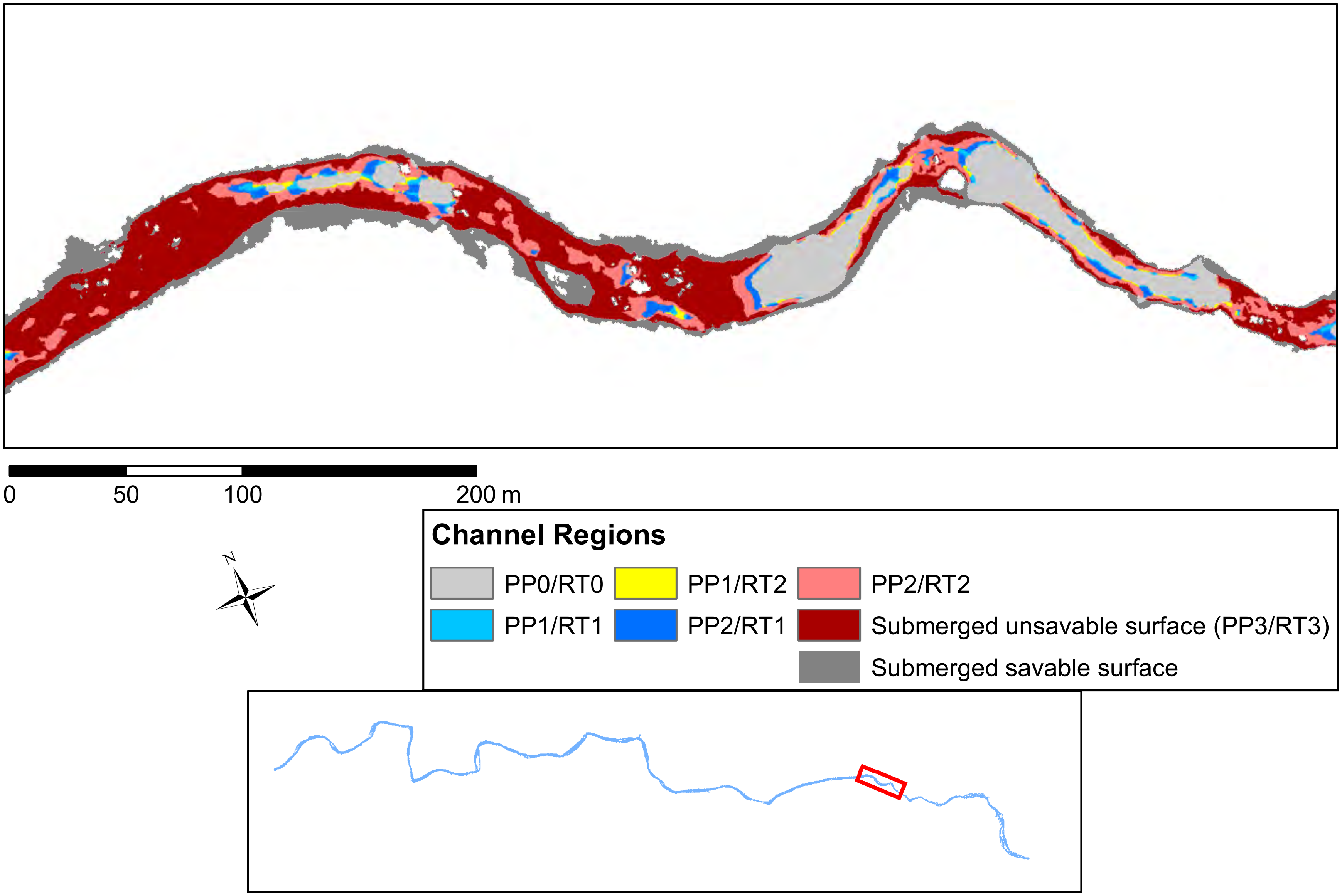

SYR Submerged Unsavable Surface Hazards for Upright Body at 31 m^3/s, p. 6

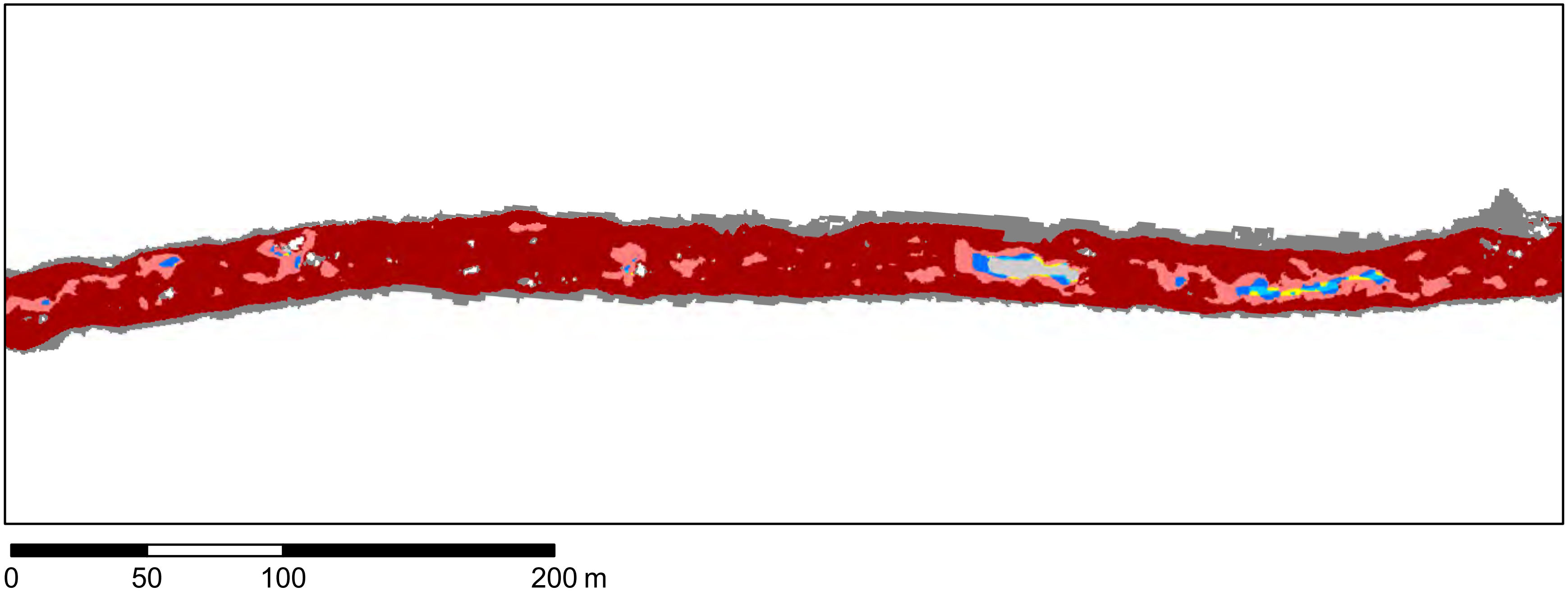

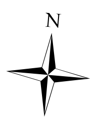

Channel Regions

- PP0/RT0
- PP1/RT2
- PP2/RT2
- PP1/RT1
- PP2/RT1
- Submerged unsavable surface (PP3/RT3)
- Submerged savable surface

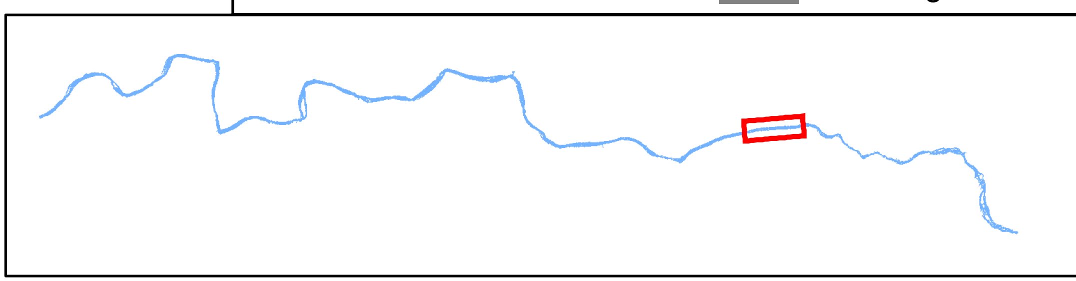

SYR Submerged Unsavable Surface Hazards for Upright Body at 31 m^3/s, p. 7

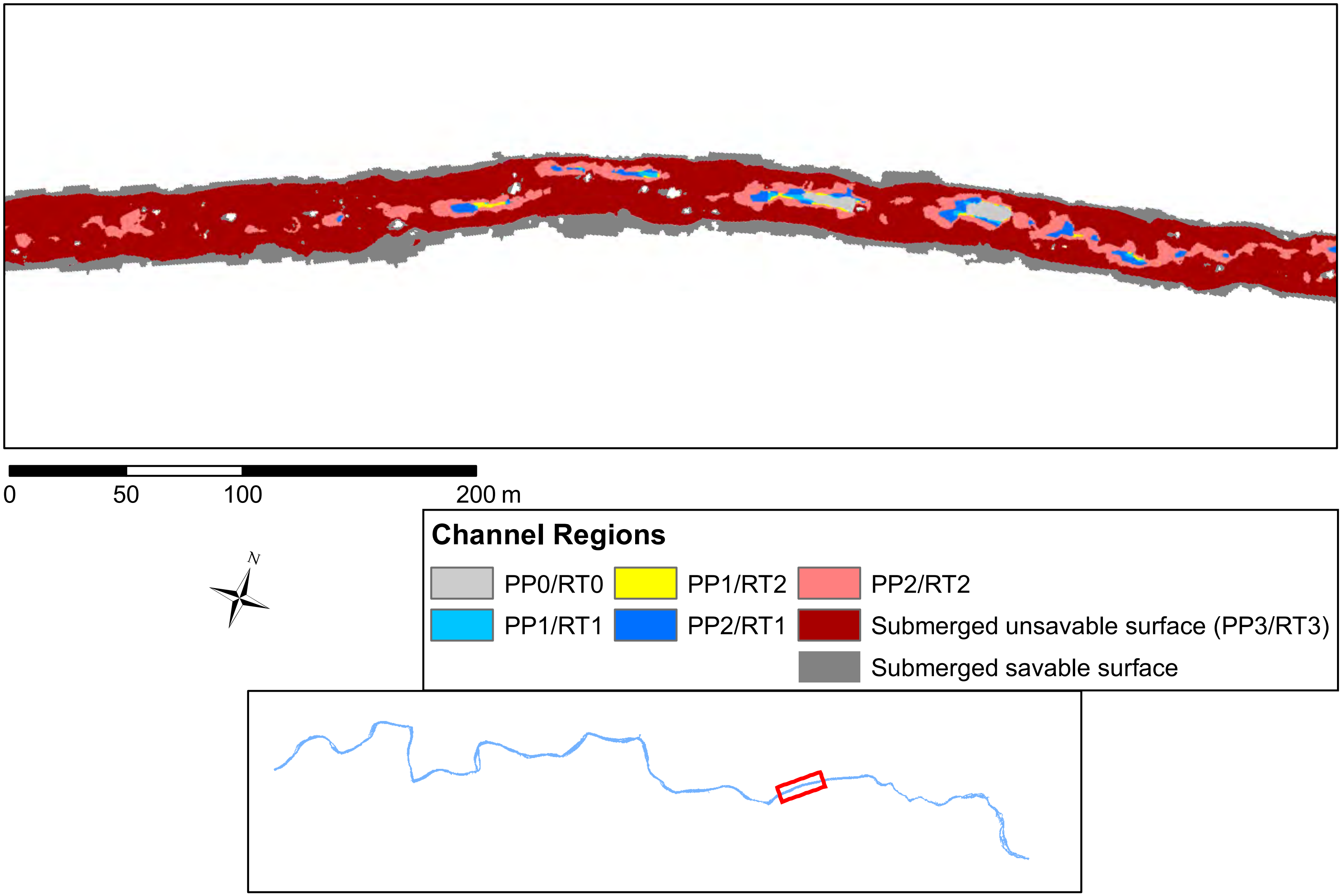

SYR Submerged Unsavable Surface Hazards for Upright Body at 31 m^3/s, p. 8

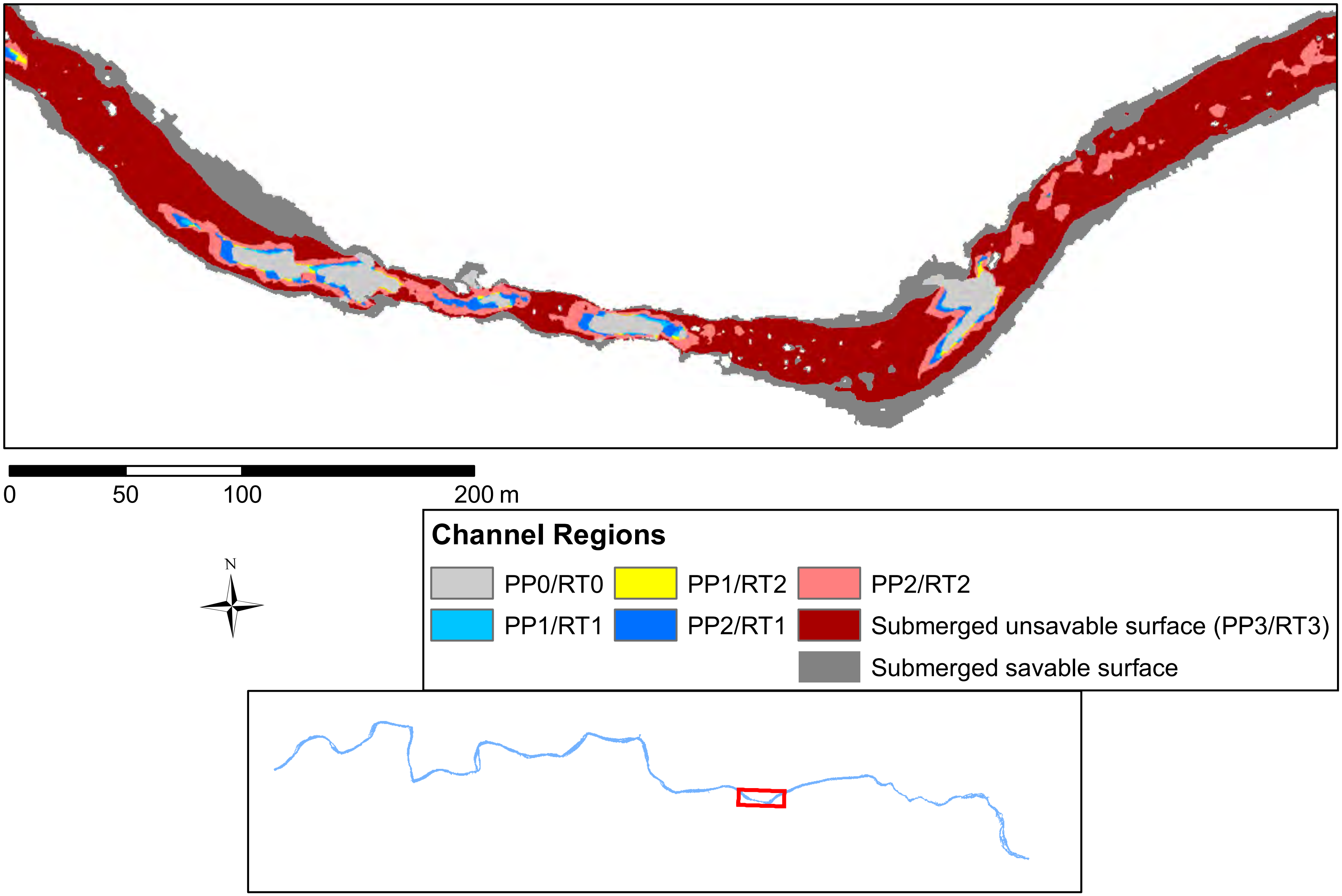

SYR Submerged Unsavable Surface Hazards for Upright Body at 31 m^3/s, p. 9

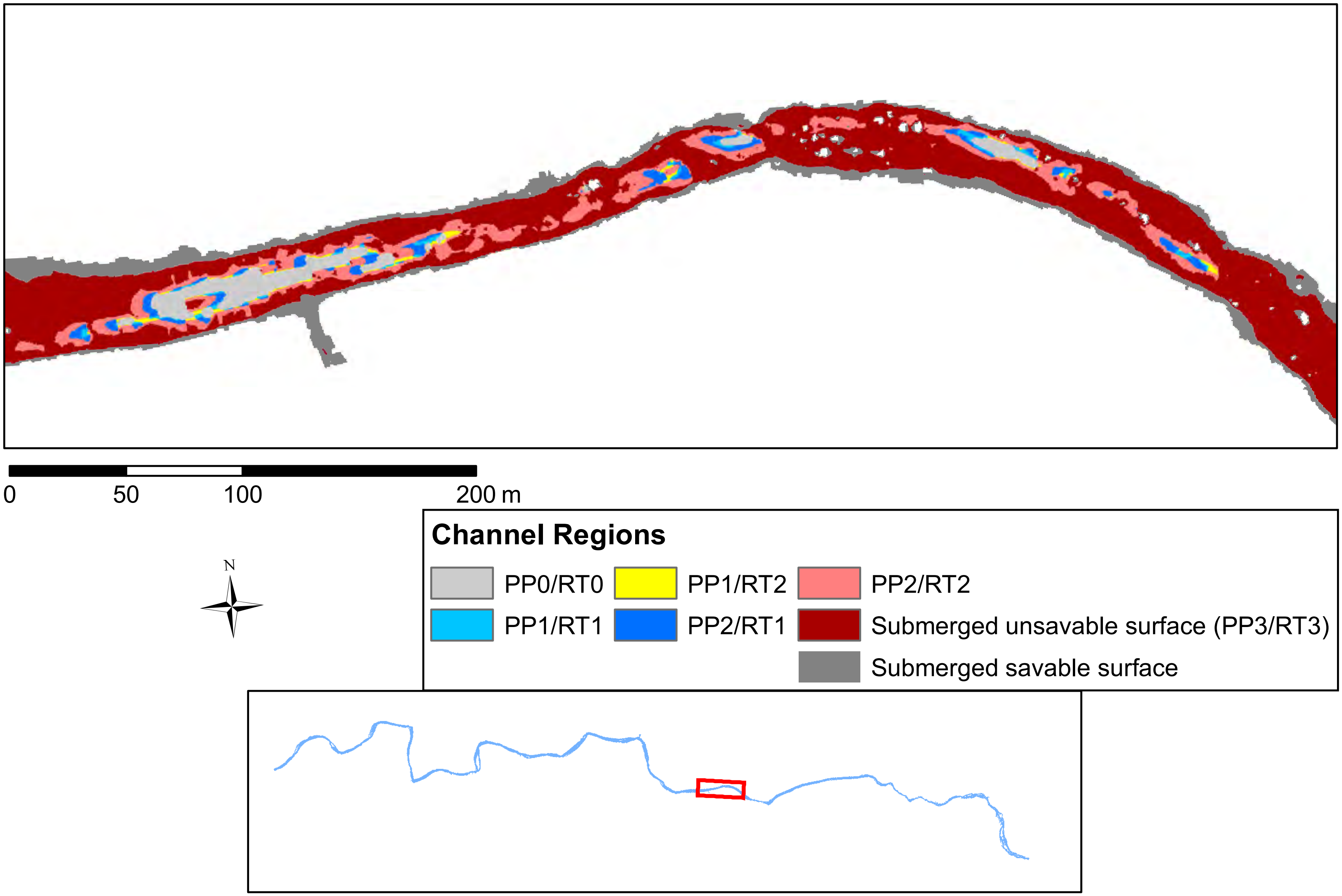

SYR Submerged Unsavable Surface Hazards for Upright Body at 31 m^3/s, p. 10

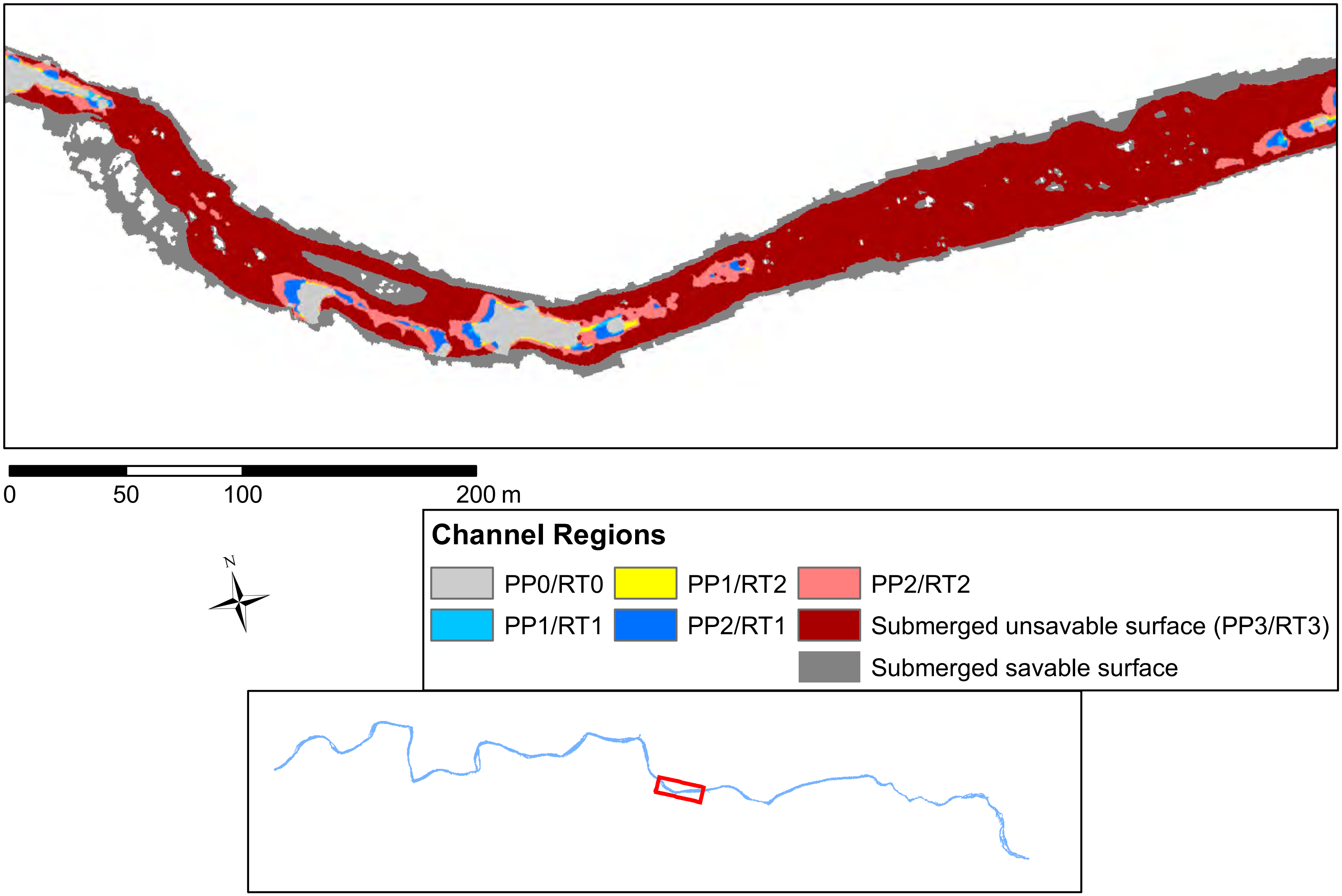

SYR Submerged Unsavable Surface Hazards for Upright Body at 31 m^3/s, p. 11

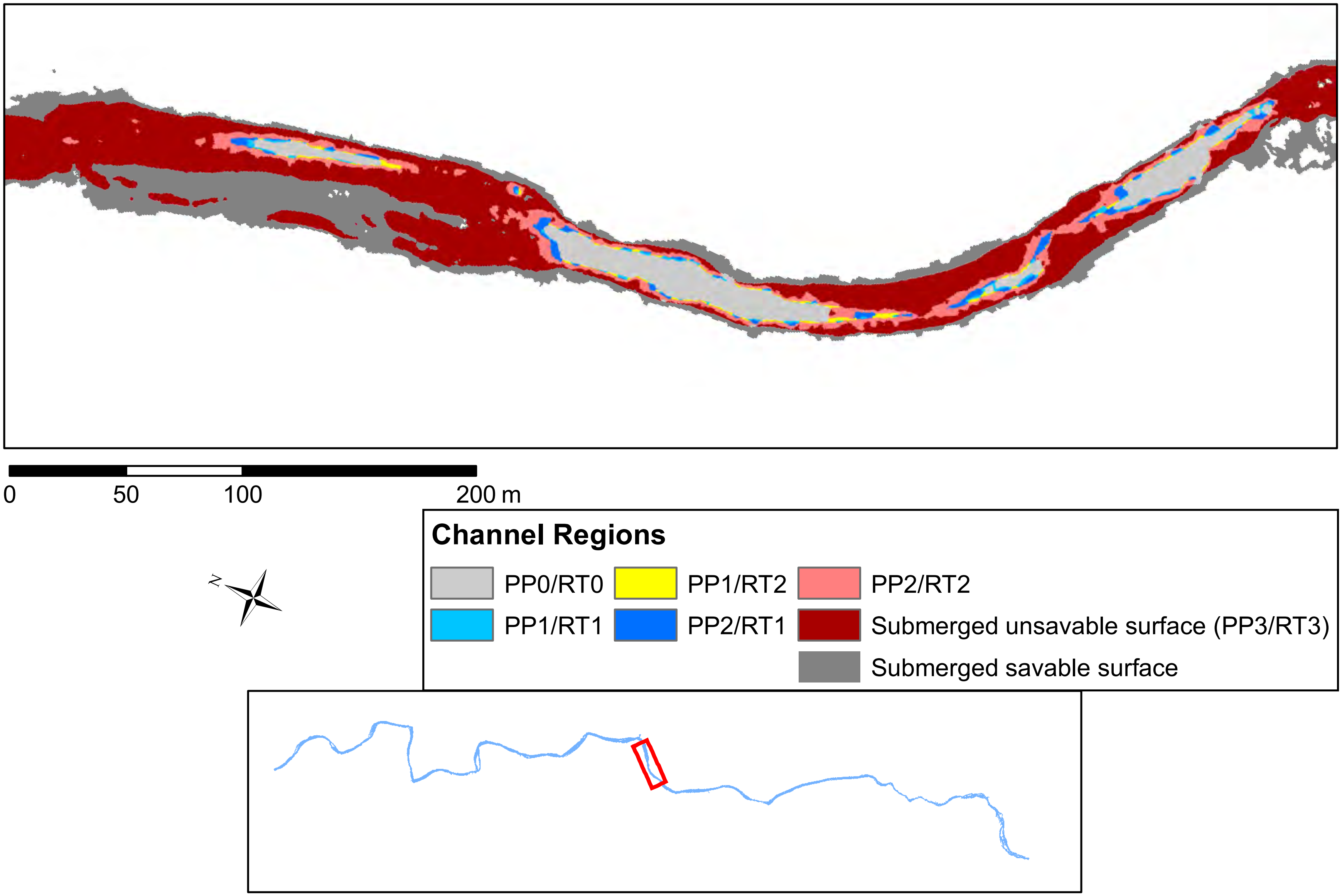

SYR Submerged Unsavable Surface Hazards for Upright Body at 31 m^3/s, p. 12

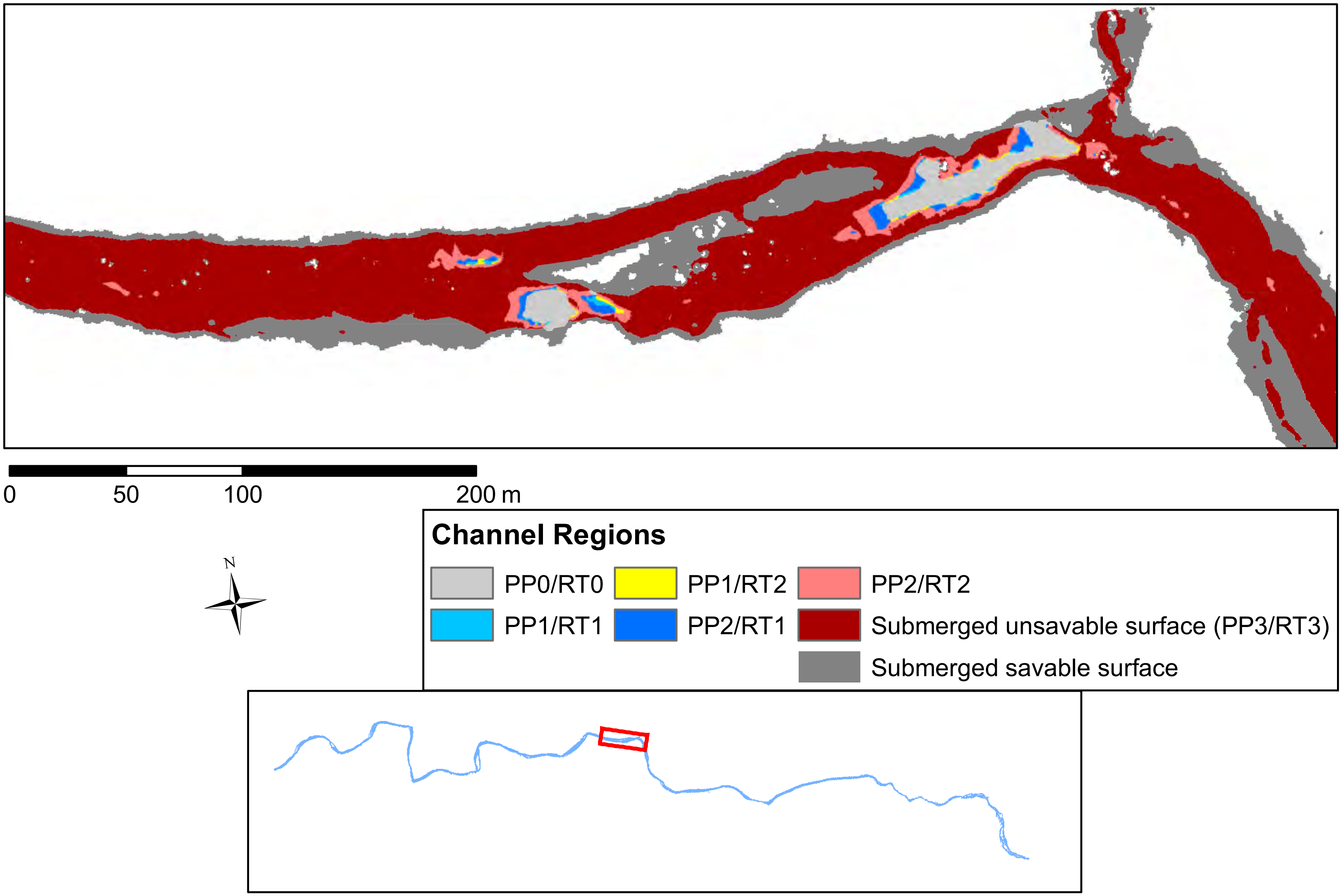

SYR Submerged Unsavable Surface Hazards for Upright Body at 31 m^3/s, p. 13

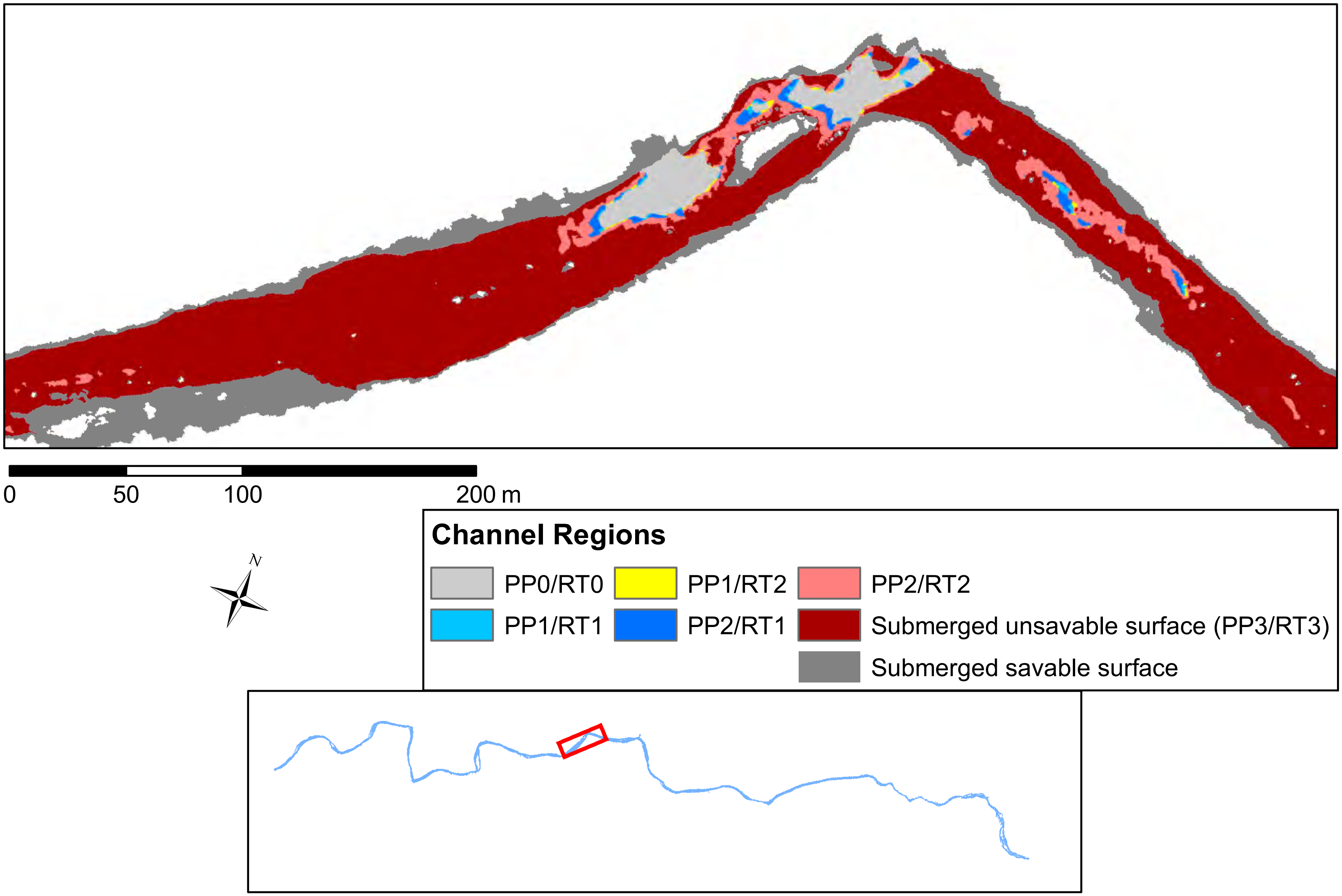

SYR Submerged Unsavable Surface Hazards for Upright Body at 31 m^3/s, p. 14

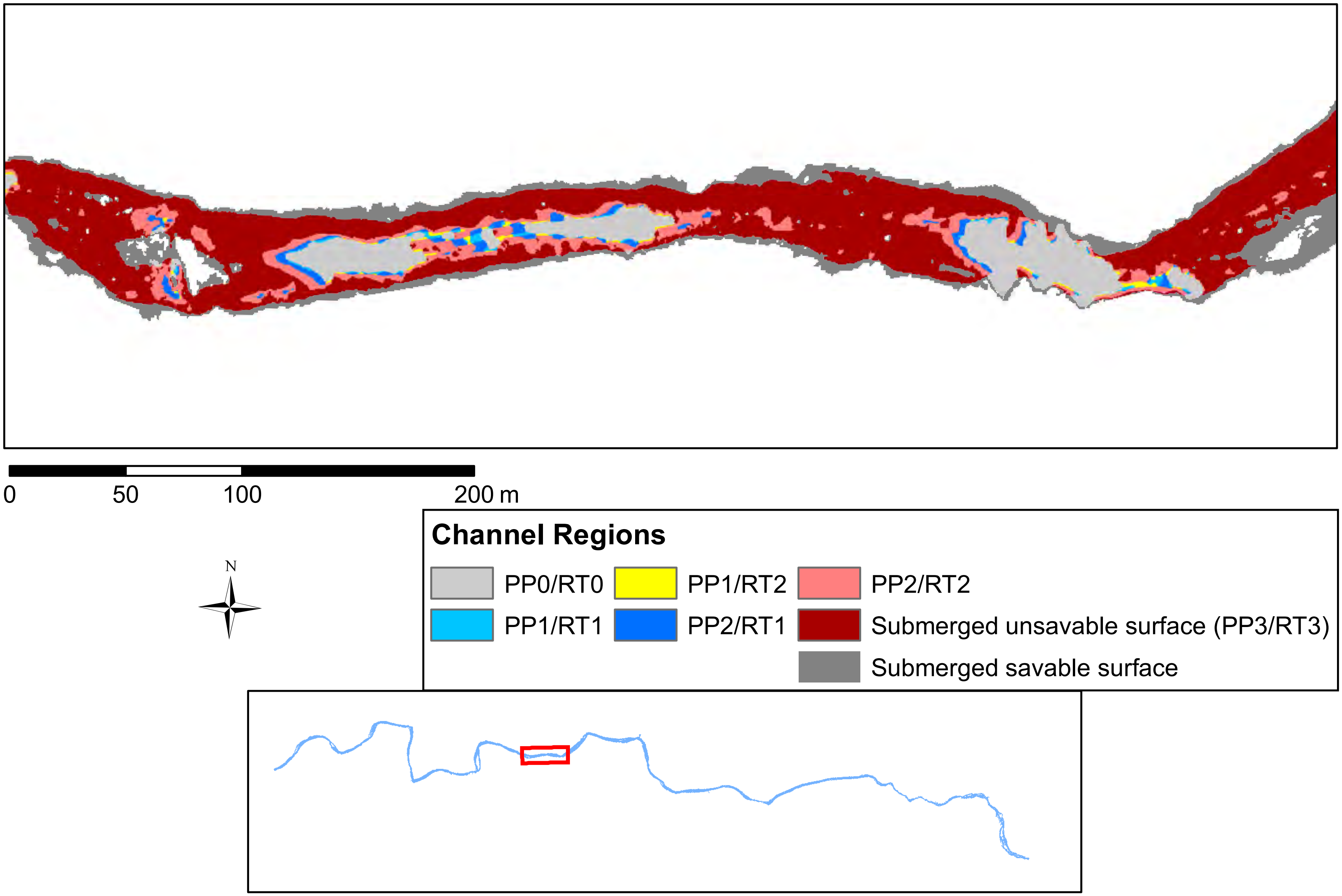

SYR Submerged Unsavable Surface Hazards for Upright Body at 31 m^3/s, p. 15

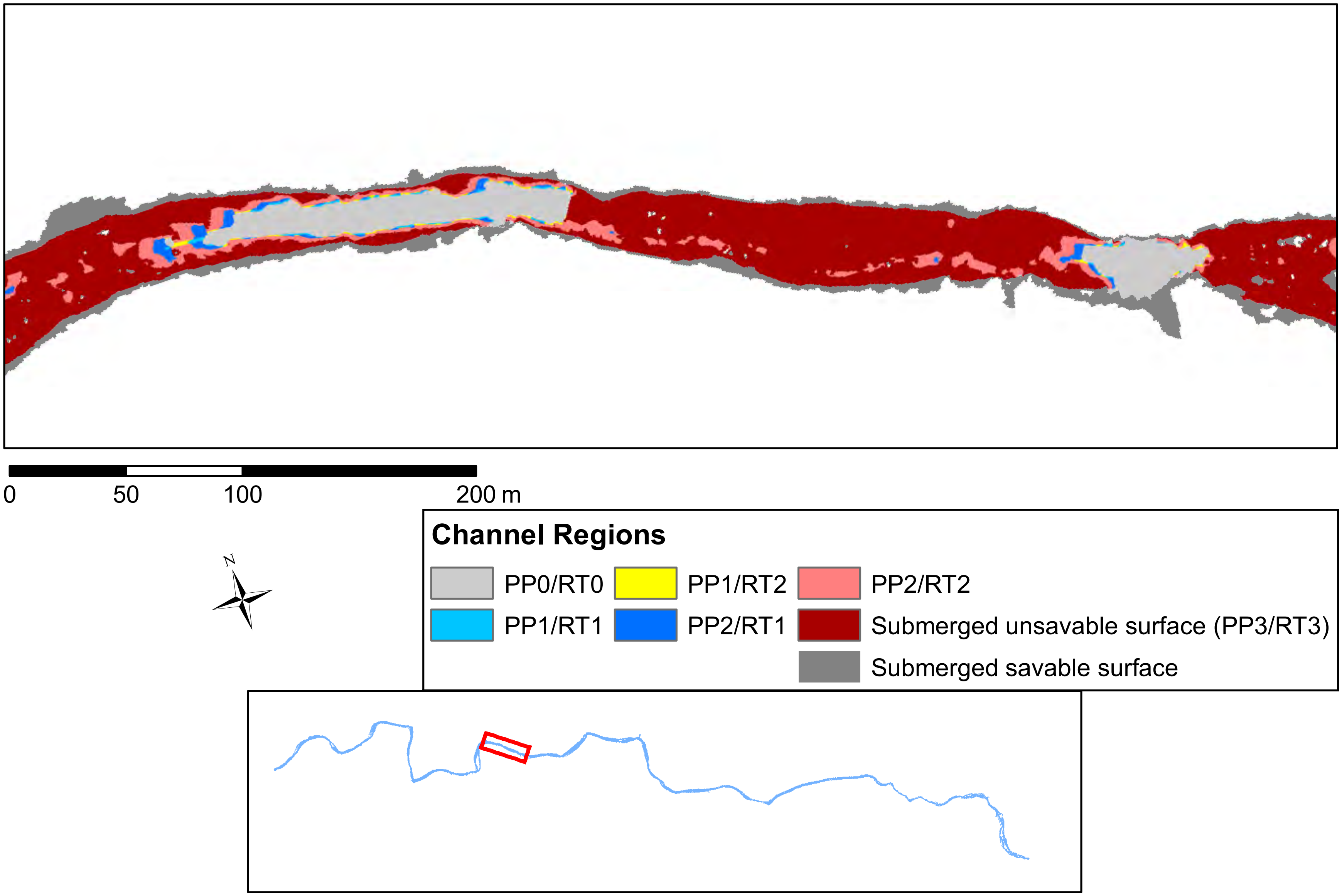

SYR Submerged Unsavable Surface Hazards for Upright Body at 31 m^3/s, p. 16

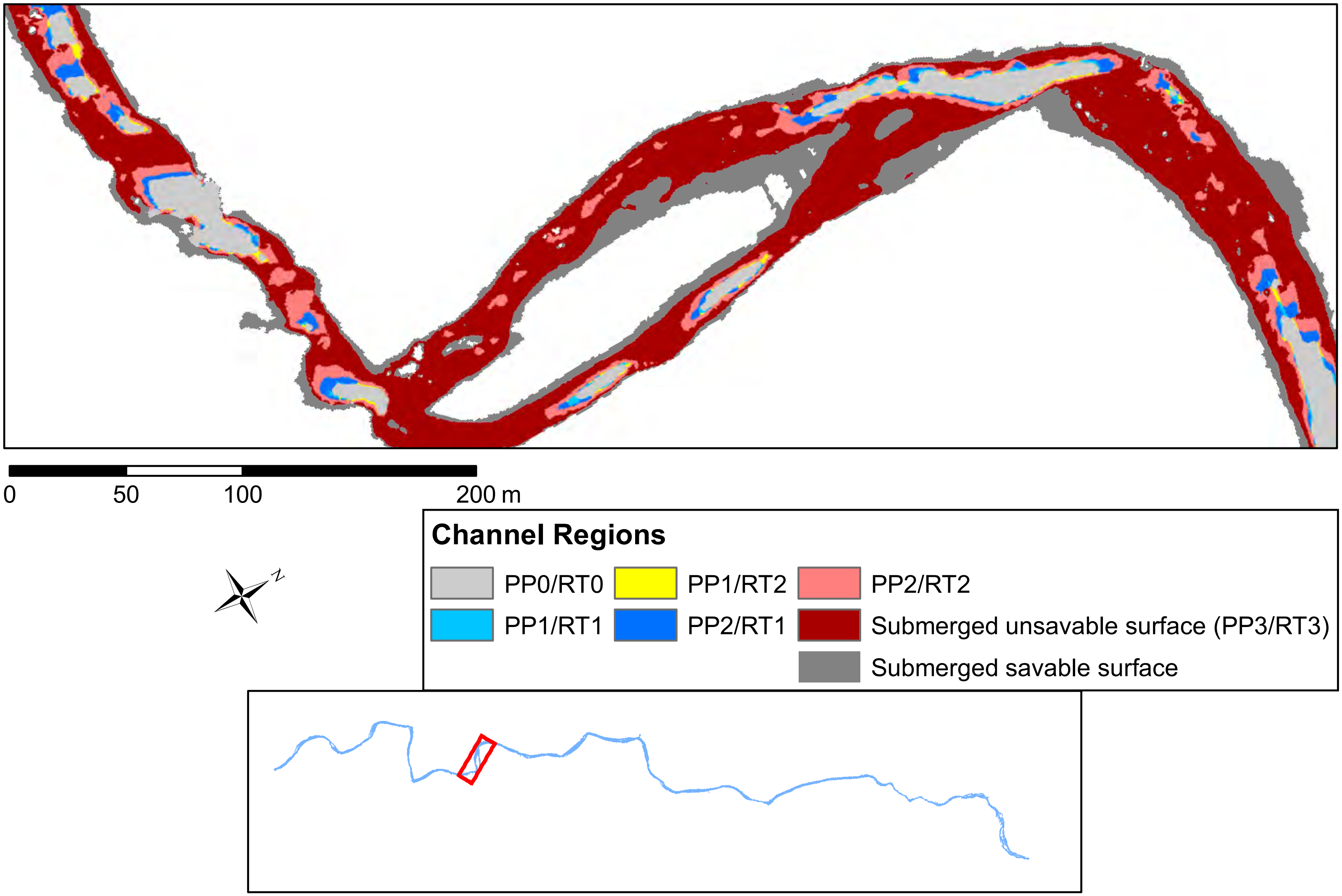

SYR Submerged Unsavable Surface Hazards for Upright Body at 31 m^3/s, p. 17

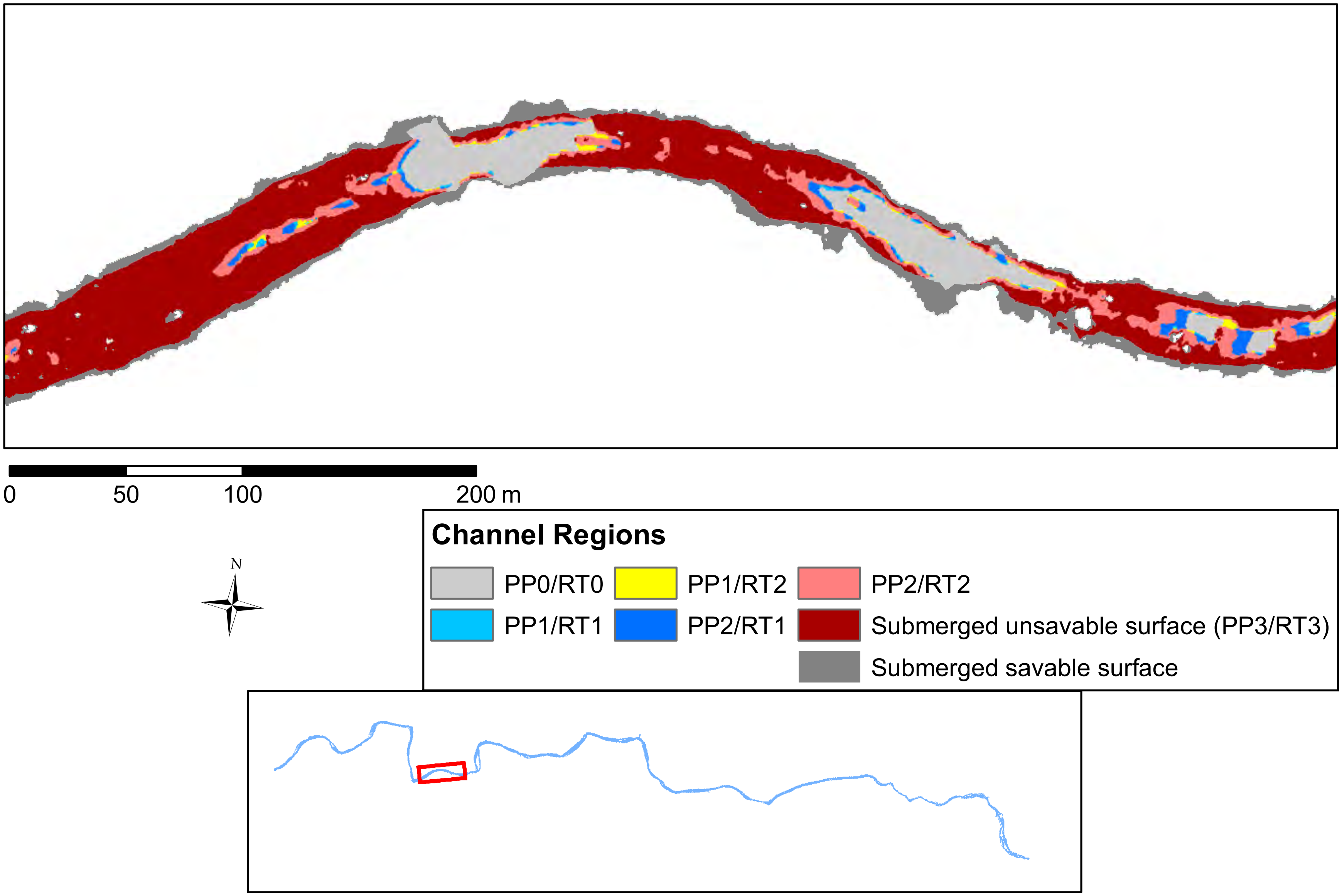

SYR Submerged Unsavable Surface Hazards for Upright Body at 31 m^3/s, p. 18

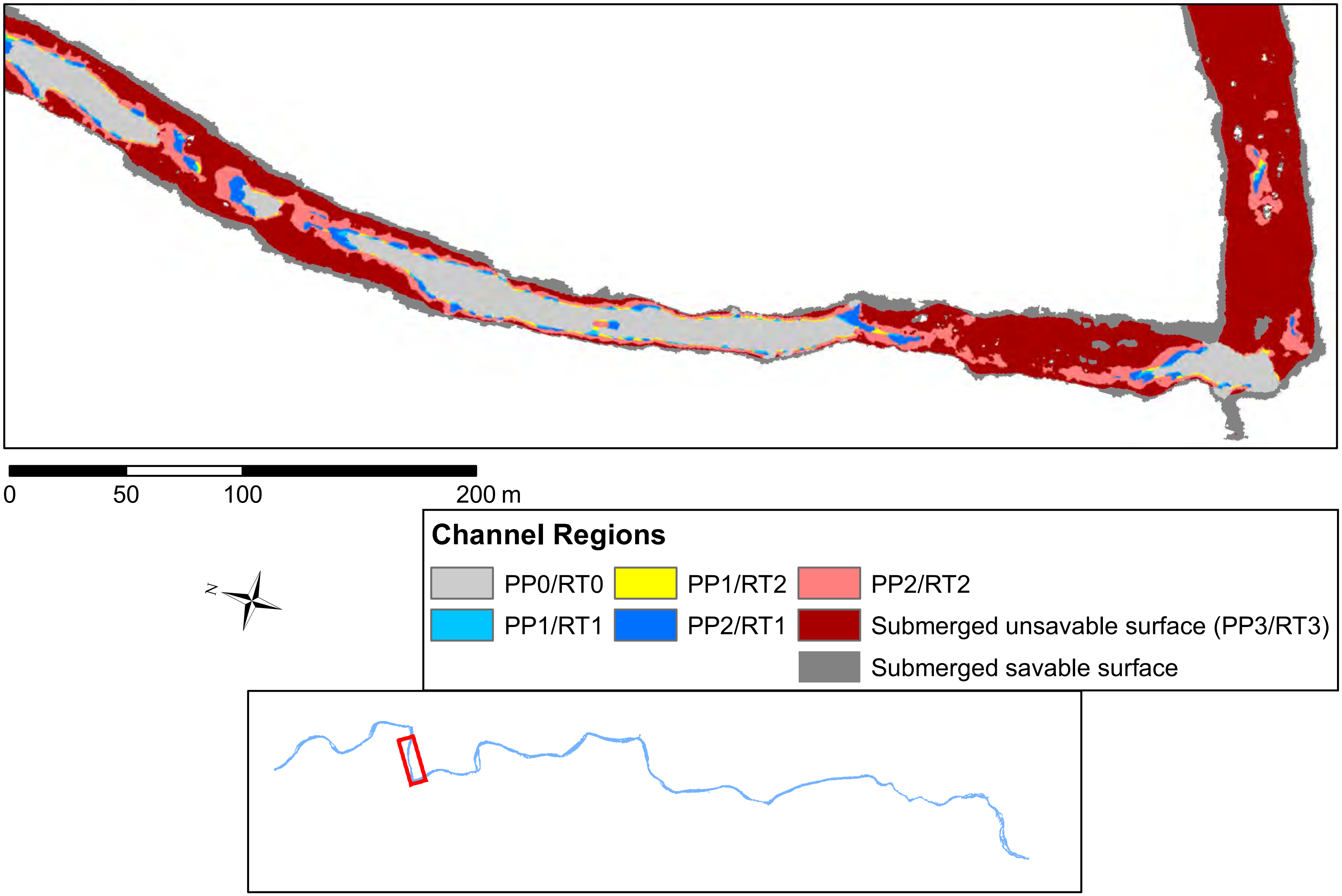

SYR Submerged Unsavable Surface Hazards for Upright Body at 31 m^3/s, p. 19

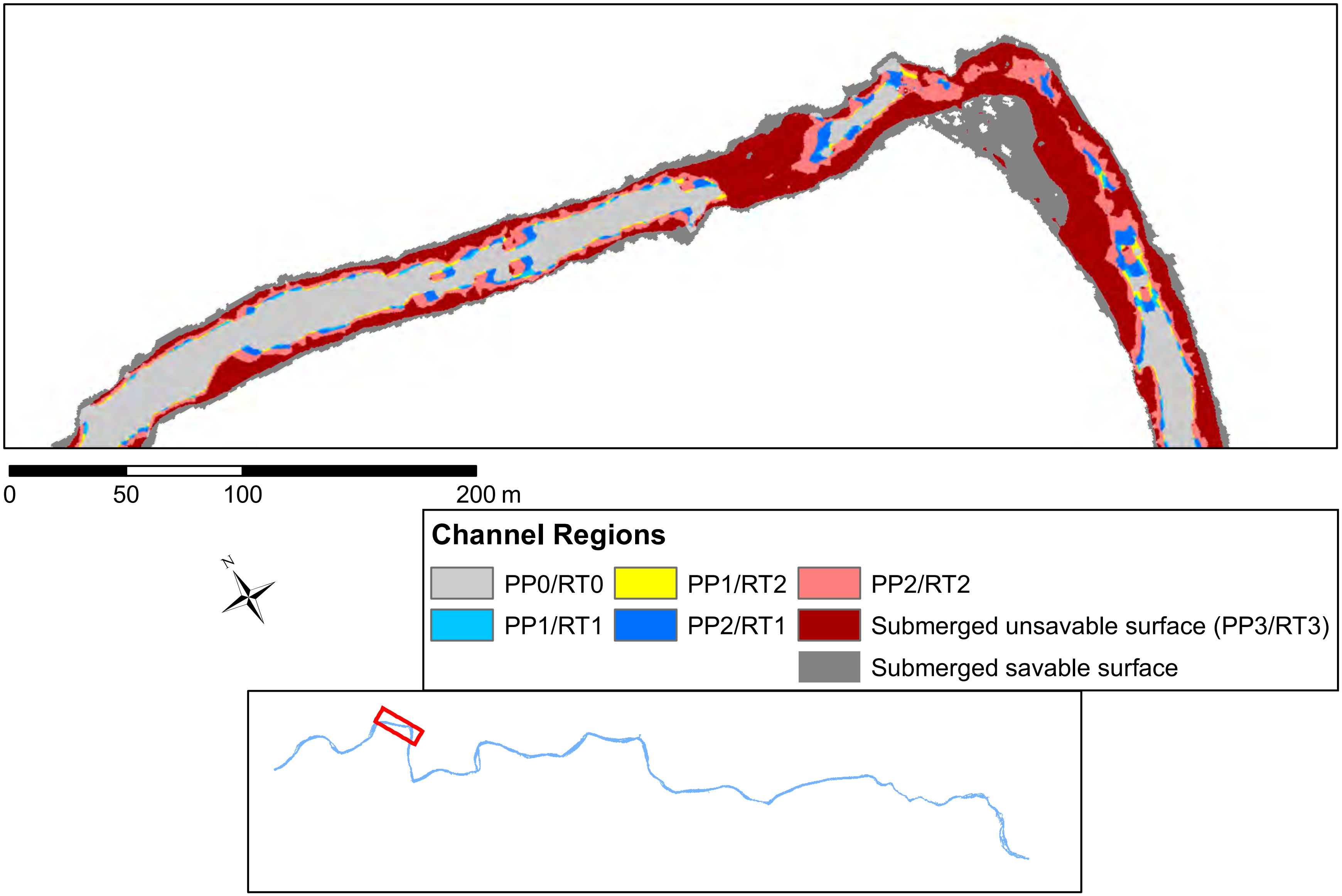

SYR Submerged Unsavable Surface Hazards for Upright Body at 31 m^3/s, p. 20

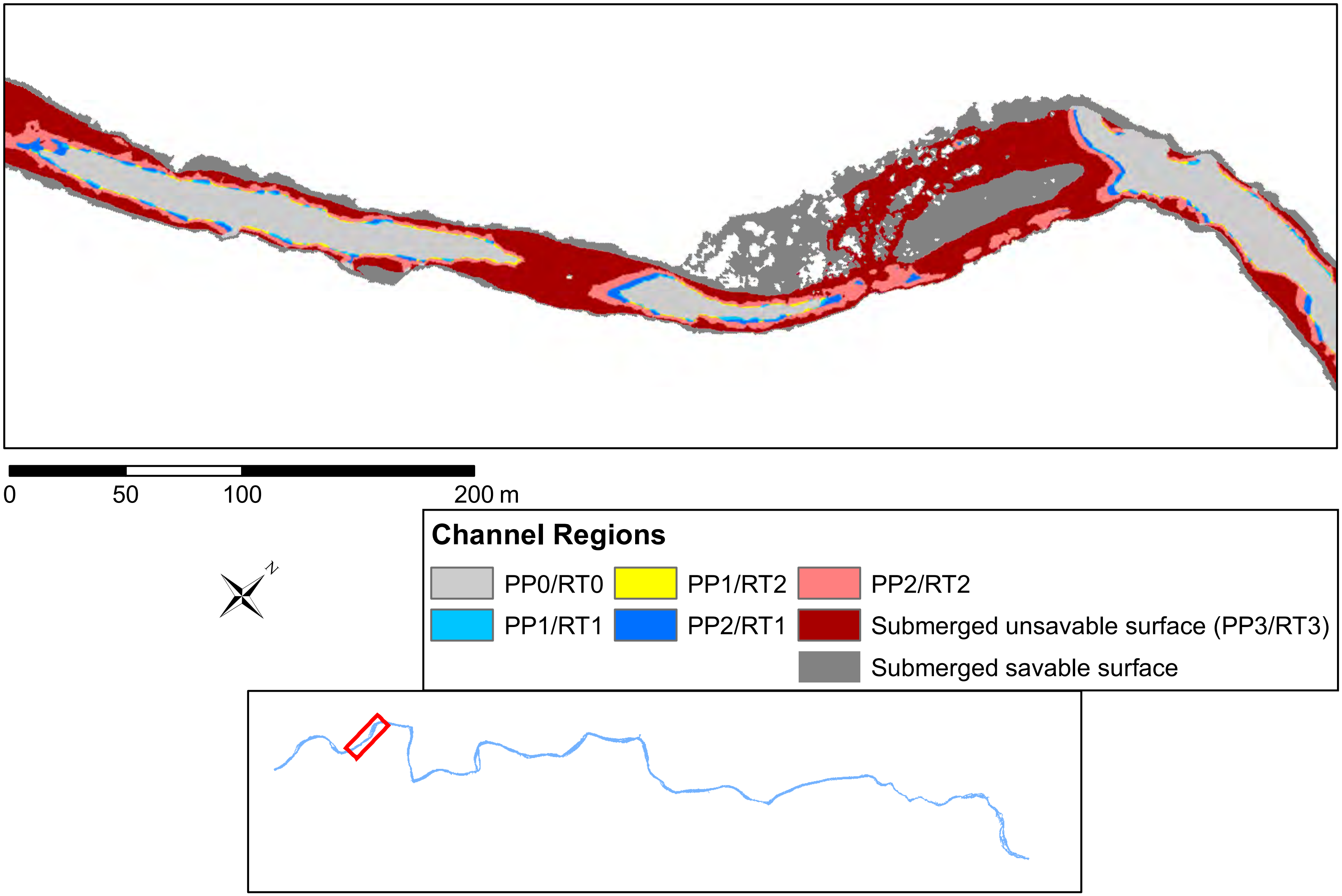

SYR Submerged Unsavable Surface Hazards for Upright Body at 31 m^3/s, p. 21

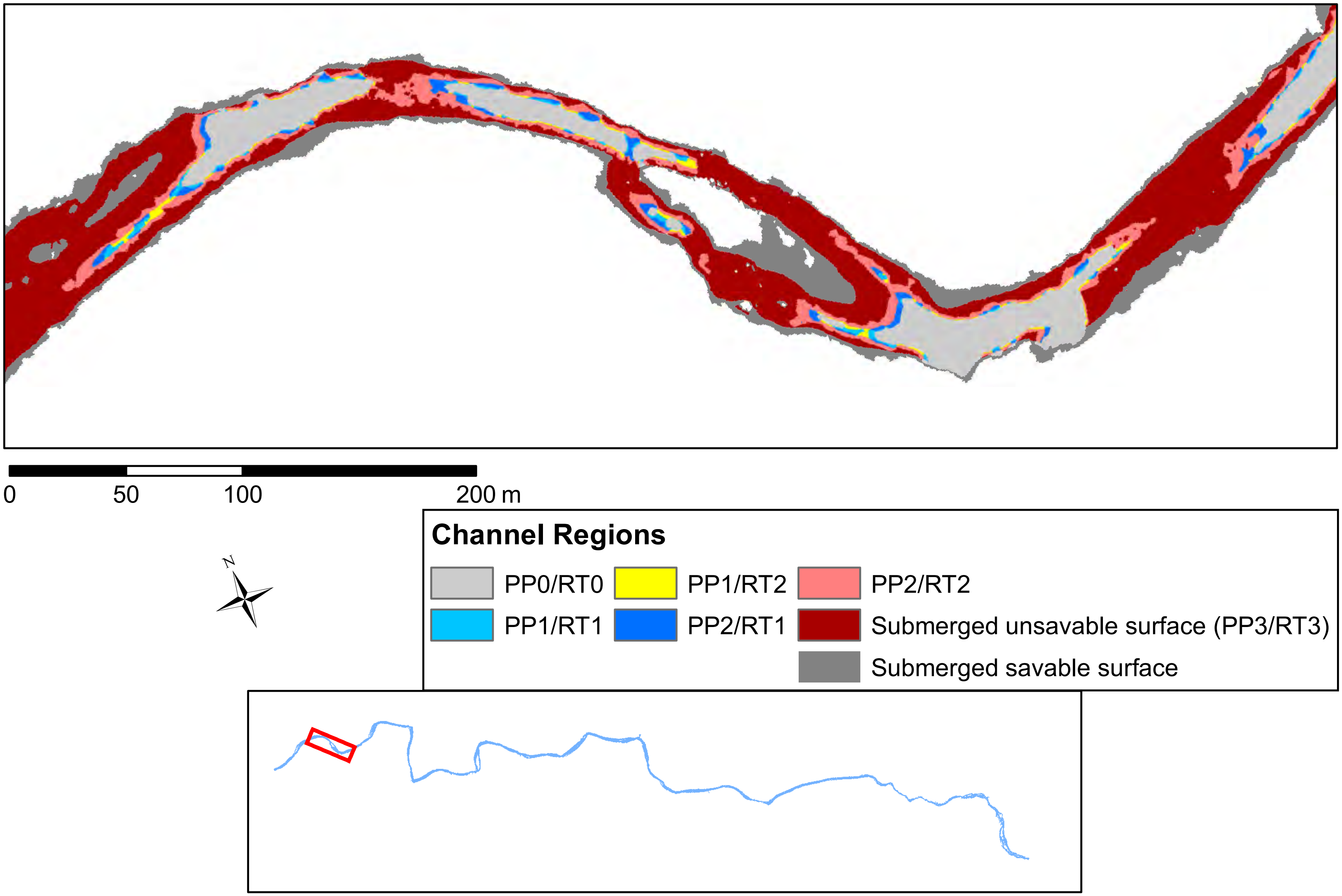

SYR Submerged Unsavable Surface Hazards for Upright Body at 31 m^3/s, p. 22

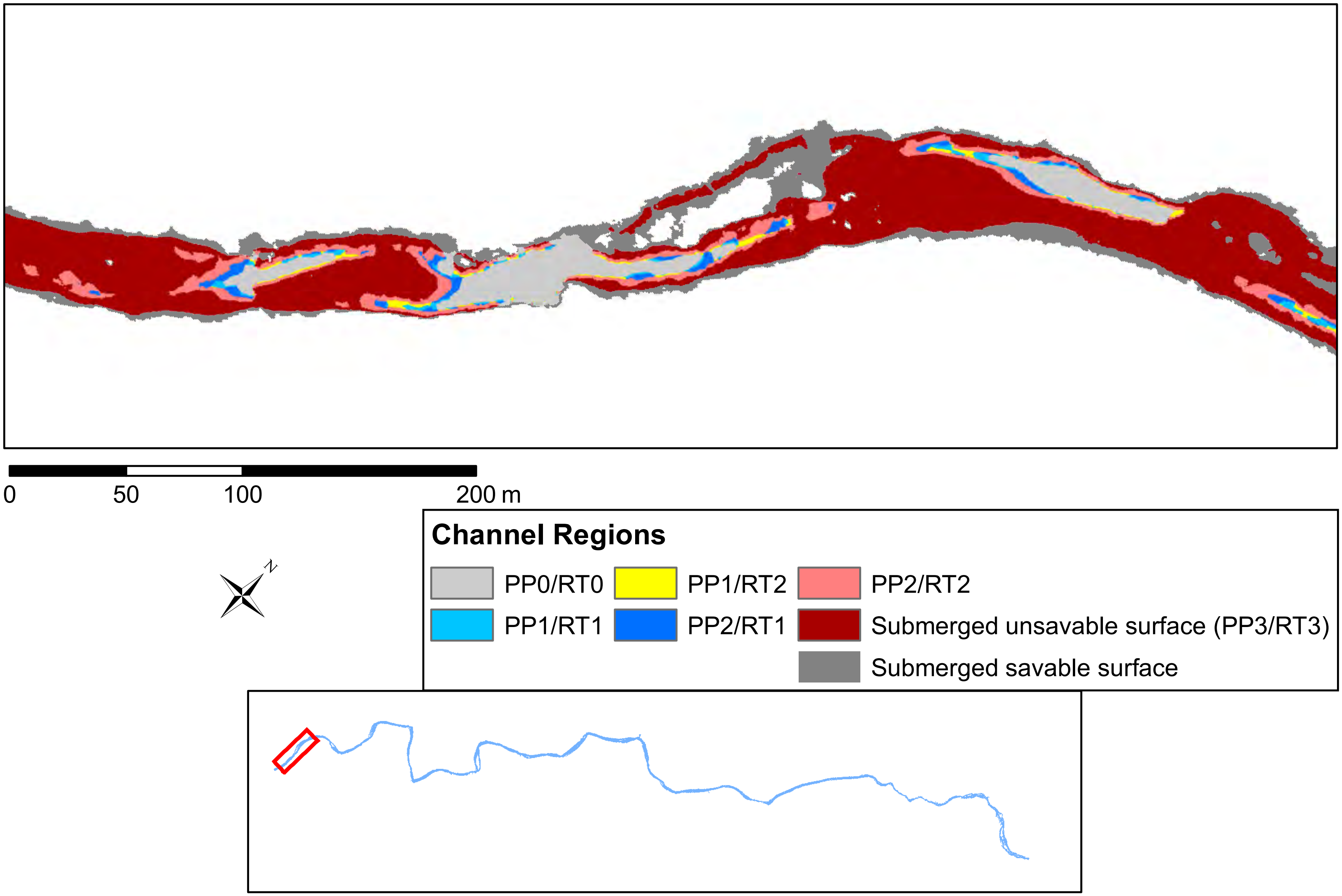

SYR Submerged Unsavable Surface Hazards for Upright Body at 31 m^3/s, p. 23

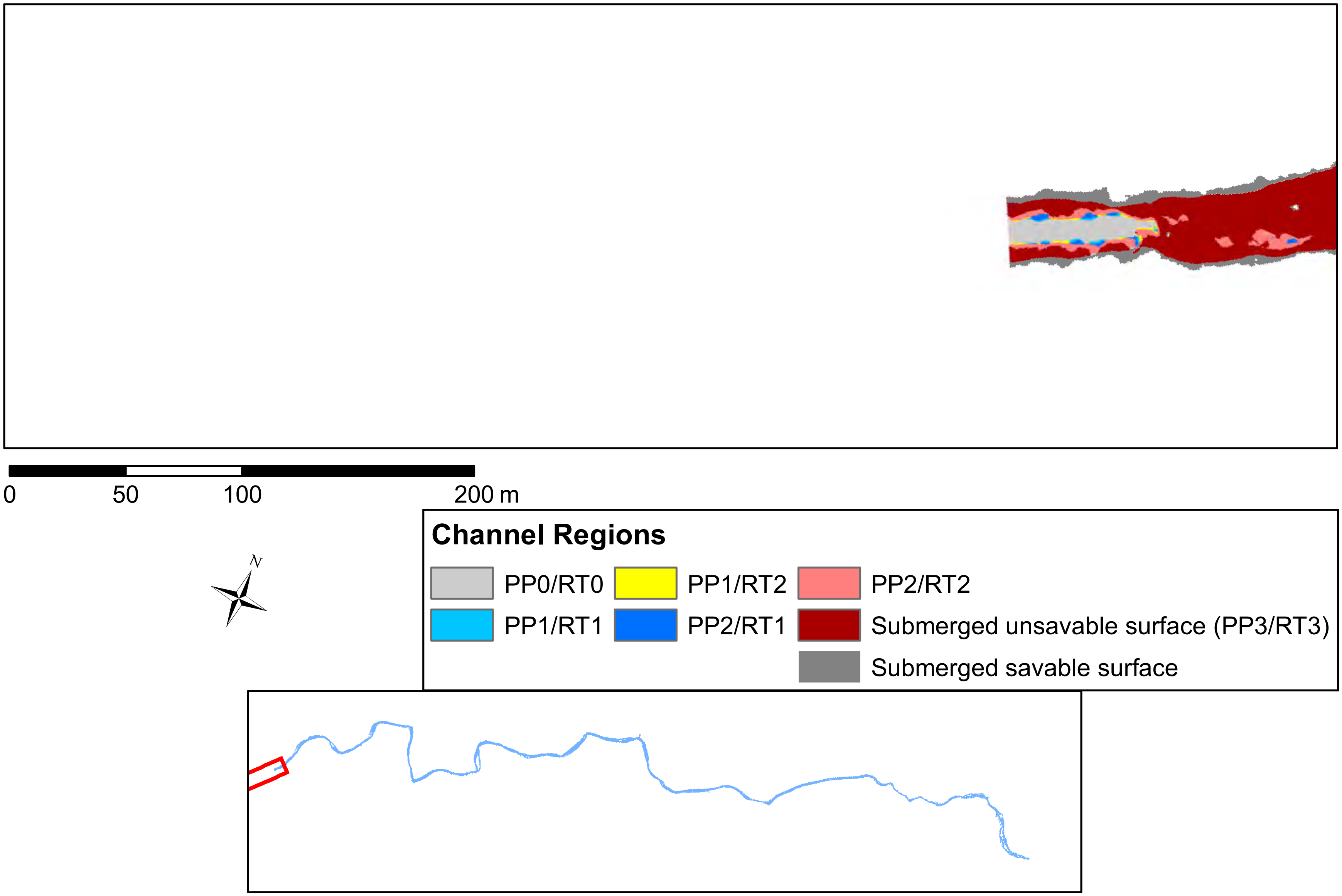

SYR Total Hazards for Upright Body at 31 m^3/s, p. 1

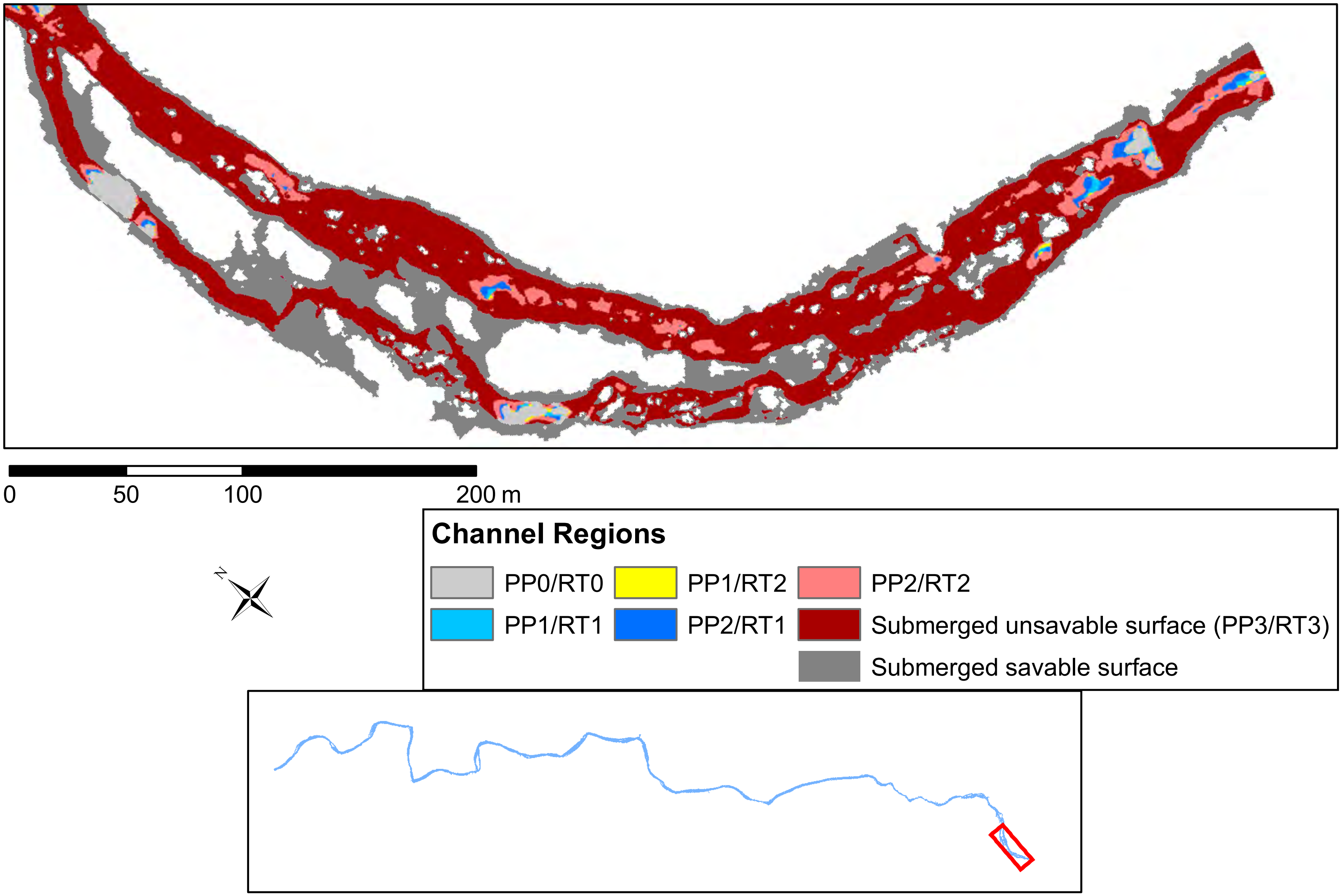

SYR Total Hazards for Upright Body at 31 m^3/s, p. 2

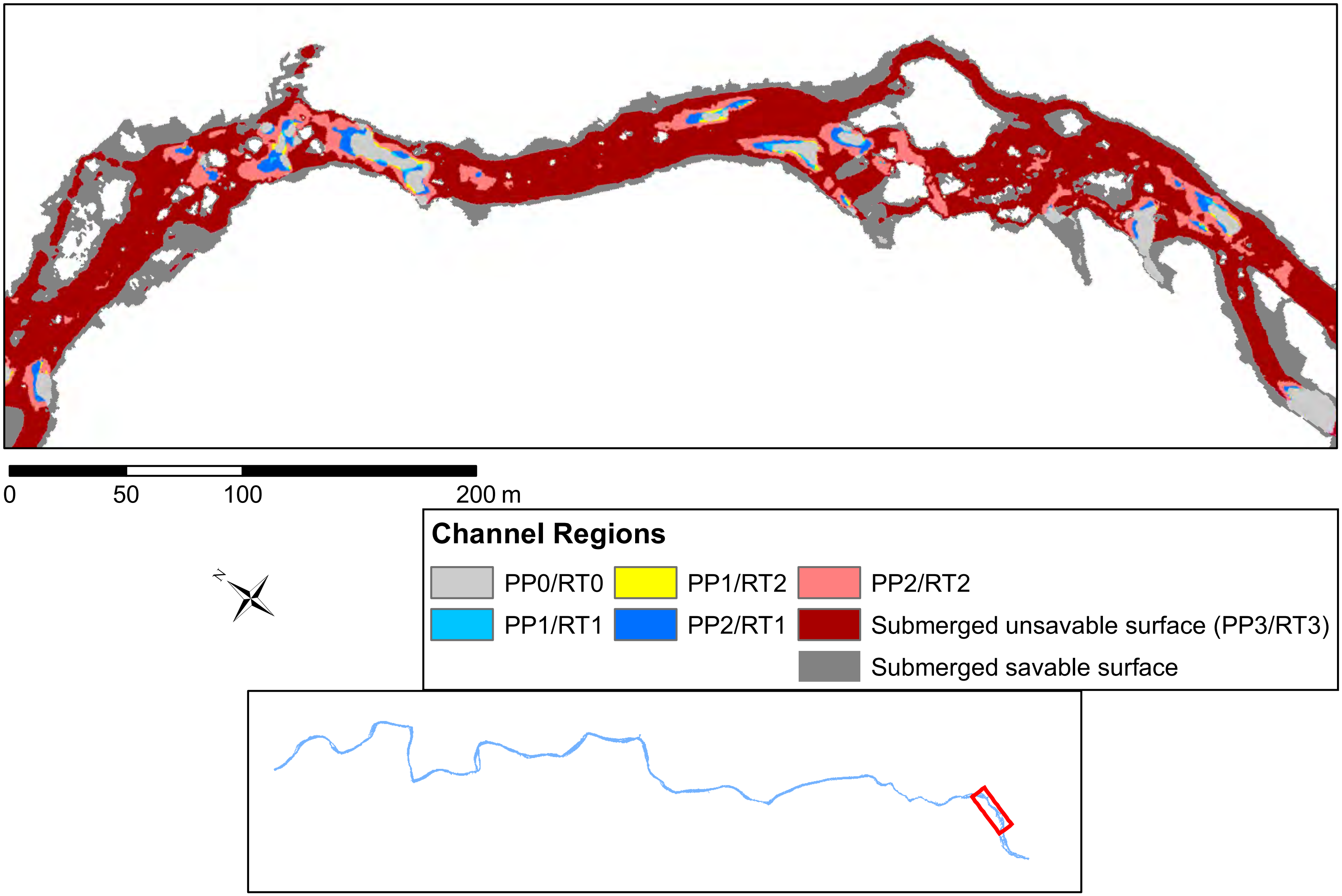

SYR Total Hazards for Upright Body at 31 m^3/s, p. 3

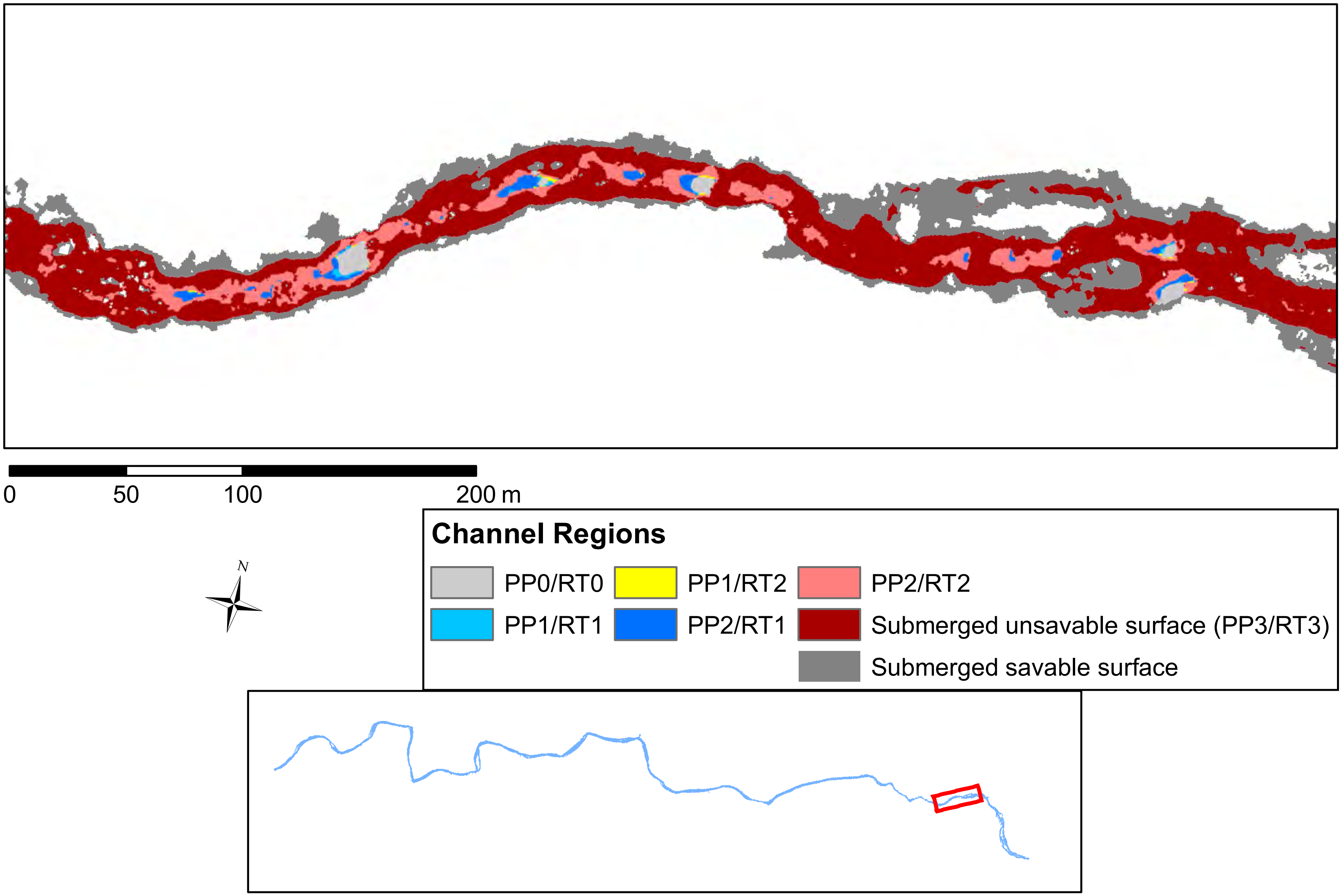

SYR Total Hazards for Upright Body at 31 m^3/s, p. 4

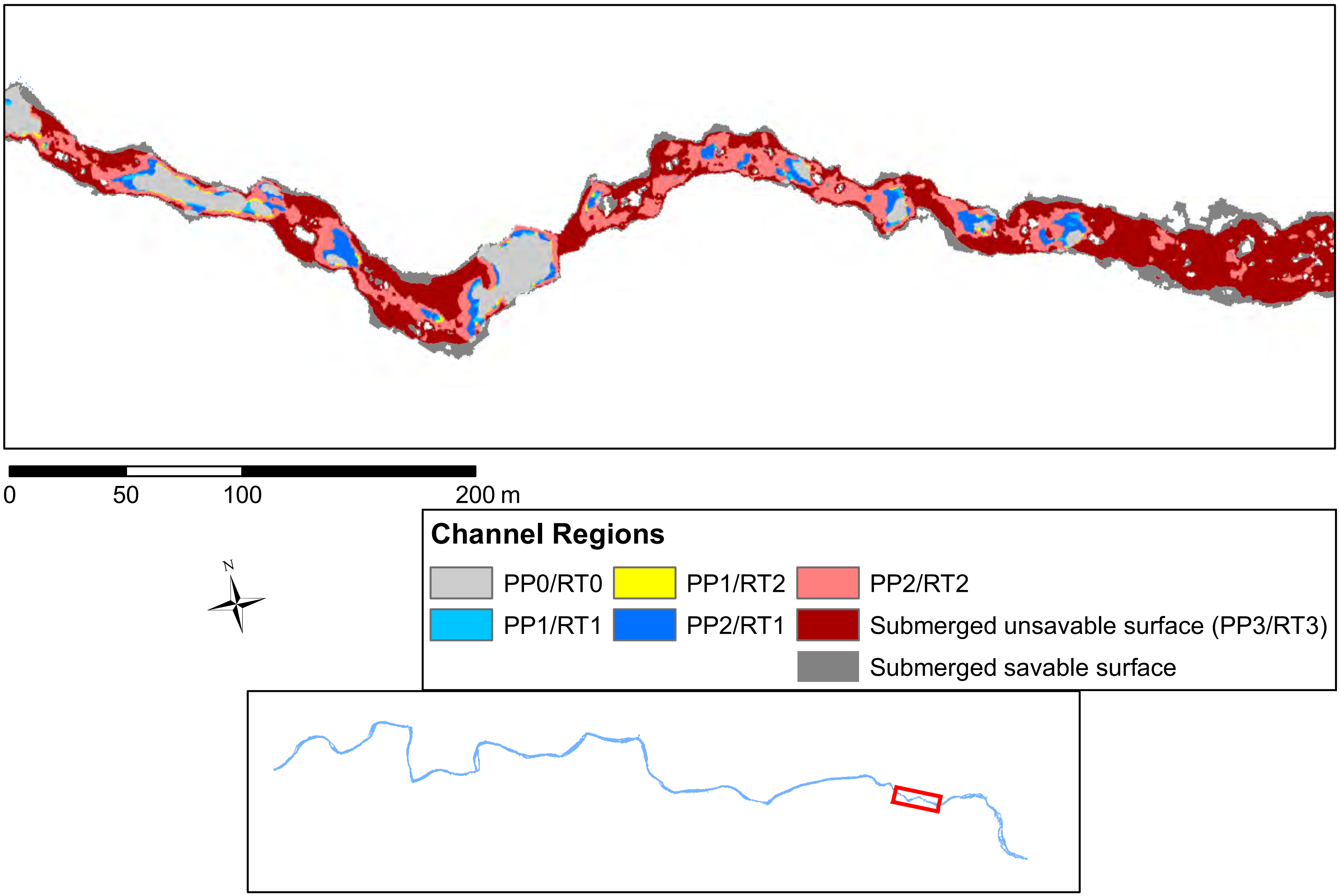

SYR Total Hazards for Upright Body at 31 m^3/s, p. 5

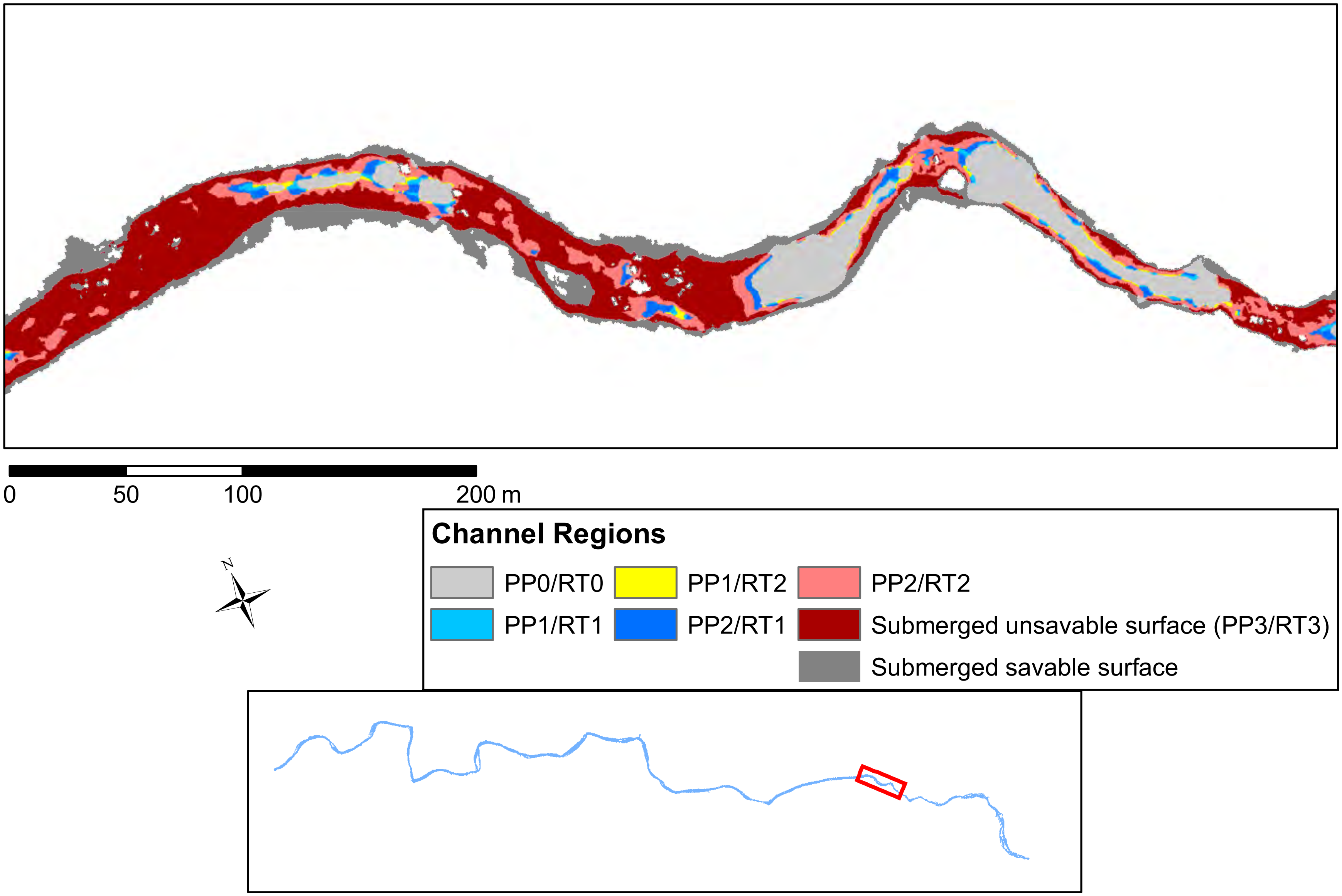

SYR Total Hazards for Upright Body at 31 m^3/s, p. 6

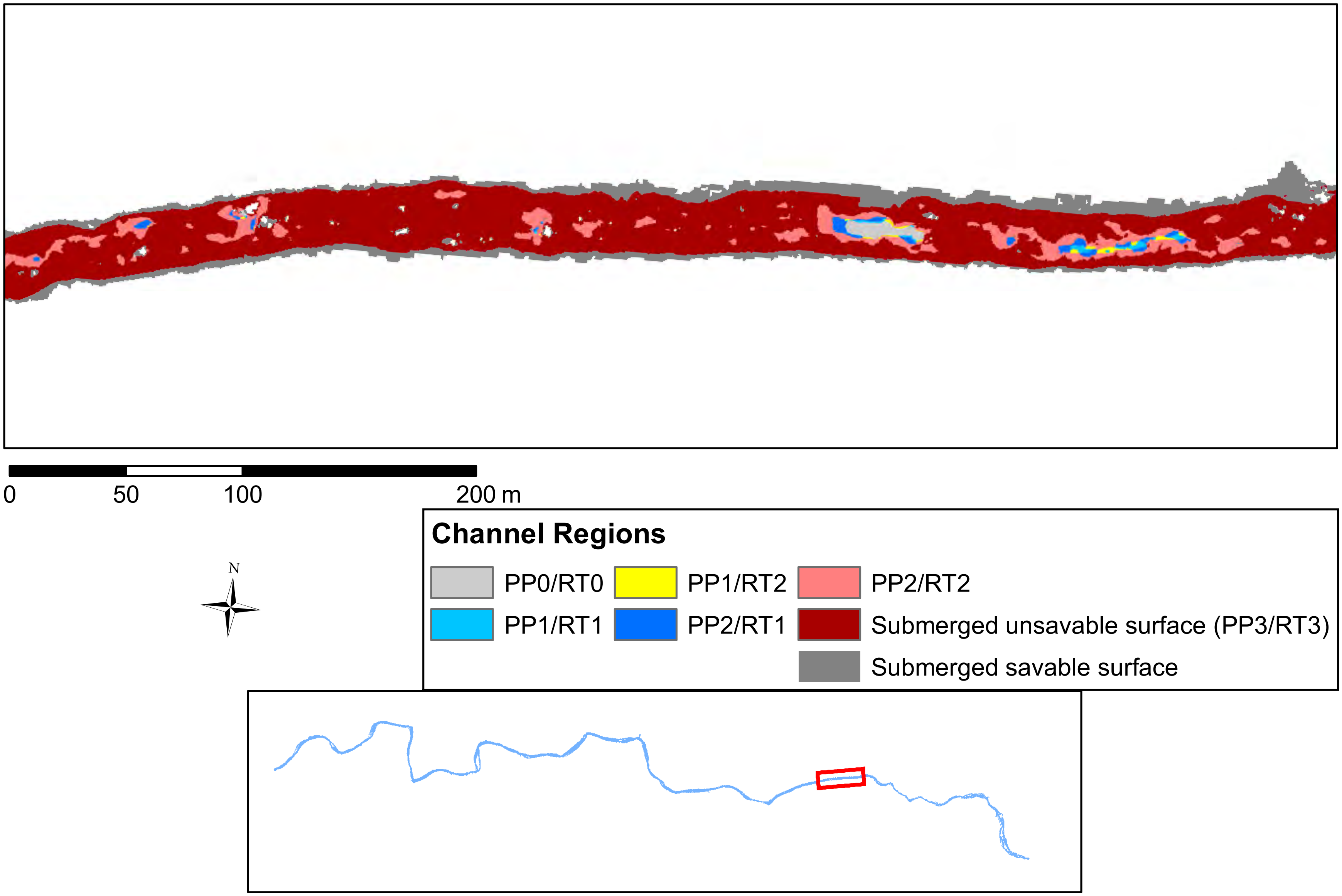

SYR Total Hazards for Upright Body at 31 m^3/s, p. 7

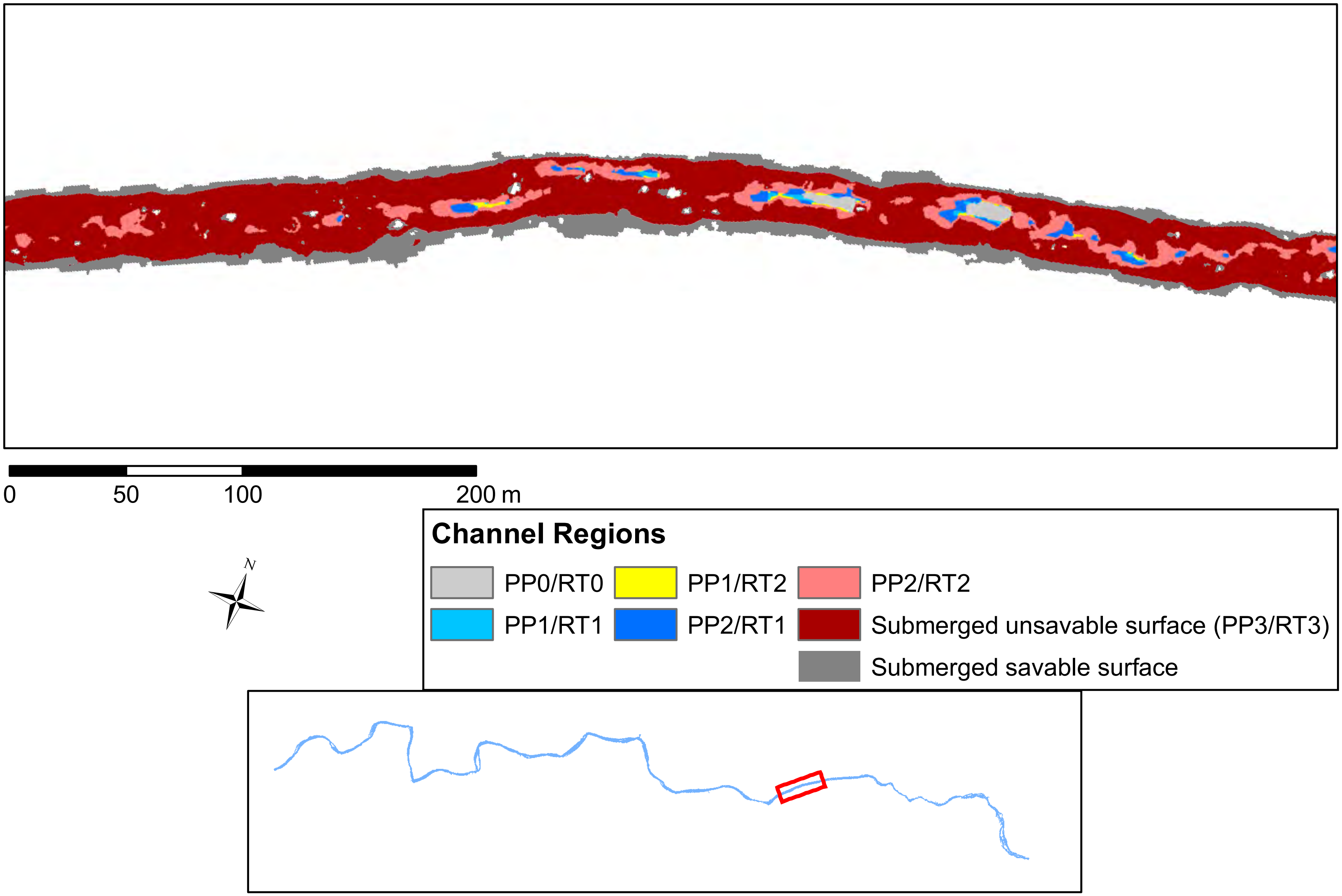

SYR Total Hazards for Upright Body at 31 m^3/s, p. 8

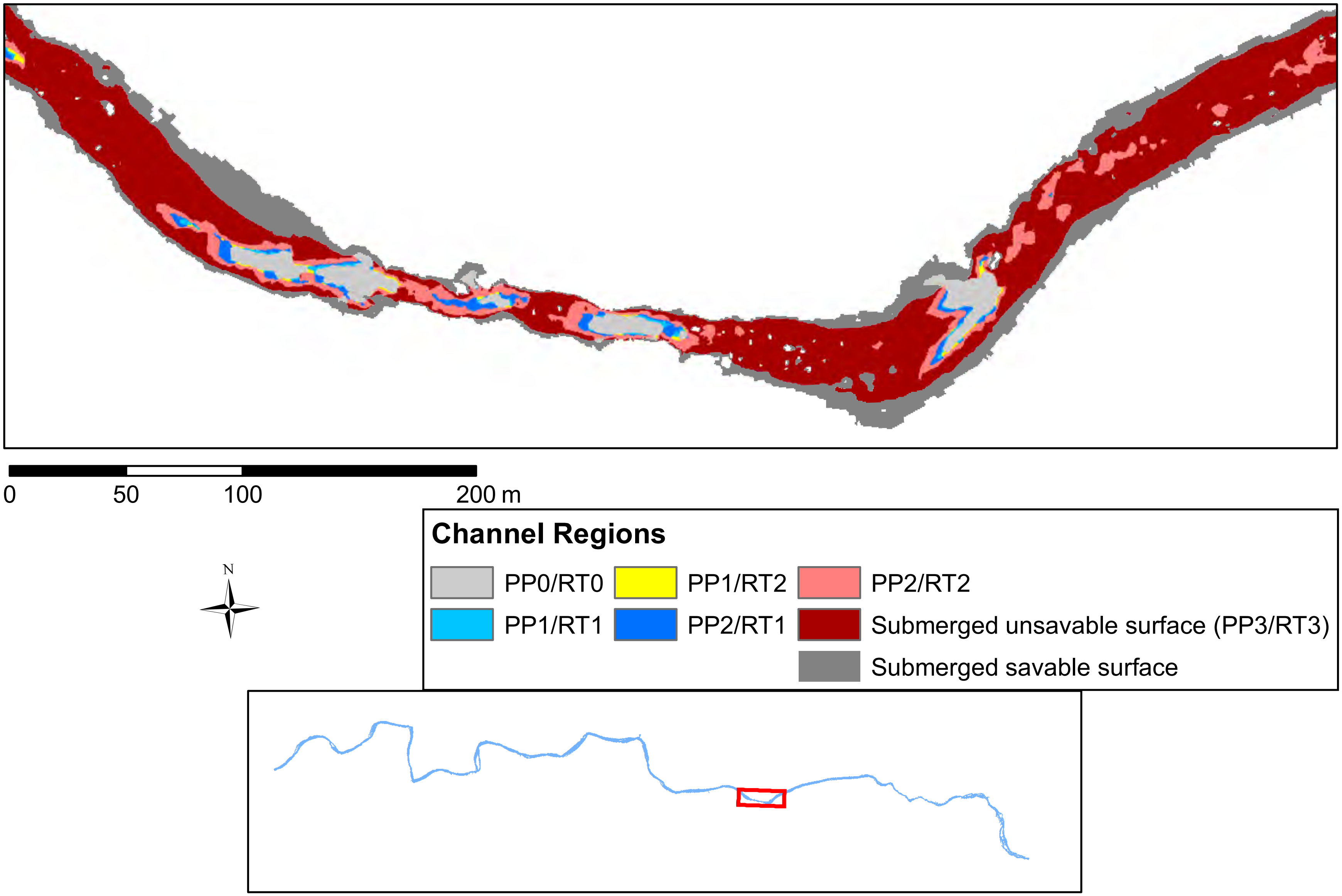

SYR Total Hazards for Upright Body at 31 m^3/s, p. 9

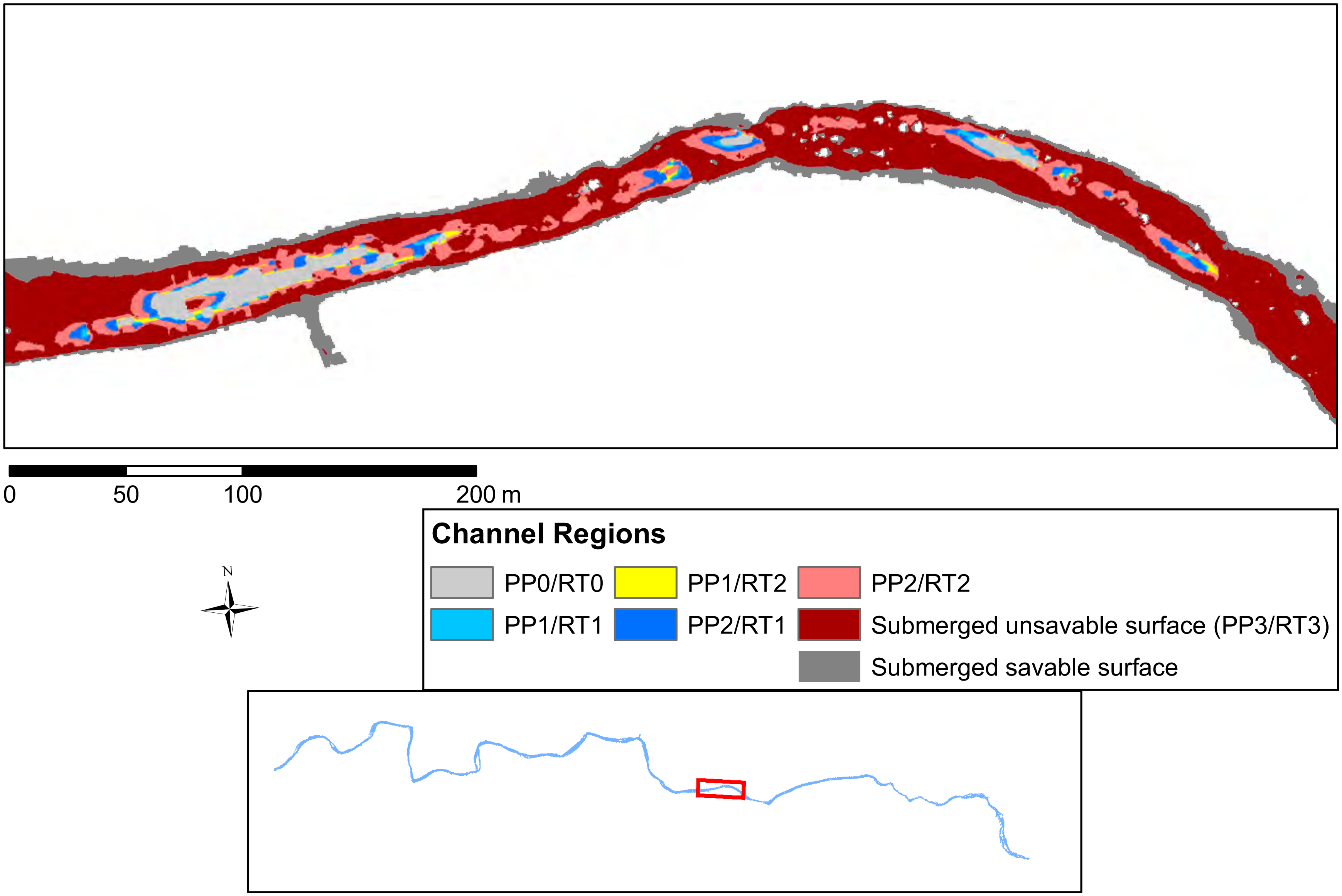

SYR Total Hazards for Upright Body at 31 m^3/s, p. 10

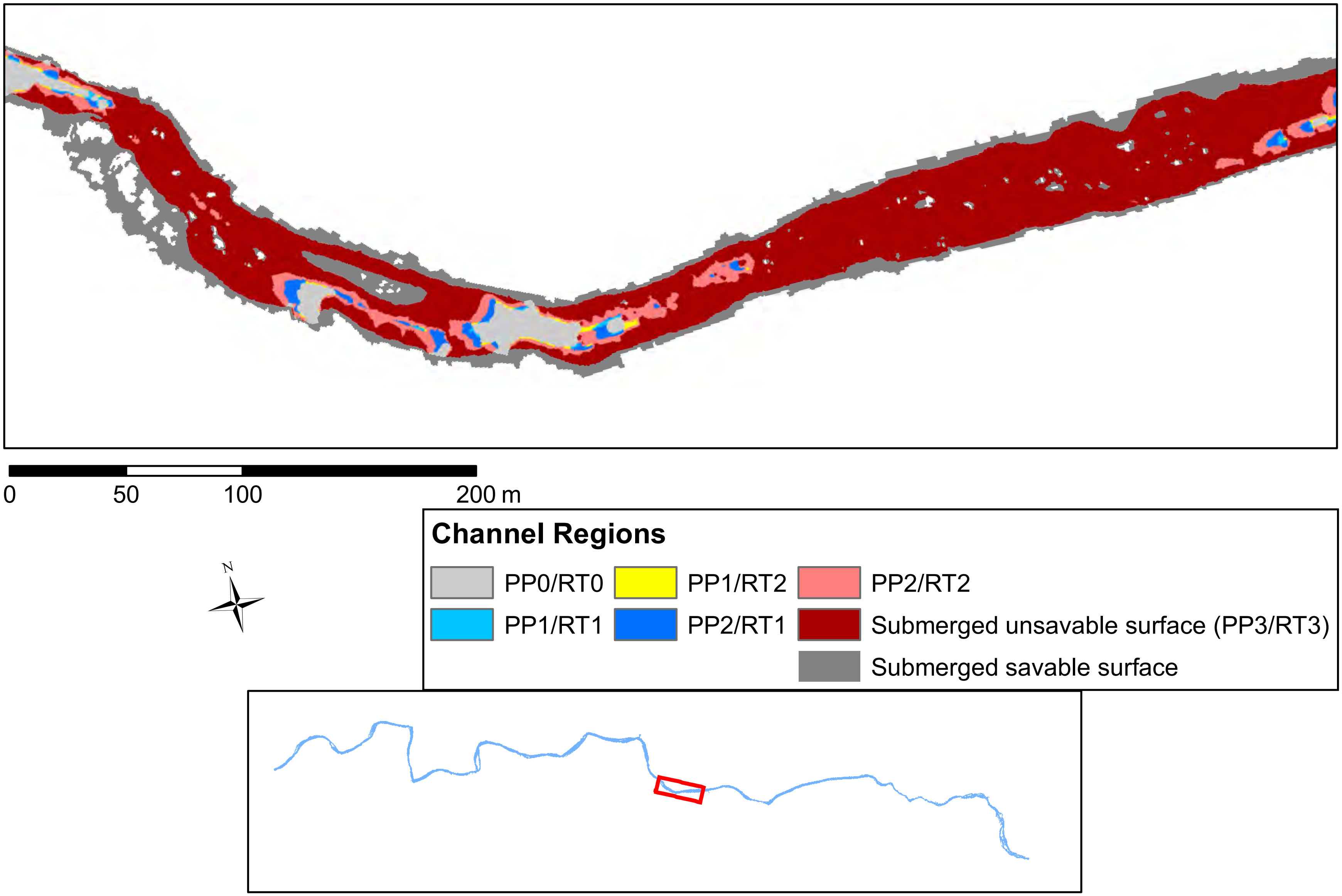

SYR Total Hazards for Upright Body at 31 m^3/s, p. 11

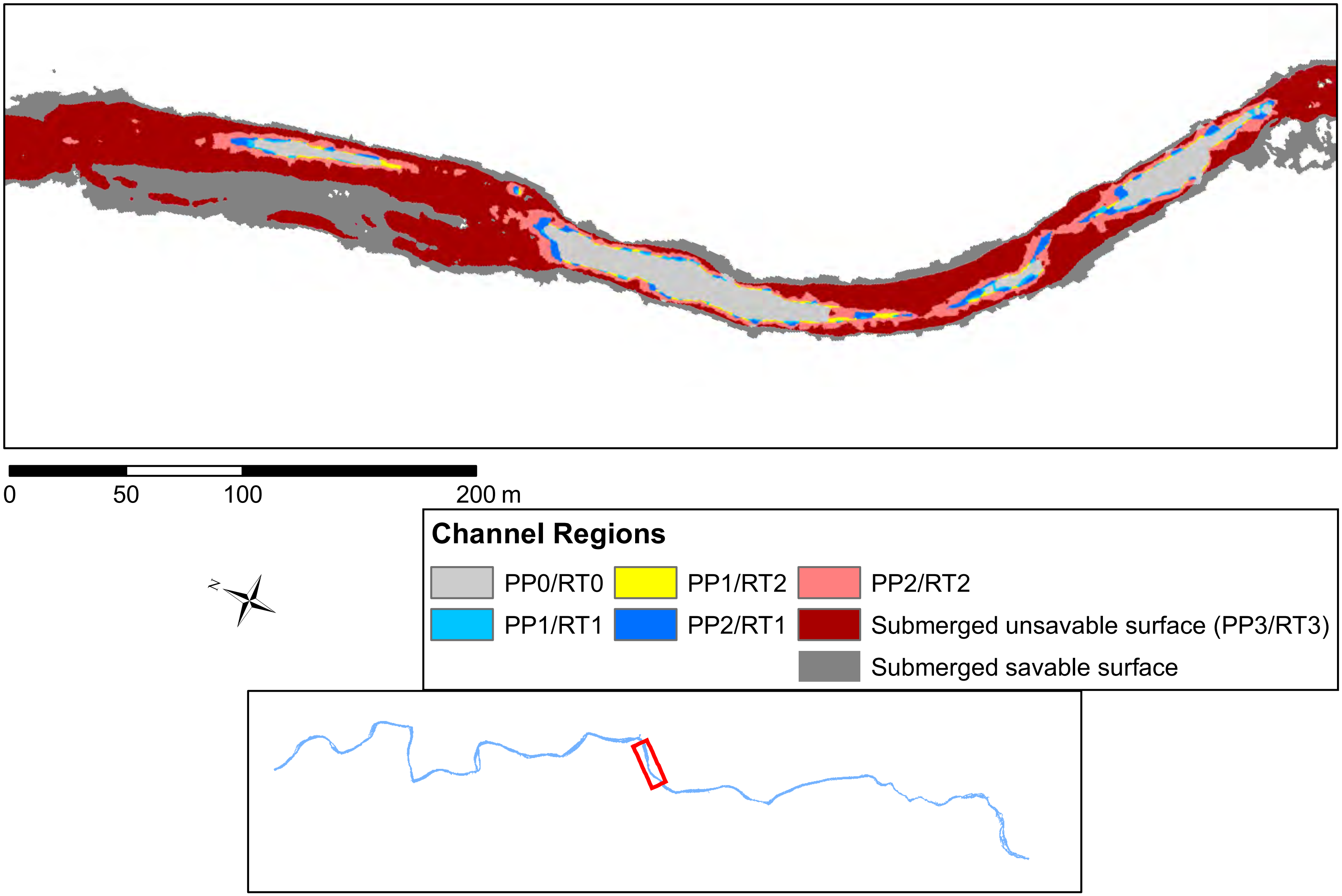

SYR Total Hazards for Upright Body at 31 m^3/s, p. 12

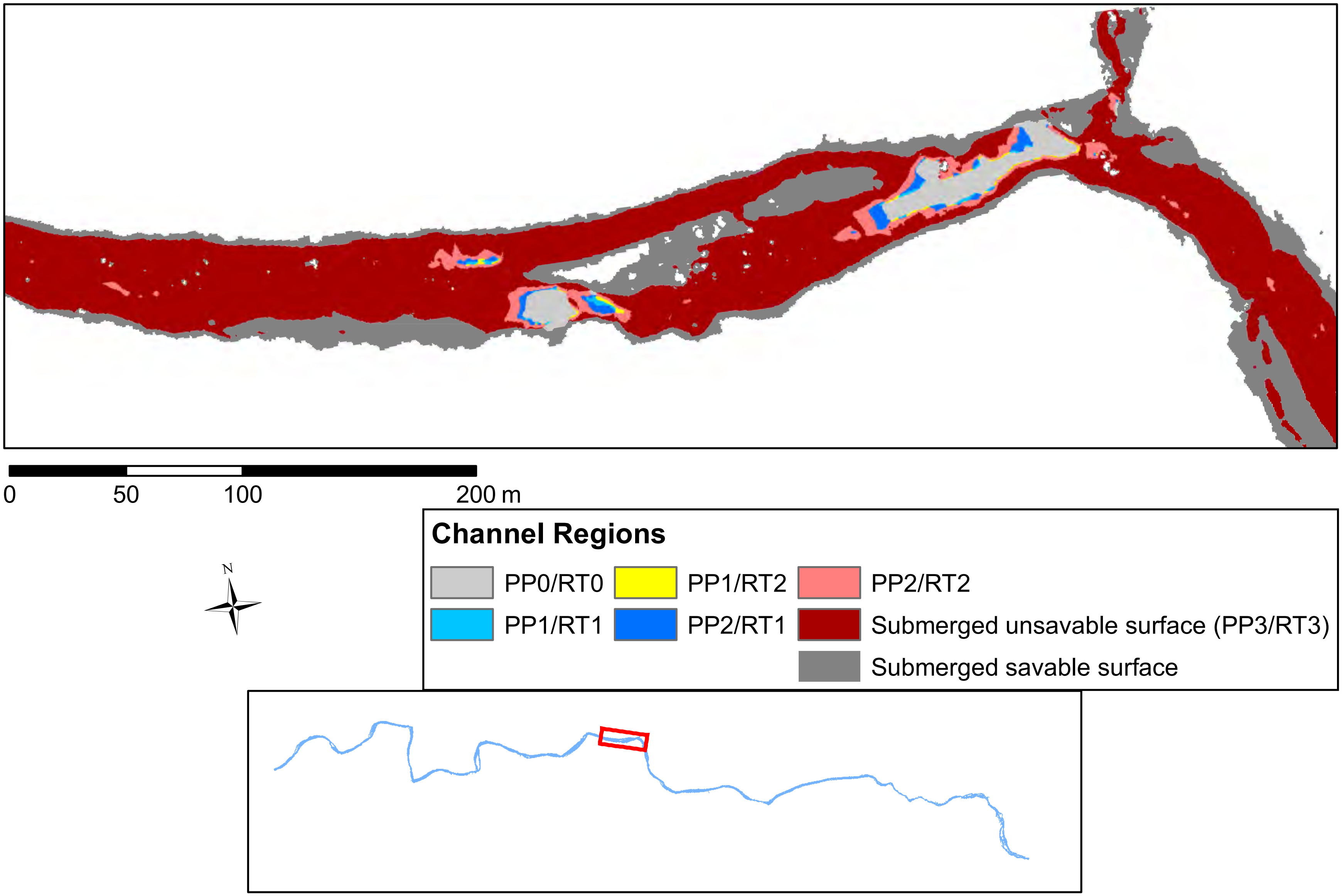

SYR Total Hazards for Upright Body at 31 m^3/s, p. 13

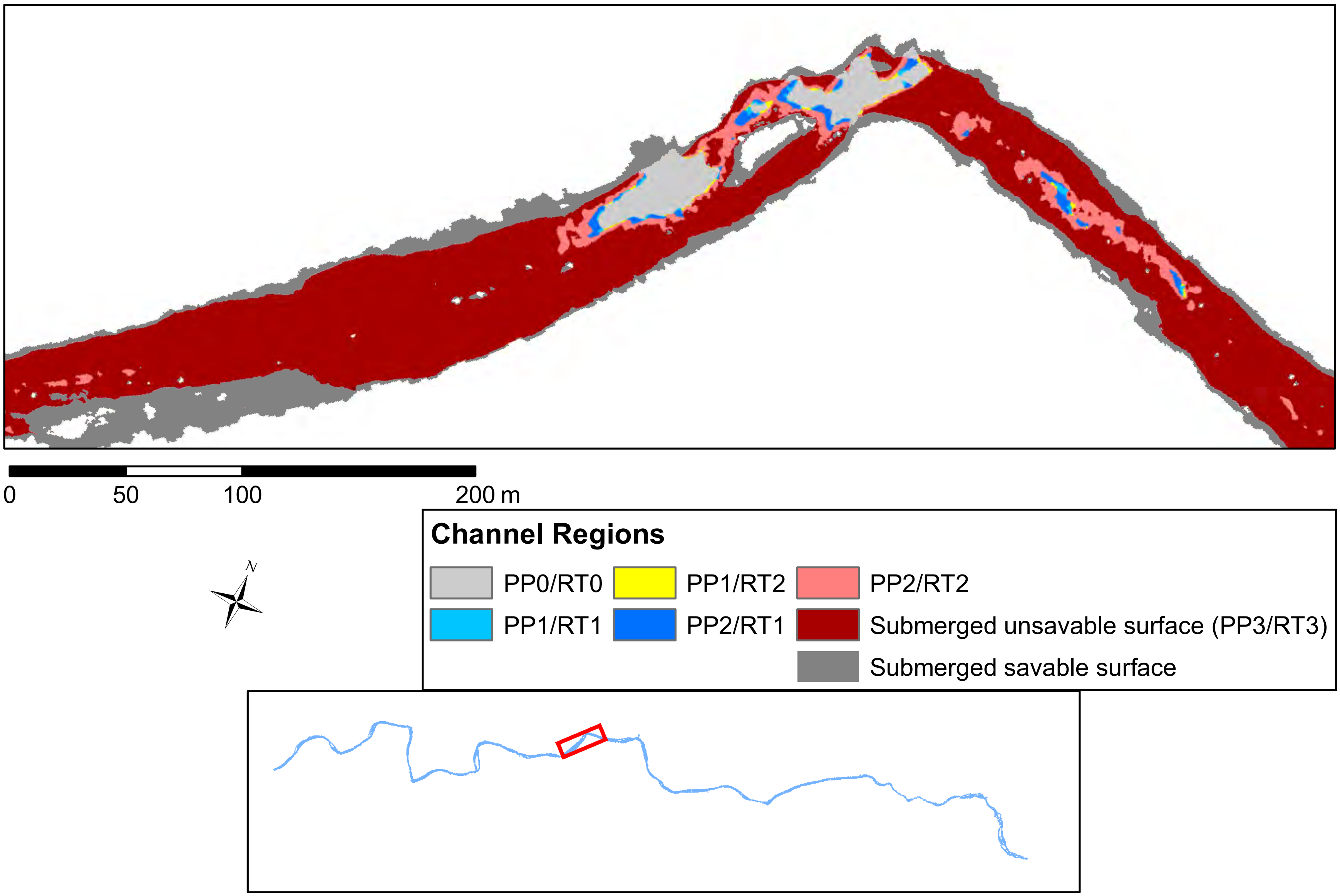

SYR Total Hazards for Upright Body at 31 m^3/s, p. 14

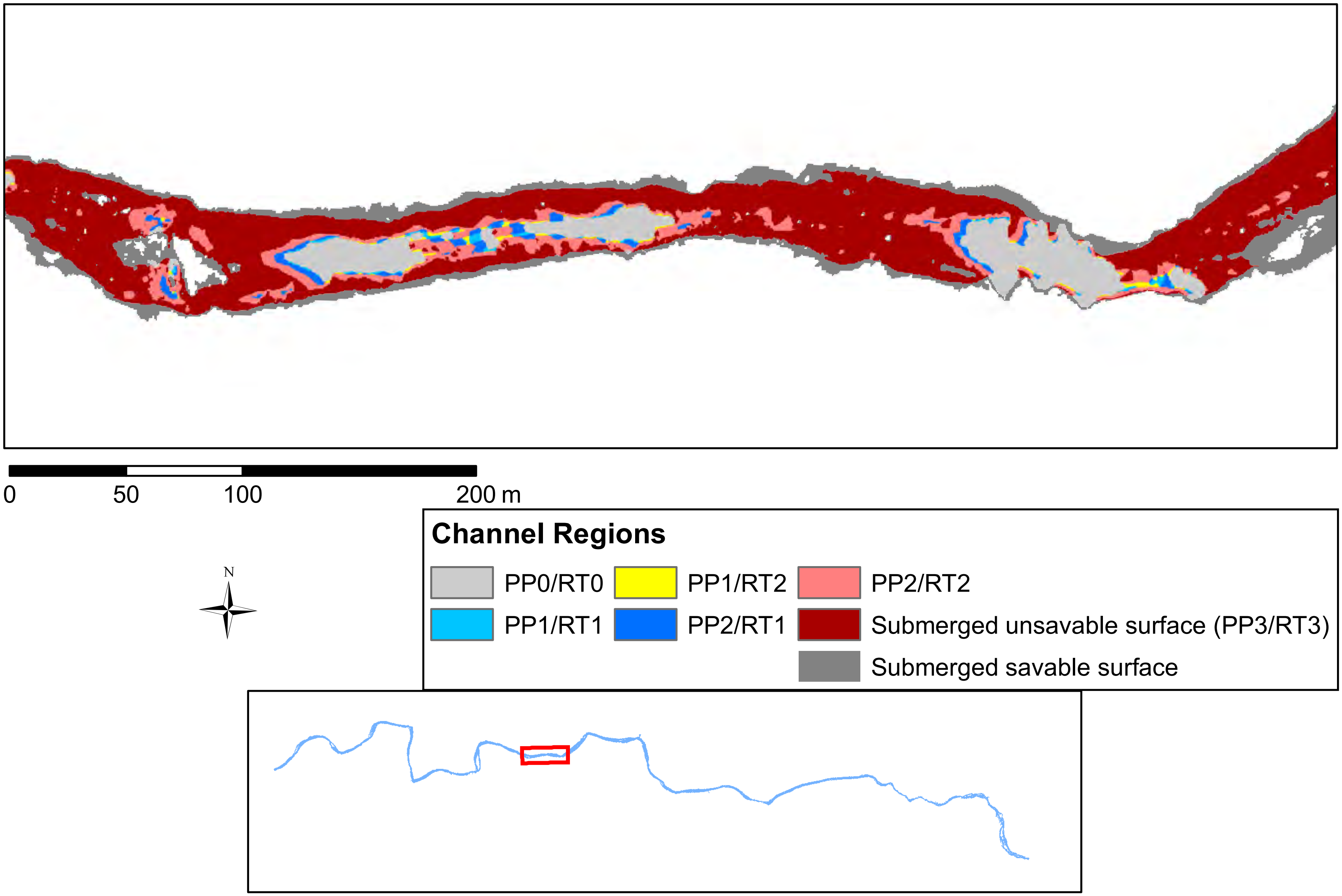

SYR Total Hazards for Upright Body at 31 m^3/s, p. 15

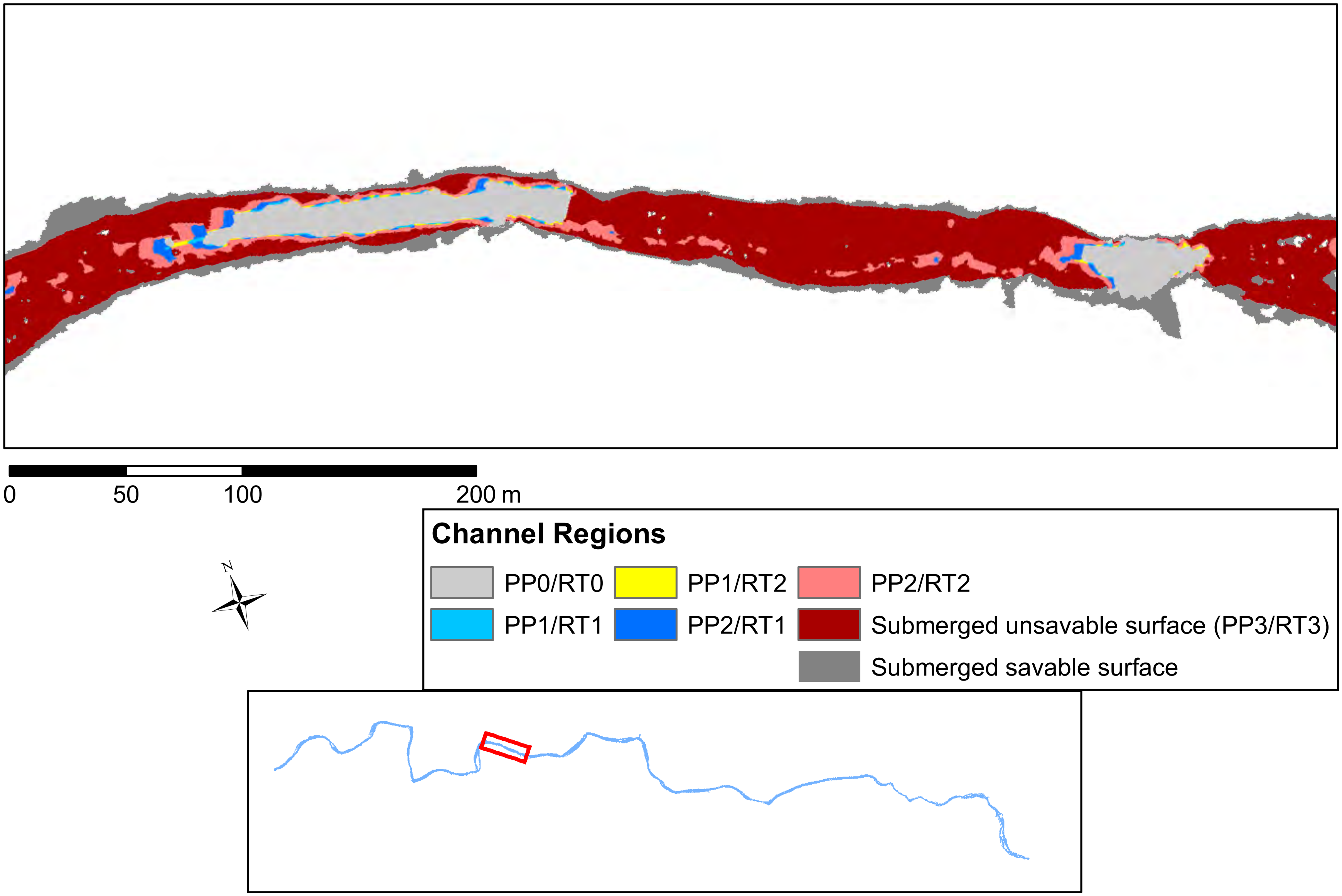

SYR Total Hazards for Upright Body at 31 m^3/s, p. 16

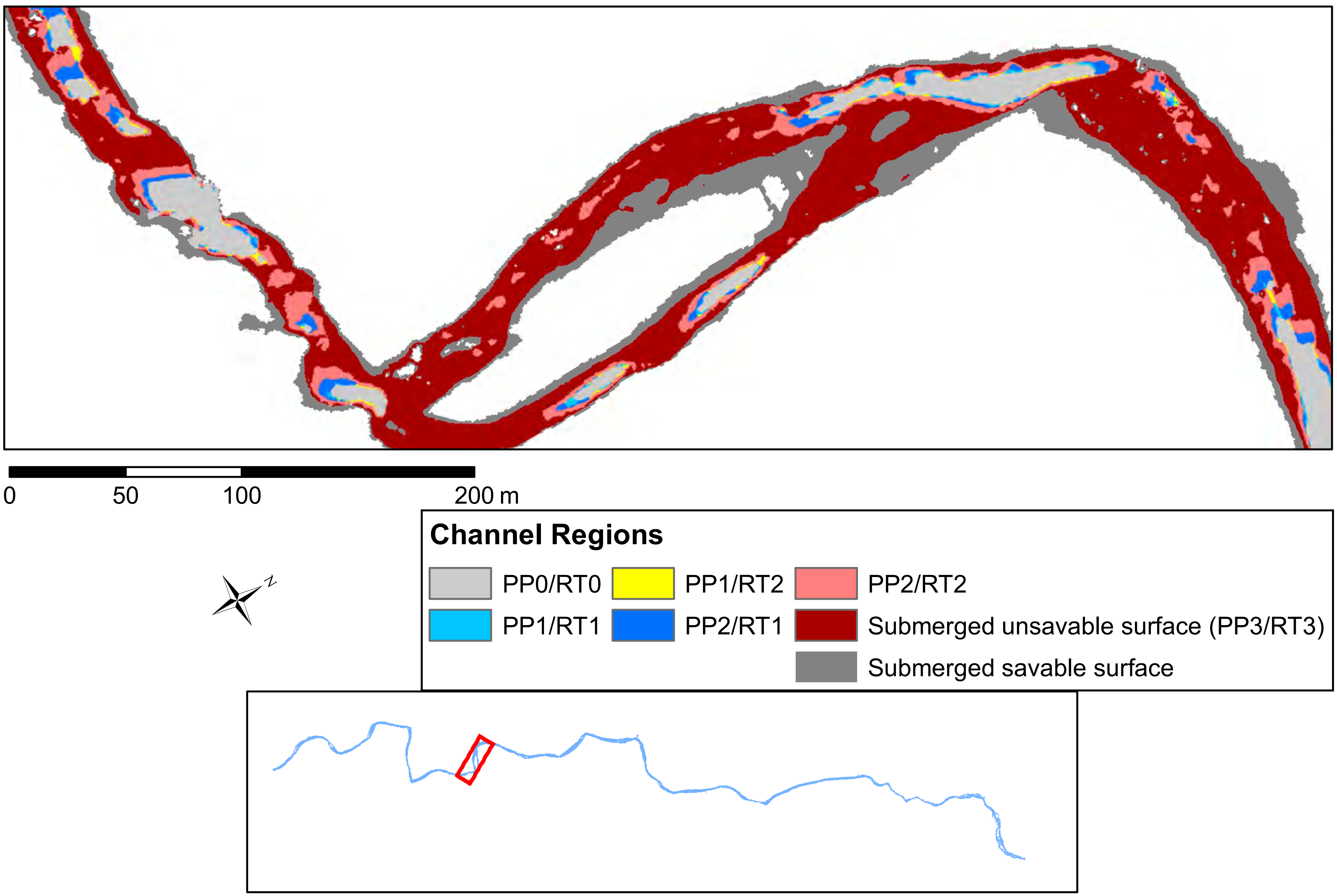

SYR Total Hazards for Upright Body at 31 m^3/s, p. 17

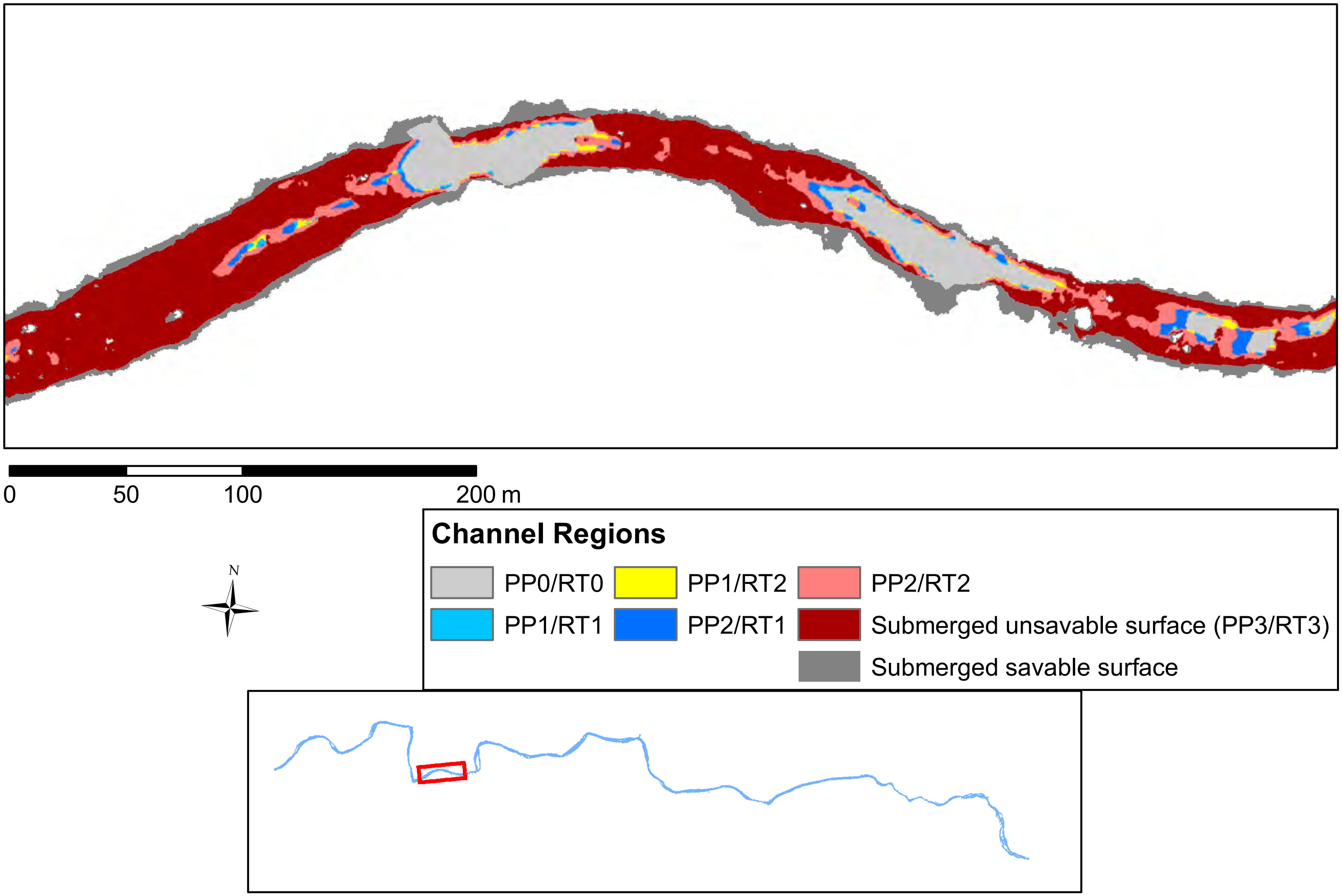

SYR Total Hazards for Upright Body at 31 m^3/s, p. 18

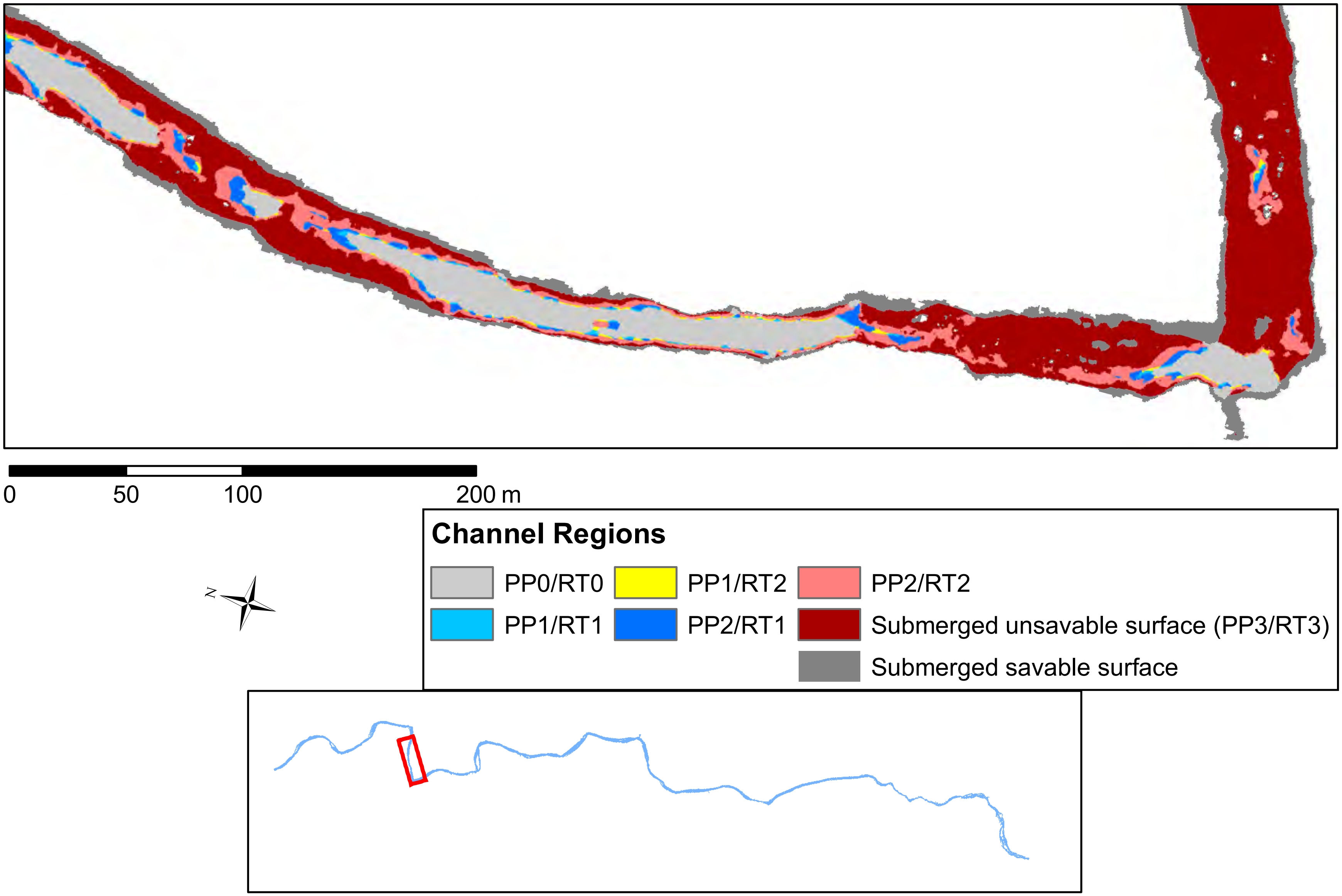

SYR Total Hazards for Upright Body at 31 m^3/s, p. 19

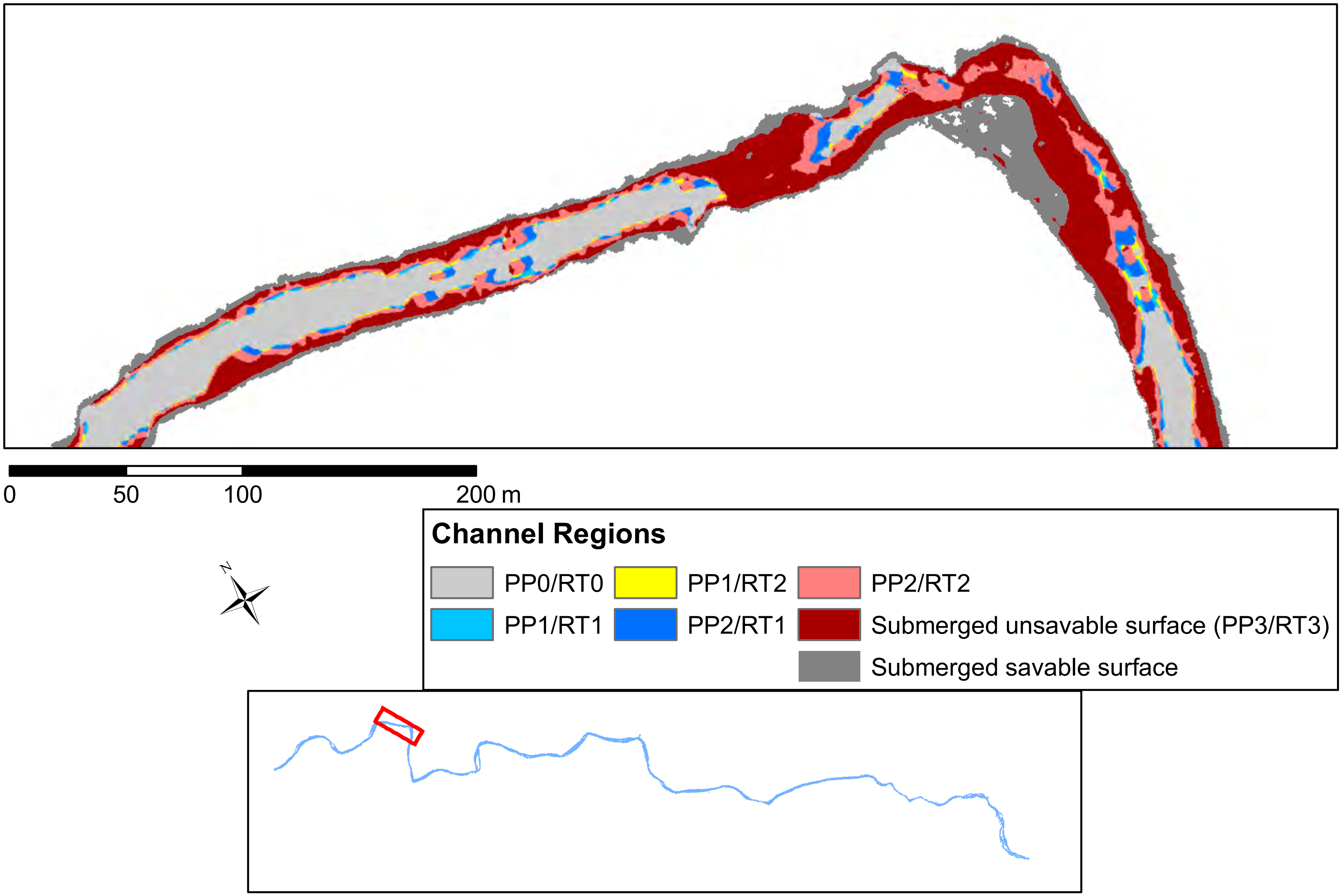

SYR Total Hazards for Upright Body at 31 m^3/s, p. 20

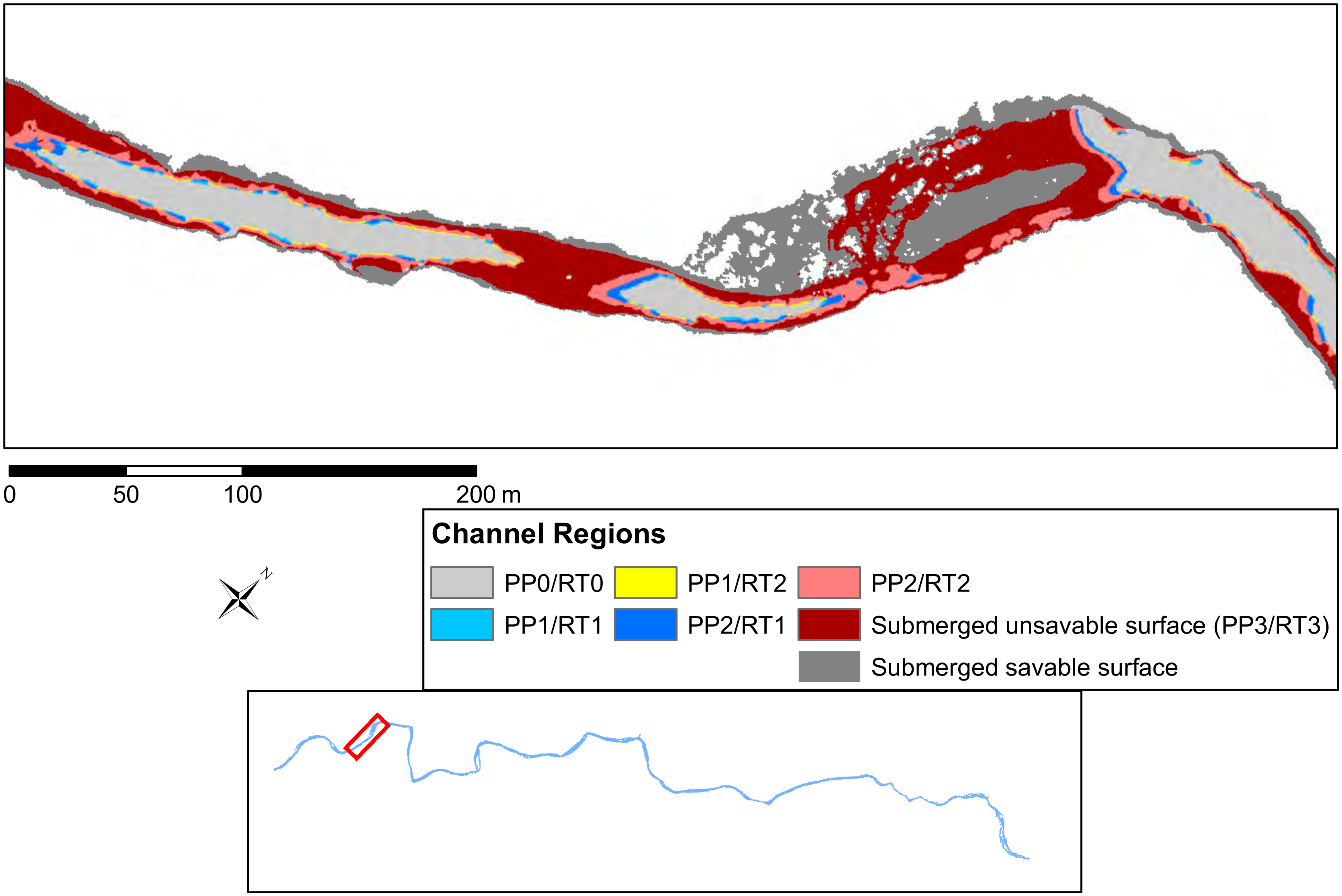

SYR Total Hazards for Upright Body at 31 m^3/s, p. 21

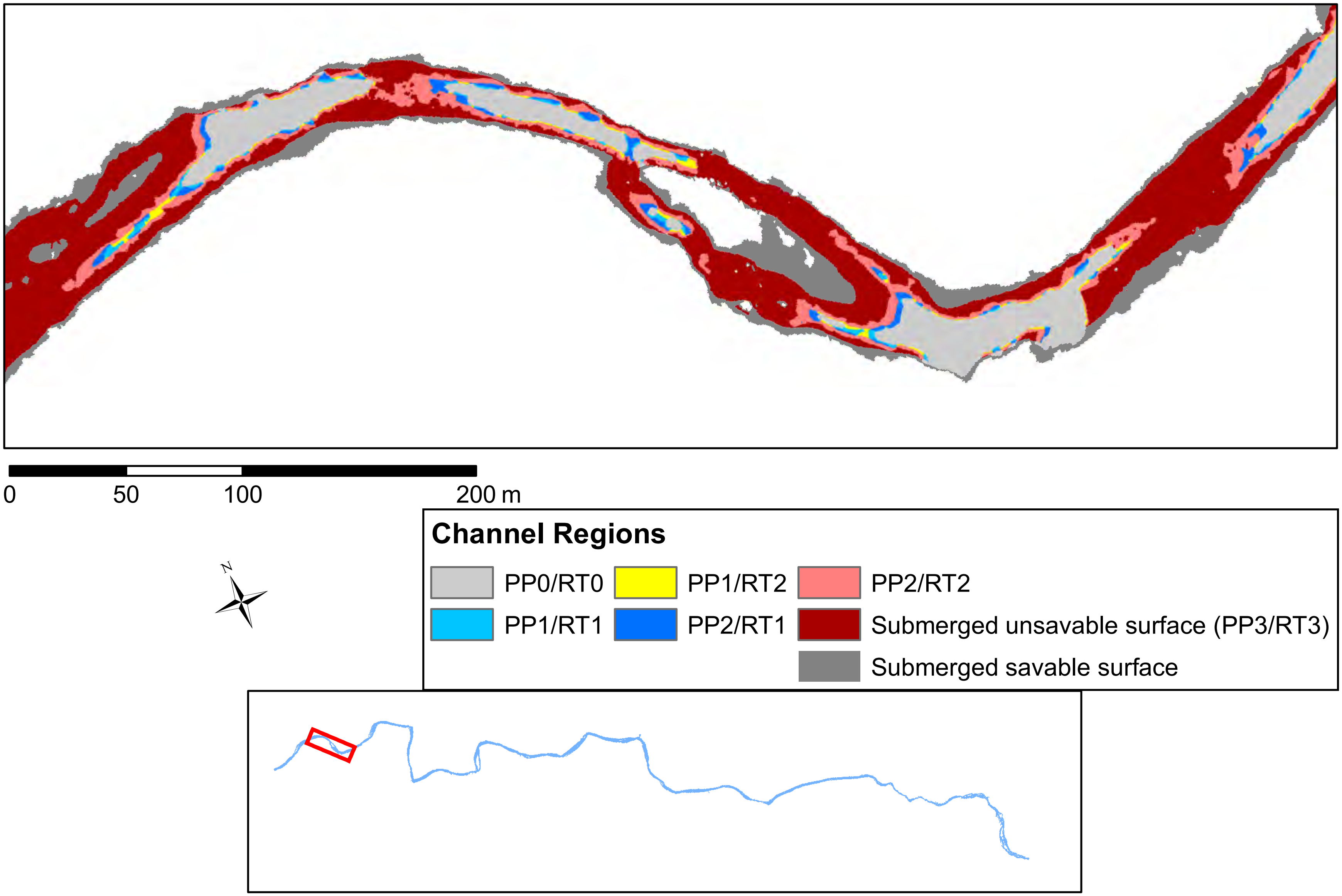

SYR Total Hazards for Upright Body at 31 m^3/s, p. 22

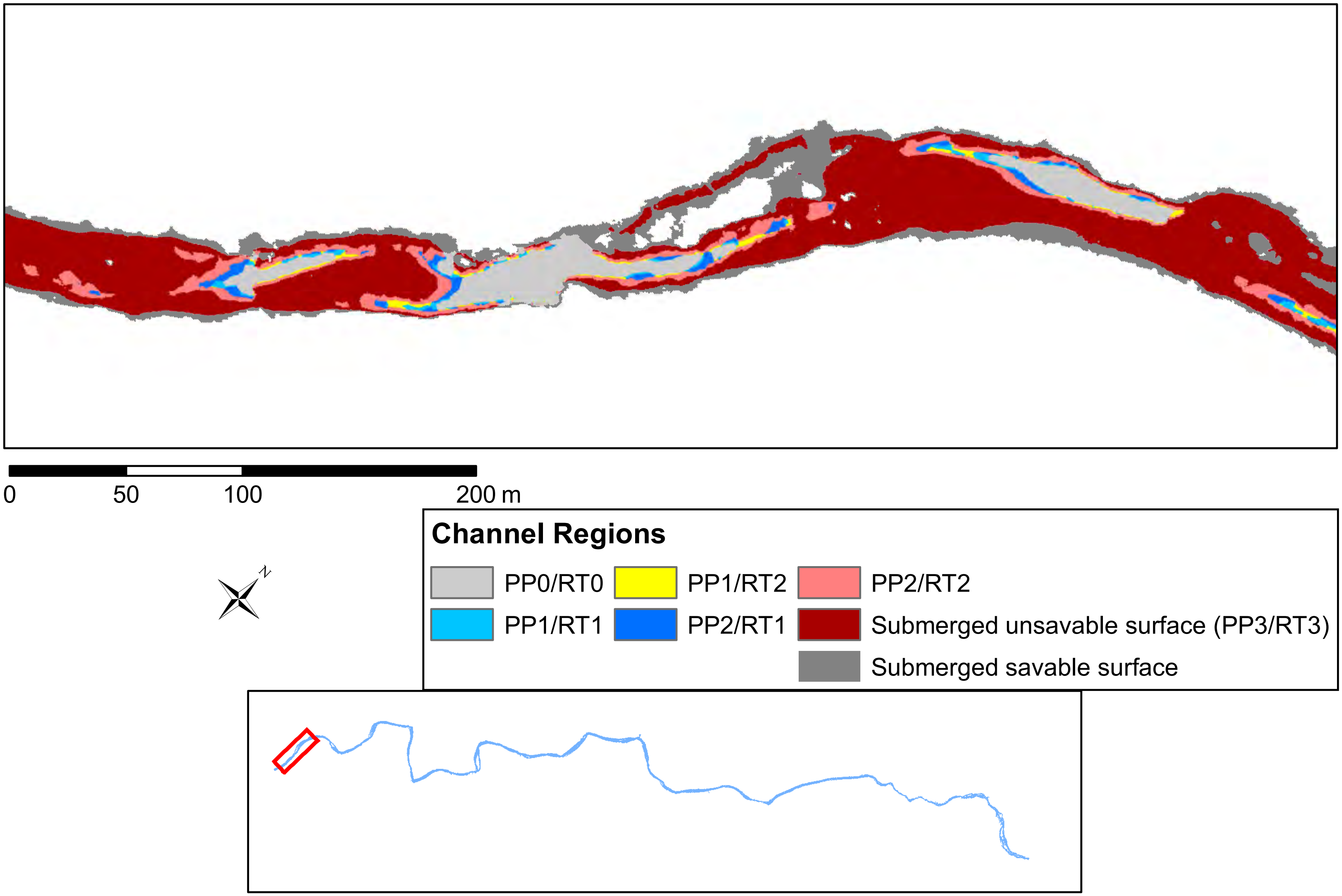

SYR Total Hazards for Upright Body at 31 m^3/s, p. 23